Charged Colloidal Suspensions in Confined Geometries

Dissertation Thesis

to obtain the degree

"Doktor der Naturwissenschaften"

at the Fachbereich 08,

Physik, Mathematik und Informatik

of the Johannes Gutenberg Universität, Mainz

Submitted by

Ana Barreira Fontecha

born in Valencia, Spain

Mainz, March 2009

A Ferxu

Abstract

The behaviour of charged colloidal suspensions under geometrical confinement has been studied. We used different wedge-like geometries which allow a continuous variation of the distance between the plates. At low salt concentrations the confinement of suspensions in fluid phase cells revealed that the particles accumulate in the cusp of the wedge forming crystalline ordered structures. We present systematic experiments to understand the accumulation effect in the narrow part of the cell. We conclude that the effect is due to electrostatic trapping, which is confirmed by a simple theoretical model proposed by Löwen et al.. Crystalline structures appear forming a characteristic sequence with increasing plate separation. This structural sequence has been already observed previously in confinement at wedge geometries, however, the small wedge angles achieved in our experiments allowed the observation of new structures. Some of these new structures show exotic arrangements and have no atomic counterpart. We also propose different transition mechanism models between the different structures based in the experimental observations. For that we assume that the particles behave as hard spheres subject to a high pressure. Finally, a cell with variable height was designed in order to study the complete phase behaviour of charged spheres confined between parallel plates. The preliminary results are compared with theoretical predictions.

Index

List of terms

Φ	Volume Fraction
n	Number of crystalline layers
$\mathbf{n_p}$	Particle number density
σ	Diameter of a spherical colloidal particle
$\mathbf{c_s}$	Salt concentration
κ	Screening parameter; its inverse is termed Debye length.
Z*	Effective charge
e	Electron charge
a	Radius of a spherical colloidal particle
a, b	Arbitrary lengths
d	Distance between crystalline layers
$\mathbf{k_B}$	The Boltzmann constant
T	Temperature
ε	Dielectric constant of the solvent
$\boldsymbol{\varepsilon_0}$	Vacuum permittivity
$\boldsymbol{\varepsilon_r}$	Relative dielectric constant
$\mathbf{N_A}$	Avogadro's number
$\boldsymbol{\sigma_s}$	Conductivity
ν_s	Refractive index

1 Introduction

Colloidal suspensions are a particular class of soft-matter systems where solid particles, ranging at least in one dimension in the mesoscopic scale, are suspended in a molecular fluid solvent. Examples of these systems are paints, blood and pigmented ink. The interest concerning colloidal suspensions is diverse. On one hand, colloidal suspensions can exhibit, gas, liquid, crystal and glass phases similar to those found in atomic systems. Under appropriate conditions they are suitable as ideal model systems to study soft matter physics at atomic or molecular level or even, more complex colloidal systems. Although the dynamics of both systems is different (ballistic in the case of atoms and Brownian for colloidal suspensions), the statistical thermodynamic properties of a colloidal system can be derived in the same way as for atomic systems by treating the solvent as a fluctuating background with well defined properties. Within this framework it is possible to define a mean force potential which contains the contributions from solvent and small ions as well as the correlations between the particles. Then the thermodynamic properties of a colloidal suspension are identical to those of atomic systems defined by an interaction potential of the same form. At the same time, the typical length and time scales ($\sim 10^{-8}$-10^{-5}m; $\sim 10^{-3}$s) of the colloidal systems and the possibility to easily control the particle interactions make them ideal candidates to perform experiments as well as to propose simple theoretical models and simulations without many fitting parameters. For instance, from a thermodynamic point of view, colloidal suspensions are very suitable models systems in exploring the dynamics of nonequlibrium processes as crystal nucleation and growth and the phase transitions. On the other hand, colloidal suspensions are often used as the major components of

industrial products or to manufacture many different devices in different technological fields. A very important characteristic of colloidal suspensions is that they can present long-range order. In this case, the ordered structures exhibit iridescence from the Bragg diffraction of visible light due to their characteristic mean interparticle distances. This feature makes monodispersed colloidal spheres very suitable for a wide variety of technological applications. For instance, colloidal assemblies can be used for catalysis [Vel00], membranes [Gat99], coatings [Pre07], sensors [Oka00], optoelectronics [Lau97], and photonics [Xia00] where the colloidal assemblies are also used as templates for the fabrication of porous materials.

Besides the relevance of colloidal suspensions as model systems as well as for technological applications, they are fascinating systems themselves. It is not really necessary to find any underlying utility or applicability since these colloidal systems are a particular class of matter which is part of our environment. The strength and even the sign of the effective force acting on the colloids depend on the details of the solvent-solvent and solvent colloid direct interactions. Furthermore the particle interactions can be tuned by using different particle synthesis techniques, changing the solvent composition or applying external fields. This leads colloidal suspensions to a rich variety of phase behaviour. Far from being simply a scale model for atomic systems, colloidal suspensions can form new states of matter [vBlaa04], [Lö01].

Nowadays the phase behaviour of monodispersed colloidal suspensions in the bulk is well understood. The research interests are now focused in new challenges which go a step further in the understanding of common technological processes as well as increasing complexity giving the possibility of inducing novel effects in such systems. We could probably say that the state of the art of colloidal suspensions regards three main general topics. On one hand, the application of external perturbations produced by the application of electric, magnetic, laser optic and shear fields as well as their confinement in restricted geometries. On the other hand the study of more complex systems as binary mixtures, polydisperse spheres, rod-like or plate-like particle systems and mixtures of particles with different shapes [Lö01]. Obviously both topics can appear together when complexes systems under the influence of external fields are studied. Finally, the synthesis of new core-shell morphologies [Zol05] as well as more complex shapes in monodisperse form [Ma03], [Cho05] can contribute to new advances in the field of colloids and consequently contributing to increase progress in novel technologies.

This thesis deals with the study of one of the former topics: the geometrical confinement of charged spheres in water. Confinement can be also achieved by trapping the particles at air/water interfaces [Pie80] or by using optical tweezers [Beh01]. Confined systems have been investigated during the last few decades paying particular attention to the packing phenomena and their phase behaviour. It is known for instance, that the properties of fluids confined between solid surfaces –or nanopores- differ greatly from their bulk properties. In particular, confinement induces an abrupt, discontinuous liquid-to-solid transition at a well-defined width of the gap in simple liquids [Al88], [Kle95], [Cui01]. Because of that, the physics of phase transformations in confined systems has attracted considerable interest in technology since they occur naturally in process like adsorption, wetting and lubrication. In particular, geometrical confinement is ideally suited to study the transition regime between two and three dimensions [Pie83] and to obtain crystalline colloidal films with novel particle arrangements which can have powerful applications in new technological areas like photonics or nanopatterning [Xia00].

Different aspects of confined colloidal systems have been studied in this thesis using different cell geometries and experimental techniques. The different cells designs can be classified in cells with parallel plates and cells with the plates forming a wedge. The advantage of working with wedge cells is that the height between the confining walls varies progressively. In these kind of cells it has been found that the crystalline structures follow a structural sequence of the form, $n\triangle \rightarrow (n+1)\square \rightarrow (n+1)\triangle$, being n the number of layers of the crystal. The symbol $\triangle$ represents structures with hexagonal symmetry and $\square$ represents structures with square symmetry. The low angles achieved when building the cells allowed the observation of a rich variety of crystalline structures as well as the structural transition between them. Some of the structures are reported for the first time. The crystalline structures were identified and characterized using different techniques as high resolution optical microscope in stereoscopic mode as well as conoscopic mode (real and Fourier modes respectively), Scanning Electron Microscope (SEM) or Atomic Force Microscope (AFM). Within these cells the particles are trapped in the narrow part of the cell independently of the initial particle density of the suspension. As a result when the particle density exceeds the freezing density, a crystalline region is observed. Systematic experiments were performed in order to find out the origin of this behaviour. Complementing the experimental results we report here the predictions of Löwen, Härtel and Allahyarov [Lö08] which give valuable information in the understanding of this behaviour. In this thesis also a confinement cell with variable height was designed in order to obtain the complete phase diagram of a charge sphere system in confinement. The preliminary

experiments as well as the detailed description of the experimental details are reported. The experimental results obtained for a bilayer system has been compared with the predictions for a bilayer of charged spheres between two parallel plates reported by [Mes03].

This thesis is structured as follows: In Chapter 2 the most relevant features of charged colloidal systems are given. We are also going to summarize some concepts of crystallography which will be useful. Chapter 3 starts with a brief introduction about colloidal systems in confinement. After that, previous experimental and theoretical results from literature about geometric confinement which I consider relevant are described. The different experimental techniques dealing with the samples observation are described in Chapter 4. The samples preparation, cell design as well as the technical details concerning the experiments can be found in Chapter 5. The different experiments concerning the unexpected behaviour of the particles in the narrow part of the wedge-cells as well as the theoretical predictions are found in Chapter 6. Next, in Chapter 7 the experimental preliminary results concerning the phase diagram of charged colloidal suspensions in confinement are presented. In Chapter 8 I describe all the different crystalline arrangements involved in the structural sequence of colloidal particles confined in wedge cells. Following with the pioneer work of Pansu et al. [Pan84] a model of hard spheres system in the high pressure limit will be used to explain some of the structural transitions found in confinement. Chapter 9 is dedicated to exotic arrangements which have been found also in the crystalline sequence but which are not involved in the transition mechanism between structures. The thesis concludes with Chapter 10 where the summary and the outlook are presented.

2 Charged Sphere Systems

From all kinds of colloidal particles, monodisperse colloidal spheres posses the simplest and highest possible symmetry. Furthermore, they are easily synthesized and characterized in a controlled way. Because of that they are commonly used as model systems. Synthetic colloidal particles have to be stabilized in order to prevent irreversible coagulation or reversible aggregation. There are two ways to synthesize stable colloidal suspensions: by means of steric stabilization methods and by means of charged stabilization methods. In the first method particles are stabilized by the absorption or chemical binding of large molecules to the particles. The repulsive interaction between steric stabilized particles is short-range and the particles nearly behave as hard spheres. In the second method the particles posses a surface charge which prevents flocculation. The advantage of choosing charged spheres for the experiments is that the interparticle interaction ranges from the theoretical limits of hard spheres to the one-component plasma.

2.1 Particle interactions in charged sphere systems

The study of the interactions between colloidal particles, and hence the determination of the interparticle interaction potential U(r) is fundamental to understand the behaviour of colloidal suspensions, especially with respect to its stability, crystallization and flow [Bell00]. The stability of a colloidal suspension is determined by the interplay between direct interactions among the particles

(arising from their specific shape and composition) and the Brownian motion (arising from thermal fluctuations in the suspending medium). The direct interactions are of both attractive and repulsive nature. Repulsive interparticle forces tend to push the particles apart whereas attractive forces can cause particle aggregation.

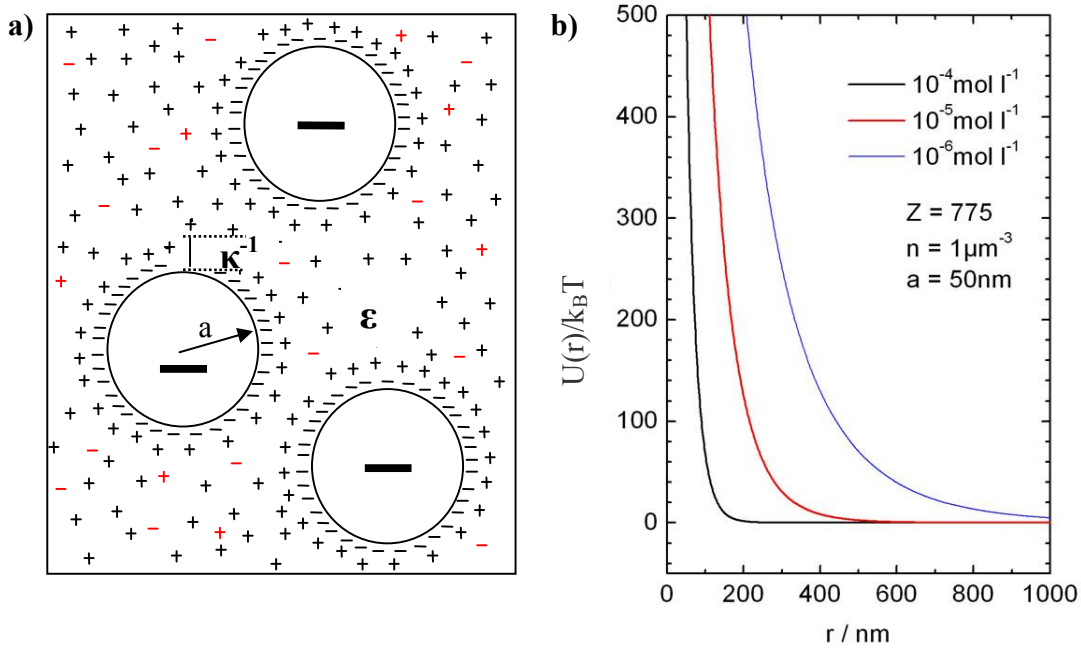

FIG.1: a) Charged stabilized colloidal particles immersed in a solvent of dielectric constant ε. In water, the acid groups of the spheres' surface dissociate leading a net charge per unit area. The counterions (+) resulting from the dissociation, screen the repulsive interaction between the particles forming a double layer of "width" κ^{-1}. The solvent also contains stray ions (in red). b) Different strengths of the interaction energy between charged spheres in the DLVO theory when varying the amount of stray ions present in the solvent. In these calculations the attractive part of the potential has been neglected.

2.1.1 Interaction potential between charged particles

Charge stabilized particles are synthesized through a process called emulsion polymerization [Soo91]. These polymeric particles (typically known as latex particles) are uniform spheres with 10^2 to 10^4 acid groups on their surface. When the particles are immersed in a polarizable medium like water, the high dielectric constant ε of the solvent favours the dissociation of the ionizable groups on their surfaces. As a result the particle acquire a net charge per unit area and the dissociated ionic groups (counterions) distribute around the particles (macroions) forming an electric double layer. In addition, other anionic and cationic species (stray ions) can be present in the solvent contributing

then to the charge density distribution around the macroions. This has been schematized in Fig.1a) where κ^{-1}, known as Debye length is the inverse of the Debye screening parameter and gives the "thickness" of the double layer. When the concentration of ions in the solvent is low, the electrostatic repulsion between the particles is enough to stabilize the suspension.

Charged colloidal particles suspended in water interact through hard core repulsions, van der Waals attractions, Coulomb interactions and hydrodynamic coupling. The effective interaction between the particles and hence the stability of homogeneous suspensions of charged particles can be understood by means of the Derjaguin-Landau-Verwvey-Overbeek (DLVO) theory [Ver48]. To obtain the interaction potential between two charged spheres we first consider a charged surface in a electrolyte solution. In order to determine the relation between the surface charge density, the surface electric potential and the concentration of ions around the particles the Poisson's equation has to be solved. Assuming a Boltzmann ion distribution around the particles and introducing a mean field approximation to neglect fluctuations and higher-order correlations among the simple ions, we obtain the Poisson-Boltzmann (PB) equation which has no analytic solution except for the simplest geometries. The DLVO theory assumes that the electrostatic energy of the microions near the colloid surface is much lower than the thermal energy of the system (Debye-Hückel approximation). In that case, the PB-equation can be linearised. Solving this equation for a sphere of radius a, carrying a charge Ze, we can obtain the effective pair potential between two spheres with the same radius and the same charge which is given by,

$$U(r) = \frac{(eZ)^2}{4\pi\varepsilon_r\varepsilon_0}\left[\frac{e^{\kappa a}}{1+\kappa a}\right]^2 \frac{e^{-\kappa r}}{r} \qquad (2.1)$$

where, ε_0 and ε_r are the vacuum dielectric permittivity and the solvent relative dielectric constant respectively, k_B is the Boltzmann constant, T the temperature of the system and κ is the Debye-Hückel screening parameter which takes into account all the ionic species present in the solvent.

Usually the effective charge and the stray ions are treated as the fitting parameters in calculations being later compared with experiments. Charge numbers are often smaller than the number of titrated surface groups because the degree of dissociation of the ionizable groups is always much less than unity. As a consequence the interaction is discussed in terms of an effective charge Z* instead of the bare charge. Z* can be determined from different methods. For instance Alexander et al [Al84] suggest a charge renormalization method where the effective charge usually

agrees well from the Z* obtained from conductivity methods [Pal99]. In this case the form of the potential energy given in (2.1) remains unaltered and Z is replaced by Z*. The expression for κ is then,

$$\kappa^2 = \frac{e^2}{\varepsilon_0 \varepsilon_r k_B T}(n_p Z^* + 2 \cdot 1000 N_A c_s) \tag{2.2}$$

where n_p is the particle number density, c_s the salt concentration and N_A is the Avogadro's number [Ev98]. The full DLVO potential includes a term accounting for dispersion interactions. However for well separated spheres it can be omitted. In our case, since ordering is observed in our experiments it is enough to consider the repulsive part of the potential which is given in equation (2.1).

As we see, the interaction of charged spheres in suspension can be explained by means of the screened Coulomb repulsive pair interaction given by the DLVO-theory. These interactions are mediated by the ions distributed around each particle. High repulsive interactions can be achieved by removing the excess of stray electrolytes in the solvent. In this case we say that the sample is deionized. On the contrary, adding moderate stray electrolyte concentrations in the solvent screens the repulsive interaction. When the repulsive interaction is highly screened and therefore the Debye length is very small, the particles are considered to have hard-sphere behaviour and they will not influence each other unless they are in physical contact. In general the interaction of charged spheres can be tuned by varying the surface charge of the particles, the stray ions concentration present in the solvent and the volume fraction, $\Phi = \pi n_p \sigma^3/6$ being n_p the particle number density and σ the diameter of the particles. In Fig.1b) equation 2.1 has been plotted at three different salt concentrations. When the presence of added electrolytes is low the interaction is clearly repulsive. However as the ion concentration increases the repulsive interaction is progressively screened.

2.1.2 Phase diagram of charged colloids in the bulk

In order to use colloidal suspensions as model systems to study the phase behaviour of atomic systems it is necessary to choose properly the state variables. In general, the parameters which drive phase transitions and consequently, influence the structural ordering include particle volume fraction, surface charge density, polydispersities of size and charge, ionic impurities and also external fields as

laser optical fields, shear, electric and magnetic fields of confinement in at least one of the dimensions. Volume fraction and ionic strength in charged colloidal suspensions play the same role as the thermodynamic variables pressure and temperature in atomic systems. A variation in the volume fraction implies a variation in the osmotic pressure of the system which is equivalent to the pressure in atomic systems. On the other hand an increasing of the temperature in atomic systems is equivalent to increase the ionic strength in charged colloidal systems. This analogy arises because an increasing in the salt concentration implies the decrease of the repulsive interaction between the particles. Since the stability of any ordered system is the result of the interplay between the interaction energy and the thermal energy, lowering the interaction between the particles will result in a dominance of the thermal energy causing the melting of the system. In principle an equivalent result would be obtained if we increase the temperature. However in colloidal systems the tempereature dependence of the dielectric constant of the solvent could produce undesirable effects for colloidal phase transitions like dissociation of salts and solvation of acidic or basic groups on the particles [Chai82]. The generalized phase behaviour of single component charged particles interacting with the screened Coulomb potential can be found in [Rob88]. Robbins et al. used molecular and lattice dynamic techniques in order to study the phase transitions as a function of the potential shape depending on the screening length. The results were obtained for moderate and low volume fractions.

The complete phase behaviour of charged colloidal systems in the bulk was experimentally determined by Sirota et al. in 1989 using high-resolution small-angle synchrotron x-ray[1][Sir89]. The different phases were determined from structure factor measurements. The phase diagram of Fig.2 shows fluid (white circles), crystalline (triangles and squares) and glass (black circles) phases depending on both the particle concentration and the salt concentration. The full lines are guides to the eye indicating the approximate melting and freezing boundaries. Ordered structures other than face centred cubic (FCC; white triangles) and body centred cubic (BCC; black squares) have been not seen in bulk suspensions of monodisperse charged colloids. The phase diagram shows that as the salt concentration increases the ordered phase is formed at higher volume fractions. For low volume fractions and ion concentrations, FCC and BCC structures coexists (white squares). Under the absence of external forces, in equilibrium, structures other than FCC, BCC or random hexagonal packing (RCP) have not been observed in charged colloidal suspensions. This phase diagram gives

[1] Before the work in reference [Sir89] other experimental works related with the phase transitions and the stability limits of the different phases of charged colloidal systems have been reported. For instance, [Luck63],[Hach74] or [Mo89].

us a qualitative understanding of the different phases because the exact Φ and c_s values of the phase transitions as well as the phase stability regions depend on the effective charge of the particles as well as the dielectric constant of the solvent. Some sections of this thesis are focused in the crystalline phases and the solid-solid phase transitions observed in confinement. Because of that it is convenient, before we continue, to introduce some basic concepts about how to classify the different crystalline structures attending to their geometry as well as defining the main parameters which characterize their physical properties.

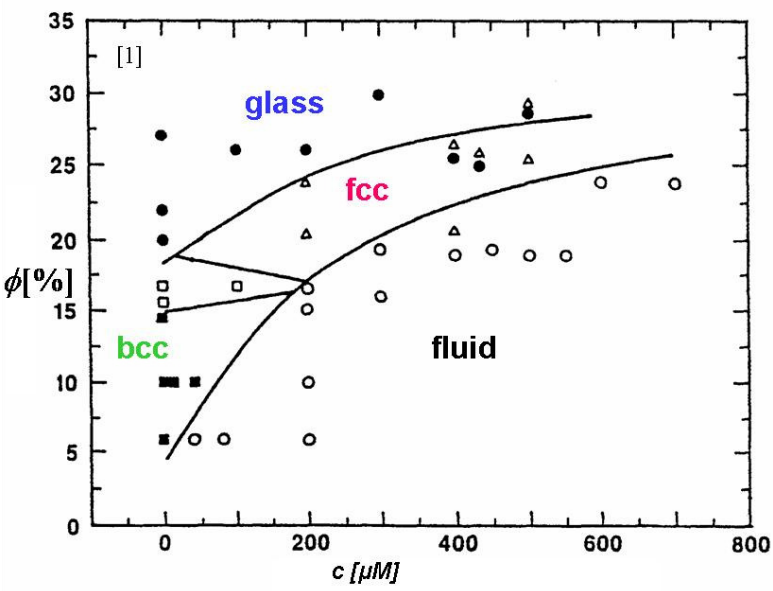

FIG.2: Experimental phase diagram for polystyrene particles of 83.7 nm in diameter. The different phases were obtained varying the volume fraction Φ and salt concentration c. ○ Fluid phase, ■ BCC crystal; △ FCC crystal; □ Coexistence of BCC and FCC crystals; ● Glass phase.

2.2 Colloidal crystals

The ordered states of a colloidal system can be explained using the same criteria as for conventional crystalline solids if we attend only to their geometrical description. In that case it is possible to classify the colloidal crystal attending to the definition of Bravais lattices where each crystal is defined by a lattice and a basis. Each lattice point is defined by a translation vector of the form $\mathrm{R} = \mathrm{u}\vec{a} + \mathrm{v}\vec{b} + \mathrm{w}\vec{c}$ where $\vec{a},\vec{b},\vec{c}$ are the lattice vectors. At the same time, since we have a periodic structure, incident electromagnetic radiation of wavelength in the order of the distance between the

particles will be diffracted. The diffracted light will give us information about the structure of the crystal as well as of the constituent elements. Since an ideal or perfect crystal presents anisotropy the intensity distribution of the diffracted light will depend on the relative orientation of the crystal with respect to the incident beam. Because of that it is of great help finding out how the crystalline structure looks like in a specific direction in order to obtain a better understanding of the crystals properties. Each crystallographic direction defines a family of planes perpendicular to it. Those families of planes which contain all the lattice points receive the name of crystallographic planes and are parameterized by the so called Miller indexes [hkl] [Kit76]. Sometimes, due to the symmetry of the lattice cell we find that there are equivalent families of planes due to the symmetry of the Bravais lattice. In these cases we symbolize the set of equivalent planes as {hkl}.

Charged colloidal suspensions in crystalline phase are analogous to a large number of metals, alloys and inorganic compounds. As a result we observe the same crystalline structures as in the former metallic compounds. The crystalline arrangements, as any stable phase, arise as the result of minimizing the free energy of the system; in absence of entropic contributions this is achieved minimizing their volume (or in other words maximizing their packing fraction). The structures resulting from that situation are called close packed structures and consist of the stacking of hexagonal close planes. Starting from the simplest case, that is, in two dimensions, the closest packing of spheres is achieved when a sphere is in contact with six other spheres. To extend the problem to 3D successive compact layers have to be added in such a way that the packing efficiency continues being maximum. Let the first layer be called an A layer. It contains two types of sites called B or C as Fig.3 shows. The spheres of the next hexagonal close-packed layer can occupy either the sites B or C, but not both. If we now stack the next layer in type-B sites, the third layer will have again two possible stackings, C or A and so on. When the layers are periodically stacked, that is following staking sequences ABABABA…. or ABCABCA…we will have ideal or perfect close-packed crystalline structures. In these structures each sphere is surrounded by 12 spheres and is easy to demonstrate that the volume fraction occupied by identical spheres is maximum, having a value of ~ 0.74 in the bulk. This means that the number of interactions which stabilize the structure is very high. Once we have these structures it is easy to identify the crystalline lattices. In the case of an ABC… stacking sequence we have a FCC structure. If the stacking sequence is ABA… we have a hexagonal close packing structure, HCP. For other stackings different to those in the perfect crystals, for instance ABACBA…, we speak of random (hexagonal) close packing, RCP.

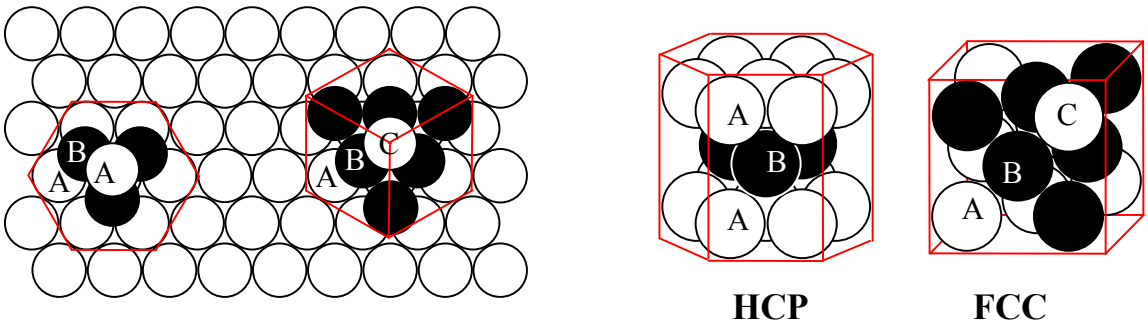

FIG.3: Different packing possibilities from top and side view and the corresponding unit cell of the crystals that those packings generate. ABA…packing generates hcp structures whereas ABC… packings generates fcc structures.

Although most metals crystallize maximizing their packing density there are other metallic compounds which crystallize in the form of the base centred cubic, BCC structure where each sphere is surrounded by 8 spheres and their packing fraction is 0.68. This is possible due to a higher interaction range between the particles which makes the differences between the first and second neighbours are small and consequently the effective coordination number will be higher than for compact structures[2].

One of the interests in this thesis was to obtain an experimental phase diagram of charged spheres confined between two solid surfaces. To do this, besides the particle density or the stray electrolyte concentration present in the solvent we should take into account the thickness of the confining cell. As we have already said, for colloidal crystals in the bulk, BCC structures are observed at long ranged repulsions whereas face centered cubic FCC or randomly stacked planes, are thermodynamically stable for short range interactions including the hard sphere limit. However, under confinement the restricted space forces the suspension to arrange respect to the packing constraints which leads to the apparition of a rich variety of structures as the distance between the confining walls varies [Neser97]. Some of these crystalline arrays can be interpreted as partly derived from close packed structures [Pie83] but others present more exotic packings.

[2] In the compact structures there are 6 second neighbours relatively far away, however in the BCC structure there are 6 second neighbours relatively close. For short-range interactions the compact structures are more stable however for long-range interactions the differences between the first and second neighbour spheres are not important and the effective coordination number is higher than in the compact structures [Ib02].

2.2.1 Crystalline structures in confinement

Some of the structures reported here are the result of confining colloidal suspensions between solid surfaces can be easily identified as Bravais lattices. In particular they correspond to close packed structures consisting of few crystalline layers. However, other structures with more complex symmetries were also observed. Some of them are assembled prism structures where the particles give rise to different basal symmetries, others are irregular rhombic structures. These structures can be interpreted as Bravais crystals with a significant presence of stacking faults or dislocations. Both crystalline features are known as defects, that is, a deviation from the perfect or ideal periodic structure. A dislocation is (macroscopically) a linear defect (involves rows of particles), whilst a stacking fault is a planar defect (involves complete crystalline planes) Fig.4. The remarkable fact of their presence in our samples is that these kinds of defects appear in a periodic fashion for specific distances forming the same structures in any cell. In this thesis we will present these crystalline phases but also the structural phase transition which takes place between them when varying the distance between the plates.

In conventional solid state physics a structural phase transition -or solid-solid phase transition- can take place in a crystal when some distortion or reorientation in the active groups is collectively developed. This is characterized macroscopically by a change in the crystal symmetry. The solid-solid phase transitions are usually studied in the Landau theory framework [Cow80] where the stability conditions are imposed by the free energy minimization of the assembly as a function of the particles displacements. Due to the experimental results obtained in this thesis, however, we will propose a geometric model assuming that the particles behave as hard spheres subject to a high lateral pressure. This implies that the packing fraction will be always maximum when, for any distance between the plates, all the other thermodynamic parameters remain constant. In particular, we continued the pioneer work of Pieranski in finding out a theoretical phase diagram: volume fraction - cell gap [Pan84]. In our experiments, with wedge cells we observed indeed that for small cell gaps, the mean interparticle distance of the particles in all the different crystalline structures was very close to the particle diameter. This means that, at least in the cusp of the cells, the repulsive interactions between equally charged spheres are sufficiently weak. Because of that, it was assumed that this region the particles behave as if they were electrically neutral unless another particle is close

enough. We consider appropriate to use this model to study the structural transitions which take place in confinement as we will see in Chapter 8.

.

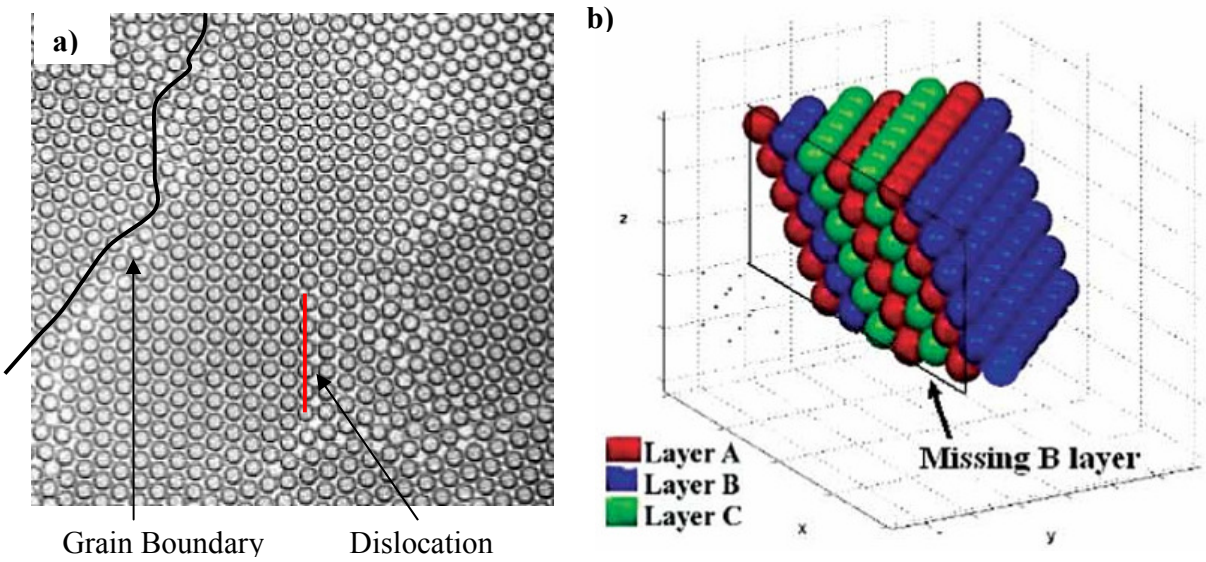

FIG.4: a) Bubbles forming ordered structures where is possible to observe a dislocation (red line) and grain boundaries separating crystalline domains with different orientations (black line). b) Stacking fault in a FCC structure. The arrow indicates the stacking of the hexagonal layer in C sites instead of in B sites. Both pictures have been found in [Net06].

3 Former results in geometrical confinement

The aim of this chapter is to describe some relevant results, from the first evidences to posterior advances in the confinement of colloidal spheres between solid surfaces. These kinds of geometries are suitable to study phase transitions in reduced dimensions, crystallization phenomena and transition from two- to three-dimensions (2D to 3D). In particular the chapter is focused in the results found in literature for geometries with parallel surfaces as well as non-parallel surfaces, where the plates are forming a wedge. The former geometries give a wide surface being possible to consider that the system is confined only in one dimension. However we also find in literature confinement which is achieved along two dimensions. For instance, the phase behaviour of paramagnetic spheres confined in a 2D-circular hard wall cavity has been studied [Bu99]. The depletion mechanism using a binary mixture of hard spheres allows the pre-freezing of the big spheres at the corners of a irregular surface. Moreover, the resulting crystals are aligned respect to the corner geometry and therefore it is a possible method for obtaining colloidal crystals with defined orientations [Dins99]. Some literature has been also found reporting experimental results on the confinement of colloidal suspensions in capillary columns for diverse technological applications as coatings or photonics [Kamp05].

The chapter begins with the description of the first experimental results of charged colloidal particles confined between two solid plates forming wedge. The crystalline structures found in these experiments as well as complementary work developed by the same authors will be presented. The chapter will continue with further experiments as well as theoretical work. In there new crystalline

structures will be presented complementing the pioneer work about confinement of colloidal particles. The theoretical work presented here shows the predictions on the phase behaviour of such physical systems. On the other hand all the structures appearing in this chapter have been also observed in the present thesis. Because of that I consider appropiate to discuss here these already well known structures to leave in chapter 8 the description of the new structures as well as the solid-solid phase transitions found between them.

3.1 First evidences: The structural sequence.

In 1983, Pieranski and co-workers reported the first evidences of the existence of a series of structural transitions when charged colloidal spheres where confined by the presence of boundaries [Pie83]. They studied the transition between two- and three-dimensions finding a sequence of morphological transitions as the cell height H increased. This crystalline sequence can be represented by:

$$n\triangle \rightarrow (n+1)\square \rightarrow (n+1)\triangle \qquad (3.1)$$

where n is the number of layers and the symbols $\triangle$ and $\square$ denote structures with hexagonal and squared symmetry respectively. In this sequence we can distinguish two different regions: transitions characterized by morphological changes in the structures $n\square \rightarrow n\triangle$ and transitions characterized by both morphological changes in the crystal and changes in the number of crystalline layers $n\triangle \rightarrow (n+1)\square$.

In these series of experiments they used polystyrene particles of diameter σ = 1.1 μm dispersed in water. The particles and the salt concentrations were adjusted in order to obtain crystalline suspensions in the bulk. After the three-dimensional crystal was formed, the upper plate of the cell was adjusted to confine the suspension. The suspension inside the confinement cell was in contact with a bulk reservoir. The experiments were performed "in time" when the distance between the cell-plates was increased progressively or "in space" when the cell-plates formed a wedge cell of angle α. The election of the wedge geometry permits to have a continuous variation of the distance between the plates, all the other parameters of the system remaining constant in the equilibrium state.

In it, by means of an inverted microscope with a low magnification objective, a series of parallel bands of different colours were observed (Fig.5). The position of these bands in the wedge was correlated with the cell thickness and therefore the sequence can be expressed as S(H).

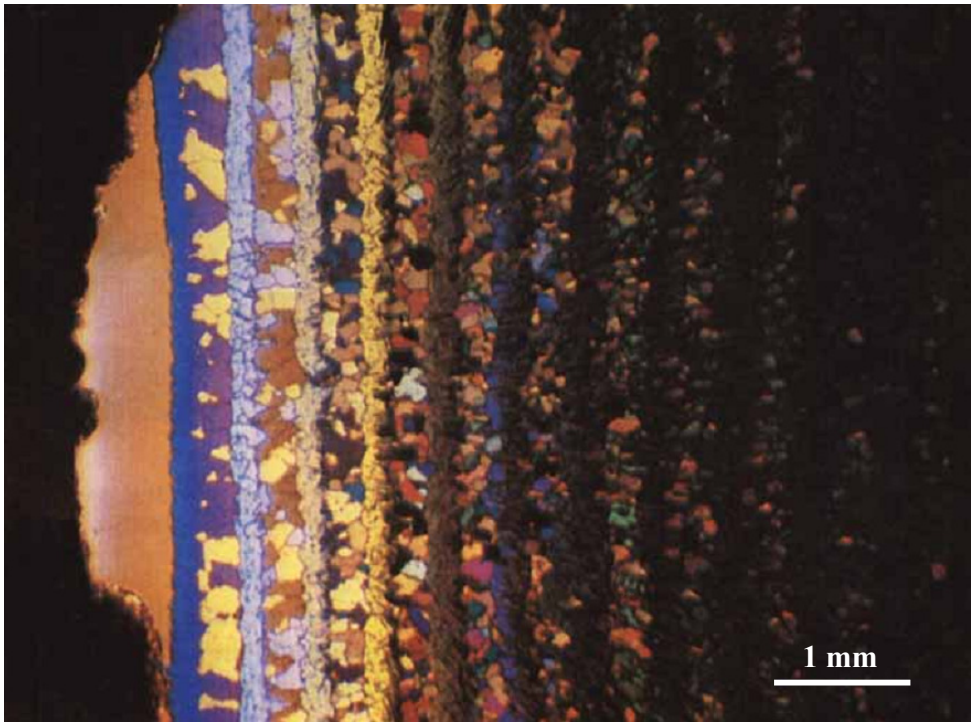

FIG.5: Transmitted light microscopic picture at low magnification showing the sequence of crystalline colloidal structures in a wedge cell obtained by Pieranski [Pie79]. The distance between the plates increases from left to right.

The observed colours are the result of phase differences of the light waves when passing the sample due to the differences in the refractive index between the polystyrene and the water as well as the size of the spheres. Therefore each colour in the sequence indicates a different particle density and/or particles arrangement. At the same time, since these observations have been made with an optical microscope the characteristic colour of the structures that we observe also depends on the amount of diffracted light which is collected by the objective. This dependence will be explained in next chapter.

The use of a high magnification objective permitted the identification of the crystalline structures. Increasing the distance between the plates from zero, first a fluid phase was found. This

fluid phase was followed of a monolayer with hexagonal symmetry. The beginning of the bilayer started with square symmetry and ended with hexagonal symmetry. From there, the same alternation of square-hexagonal structures was repeated. As H increases, the observation of the square structure indicates the presence of a new layer in the crystalline sequence.

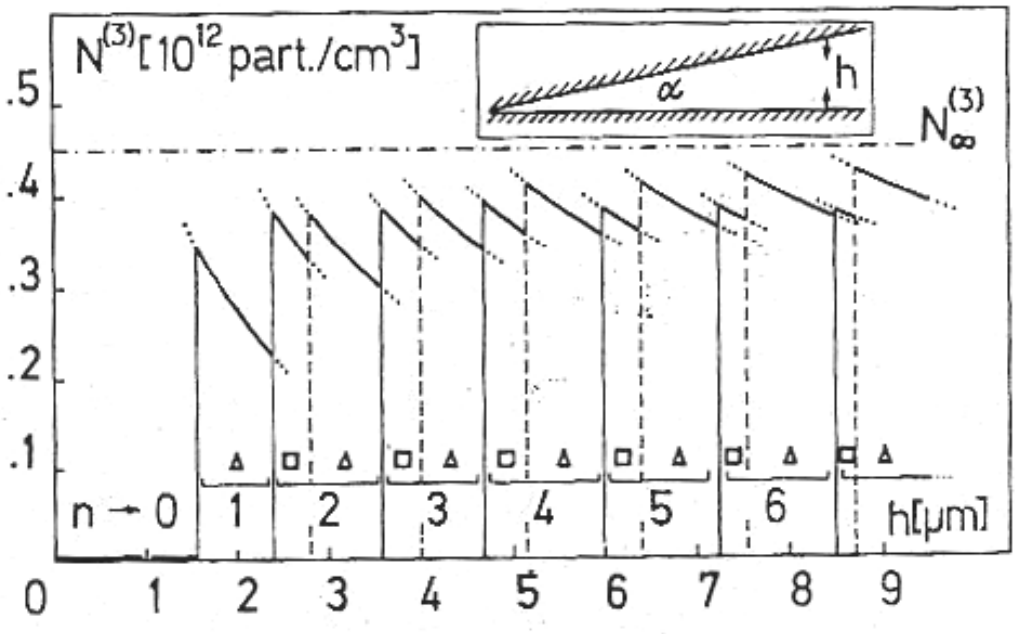

FIG.6: Particle number density versus the cell thickness. The angle of the wedge cell α *was about* 10^{-2} *rad. The corresponding particle number density of the suspension in the bulk* $N_{\infty}^{(3)}$ *is represented by a semi-dotted line [Pie83].*

Fig. 6 shows the experimental phase diagram obtained from one of the samples. In it, each structure starts having the maximum particle density $N^{(3)}(h)$ where h is cell thickness and the symbol $^{(3)}$ indicates that is a volume density. By increasing the cell thickness the concentration of particles decreases progressively until the distance between the plates allows the formation of a more stable configuration. In the sequence, the corresponding n△ → (n+1)□ transition is very sharp except in the case of n = 1 where strong vertical fluctuations were observed. In the other transition, n□ → n△, the transformation was mediated by the appearance of a high density of defects of specific type. On the other hand, as h increases, the stability zone for n□ decreases in width disappearing above n=7. The particle number density in the bulk, $N_{\infty}^{(3)} = 0.45 \cdot 10^{12}$ particles/cm^3, is represented by a semi-dotted line. We can see in the graph how the particle number density

$N^{(3)}(h)$ measured in the sequence increases progressively with the number of layers approaching to $N_{\infty}^{(3)}$. The condition $N^{(3)}(h) = N_{\infty}^{(3)}$ establishes the upper limit to consider the suspension as confined.

3.2 Model of hard spheres in the high-pressure limit

The measurements of the surface density in the crystalline layers done by Pieranski et al. revealed that for a fix number of layers the mean interparticle distance was the same in the square layers than in the hexagonal layers. The same result was obtained measuring the mean interparticle distance for a crystalline layer along the height interval where a given strucutre was stable. Because of that, they considered that the particle number density $N^{(3)}$ varied only with *h*. In this case the interaction between particles could be approximated by a hard-sphere interaction with an effective radius a* = a + D where D is an unspecified length. In that case, the effective volume fraction is given by $\Phi^* = n_p \cdot (4/3)\pi a^{*3}$. In the same way they also approximated the interaction between the particles and the walls by hard-sphere interaction. This kind of approach it was originally proposed by Hachisu to theoretically study the phase separation of a suspension of monodispersed latex particles with high electrolyte concentration [Hach74]. Under these assumptions the phase diagram would depend on the pressure, the temperature, the volume fraction and the distance between the plates. On the other hand since in these experiments the reservoir which surrounds the confined sample is in a container about 3 mm high, the pressure in the bottom of the cell can be considered high enough to neglect the entropic term in the free enthalpy. Thus, in the equilibrium we can consider that the particles are in the high pressure limit and will form crystals following the maximum packing criteria [Pan84]. Except for dimensionality, the problem is now purely geometrical (athermal). Despite the fact that the behaviours of a real colloidal crystal of charged spheres is more complex than a system of hard spheres in the high pressure limit, the geometrical model obtained whit this method was in agreement with experiments. The theoretical phase diagram obtained by Pansu et al. using this model is shown in Fig.14. By simplifying so strongly the particles interaction the possibility of crystallization into other than close-packed structures is excluded and just by looking at the phase diagram of Fig. 2 we clearly see that the model has important limitations for highly repulsive particles since does not predict the bcc structure as stable.

3.3 The hexagonal and square structures in the structural sequence

When the position of one kind of atoms or ions in inorganic structures correspond approximately to those of equal spheres in a close-packing with the other atoms distributed among the voids we speak about close-packed structures although they may not be ideally close-packed. This is just the case of the square and hexagonal structures, n□ and n△ respectively which appear in the sequence. The hexagonal and the square structures observed in confinement can be considered in a first approximation as a *slice* of a FCC crystal with their (100) planes for n□ or (111) planes n△ oriented parallel to the cell plates. The square structure can be considered as the projection, parallel to the cell plates, of the (100) planes of an FCC crystal. The hexagonal phase consists in stackings of hexagonal close packed layers oriented parallel to the cell plates. Depending on the number of layers n we can find until 2^{n-2} stacking possibilities for n > 2. As we have already explained in Chapter 2, the different stackings give rise to FCC, HCP or RCP structures. Depending of the stacking sequence, the RCP structure can be considerer both FCC and HCP structures with stacking faults. The coexistence of the different stacking sequences in the hexagonal phases arises from the fact that for n layers, the volume fraction is the same independently of the stacking sequence [Kit76]. However, since they are structurally distinct, they might have different thermodynamic properties and stabilities. The free energy differences between FCC and HCP structures have been extensively studied for bulk systems of hard spheres [Wood97], [Bol97], [Mau99], [Koch05]. The result shows than although the free energy difference is very small, the FCC is the most stable structure.

We are going to see that apart from the formers, there is more than one close packed structure present in the sequence. In confined systems where the crystal is finite at least in one dimension the maximum packing density depends on the allowed space. In particular, in these wedge cell experiments, the dependence of the packing fraction with the available cell thickness is fundamental to understand the alternation of structures inside the confinement cell. For the n□ structure, the height of n layers from centre to centre of the spheres is $h_s = (n-1)\sqrt{2}a^*$. For n△ this height is $h_h = (n-1)\sqrt{8/3}a^*$. Since $h_s < h_h$ the alternation of the square or hexagonal orders allows a better filling of the available space. For a constant number of layers, the increasing of the cell thickness implies a transition n□ → n△. In the same way, the transition n△ → (n+1)□ is due to the fact that $nh_h < (n+1)h_s$ which is just what it was observed in the experiments. In the monolayer, in principle both configurations could be possible. However the 1□ lattice is unstable relative to the

packing of the particles in a 1△ lattice since in this configuration the contact surface points between spheres are higher. In other words, in a one layer system in which the particles interact via central forces, the lowest energy configuration has the maximum number of nearest neighbours [Zan00].

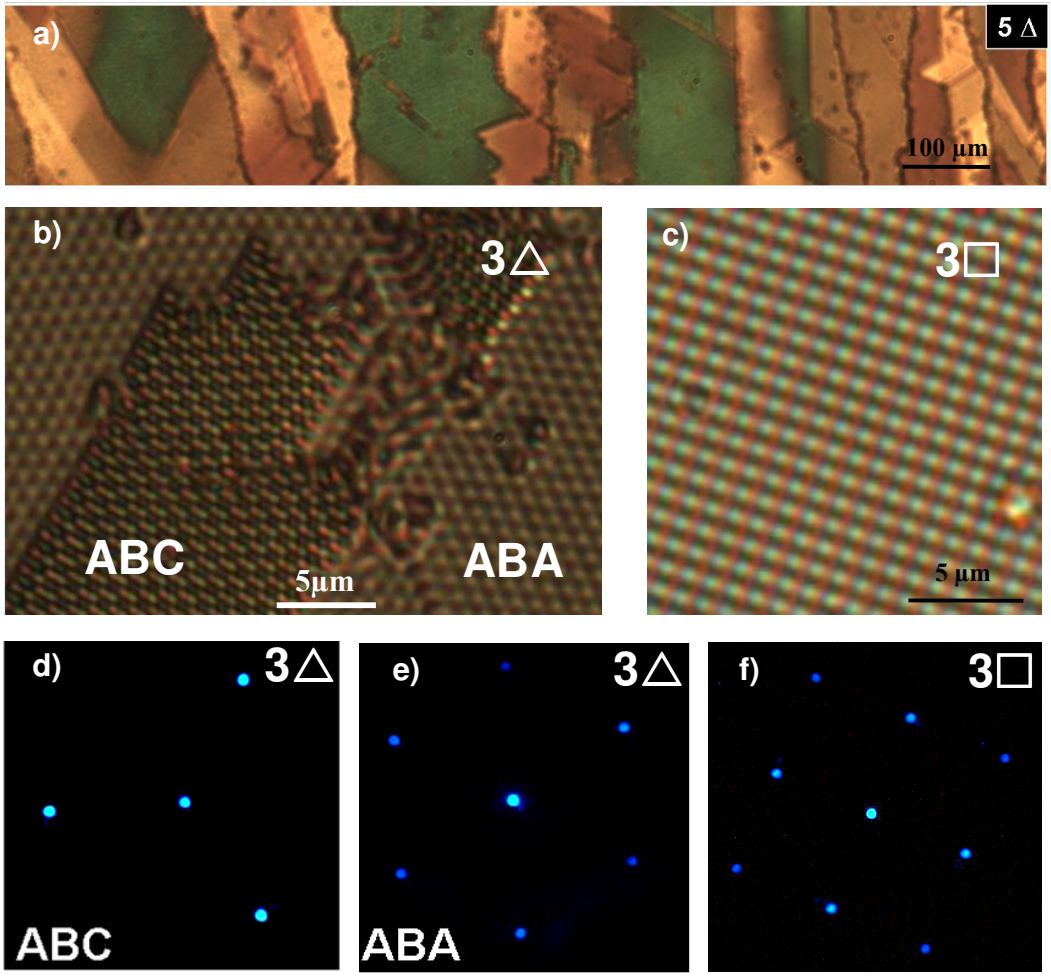

FIG.7: Square and hexagonal structures in real and reciprocal space of a sample containing polystyrene spheres of 1100 nm in diameter in water. a) Low magnification picture showing a general view of the 5△ structure and the different colours which characterize each strucutre. b) Real space image picture of the 3△ phase indicating the two possible stacking sequences. c) Real space image picture of the 3□ structure. d) – f) Reciprocal space pictures of the 3△(ABC), *3△*(ABA) and 3□ structures respectively. Notice in image d) that in absence of twinning, the FCC structure only shows three-fold symmetry.

In Fig.5 we can distinguish uniformly coloured bands alternated with multicoloured bands. The bands with only one colour do correspond to the square structure. The square layers Fig.7c) have

only one stacking possibility and because of that we observe only one colour for each of the bands with square symmetry. The diffraction pattern of this structure is characterized by a four maxima in the first order as indicated Fig7f). The bands with more than one colour are those presenting hexagonal symmetry. Each colour indicated the existence of different layer stackings for the n△ structure Fig7a). In the sequence, the number of different colours in the multicoloured strips increases with thickness. Specifically, we can say that for n > 2 hexagonal layers, 2^{n-2} different stackings are possible. For instance, for four layers we found three different possible stackings: ABAB which corresponds to a HCP crystal (where the (001) planes are parallel to the cell plates), ABCA which is the stacking of a FCC crystal ((111) planes oriented parallel to the cell plates) and ABCB which corresponds to a RCP structure. From the diffraction patterns we can distinguish the pure FCC structure from the hcp or the RCP structures. Fig.7b) shows these differences for n = 3. The FCC structure presents three maxima which is characteristic of the trigonal systems in absence of crystal twinning whereas the HCP structure presents six diffraction spots. The volume fraction for these two close packed structures as a function of the number of layers n is given by:

$$\phi_s(\mathrm{n}) = \frac{\pi}{6}\sqrt{2}/(1+\sqrt{2}-1/\mathrm{n}) \qquad (3.2.a)$$

$$\phi_h(n) = \frac{\pi}{6}\sqrt{2}/(1+\sqrt{3/2}-1/n) \qquad (3.2.b)$$

where the subscripts *s* and *h* denote square and hexagonal symmetry respectively. When n is very large both expressions converge to 0.74078 which is the volume fraction of a compact 3D crystal.

3.4 Other structures

D. H. Van Winkle and C. A. Murray also studied confinement of colloidal suspensions in a wedge [Win86]. They performed the experiments using smaller polystyrene particles in water ($2a \approx 0.3\mu m$). They used several suspensions with different particle densities and electrolyte concentration. In these experiments the same structural sequence was found but since in this case, the wedge cell had a lower angle (10^{-4} *rad*), the extension of each crystalline phase was larger. This implied than the structural changes inside the wedge cell were easier to observe allowing the

observation of new confinement effects. Although the result for the sequence was very similar, an abrupt n△ → (n+1)□ transition was not observed. On the contrary, they observed a quite distorted lattice where both, the n△ and n□ structures appeared in coexistence. These fluctuations were especially prevalent in the 1△ → 2□ transition, as it was also mentioned from previous observations [Pie83]. They included this region, termed hopping phase, in the phase diagram Φ vs. H. We can consider the work of Winkle et al. the first mentioning the existence of intermediate phases between the square and hexagonal structures since at least one of them appears explicitly in the phase diagram.

3.4.1 From the monolayer to the bilayer: the buckling and the rhombic phases

As early as 1984, Pansu and Pieranski brothers had used the hard sphere model in the high pressure limit motivated by their experimental observations about the 1△ → 2□ transition together with former results about the 2D-confinement for hard-discs confined between two hard plates [Pie79]. They studied the volume fraction variation for close hard-sphere packings of thin films with either square or hexagonal symmetry when varying the cell thickness. From that, they predicted the existence of a buckled phase which will mediate in the transition 1△ → 2□. At the same time, for the transition n□ → n△ they proposed another continuous transformation which took place via a rhombohedric lattice. Later, the existence of these crystalline phases was confirmed by experiments as well as by simulations of both, hard and soft spheres. In 1993, Chou and Nelson applied the Landau theory of structural phase transitions for an assembly of repelling colloidal particles in confinement. The model was applied for the transition 1△ → 2□ finding three degenerate instable buckling phases. The symmetry of these phases allows second-order transition even in the presence of gravity or plate asymmetry [Cho93]. The buckled phases presented in this way could be understood as a perturbation of a 2D-crystal. However the buckling phases are present in quite different physical systems, as amphiphilic membranes [Net92], [Cam92], [Rup83] or Langmuir monolayers [Sai94]. In 1997, Neser and co-workers reported the first experimental evidences about the existence of these intermediate crystalline phases for a system of soft spheres in the hard- sphere limit [Nes97]. In this case, the experiment consist in polystyrene particles in water (σ = 840 nm) confined using also wedge cells. The permeability of the cell sides allowed slow evaporation of

water[3] which generates a very small flow. Due to these water currents the particles are swept towards the edges of the cell and the concentration of particles in the narrow part of the cell increases forming a crystalline phase. The system is later affected by a lateral pressure coming from capillary forces between particles during the evaporation. During this process the structural sequence is developed obtaining a sequence rich in crystalline structures due to the suitable small angles achieved for the wedge cells (in the order of miliradians). The resulting crystalline sequence is characterized again by colour striped patterns parallel to the wedge cusp where now bucking and rhombic phases appear as in the following manner:

$$1\triangle \rightarrow b \rightarrow 2\square \rightarrow r \rightarrow 2\triangle \tag{3.3}$$

On the other hand, Schmidt and Löwen investigated the freezing transition for a system of hard spheres confined between parallel hard plates using both extensive Monte Carlo computer simulations and free-volume theory [Sch97]. The calculations were made for plate-plate distances ranging from one to two particle diameters. The obtained phase diagrams showed a variety of phases including the buckling b and the rhombic r phases previously observed by Neser (Fig.8). These phase diagrams are characterized by first-order phase transitions between different crystalline structures.

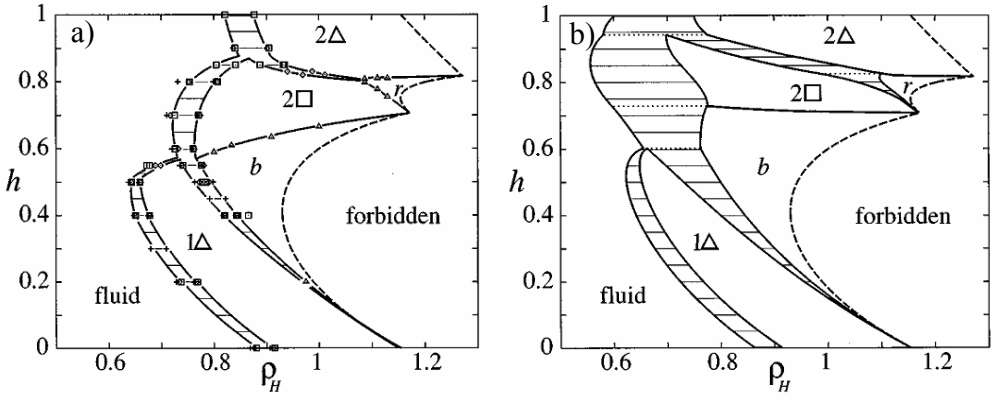

FIG.8: Phase diagrams for a system of hard spheres confined between hard plates for cell thickness h ranging from one to two particle diameters and with reduced densities $\rho_H = N\sigma^3 / AH$ *being H=(h+1)σ the gap thickness and A the surface of the plates. Thin horizontal lines represent two-phase coexistence. The letters b and r indicate the buckled and rhombic phases respectively. a) Monte Carlo simulations, b) cell theory result. [Sch97]*

[3] The samples were completely dried after 2-3 weeks.

Both the buckling and the rhombic structures were found to be highly degenerate. Each of them could appear strictly periodic linear, zig-zag or random alternation of coexistence of both. This is analogue to that in the n△ phase where we found degeneracy respect to the stacking sequence.

3.4.1.1 The Buckling Phase

This crystalline phase consists in two sublayers separated vertically between them by a fraction of the particle diameter. Each sublayer is described by a rectangular lattice with a particle in each of the lattice points as indicates Fig.10. The formation and transformation of this phase can be understood in terms of packing of hard spheres subject to a lateral pressure. Starting from the monolayer, as the distance between the cell increases, the structure is able to distort along rows of particles. With the diffraction patterns we see clearly with the intensity distribution the continuous evolution from the monolayer to the bilayer. Due to the lateral pressure, some of the rows will tend to move up and some of them will tend to move down appearing two sublayers with rectangular structure.

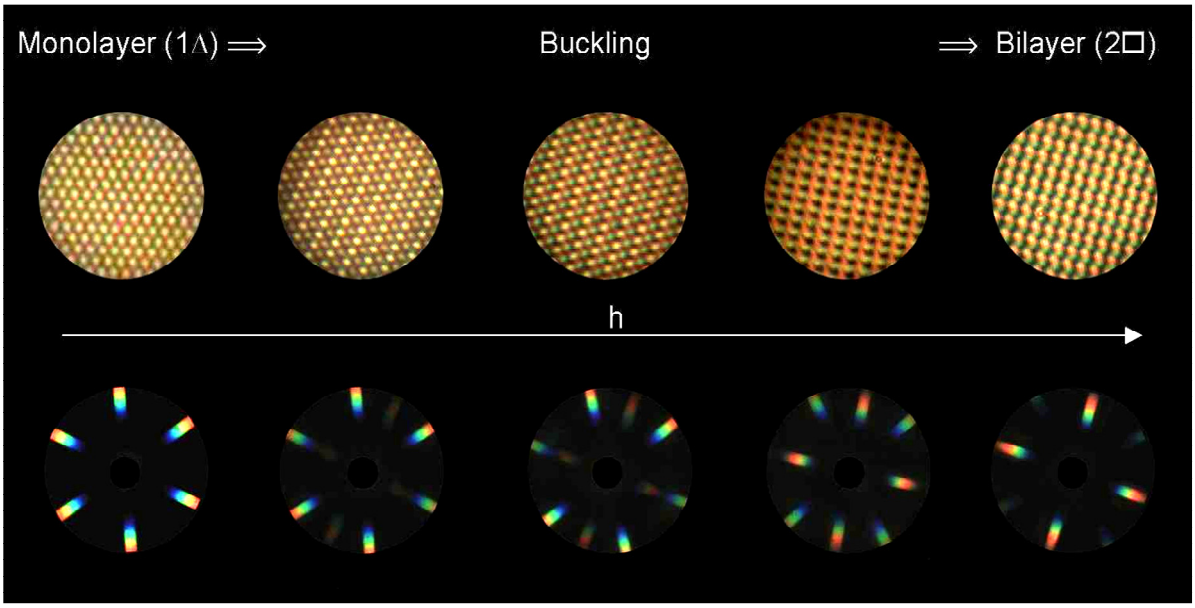

FIG.9: Smooth transformation of the 1△ → 2□ transition in real and reciprocal space. In both cases the sample was illuminated with white light.

The distance between two neighbour particles in a row *a* (do not confuse fith the particle radius a) is just the effective particle diameter σ*. At the very beginning the distance between the rows, b will be approximately twice the height of the equilateral triangle formed by three particles in the monolayer Fig.10. For higher plate-plate distances, the distance between the rows in each layer decreases continuously until the rows come in contact giving rise to the 2□ structure (b = σ*). During all the transformation each row in one sublayer will be in contact with two rows of the other sublayer in that way that the packing fraction is kept always high.

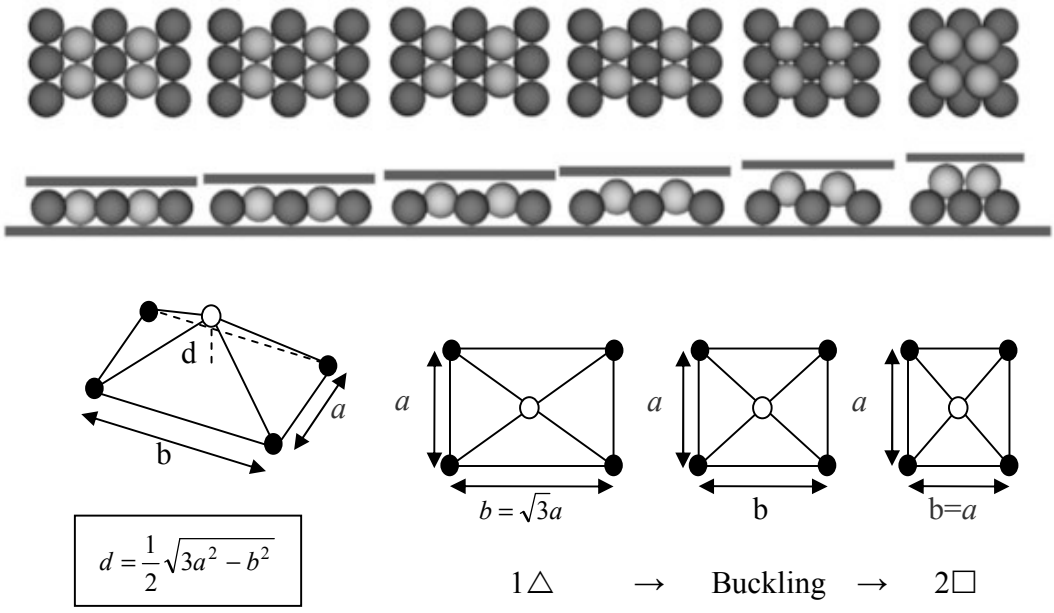

FIG.10: Model of hard spheres following the maximum packing criteria showing the morphological changes of the unit cell as the cell thickness h increases. Here a=σ.*

The equation which relates the volume fraction variation with the cell height is given by the trigonometric relations established between the length b and the distance between the layers d as appears in Fig.10. The volume fraction variation between the monolayer and the beginning of the bilayer following the maximum packing criteria is given by,

$$\phi_{1h\to 2s} = \frac{\pi}{3d\sqrt{4(1-(d-1)^2-1)}} \qquad (3.4)$$

This expression is found in [Pan84]. In Fig. 9 the experimental results found in this thesis for the buckling transition in real as well as in reciprocal space are shown.

3.4.1.2. The Rhombic phase

In an analogous way, the rhombic phase mediates in the transition between the square and the hexagonal structure in the bilayer and can be also explained in terms of close sphere packings subject to a lateral pressure. This time the height increment leaves the particles to shift respect to their neighbour particles deforming the square net into a rhombic one. Hence the upper layer achieves a higher position corresponding to an increase of h. The rhombohedric transformation continues until the formation of the two-layer hexagonal structure is formed. In Fig.11 the rhombic transition in both real and reciprocal space are shown. During the rhombohedric transformation it is possible to observe the changes in the intensity maxima distribution from the four intensity spots, characteristics of the 2□ structure to the six diffraction maxima characteristics of the 2△ phase. The volume fraction variation of the rhombic phase permits a continuous geometrical passage between the two maximum volume fractions corresponding to the square and the hexagonal structures in the bilayer as shows Fig.12. This transformation also allows a better filling of the available space.

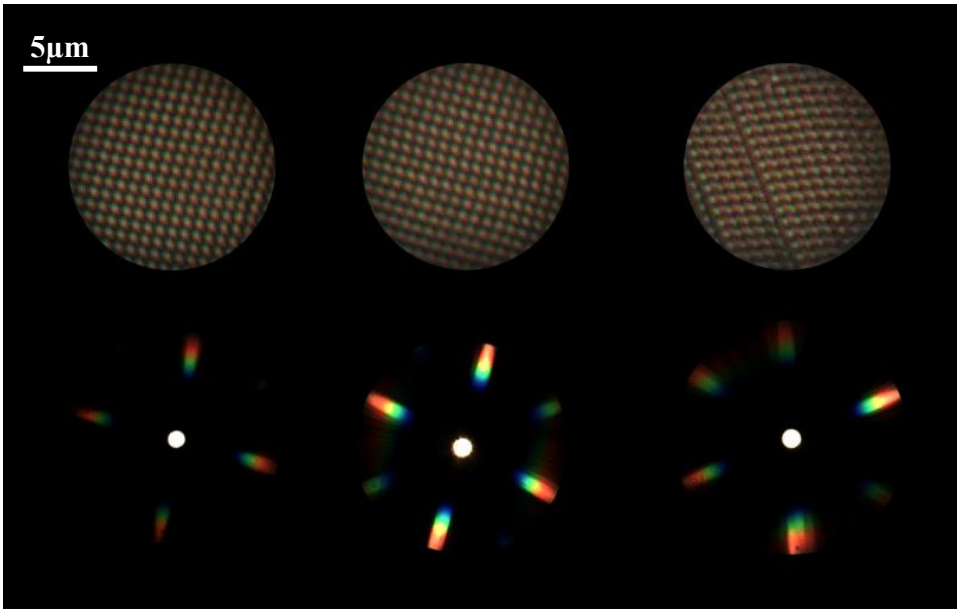

FIG.11: High magnification and diffraction patterns of the rhombic phase. The maxima intensity of the diffraction patterns nicely indicates the symmetry transformations in the reciprocal lattice.

Let's consider the 2□ phase as constituted by square pyramids with a particle in each vertex. As the transformation starts, the basis of such pyramid will distort giving rise to a pyramid with rhombohedric basis. At the same time, the particle on top of the pyramid will shift continuously from the centre of the square to the centre of one of the triangles which defines the rhombus. This transformation as illustrates Fig.12. The rhombohedric deformation of the lattice continues until $d = \sqrt{8/3}a$; the height of the close packed hexagonal structure.

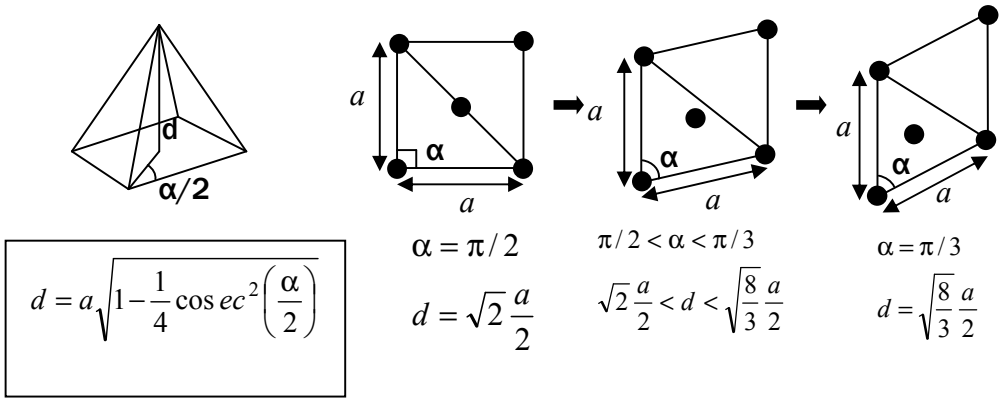

FIG.12: Hard sphere model for the 2□⟶ 2△ transition proposed by Pansu et al [Pan84] following the maximum packing criteria. A continuous transition via rhombohedric transformation is possible.Here a = σ.*

The trigonometric relations between the smaller angle α defining the rhombus and the distance between two layers d allow the calculation of the volume fraction dependence with the cell height h. The volume fraction of this intermediate structure varying with the cell thickness is given then by,

$$\phi_{2s\to 2h} = 2\sqrt{\frac{1-(d-1)^2}{d(3/4-(d-1)^2)}} \qquad (3.5)$$

3.4.2 Higher number of layers: The prism phases

For more than two layers there are few references about intermediate structures before the beginning of this thesis. In the work of Pieranski and co-workers we can find a brief comment about the n□ ↔ n △ transition for $n > 5$ [Pie83]. They found a region made up of "scores" parallel to the symmetry axes of both structures when varying progressively the distance between the plates of one of the cells used in what they called the "in time" experiments. However we can consider that Neser was the first who reported experimental evidences for stable intermediate structures when the number of layers n is higher than two. This new structure is composed of triangular shaped prisms which are interlocked and received the name of n-layers prism phases n-$\mathcal{P}$. The side lengths of such prisms ranged between two and up to eight particle diameters, at the wedge heights allow for two to eight monolayers. In Fig.13a) a SEM picture of the 4-$\mathcal{P}$ phase is shown where two prisms have been highlighted by red. The base of the prism has square symmetry, so it is easy to deduce that in a close packed structure the sides of such prisms present hexagonal symmetry in order to have the same number of particles in each side of the prism. They considered the square prism phases to be an implementation of the buckling principle for structures with more than one layer since these stripe patterns appeared each time the crystals includes a new layer. Considering the prism as rigid objects they found a mechanism which would explain a transition n□ → n-$\mathcal{P}$ → (n+1)□. Starting with any n□ phase when increasing the cell thickness the structure is dislocated forming prisms. These prisms are shifted in the vertical direction. This allows to decrease the distance of adjacent, equally oriented prisms and therefore to increase the volume fraction. Finally when the cell height is increased further this continuous transition leads to the (n+1)□ structure. The scheme for this transition model is shown in Fig.13b) and is compared with the buckling mechanism to show the similarities in the origin of both transformations.

The calculations of Neser for the n□ → n -$\mathcal{P}$ → n□ are plotted in a two dimensional phase diagram Φ(z), where z is in this case the normalized height h/σ (Fig.14). In this plot also the previous calculations from Pansu et. al are included. The dotted lines indicated the volume fraction variation from the close packed structures (n□ and n△) for intermediate cell thickness values. With this

curves Pansu et al. were able to justify for instance the possibility for the existence of a buckling phase since in their calculations the volume fraction variation of this phase was always higher than the corresponding 1△ and 2□ curves which implies a higher stability. In 1997 the buckling phase was reported by Neser corroborating the validity of the 1△ → 2□ model transition [Nes97].

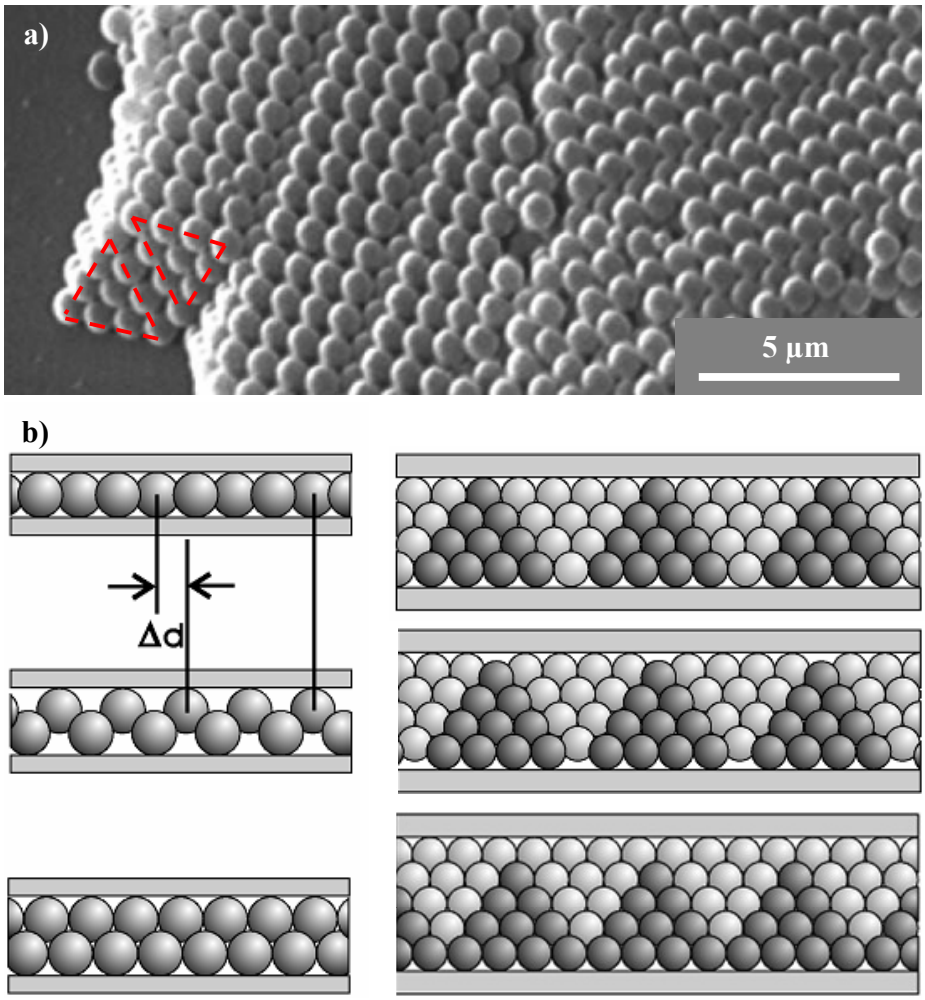

FIG.13: a) Scanning Electron Micrograph of the 4$\mathcal{P}$ structure. The red triangles indicate the triangular shape of the prisms. b) Comparison between the buckling transformation mechanism and the corresponding model proposed by Neser for the n□ → n-$\mathcal{P}$→ (n+1)□ transition. [Nes97]

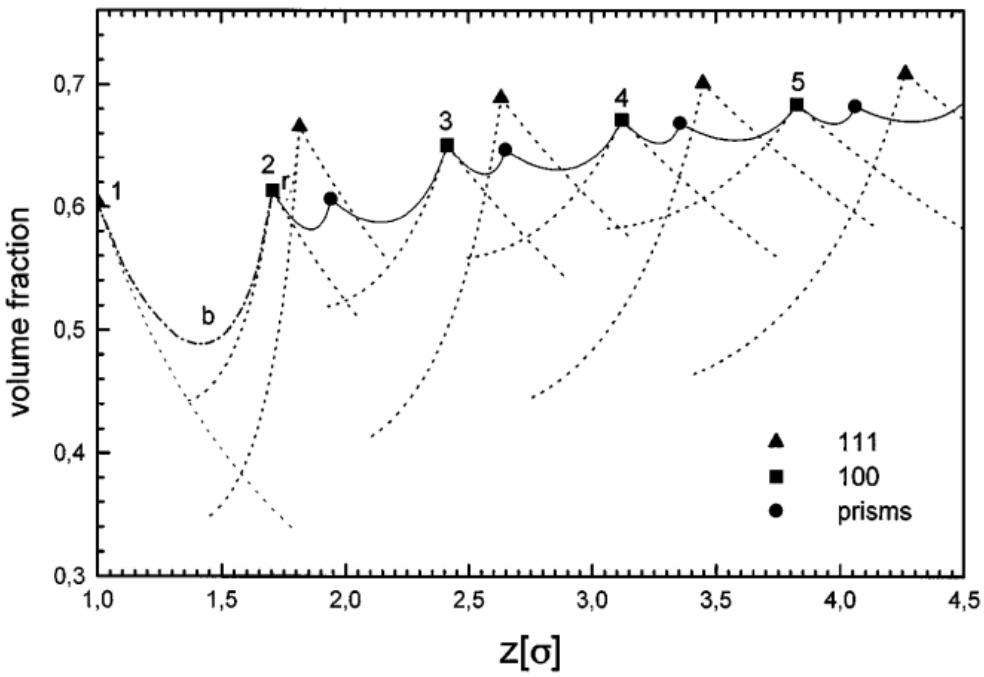

FIG.14: Phase diagram volume fraction-z, where z = h/σ for a confined system of hard spheres following the maximum packing criteria. The triangles and squares indicate the values for the close packed hexagonal and square structures. The dotted lines do correspond to the calculations of Pansu et al. for the volume fraction variation at intermediate values of the cell thickness [Pan84]. These calculations include the buckling b and the rhombic transition r. The black circles indicate the values for the n$\mathcal{P}$ structure. The continuous line does correspond to the transition model n□ → n$\mathcal{P}$ → (n+1)□ proposed by Neser [Nes97].

3.5 The complete phase diagram for a bilayer system of charged spheres

The last relevant result found before the beginning of this thesis is the work presented by Messina and Löwen [Mes03]. In it, the full phase diagram for a confined crystalline bilayer of particles interacting via a screened Yukawa pair potential at zero temperature was reported. Varying the particle density and the screening interaction they found rectangular, square, rhombic and hexagonal crystalline lattices going from one-component plasma to hard-spheres systems. The phase diagram was calculated assuming that at typical interparticle distances the pair potential is much higher than the thermal energy of the system k_BT at room temperature justifying the T = 0 calculations At this

temperature, the stable state is solid and by varying the system parameters different structures are expected for the crystalline bilayer. The total internal energy of the bilayer was calculated by lattice sum minimizations, considering that the bilayer consists in two periodic 2D-lattices with the same unit cell shifted relative to each other in the lateral direction. The main parameters of the system are the screening strength, the particle density and the distance between the layers. By using two dimensionless parameters the complete two-dimensional phase diagram is completely determined. These parameters are the reduced layer density $\eta = \rho D^2 / 2$ and the relative screening strength $\lambda = \kappa D$. κ is the inverse screening length, $\rho = N / A$ the total area density of the two layers with A denoting the system area in the (x,y) plane. D is the distance between the layers in z direction which is prescribed by the external potential confining the system. The resulting phase diagram is shown in Fig.15. In it, we can distinguish five different crystalline phases.

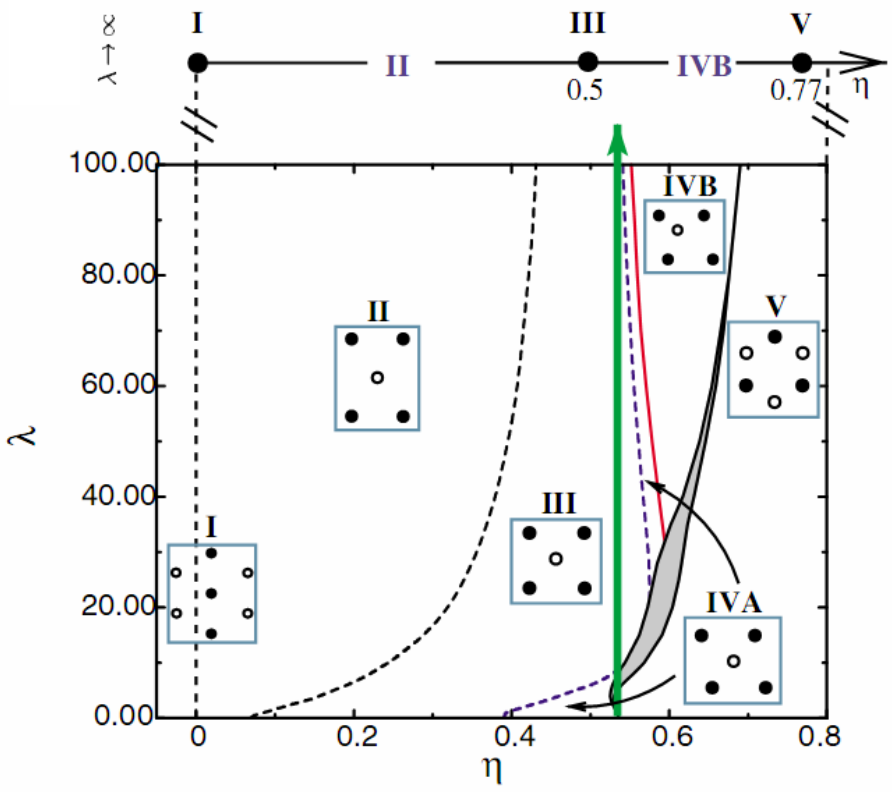

FIG.15: Phase diagram for a bilayer system of charged particles particles confined between two parallel plates. For explanation see text.

The inset drawings shows the unit cell of one of the layers (black dots) and at least one of the particles of the other layer (white dots) indicating the relative shifts in the plane xy of the layers. For the structures classification in the bilayer they followed the same notation as Goldoni et al [Gol96] which just consists in roman numbers. By keeping fix the relative screening strength to an intermediate value and increasing the reduced layer density we find first the phase I which does correspond to the monolayer (1△); phase II indicates the buckling phase (denoted from now as B); phase III does correspond to the 2□ phase; phases IV-A and -B are two possible rhombic phases and finally phase V is the 2△ phase. For high screened interactions ($\lambda \to \infty$),the hard-sphere limit is reached as the black arrow shows on top of the plot. The different curves indicate the phase transitions. In this phase diagram rich phase behaviour is shown. From this phase diagram three important predictions are remarkable: the two possible rhombic phases which coexist at finite screening strength (gray region), the single and double re-entrant scenario for phase IV-A indicated by a green arrow and finally the prediction of the phase IV-B mediating the 2□ → 2△ transition.

3.6 Final remarks

These previous work revealed to be of fundamental help in the present thesis. We can consider that all the works and references here presented are the basis for the study of colloidal spheres confined between solid boundaries. The different experimental as well as theoretical works presented in this chapter were following a chronological order. With this sequential order we can see not only the evolution in the discovering and classification of new structures but also the evolution in the complexity of the colloidal interaction reported in the theoretical works, going from hard to highly repulsive spheres. Along the thesis other relevant works have been presented complementing former investigations wich will be presented in the result analysis. On the other hand in this chapter we have maintained the original notation of the authors. However our results will present sometimes a different notation which will be specified conveniently.

4 Experimental techniques

The experiments performed on this thesis consist mainly in the study of the morphology of the different crystalline structures found under confinement as well as the structural transitions between them. Since most of our samples used in the experiments consist of colloidal particles with a diameter around 1μm in water, the observations were initially planned to be made with a high resolution microscope. In particular we used an inverted compound microscope Leica IRB working in transmission bright-field operation mode and using different magnification objectives. Also some optical devices were implemented in the optical light path. The pictures were taken with different CCD and digital cameras. The pictures and videos were stored to be later analyzed. To characterize each crystalline structure, besides the former, we also used other techniques being the most relevant Fourier microscopy, Scanning Electron Microscope (SEM) and Atomic Force Microscope (AFM).

In this chapter we will explain how an optical microscopy works in transmission mode to obtain the magnified image of an object. We will also speak about the factors involved in the image formation as well as the main features to obtain quality images. After that we will speak about a conventional technique using the microscope to observe the intensity distribution of the light diffracted by the object. This technique is known as Fourier microscopy. To explain the physics underlying this technique, first the basic concepts about light scattering in the Rayleigh-Debye-Gans approximation will be given. In this case, several assumptions have to be made in order simplify the general solution of the diffracted intensity by an object, like consider elastic scattering or non-absorbing media. Then these concepts are applied to the particular case of scattering of light in

ordered structures which is a powerful technique to obtain some of the crystal properties. The section is finished explaining the details to obtain information from the scattered light when working with the optical microscope. At the end of the chapter we will speak briefly about other useful techniques using in this thesis to study the morphology of the confined crystals once the samples were dried.

4.1 Bight-Field Microscopy

The main task of a microscope is not only to form a magnified image of an object, but rather it has to be capable to separate the details in the image and render them visible to the human eye or camera. There are three basic principles in the formation of an image: magnification, image resolution and image contrast. The magnification of an object is defined as the aspect ratio between the object's image and the object itself. Its mathematical expression is derived by using the principles of geometric optics (See for instance, [He86]). The other two tasks are intrinsically related to the illumination system and therefore, an optimized illumination system is fundamental to obtain best optical performance in light microscopy. In Fig.16 a scheme of the optical components and focal planes of the compound microscope working in transmission mode are shown. In such microscope, the cone of light outcoming from the microscope lamp is controlled by an iris diaphragm (the field diaphragm). The light then passes through a condenser which consists of a set of lenses. In the front focal plane of the condenser there is another iris diaphragm which controls the amount of light that arrives to the sample (aperture diaphragm). Once the light has passed through the sample, it is focused by the objective forming a magnified intermediate image of the sample. Finally, the ocular (also called eyepiece) further magnifies the image projected by the objective producing a secondary enlarged image. The ocular also has a diaphragm in order to control the cone of light. The word *compound* refers to this two-stage enlargement where objective and ocular work together producing a final image magnification,

$$\mathbf{M}_{\text{final}} = \mathbf{M}_{\text{objective}} \times \mathbf{M}_{\text{ocular}} \tag{4.1}$$

Nowadays most commercial optical microscopes are infinity-corrected. This means that the intermediate image will be formed at infinity. For that, a lens (termed tube lens) is added between the objective and the ocular. The tube lens will focus the light coming out from the objective, forming the intermediate image at the diaphragm of the ocular. In this case the total magnification is also

dependent upon the tube lens. As a consequence, in inverted microscope designs, the objective can be freely moved with the advantage of focusing at different specimen planes avoiding undesirable stage shift during focusing as in non-inverted microscopes. Furthermore, the infinity corrected microscope configuration allows also the insertion of additional optical elements like additional lenses between the objective and the tube lens without the necessity of compensating optics.

We next explain how to obtain images with optimal resolution and contrast. The illumination method for microscopy introduced by A. Köhler in 1893 guarantees that the intensity variations in an image are due only to the sample and not to irregular illumination from the light source. Köhler illumination is achieved when, simultaneously, the light emitted from the lamp is focused at the front focal plane of the condenser whereas the condenser lens focuses an image of the field diaphragm into the plane of the sample yielding optimal contrast enhancement of the finer sample details. These adjustments give rise to two different sets of conjugate planes[4] between the illuminator and the eye: The set of *aperture* or *illumination* planes and the set of *field* or *image forming* planes. The aperture planes are the lamp filament, the aperture diaphragm, the rear focal plane of the objective and the eye point (or camera lens). The field planes are the field diaphragm, the sample plane, the fixed diagram of the ocular and the retina (or camera chip). These planes are called conjugate, because for a given set, all of the planes are seen simultaneously when looking through the microscope [Mur01].

In Fig.16 the optical path and image planes are drawn, for each set of planes. In blue are represented the optical rays corresponding to the illuminating system and in green are represented the optical rays corresponding to the image forming planes. These two simultaneous optical paths of the light are described next.

- *Optical path through the* a*perture planes*: The collector lens forms a magnified image of the light source (L_1) onto the aperture diaphragm of the condenser (L_2). As this diaphragm is placed at the front focal plane of the condenser, the light refracted by the condenser lens will emerge parallel (the image will be formed at infinity). The objective gathers this light forming an image of L1 onto the rear focal plane of the objective (L_3). The ocular which is focussed at the rear focal plane of the

[4] In an image forming system we say that two planes are conjugated to each other when any image point is geometrically related to another point in the object and vice versa. In the case of an optical system formed by several lenses the image formed by the first lens will be the object for the second lens and so on.

objective will form the final image at the eyepoint (L_4) which is the place were the pupil of the eye (or the focal plane of the camera lens) should be placed.

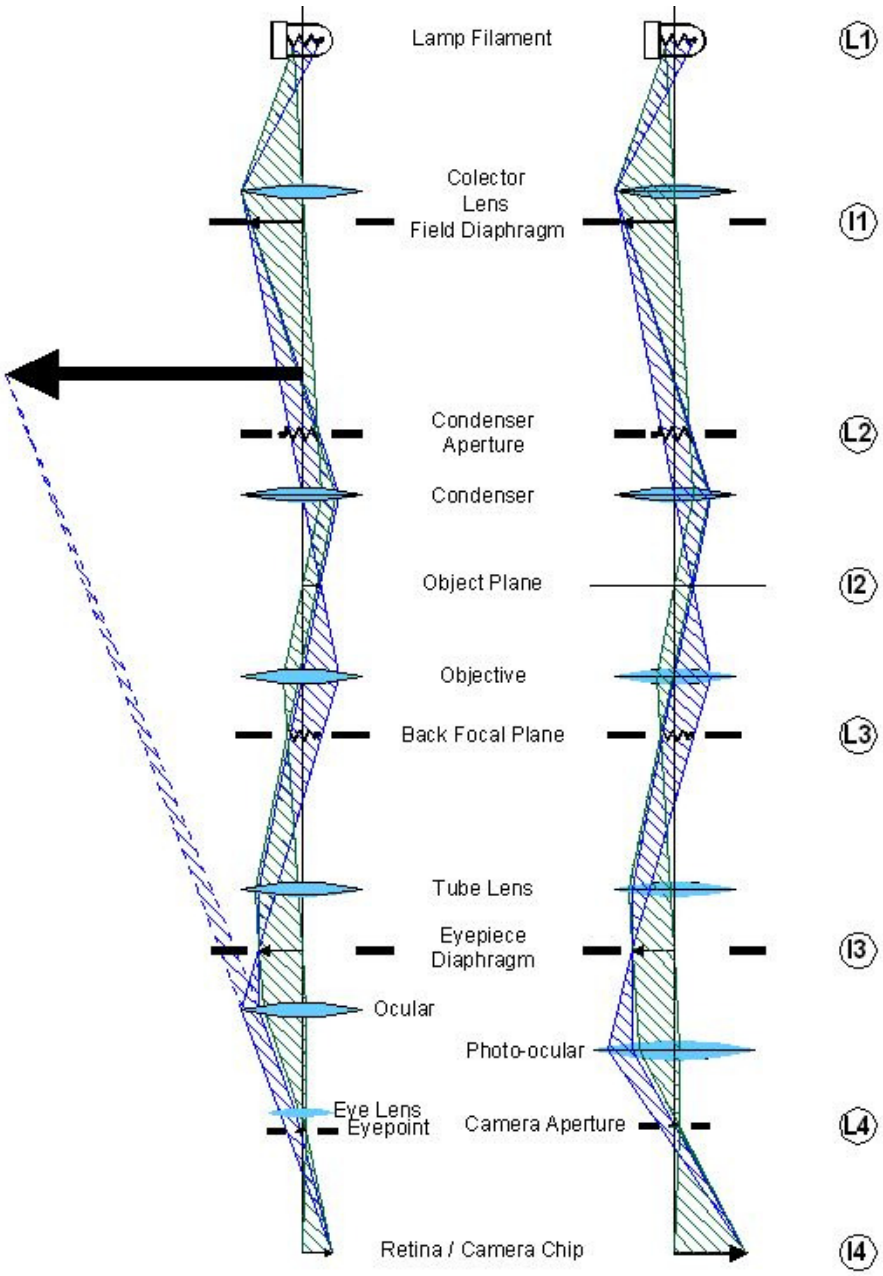

FIG.16: Basic scheme of the light passing through the main components of the microscope with Köhler illumination. L1 to L4 are the set of aperture conjugate planes while I1 to I4 are the set of field conjugate planes. The scheme of the left is the corresponding to use the eye as a detector whereas the scheme in the right side is the corresponding when using a camera. The light rays are separated in two different beams to facilitate the visualization of the part of light which contribute to the image formation (blue) and the part of the light which contributed to the illumination of the sample (green).

- *Optical path through the* f*ield planes*: The condenser lens produces a small inverted image of the field diaphragm (I_1) onto the plane of the sample (I_2). The sample is then focused by the objective which produced a magnified image of it together with the field diaphragm (the intermediate image before mentioned) in the fixed diaphragm of the ocular (I3). Finally the ocular and the refractive elements of the eye or camera will form an image on the retina or camera chip (I_4).

When looking through a microscope, what we observe are the field planes. In that case we say that we are working in orthoscopic mode (or in real space). On the contrary, to observe the aperture planes we have to form an image of the back focal plane of the objective. This is achieved placing a lens (Bertrand lens) behind the objective or using an eyepiece telescope. By doing so we say that we are working in conoscopic mode (or in reciprocal space). In Fig.16, we can see that converging rays in one set of conjugate planes are nearly parallel rays in the other set of planes and vice versa. This indicates the existence of some kind of reciprocity between the two sets of planes. Experimentally, J.C. Gall proved this reciprocity by placing a periodic object in the back focal plane of an objective [Gall67]. By doing this, he observed the diffraction pattern of the object in the final magnified image plane[5]. With Köhler illumination the two different sets of interlaced focal planes in the microscope are correctly positioned along the optic axis of the microscope achieving optimal image formation and maximal spatial resolution. Condenser misalignment and an improperly adjusted condenser aperture diaphragm are the main sources of image degradation and poor quality photomicrography.

Until now I have described how the microscope forms images and the existence of conjugate planes which correct position will enhance the quality of the final images. However we have not explained yet how the microscope elements affect the resolution and contrast in the image formation. Both factors strongly depend on the nature of the light and how the electromagnetic waves act when interacting with matter. When any object is illuminated, the light can be refracted, absorbed, reflected or scattered by the object. In particular, diffraction plays a relevant role if we want to observe objects or details in objects close in size to the wavelength of light. As we are going to see, diffraction sets up a lower limit below which an optical system cannot resolve structural details. Over

[5] This also demonstrates that the microscope can work as an optical difractometer.

this limit the image can be enlarged but no additional details are resolved, i.e. there is magnification but without a corresponding increase in resolution. This is called *empty magnification*.

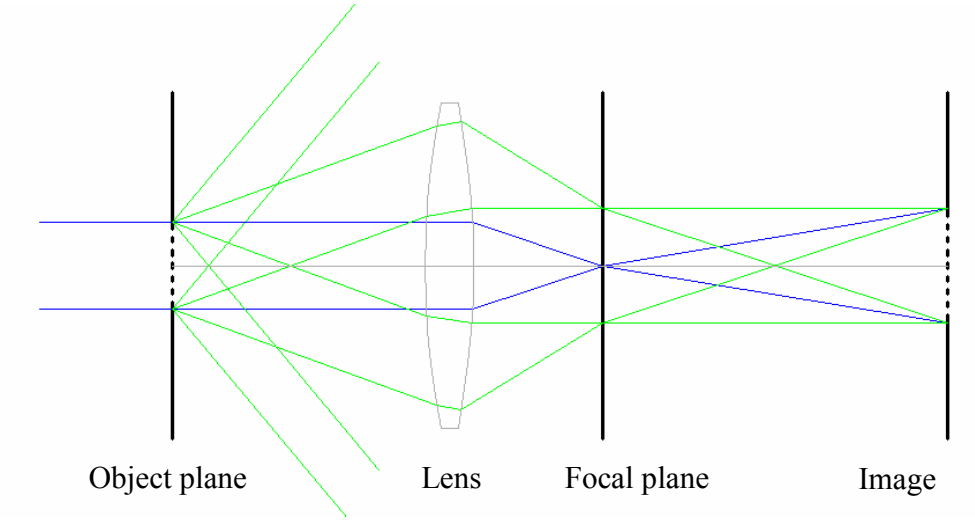

FIG.17: The optical rays and wave fronts in an image forming system after passing through a periodic object. In blue the non diffracted rays. In green the diffracted light by the sample is shown.

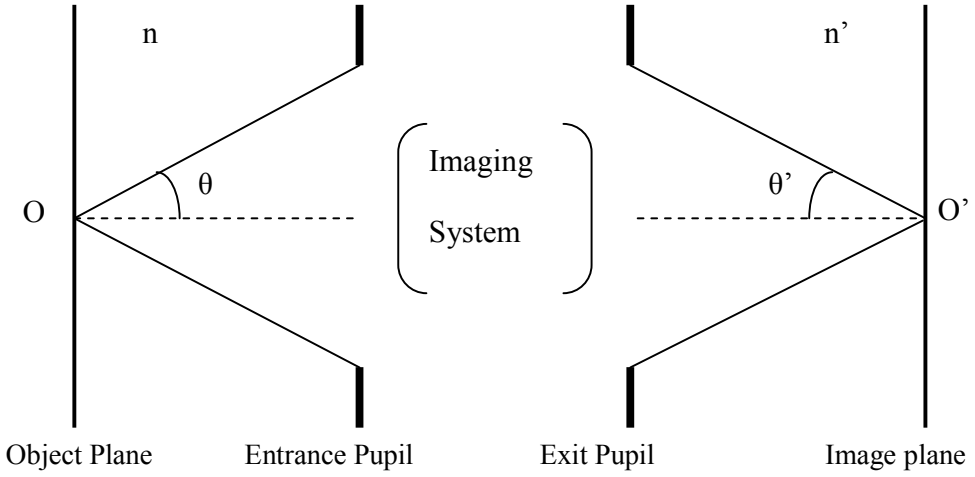

FIG.18: Imaging forming system showing the entrance and exit pupils, the object- and image-side angular apertures, θ and θ' respectively and by the corresponding refractive indexes, n and n'. The light cone emerging from the object at point O, is limited at the entrance of the imaging system. In the same way, the outcoming light from the imaging system which forms the image is limited by the exit pupil.

Ernst Abbe in 1873 [Ab73] and Lord Rayleigh in 1896 [Ray96] were the first who studied the implications of diffraction in image formation. In optical microscopy, when we illuminate a sample, some of the light passes undisturbed through the sample and some of the light is diffracted. Non-diffracted (0^{th}-diffraction order) and diffracted light will be focused first in the back focal plane of the objective as shown in Fig.17. From this plane, diffracted and non-diffracted light interferer in the eyepiece diaphragm to form the intermediate image. According with Abbe's theory, there will be no resolved image if diffracted light from the object is excluded from the objective. Or the other way around, the larger the number of diffracted orders is collected the better the resolution and the contrast the image will have. Since the diffracted light is "spread" in all directions and there is no lens capable to gather all the light diffracted by an object, an image will never perfectly represent the real object. Because of that we speak about the resolution limit of an optical system. In general, the physical entity which limits the cone of light that passes through a lens system is called the aperture of the imaging system. Apertures are limited by the finite width of some component in the imaging system. The calculation of the images of these limiting component permits to know the size of the cone of light that the objective is able to collect and transmit and receive the names of entrance and exit pupils respectively. They are schematically shown in Fig. 18. The relevant parameters which determine the cone of light are the aperture angles θ, θ' and the refractive indexes between the object and the system n and between the system and the image n'. We define the numerical apertures of the object-side NA and the image-side NA' by

$$NA = n \cdot \sin(\theta) \qquad \text{and} \qquad NA' = n' \cdot \sin(\theta') \tag{4.2}$$

In these equations we see that by increasing the refractive index or the angular aperture will increase the resolution of the intermediate image. Fig.19 shows the effect of reducing the numeric aperture of the objective at constant magnification in real as well as reciprocal space. In those pictures the refractive index is constant and the angular aperture is successively decreased from pictures a) to d). In this set of pictures we can also see the exemplification of the Abbe's criteria; by reducing the cone of light, less diffracted light is collected by the objective which implies the loose of fine details in the image. The effect of varying the angular aperture can be also seen when working with different magnification objectives; lower magnification implies objectives with longer focal distances than those with high magnification. Consequently the aperture angles and hence the numerical aperture of the objectives will increase with the magnification. At the same time, since

higher magnifications implies higher numerical apertures, with this kind of objectives more diffracted light will be collected increasing the resolution of the images.

Another important effect related with the colour of the samples is shown in Fig. 19. Working with objectives of low numerical aperture where the image is formed from only non-diffracted light allows us to classify the structures. The illumination of a sample composed by elements of different refractive index will originate phase differences between the emerging waves. When these waves interfere to form the image, we will observe as a result, that each structure is characterized by a characteristic colour. This is interesting in our case, when studying properties of crystalline colloidal structures. For samples with identical size and shape of the particles, refractive index of the particles and solvent, we can associate a colour to each crystalline structure. With this colour code we can easily distinguish the structures without necessity of resolving fine details [Schö06]. As we observe in Fig.19 the loss in resolution increases the colour enhancement. It is also interesting to notice that the colour in these pictures varies from a) to d), which indicates the contribution of the diffracted light to the colour of the image.

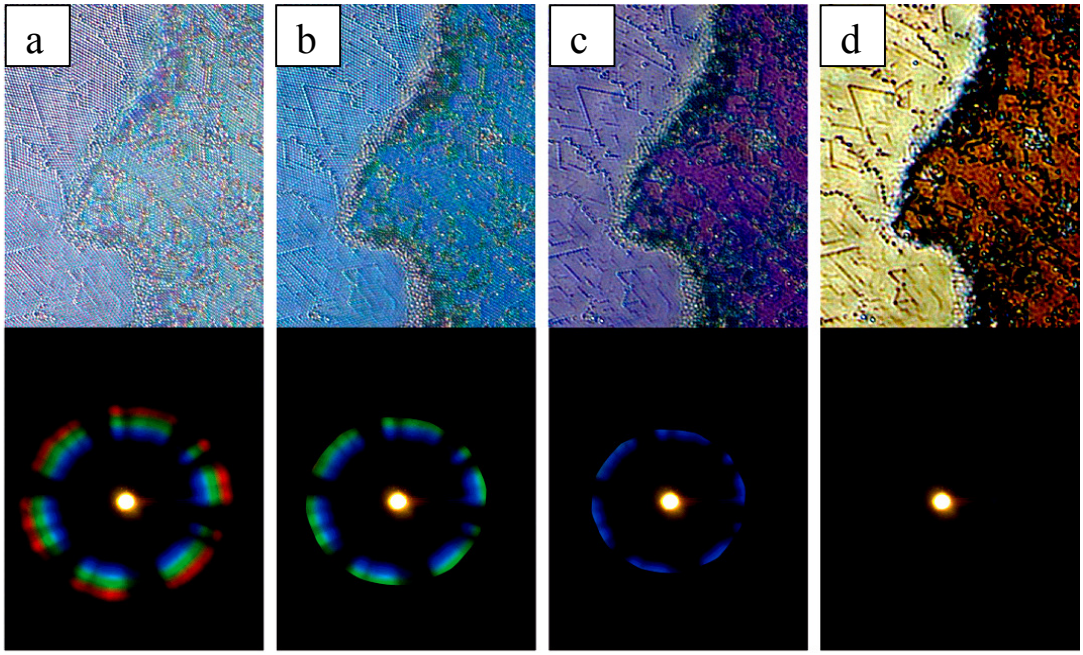

FIG.19: Pictures of the same region of a colloidal crystalline sample of polystyrene particles of 590nm in real and reciprocal spaces showing the effect of decreasing the numerical aperture from a) to d). [Schö06]. The images in real space have a size of 63.5 X 57.5 μm^2.

Once the numerical aperture of an optical system has been defined we can explain how the diffracted light contributes to the formation of the resolved image. The finite size of the objective's pupils limits the brightness of an image but diffraction at the pupils will also limits resolution. In the case of illuminated samples in a microscope, there are two primary sites for diffraction which strongly affect the resolution of the image: one at the specimen itself and another at the aperture of the objective lens, so the image formation of any lens system can be understood as a double diffraction process. To understand how the pupils of a lens system affect image resolution in general, we apply the Huygens-Fresnel construction for diffraction at the borders of any illuminated object [He86]. Considering that every point in the border of the object acts an individual source of light and assuming that the diffracted light is characterized by a spherical wave front, it is found that the image of each point object is an intensity distribution known as Airy pattern (Fig.20a)). The central lobe, called Airy disk contains 84% of the intensity of the point image and is considered the limit of useful object information. The image of an extended object is a distribution of superimposed Airy disks where outer rings reduce the contrast of the image by brightening the background. How these diffraction patterns interfere to form the image will depend on the degree of coherence of the illumination. Two waves are said to be coherent if they have a constant relative phase, which also implies that they have the same frequency. In conventional bright-microscopy a tungsten filament is typically used as source of light. This is considered partially coherent light which means that the photons are slightly out of phase with each other. In that case the degree of coherence will depend on the angle cone of light which arrives to the object. This angle is controlled by the numerical aperture of the condenser. Assuming a system free of aberrations and working in bright field microscopy, we define the resolving power of the microscope as the minimum distance necessary to distinguish two diffraction spots in the image plane. In practical terms, this happens, when the centre of the Airy pattern of one point in the image plane will coincide with first dark ring of the other one (Fig.20c)). The equation which describe this separation is the so called Rayleigh resolution,

$$d = \frac{1.22\lambda}{NA_{condenser} + NA_{objective}} \tag{4.3}$$

where d is the minimum resolving distance, λ is the wavelength of the incident light and $NA_{condenser}, NA_{objective}$ the numerical apertures of the condenser and objective respectively. When the

distance of the individual spots is smaller than d then we say that the image is not well resolved (Fif.20b)). Finally the spacing of the elements of the detector will affect the resolution of the final image. The pixels of the camera chip or the cones of the retina have to be smaller than the minimum resolving distance of the imaging forming system to appreciate fine details. Therefore we can conclude that the basic factors limiting the resolution in the microscope are the image system aperture, the degree of coherence and the detector segmentation whereas, image formation, spatial resolution and contrast are governed by diffraction.

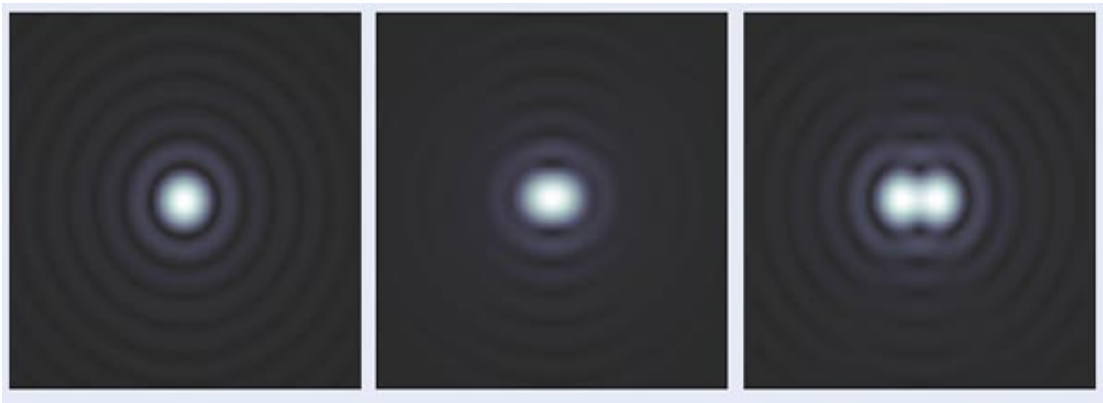

FIG 20: a) The image of a point object is given by an intensity distribution called the Airy disc. b) Two points separated by a distance smaller than the Rayleigh resolution are not resolved, c) Two points are said to be resolved when the first minimum of one distribution coincides with the maximum of the other [OSh08].

The main principles of bright field microscopy as well as the steps to get best observations and quality images have been described. Since we work with periodic objects their diffraction patterns will give us qualitative and quantitative information about the morphology of the crystals. As have been already explained, with the microscope we can observe the diffraction patterns in the conoscopic mode by adding a Bertrand lens after the objective. This lens is focused at the rear focal plane of the objective and, together with the tube lens and the ocular, forms an image of the aperture planes at the optical detector. This technique is called Fourier microscopy and its basic principles are explained next.

4.2 Fourier microscopy

4.2.1 Fundamental Concepts in Light Scattering

Light scattering is a powerful technique to characterize the structure of colloidal crystals since the interparticle distance of the crystals is comparable to the wavelength of visible light. Typical light scattering experiments in colloid physics gives information about the dynamical and structural properties of the colloidal suspensions. The physical principles of light scattering from colloidal systems are equivalent to X-ray or neutron diffraction for atomic ones. In general, scattering of electromagnetic waves by matter is the result of the heterogeneity of the system. Except vacuum, any system is heterogeneous at a given scale so, all media scatter light. Independently of the kind of heterogeneity, the physical principles are the same: Since matter is composed by discrete electric charges, the electric field of an incident electromagnetic wave will induce oscillatory motion on them. The charges when accelerated radiate secondary electromagnetic waves in all directions. The excitation of a charge by light and posterior radiation of secondary light waves is what we know as scattering of light. The total scattered radiation from an assembly of individual charges in a certain direction is the sum of the each scattered wave in that direction. A measurement of the scattered intensity contains information concerning the relative positions of the charges and the relative distances between them because the phase difference of the scattered waves from two charges depends just on those positions as well as on the direction in which the intensity is measured. In the interaction of light with matter, we have to take also into account that the charges can transform part of the incident radiation in other forms of energy like thermal or chemical energies, a process called absorption. Scattering and absorption are mutually dependent processes. However, here we will consider non absorbing samples. The former means that the energy (and hence the momentum) is the same before and after the interaction changing only the direction of the waves.

For colloidal systems, (and in general for any atomic or molecular system), each particle consists of a charge distribution. Under this situation an incident beam of light will induce an oscillating dipole moment in each of the volume elements of the particle. The induced dipoles will have the same direction as the polarization of the incident field and will emit radiation isotropically in all directions perpendicular to the oscillators. As in the case of the individual electric charges, the

scattered light will be the resulting interference of the individual waves from each oscillator (or scatterer). We are going to give its expression using some assumptions and approximations and explaining only some intermediate steps. The complete demonstration can be found in [Dhont83].

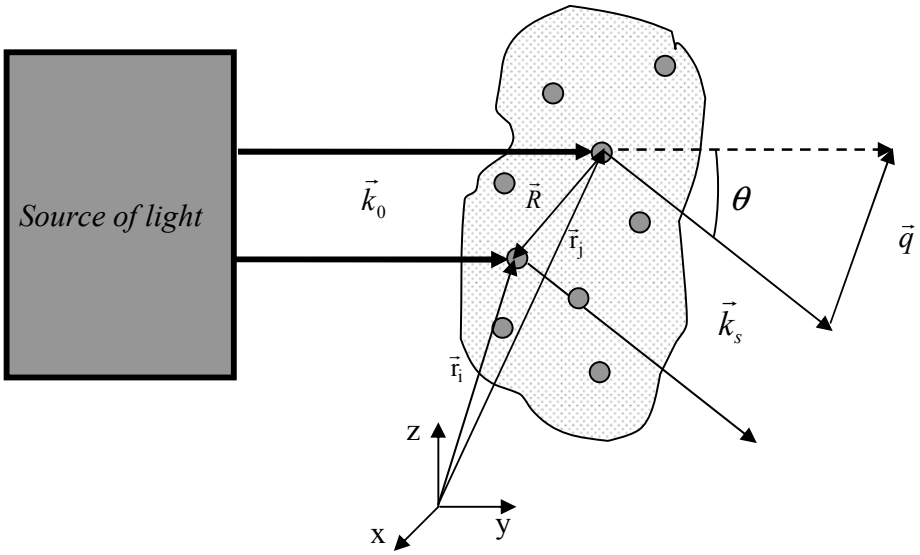

FIG.21: Scheme to visualize the scattering of light by a system of particles (gray dots).

Lets consider a monochromatic source of light characterized by its wave vector $\vec{k}_0 = 2\pi\hat{n}_0 / \lambda$, along the direction given by $\hat{n}_0$ and wavelength λ as shows Fig.21. If the sample is away from the light source we can consider that we have plane waves where the incident electric field $\vec{E}_0(\vec{r},t)$ at position $\vec{r}$ and time t can be expressed as

$$\vec{E}_0(\vec{r},t) = \vec{E}_0 \exp\{i\vec{k}_0\vec{r} - \omega t\} \tag{4.4}$$

where $\vec{E}_0$ is the wave amplitude and ω the frequency of the incident radiation. After incidence of the light in the sample, the phase difference between the incident and the scattered waves is then,

$$\Delta\phi = (\vec{r}_i - \vec{r}_j).\vec{q} \tag{4.5}$$

Considering elastic scattering, $\left|\vec{k}_0\right| = \left|\vec{k}_s\right| = 2\pi\nu_s / \lambda$, where ν_s is the refractive index of the solvent and $\vec{q} = \vec{k}_0 - \vec{k}_s$ is the scattering vector of modulus,

$$q = \left|\vec{k}_0 - \vec{k}_s\right| = \left(4\pi\nu_s / \lambda\right)\sin\left(\theta / 2\right) \tag{4.6}$$

being θ the scattering angle. To obtain the scattered intensity we should first obtain an expression for the scattered electric field $\vec{E}_S$. To do that we apply the Maxwell equations to the total electric field, $\vec{E}(\vec{r},t) = \vec{E}_0(\vec{r},t) + \vec{E}_s(\vec{r},t) = \vec{E}(\vec{r})\exp\{-i\omega t\}$. Assuming that the colloids behave as linear dielectric material with dielectric constant $\vec{\varepsilon}(\vec{r})$ and a magnetic permeability equal to that of the vacuum, μ_0. Thus the relations between the fields are,

$$\vec{D}(\vec{r},t) = \vec{\varepsilon}(\vec{r}) \cdot \vec{E}(\vec{r},t) \tag{4.7.a}$$

$$\vec{B}(\vec{r},t) = \mu_0 \cdot \vec{H}(\vec{r},t) \tag{4.7.b}$$

with $\vec{B}$ the magnetic induction, $\vec{H}$ the magnetic field strength and $\vec{D}$ the electric displacement. Since the material inside a scattering volume element may be optically anisotropic, the dielectric constant $\vec{\varepsilon}(\vec{r})$, is in general a tensor. Assuming that the fluid is homogeneous, neglecting fluctuations of the dielectric constant of the fluid, ε_f, and considering only the scattering coming from heterogeneities in the dielectric constant due to the presence of the colloidal particles (that is,

neglecting the scattering from the molecules of the solvent), $\vec{\varepsilon}(\vec{r})$ is equal to the dielectric constant of the fluid and is independent of the position. From that we can obtain a general expression for the total electric field in a scattering process which is non-linear in the dielectric constant [Dhont83]. For obtaining analytical solution we need to do first some approximations which are described next.

4.2.2. Light scattering in the Rayleigh-Gans-Debye approximation

Since in a colloidal suspension the particles and the surrounding fluid have different permitivities the optical path of an incident electric wave will be different by passing through a particle o through the fluid. This implies than the existence of phase differences in the incident waves before scattering. If the differences between the permitivities of the particles and solvent are small the phase shift should be also small. By doing so we are neglecting implicitly phase differences inside the particles which is equivalent to say that the particles are optically homogeneous. This is one of the assumptions of the Rayleigh-Gans-Debye (RGD) approximation. Without it we have to use Mie theory for finding an expression of the field [Hul81]. Other important assumption in the RGD approximation is that the particles as well as the solvent do not absorb light (as it was mentioned before) only a small part of the incident light being scattered. Finally, also has to be assumed that the distance from the sample to the detector is much larger than the characteristic distances inside the scattering volume. In that case we can obtain an analytic expression for the electric field which implies consider only single scattering.

4.2.3 Static Light Scattering

In light scattering experiments the detected physical magnitude is the scattered intensity. The intensity I is proportional to the squared amplitude of the electric field,

$$\mathrm{I(t)} \propto \vec{\mathrm{E}}(\mathrm{t}) \cdot \vec{\mathrm{E}}^{*}(\mathrm{t}) \tag{4.8}$$

In the case of colloidal particles the scattered amplitude is in general time dependent since the particles exhibit Brownian motion. For our purposes, the intensity fluctuations due to particle shifts over a short time interval are not relevant and it is enough then to give the time averaging expression for the scattered intensity. This assumption is known as static light scattering. Moreover, since we work with spherical particles, their relative orientation with respect to the detector is not relevant and we can suppress this position dependence when calculating the scattered intensity. For identical, isotropic and optically homogeneous particles we obtain that the scattered intensity $I(\vec{q})_s$ has the form,

$$I(\vec{q})_s = I_0 V_S n_p \frac{k_0^4}{4\pi} \frac{(\hat{n}_o \cdot \hat{n}_s)^2}{r^2} \left(\frac{\bar{\varepsilon}_p - \varepsilon_f}{\varepsilon_f} \right)^2 V_p^2 \cdot P(q) \cdot S(\vec{q}) = C \cdot P(q) \cdot S(\vec{q}) \qquad (4.9)$$

where I_0 is the incident intensity, V_S is the scattering volume, n_p the particle concentration, $\hat{n}_0 = \vec{E}_0 / E_0$ is the polarization direction of the incident light $\hat{n}_S$ the in the polarization direction of the detected light, r de distance between the scattering point and the detector, $\bar{\varepsilon}_p$ is the averaged dielectric constant of the particles, ε_f the dielectric constant of the solvent, V_p the volume of the particle, P(q) is the form factor and $S(\vec{q})$ the structure factor. The form factor describes the intraparticle interference effects of the scattered intensity giving information about the size and shape of the particles. In case of having optically homogeneous particles where $\varepsilon(\vec{r}) \equiv$ constant, we obtain the next expression,

$$P(q) = \left[3 \frac{qa\cos(qa) - \sin(qa)}{(qa)^3} \right]^2 \qquad (4.10)$$

For particles of diameter comparable to the wavelength of the incident light, the expression for the form factor has to be obtainded by analytic solution of the Maxwell equations [Stra41]. This is called Mie theory. Since the particles used in this thesis ranges between 500nm and 1100nm for quantitative measurements, the RGD approximation is not valid in our particular case the form factor has to be obtained usind the Mie theory. As we will see in Chapter 9, we used an online calculator to obtain it in order to calculate the scattering patterns of some proposed structure models. However I

decided to give anyway a simple expression for the form factor just to show the dependence of the form factor with the scattering angle.

The static structure factor $S(\vec{q})$ defined by the ensemble average is,

$$S(\vec{q}) = \frac{1}{N}\sum_{i,j=0}^{N}\left\langle e^{iq(\vec{r}_i-\vec{r}_j)}\right\rangle_t \tag{4.11}$$

where N is the number of scatters. While the form factor describes the interference of scattered waves from different volume elements within a single particle, the structure factor describes the interference of scattered waves from different particles. In the experiments the form factor is obtained from very dilute suspensions where $S(\vec{q}) = 1$. Once we know the variation of the form factor with the scattering angle, the structure factor is obtained by measuring the scattered intensity and dividing it by $P(q)$. As we see in (4.9), no information about the structure factor will be obtained for those angles verifies that $P(q) = 0$.

We have show that the scattered intensity from an ensemble of particles arises from several contributions. There is scattering coming from the sample structure given by $S(\vec{q})$ and there is scattering coming from the particles themselves *P(q)* which gives us information about the size and shape of the particle. Now we will continue explaining the main advantages of using light scattering techniques when working with periodic structures.

4.2.4. Light scattering from periodic structures: diffraction in crystals

If we consider matter as an ensemble of scatterers, a crystal is then a periodic distribution of scatteres each of them being at position $\vec{r}_i$ from the origin. These vectors are just the Bravais lattice vectors of the crystal $\vec{R}$. Our aim here will be to explain the conditions to have constructive interference after scattering when working with crystals. Formally, when we refer to the interference pattern of the scattered light we speak about diffraction of light and the intensity maxima distributions are known as diffraction patterns. Consider a plane wave, $e^{i\vec{k}\vec{r}}$ coming in contact with a

Bravais lattice characterized by a set of points described by the vector $\vec{R}$. We define the reciprocal lattice as the set of all the plane waves which verifies that,

$$e^{i\vec{q}(\vec{R}+\vec{r})} = e^{i\vec{q}\vec{r}} \tag{4.12}$$

Where $\vec{q}$ is just the scattering vector, $\vec{q} = l\vec{a}^* + m\vec{b}^* + n\vec{c}^*$. The relation between the vectors of the reciprocal and the direct lattice $\vec{a}$, $\vec{b}$, $\vec{c}$ is [Ash76],

$$\begin{aligned}
\vec{a}^* &= 2\pi \frac{\vec{b}\times\vec{c}}{\vec{a}\cdot(\vec{b}\times\vec{c})} \\
\vec{b}^* &= 2\pi \frac{\vec{c}\times\vec{a}}{\vec{a}\cdot(\vec{b}\times\vec{c})} \\
\vec{c}^* &= 2\pi \frac{\vec{a}\times\vec{b}}{\vec{a}\cdot(\vec{b}\times\vec{c})}
\end{aligned} \tag{4.13}$$

Since we want to know the intensity distribution after the light has been scattered we have to look for the condition of constructive interference. Two waves will interfere constructively if the phase difference of two scattered waves, $\Delta\phi$ is an integral number m of wavelengths λ. Using equation (4.5) and considering for a crystal $\vec{r}_i - \vec{r}_j = \vec{R}$ we obtain that,

$$\Delta\phi = \vec{R}\cdot\vec{q} = 2\pi m \Rightarrow e^{i\vec{R}\cdot\vec{q}} = 1 \tag{4.14}$$

The former is known as Laue condition which shows that the condition for having constructive interference is that the scattering vector $\vec{q}$ has to be a vector of the reciprocal lattice. If we combine equations (4.5) and (4.6) applying the condition of constructive interference we obtain,

$$m\frac{\lambda}{\nu_s} = 2d_{hkl}\sin(\theta/2) \tag{4.15}$$

This result is the well known Bragg equation for diffraction in crystals. Where d_{hkl} is the distance between the scatterers? The subindex hkl indicates that each of the scatterers belong to a different crystallographic plane of the same family. They are known in this case as Bragg planes. The former means that we will observe a maximum in the scattered intensity if equation 4.15 is satisfied. An easy way to visualize the Laue condition is by means of the Ewald sphere. This is a geometrical construction which consists in drawing a sphere in the reciprocal space of radius k_0 and centred in the tip of wave vector $\vec{k}_0$ (See Fig.22). The Laue condition is satisfied if some points of the reciprocal lattice lie on the surface of the sphere. In case of having a single crystal, that is, a crystal oriented in a unique direction, the diffraction pattern will consist in of single spots. Each point will be characteristic of a complete family of planes. If we work with polycrystalline samples where the crystalline planes are randomly oriented we will observe a scattered intensity distributed along concentric rings. These rings receive the name of Debye-Scherrer rings [Ash76].

If we now come back to equations (4.9) and (4.11) we can clearly see that the condition for having intensity maxima in crystals is entirely contained in the geometric structure factor. The form factor and the other parameters that appear in this equation will modulate the total scattered intensity, but the position of the intensity maxima will be given by $S(\vec{q})$. Since we are only interested in the internal structure of the crystals formed under confinement we will focus our attention in the structure factor, i.e, at the particular positions of the intensity maxima on the detector or observation screen.

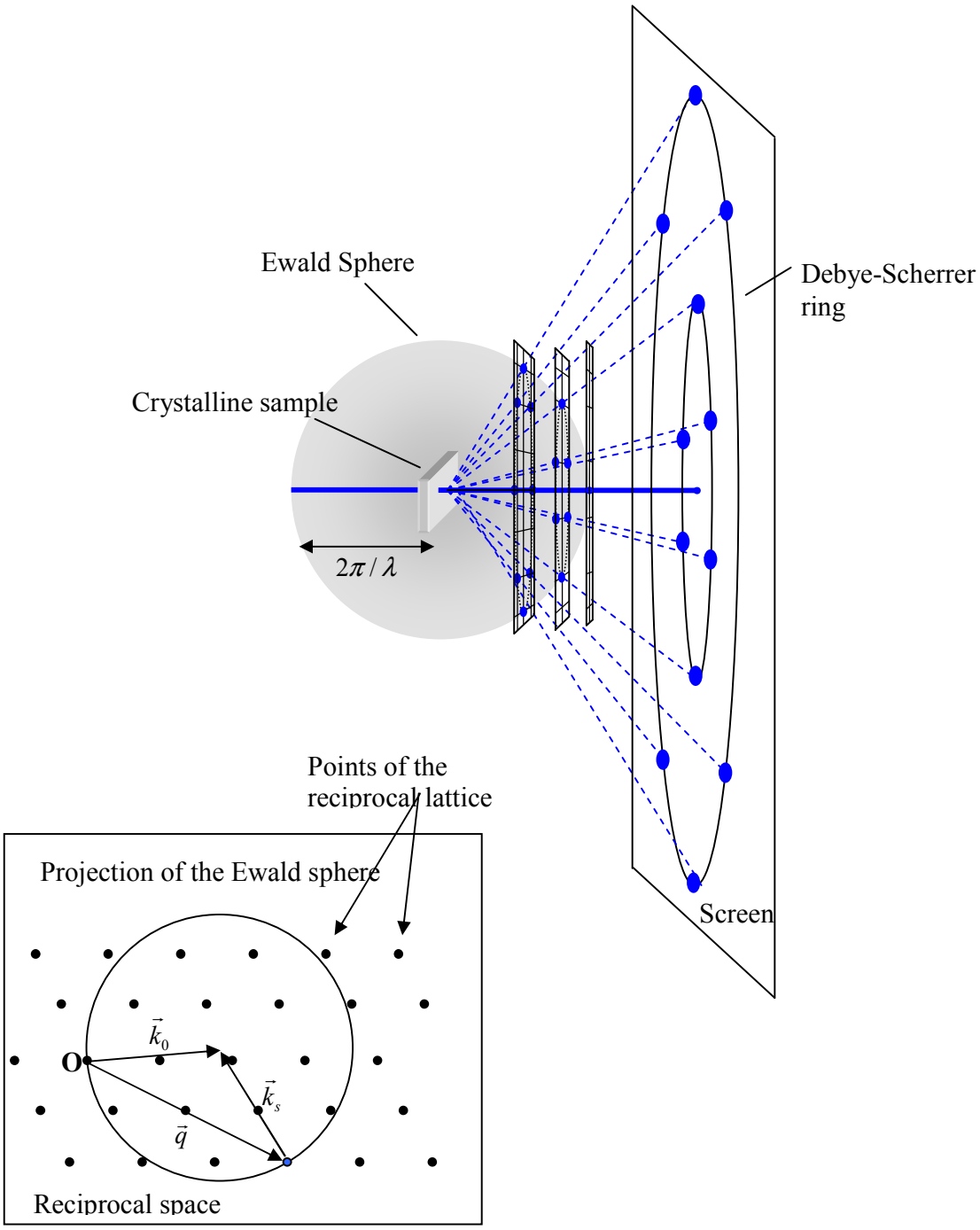

FIG.22: Schematic representation of a light scattering experiment showing the Ewald sphere of radius $2\pi\nu_0 / \lambda$ *and the points of the crystal reciprocal space that intersects with it. The points which intersects satisfies the Bragg condition and therefore we will observe a intensity maxima at this location.*

As occurs with diffraction through optical gratings where the width of the intensity maximum distribution is inversely proportional to the number of grating grooves, diffraction in single crystals will result in sharper spots as the crystal size increases. A two-dimensional crystal oriented normal to the incident beam gives a diffraction pattern consisting of an array of constant intensity lines along the scattering direction space commonly called Bragg rods [Gui63]. As the crystal increases in size, these intensity rods modulate, and if we change the wavelength of the incident light we will observe intensity variations along them. For an ideal crystal these rods will consist of intensity spots. These spots are located at the reciprocal lattice points. That is, the thinner is the crystal the broader is the intensity distribution along the direction perpendicular to the reduced dimension. In the limiting case, where the crystal can be considered two-dimensional this broadness is so extended that we will observe a continuous line (the Bragg rod). Therefore the number of lattice planes in the crystals will modulate the scattered intensity.

A good example of the influence of the stacking sequence in the modulation of the scattering intensity is given by several authors in the calculation of diffraction patterns from models of stacked hexagonal layers [Loo94], [Hey98] shows the intensity distribution of the different stackings in both, the transversal and the parallel directions respect the scattering direction. As it was explained in Chapter 2, the stacking of hexagonal layers can give rise to three different crystalline structures: FCC (face centred cubic), HCP (hexagonal close packed) or RCP (random close packed). In the FCC structure the hexagonal planes are observed in the [111] direction whereas the hexagonal planes in the HCP structure correspond to the [001] direction. For oriented non-twinned FCC structures, we found diffraction patterns with three-fold symmetry. However the usual situation is to find this structure as an ensemble of twin domains (see Fig.23b)).

Due to this particular arrangement what we usually observe are diffraction patterns with six-fold symmetry. This intensity distribution is identical for HCP and RCP structures, so, just with this information it doesn't seem possible to distinguish them. The difference is just found in the intensity distribution along the Bragg rods as show the calculations on Fig.24. The scattering vector has been separated in components parallel to the stacking direction, q_{ll} and perpendicular to it q_{∇}. The graph shows the differences in the intensity distribution along q_{∇} for three different stacking probabilities. In Fig.24a) the effect of increasing the number of layers in the broadness of the diffracted intensity maxima is shown. In Fig 24b) we see how the hcp structure is characterized by a sharp maximum whereas for the RCP structure the maximum is less pronounced. For the FCC structure we find two

maxima symmetrically distributed around $q_{\nabla}(l) = q_{\nabla}(l_{fcc})$. In this plot, a is the stacking probability used to determine the crystalline structure. a = 1 indicates perfect fcc stacking whereas a = 0 indicates perfect HCP staking. Fig.24 c)

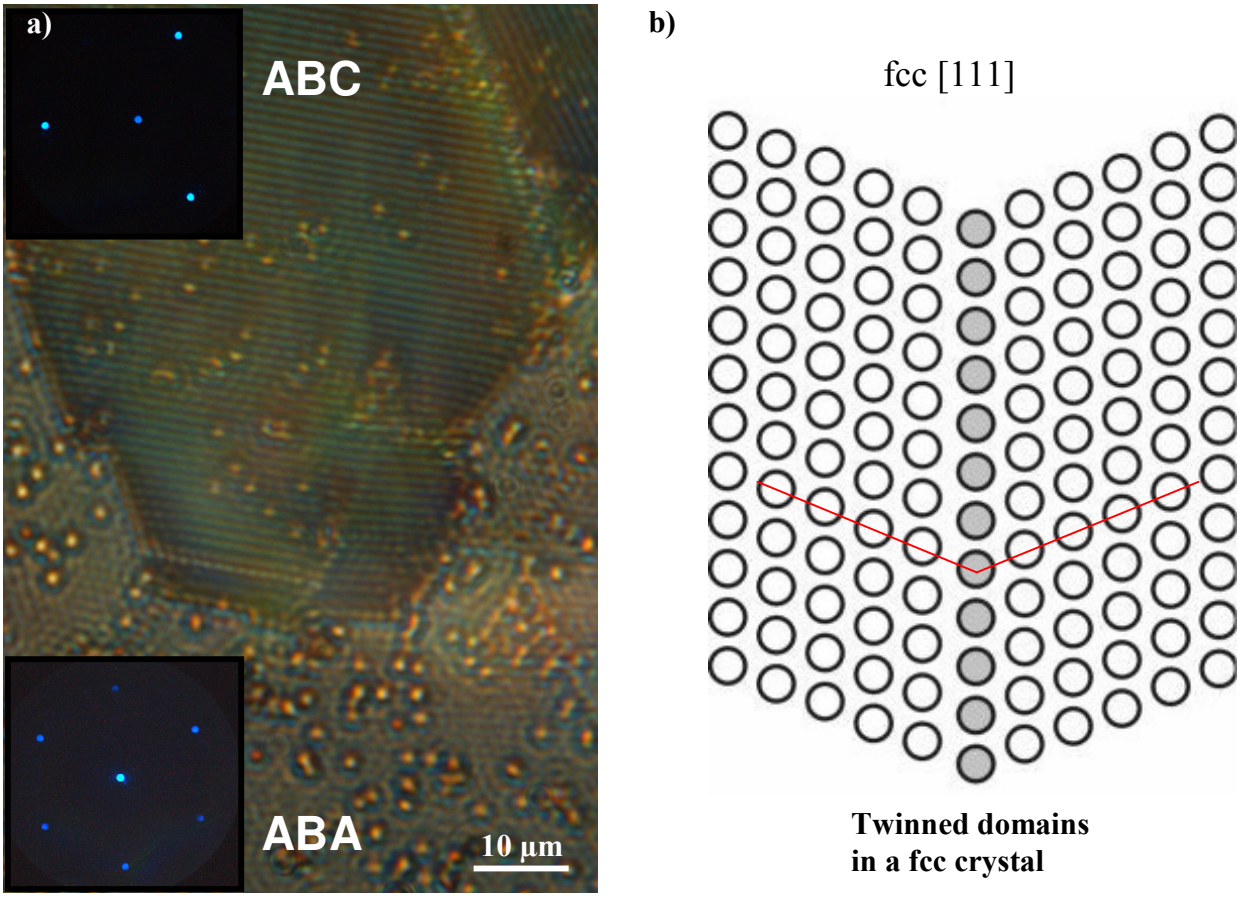

FIG.23: a) Stacking possibilities for a hexagonal closed structure. b) Twin domains in a FCC crystal.

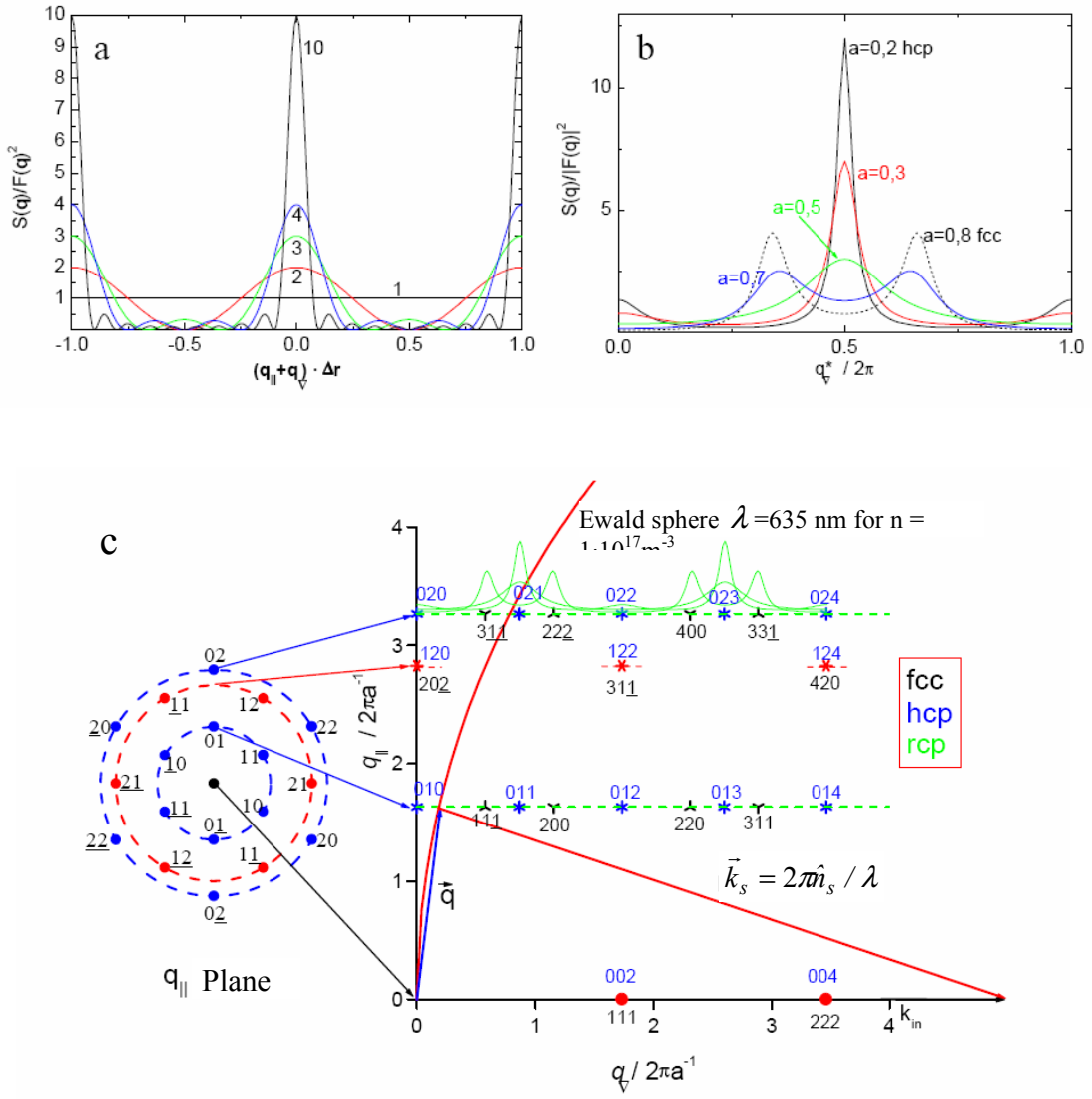

FIG. 24: a) Intensity distribution from a light scattering experiment for a crystal with different number of layers (1,2,3,4, and 10). b) Intensity distribution along the Bragg rods for different stacking of hexagonal layers at the same lattice point. a *is the stacking probability indicating* a = *1 perfect fcc crystal,* a = *0 perfect hcp crystal. c) Projections of the Bragg rods for a colloidal crystal composed by hexagonal layers in planes parallel (q_{ll}) and perpendicular (q_{∇}) to the stacking sequence. In the q_{ll} plane the rods are indexed with the (hk) Miller indices whereas in the q_{∇} plane black marks indicate the positions of the reciprocal points of the fcc crystal and the blue marks the corresponding for an hcp crystal. The rhcp structures can be found along all the Bragg rods (dotted lines .[Bi01].*

4.2.5. Working with the microscope in conoscopic mode: Fourier microscopy

With the microscope it is possible to observe the diffraction patterns of the colloidal crystals under certain conditions. In section 4.1 it has been shown that the scattered light of a sample is focused at the back focal plane of the objective. By adding a lens after it which focuses that plane, an image of the sample's diffraction pattern is formed in the detector. Since we are imaging the Fourier plane of the objective[6] this technique receives the name of Fourier microscopy. We can obtain the same results without the necessity of using a Bertrand Lens by replacing the ocular by a eyepiece telescope. Since the cone of the scattered light that enters in the objective is limited by the objective's numerical aperture, apart of working with objectives with big N.A. we have to choose those colloidal suspensions that allow us to observe at least the first diffraction order. With this technique it is possible to study the structural as well as the dynamical properties of the colloidal suspensions. However in this thesis we are only interested in characterizing the structure of the different colloidal crystals as well as the structural phase transitions found in confinement. We will present these diffraction patterns as a qualitative result together with the corresponding colloidal structures in order to use them as a basis when working with particles which have a size under the resolution limit. That is, to facilitate the structures identification in possible further experiments planned to work using uniquely light scattering techniques.

We are interested in getting diffraction patterns from crystalline structures as perfect as possible, that is, we want to illuminate single crystals to obtain diffraction spots corresponding to a unique crystal orientation. Furthermore we want to avoid modifications in the diffraction pattern due to the presence of defects, or grain boundaries (which results in undesirable intensity maxima). To solve the former we reduced the diameter of the incoming beam by placing a pinhole between the field diaphragm and the condenser. The pinhole has a diameter of 50 μm and is placed over an adapter on top of the condenser. The adapter has x,y stages to centre the pinhole in the correct position. This change is nothing else than substituting the original field diaphragm for other with lower diameter (see Fig.25). Since the position of the field diaphragm has changed, in order to achieve the correct position of the conjugated planes with this new configuration we have to shift the condenser from the original position until the pinhole is focused by the objective. An example of a diffraction pattern once a small regions empty of imperfections has been selected is shown in

[6] In optics, the focal plane of a converging lens system receives the name of Fourier plane.

Fig.26a). The sample in this case was illuminated with white light being possible to see the relation of the wavelength and the scattering angle given by the Bragg law (4.15). Sometimes it is also useful to diminish the cone of the light gathered by the objective in order to obtain sharper intensity spots. This is controlled with the objective aperture or with the condenser aperture. Both planes are valid since they are conjugated to each other, but we chose the condenser aperture because it incorporates a holder to add components. The minimum diameter of the condenser aperture was not small enough for the analysis of the structures (Fig.26a)). Because of that we placed in the holder of the condenser a pinhole with a diameter of 0.3 mm in order to obtain sharper maxima as can be seen in Fig.26b).

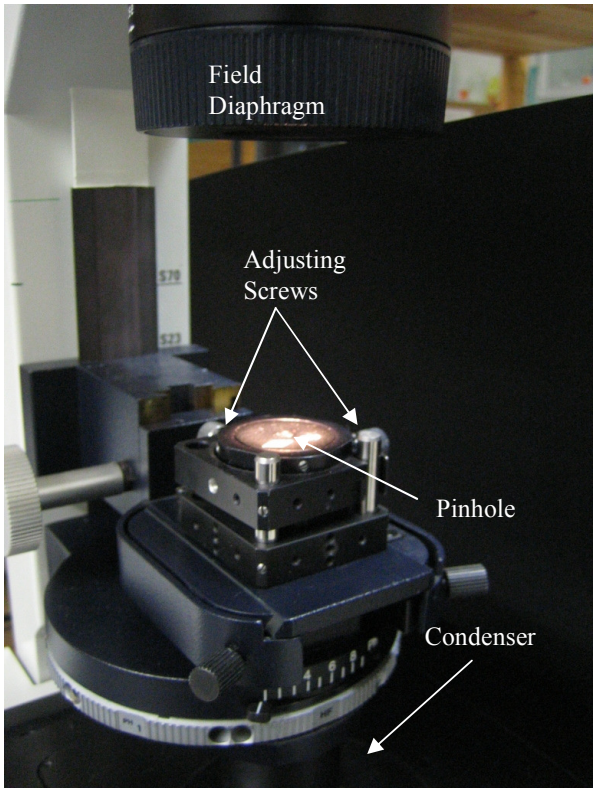

FIG. 25: In order to reduce the size of the field stop, a pinhole of 50 µm in diameter was added on top of the condenser. This pinhole was aligned in the optical path by means of two screws. To obtain sharper intensity spots in the diffraction patterns we addedanother pinhole of 0.3 mm in the holder of the condenser.

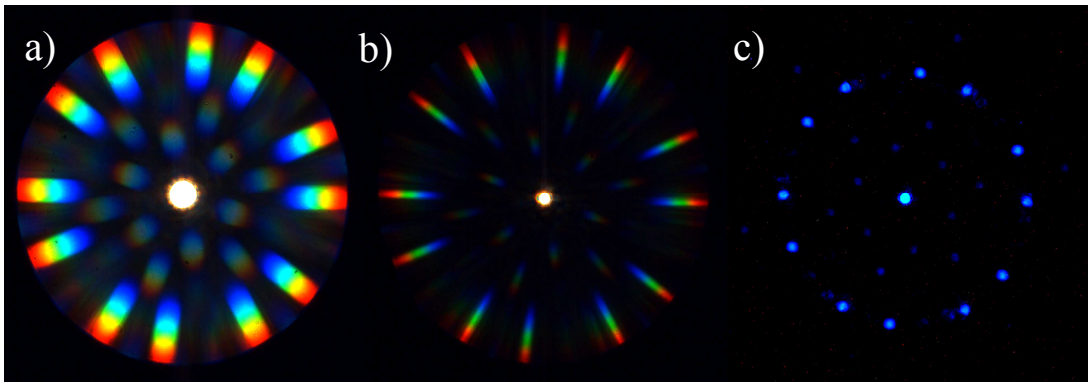

FIG.26: Diffraction patterns of a superstructure found in confinement. a) Original picture. b) After apply the pinhole in the condenser aperture. c) Same situation as photo b) but with a blue filter.

After sharper images are obtained, it is easier to calculate the modulus of the scattering vector of the diffracted light. For that we have to take in account that there is a change in the scattering angle due to refraction when changing from water to air. Thus, combining Snell's law with equation (4.6) and taking into account the microscope geometry we obtain that,

$$q(r) = \frac{4\pi}{\lambda}\sin\left(\frac{1}{2}\arcsin\left\{\frac{1}{n_f}\sin\left[\arctan\left(\frac{r}{r_{aperture}}\cdot\frac{r_{aperture}}{f_{objective}}\right)\right]\right\}\right) \tag{4.16}$$

where r is the radial position of the intensity maxima, $r_{aperture}$ is the radius of the aperture stop at the back focal plane of the objective, f_{obj}, is the objective's focal distance, n_f is the refractive index of the medium and λ is the wavelength on the incoming beam referred to the medium (air in this case). Since we need quasi monochromatic light with a high degree of coherence we used an interference filter, Coherent 35-3466 (λ = 488.7 nm), placed on top of the pinhole which acts as field diaphragm. The advantage of using an interference filter using white light in the illumination source instead of choosing monochromatic highly coherent light sources such as lasers lies in the fact that white light is more adequate to obtain nice images of the colloidal structures while working in bright-field mode. Thus adding a filter in the optical path of the light is very suitable in order to easily combine both techniques. The result is shown in Fig.26c).

4.3 Other techniques

Besides the optical microscope other techniques have been used in order to study confinement. When working with the optical microscope we are limited in resolution due to the diffractive effects of the particles themselves. This makes it difficult to distinguish the structure of the crystals when we move the objective focussing at different planes of the sample in order to identify the different crystalline layers. The former mainly depends on the number of layers and also on the symmetry of the structure. However, in the wedge cells experiments the crystals formed in the narrow part of the cell presented mean interparticle distances very close to the particles diameter. Under this situation, if we allow water evaporation, most of the crystals do not change upon drying. This situation is very advantageous because we can then use other optical techniques in order to obtain complementary information about the structure of the crystals. In particular, the atomic force microscope and two scanning electron microscopes with different features have been used. For that, once the samples were completely dried and the cell as carefully opened, and so most of the structures remain unaltered.

With suspensions of polystyrene particles in water additional techniques were also used to increase contrast when working with the optical microscope. One of them was ultramicroscopy which mainly consists in blocking the non-diffracted light coming out from the sample. Also information about some structures was obtained by adding fluorescent salt to the solvent and using a confocal microscope. These two last optical techniques were used occasionally and no special implementations were done. Because of that we will not describe here them since the reader can find the technical details elsewhere. In particular the ultramicroscopy is explained in detail in [Bi01]. Nevertheless in next chapter we will speak briefly about the results using fluorescent salt in suspensions of latex particles. These where thought as means to increase the contrast of the samples obtaining quite acceptable results.

4.3.1 Atomic Force Microscope (AFM)

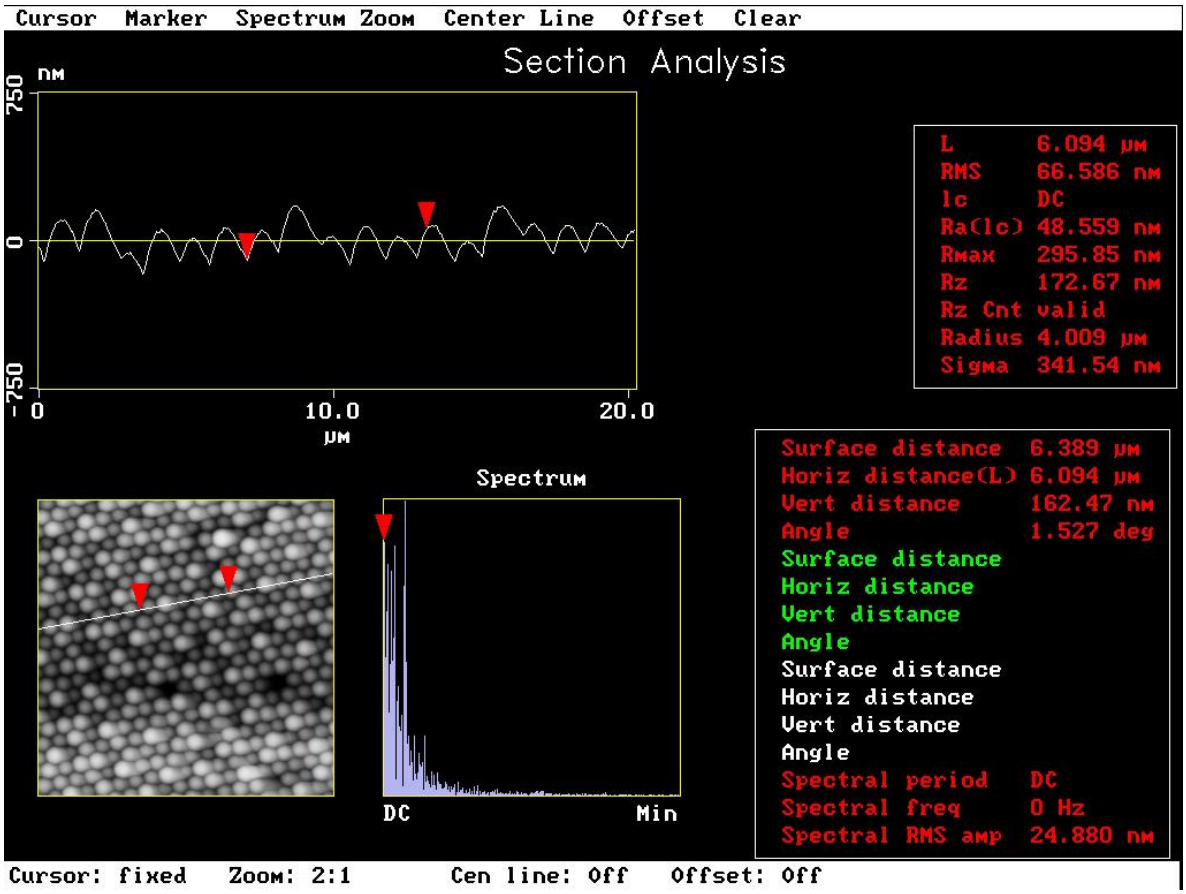

FIG.27: Special software to measure the height differences between particles belonging to the same row. The picture at the bottom left corner was previously obtained with the AFM.

This technique was used for a special kind of structures which has no atomic counter part. They are presented in Chapter 9. To obtain information about the top surface of the crystalline structures a Scanning Probe Microscope, Veeco Bioscope 3.0 Digital Instruments, Inc. was used in non-contact mode. With it the differences in heights of particles belonging to different crystalline layers were measured Fig.27. For that, once the selected region was scanned we used special software. With these data it was easier in some cases to model these structures. Once we obtain the particles distribution on top layers we can model the complete structure just by trying possible stackings.

4.3.2 Scanning Electron Microscope (SEM)

Dried samples can be also analyzed with a Scanning Electron Microscope obtaining high magnification images with high resolution. In some cases we used a Scanning Electron Microscope, FEI Nova600 Nanolab which had implemented a Ga^+ ion beam which is able to melt specific region of the samples being possible to observe transversal sections. In our case this technique was very helpful in determining some of the crystalline structures.

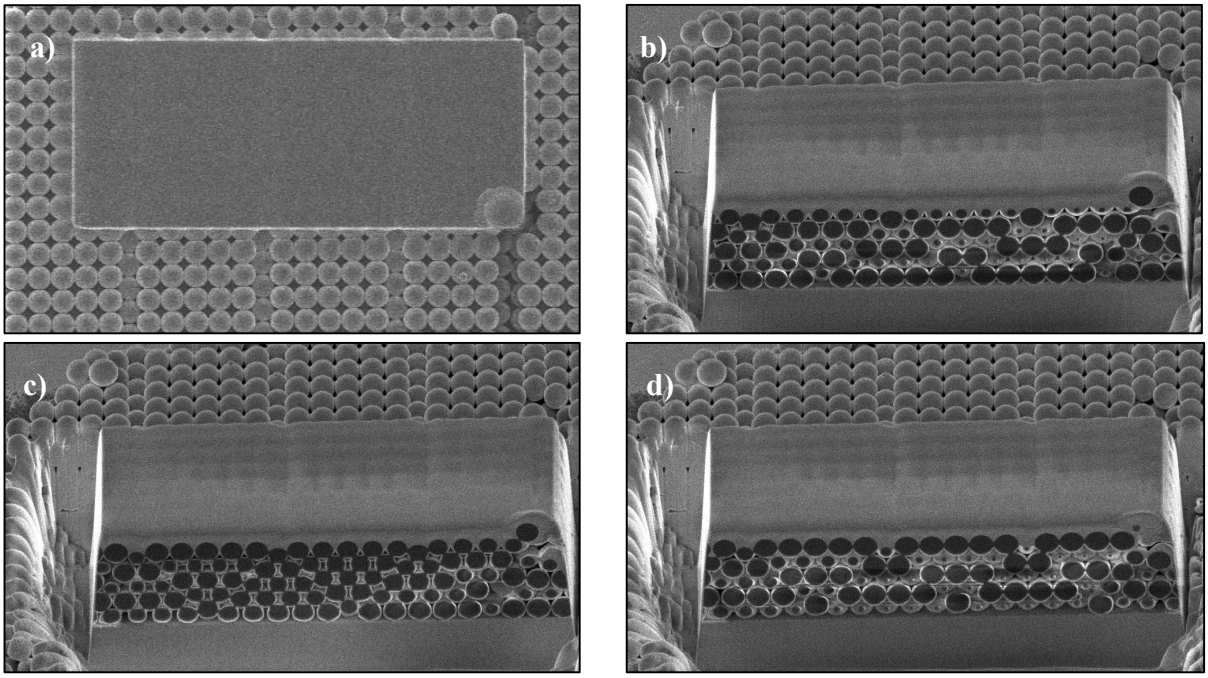

FIG.28: Scanning Electron Microscope pictures showing the Ga+ beam technique to finely slice the sample at different positions in order to reconstruct the crystalline structure. a) Top view showing the thin platinum layer which will protect the sample during the slicing process. b)-d) Side view of the sample after milling at different positions.

To avoid accumulation of electrostatic charge at the surfaces of the dry samples we first coated them with a thin gold layer. The selected sample was then introduced in the SEM following the usual proceeding. Once the sample has been focussed at convenient magnification we selected a specific region of about 10 x 20 µm2. Before using the Ga^+ beam we coated the region with a thin layer of platinum (thickness of 500nm) to avoid milling of the sample by the beam tails (Fig.28a)). The platinum was sputtered on the region using a gas injection system together with a gas assisted

deposition; first a metallo-organic precursor gas is injected using a thin needle. Once the gas has been adsorbed onto the surface, it is destroyed with the ion beam to obtain a Pt layer. After that, with the Ga^+ beam we cut the surroundings of the region making a block. For that we uses fast milling using ion beam currents up to nA. In order to obtain the structure of the selected region we cut the sample making "slices" of width between 50nm to 100nm using a beam current of 50 pA. After each slice we used the so-called "slice and view" macro of the FEI system Figs.28b), c) and d) This system automatically removes one slice after the other taking a SEM picture of each slice.

5 Samples preparation and confinement cell designs

In the former chapter the main experimental techniques used in this thesis were explained. In the present chapter we will continue with other aspects concerning the experiments as the specifications about the colloidal suspensions or the description of the different experimental confinement cells used leaving for further chapters the results obtained with them. Most of the experiments were carried out using polystyrene spheres of approximately 1μm in diameter dispersed in water. However other sizes and solvent compositions were also used for complementary experiments or just as a solution for solving some technical problems. In addition, also different cells and geometries have been designed to achieve the confinement of the suspensions.

Rectangular and circular wedge cells of small wedge angle were the first designs to study the behaviour of the confined suspensions. The difference between both geometries lies in the location of the contact point of the cell plates; in the rectangular cell the narrow part of the cell is in one extreme whereas in the circular cells it is just in their geometric centre. Also a cell with variable height was designed. With it we can control the distance between the plates as well as the tumbling of the upper plate being possible to work with either parallel or non parallel plates. This cell was also designed to be connected to a pumping setup which allows us to control the initial parameters of the experiment as particle density or salt concentration.

In this chapter first, a brief introduction about the way of preparing stock suspensions is described. After that, the experimental technique to work under controlled particle density and salt

concentration is also described. The chapter will finish presenting the different cells used in the experiments. At the end of the chapter we have included some problems derived from using a setup for continuous deionization of the samples when using big particles. We will explain the reasons which generated undesirable effects giving also possible solutions.

5.1 Preparation and characterization of the stock suspensions

In this thesis, different kinds of monodisperse spherical colloidal particles have been used. Typically we chose commercially polystyrene spheres in water with diameters ranging between 0.22-2.5 μm to perform the experiments. Big particle sizes are very suitable to make observations with the microscope in both, stereoscopic and conoscopic mode. The different particle concentrations were obtained by dilution with ultrapure water (Purelab Classic DI, Elga, UK; $\sigma = 55\,\mu S \cdot cm^{-1}$). Since the original volume fraction of the suspension is given by the manufacturer, the desired particle number density n_p is obtained just by calculating the volume of water to add to the suspension[7]. Typically the geometric radius of the particles is obtained from turbidimetry transmission electron microscopy or dynamic light scattering [Lan95], in our case we used the value given by the manufacturer. After that, the stock suspension is passed through 5μm membrane filters (Sterile Surfactant free cellulose acetate 5μm, Minisart, Sartorius Stechim Biotech GmbH, Germany) to remove aggregates and dust. Then the suspension is placed in contact with ion exchange (IEX) resins (Amberlite UP 604, Rohm & Haas, France) to enhance the colloidal stability, i.e, to obtain samples with very low amount of ions solved in water. Argon was added before to seal the bottle in order to avoid the contact of the suspension with the air. That way, there is no possibility for chemical reaction between water and carbon dioxide present in the air which would result in the formation of carbonates in water [Lid90]. To obtain good deionized suspensions, the bottle was placed in an orbital 3D shaker for two days. Finally the suspension was stored on the fridge (T = 6°C) for later use. Once we have prepared the stock suspension, we need to check again the particle number density since during the suspension preparation that value can vary slightly (for example due to water evaporation or during filtering). In our case, the initial particle concentration of the suspensions was obtained by weighing. When the mass density of the particles in suspension is known (ρ_{PS} = 1.056 g/cm^3), we can calculate the

[7] The relation between the volume fraction and the particle number density is given in page: x

particle number density from the mass differences of the suspended particles in a small volume and the same suspension after water evaporation. However we have to take into account that the weighing technique is well suited for concentrated samples. In our case, $0.01 < \Phi < 0.03$. Comparison of weighing and conductivity measurements from a suspension of polystyrene particles of 570 nm in diameter, revealed a relative error about 5% which is a value acceptable enough for our purposes. In order to characterize the suspensions we need to determine the screening parameter, κ of the stock suspensions. For that we need to know the effective charge of the particles Z*. There are two important methods to obtain such value experimentally. From crystalline samples the shear modulus G can be obtained from torsional resonance spectroscopy. Since the shear modulus is related with the derivatives of the interaction potential, using a Debye-Hückel potential we can obtain the effective charge Z_G* [Schö01].

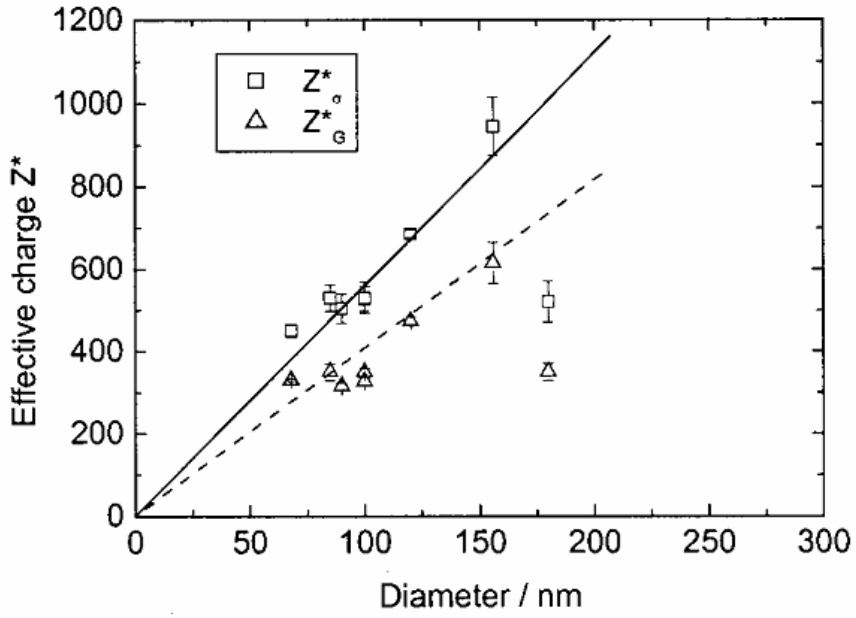

FIG.29: Experimental data comparing the value of the effective charged obtained from torsional resonance spectroscopy, Z_G and low frequency conductivity measurements Z_σ* at different particle sizes [Wet02].*

On the other hand, irrespective to the suspension structure, low frequency conductivity measurements allow the determination of the effectively transported charge Z_σ* in deionized suspensions [Hess00]. A detailed analysis of the experimental results obtained from both techniques is found in [Wet02]. The value of Z_σ* is significantly larger than Z_G* as shows Fig.29. In this graph the authors found in both cases effective charges much smaller than and not correlated to the titrated charge numbers. At the same time they found that the effective charges were independent on the particle number density and linearly dependent with the particle size. In our case we obtained Z_σ* extrapolating the value from the linear regression obtained in these experiments and also it was directly measured for later comparison. The experimental procedure is explained in next section.

The experiments performed in the present thesis can be divided in two groups attending to the kind of confinement cell used: closed cells or open cells. The closed cells are those that after filling in with the colloidal suspension, are completely sealed. On the contrary, the open cells present connections to other setups in order to control the suspension parameters as particle density or salt concentration. In general, most of the experiments performed with closed cells were done with big particles (1-2.5 μm). For these series of experiments, the suspensions were previously left in contact with air to obtain saturation with air borne carbonate. The saturation process is conveniently and accurately monitored by means of conductometer measurements [Wet01]. Closed cells were very suitable for the study of the different crystalline structures. However, once the cells have been closed we can not vary externally any parameter of the system. Because of that, in order to have systematic measurements we designed other cells suitable to be adapted to a setup where the initial parameters of the system can be conveniently varied. Due to these connections we refer to them as open cells. With the former cells the suspension is passed through a tubing system which basically includes a suspension reservoir, a conductivity measuring cell and an ion-exchange chamber. This setup is widely used because the continuous flow of the suspension trough the chamber with ion-exchange resins gives the possibility to work in deionized conditions. At the same time it allows us to control in situ both the particle number density and the salt concentration. This setup is described next.

5.2 Pumping setup

This technique was originally thought to obtain continuous deionization of latex suspensions [Pal92] at constant temperature. Nowadays this method is widely used in both, suspension characterization and phase behaviour studies since particle and salt concentrations can be controlled by optical and conductivity methods [Schö01], [Liu00], [Wet02]. A general scheme of the experimental setup is shown in Fig.30. It consists in different chambers made typically of Plexiglas connected between them with a Teflon (or Tygon) tubing system. The colloidal suspension is introduced in the circuit through the reservoir. A peristaltic pump (Typ TB, Merados GMBH, Germany) forces the suspension to flow through the circuit being possible to select the flow rate. During the time needed to completely fill the circuit, we add also Argon to remove the air inside the circuit. At the same time, special attention is paid to avoid the formation of air bubbles during the filling process which may easily lead to coagulation effects. Salt can be also added as solution through the reservoir by means of a dosimeter or syringe. The suspension passes then through a chamber which includes a conductivity measuring cell connected to a conductometer (LR325/01, WTW, Germany). An Ion exchange chamber is also attached in the circuit in order to continuously remove the presence of non-desired electrolytes being possible to work in deionized conditions. The former is connected to the circuit using a bypass to isolate it from the rest of the circuit in case of working with salty suspensions. To maintain the IEX particles inside the chamber, a special porous tissue is placed in both extremes of this cell. The suspension is pumped through this tubing system until the conductometer indicates a constant value. From that moment we can consider that the suspension is stabilized and ready for starting the experiments.

Conductivity measurements provide useful information about aqueous suspensions of charged particles. The dependence of the conductivity σ_c with the particle number density n_p for a suspension of colloidal particles assuming additivity of all conductivity contributions and monovalent salt counterions is of the form,

$$\sigma_c = n_p e\left[Z^*_\sigma(\mu_p + \bar{\mu}^+) + M(\bar{\mu}^+ + \bar{\mu}^-) \right] + \sigma_B \qquad (5.1)$$

where *e* is the elementary charge, μ_p is the mobility of measured from electrophoresis experiments [Ev98], $\overline{\mu}^+$ and $\overline{\mu}^-$ are the arithmetic-mean small-ions mobilities, $M=c_s 1000 N_A/n_p$ is the number concentration where c_s is the salt concentration and σ_B is the background conductivity stemming from residual impurities. In these experiments we used small concentrations of NaCl to modify the interaction between the particles. Their mobilities are $5.02 \cdot 10^{-8}$ m^2/Vs and $7.1 \cdot 10^{-8}$ m^2/Vs respectively.

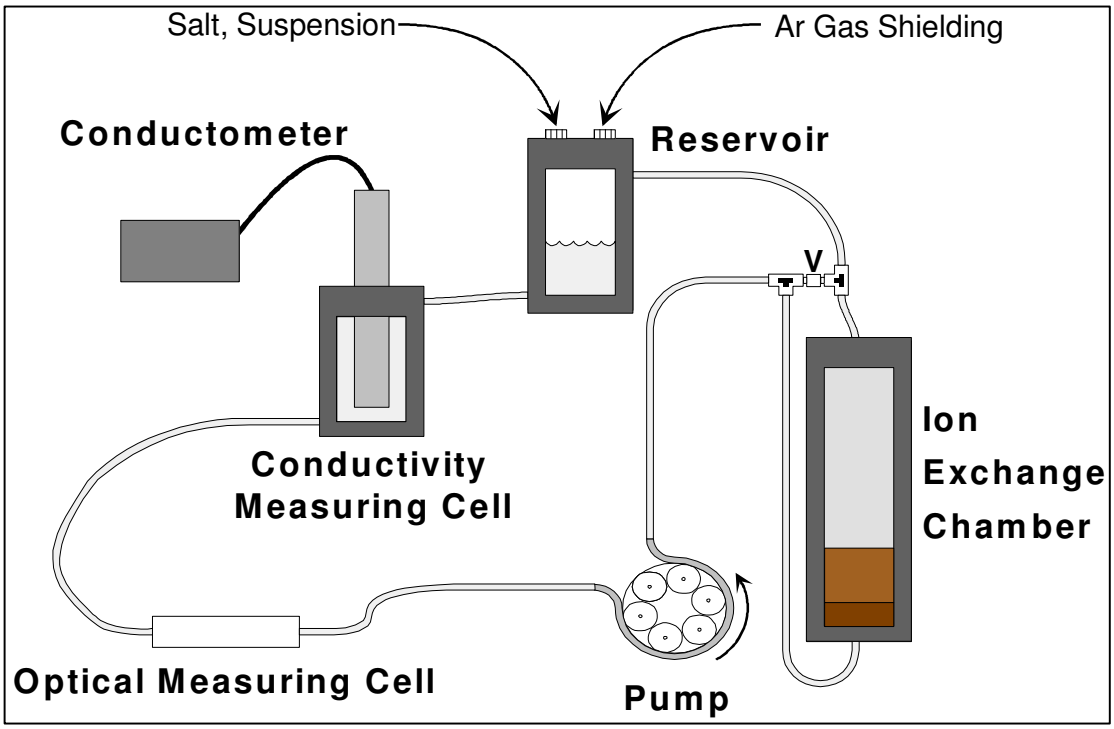

FIG.30: Scheme of a typical tubing system also called pumping setup to work under controlled particle and salt contents [Schö00]]

When working in deionized conditions the second addend in equation (5.1) is not necessary. Conductivity measurements combined with other experimental techniques are very useful to describe the phase behaviour, diffusional properties, phase transition kinetics, elasticity and other properties of charged sphere suspensions. For instance we can include in the tubing system an optical measuring cell to perform light scattering experiments or torsional resonance spectroscopy [Schö01], [Wet06]. For instance, in an SLS experiment which includes this deionization technique, the particle

number density is determined from the intensity of the diffracted light by the sample. Thus, in deionized conditions, for different particle concentration the effective charge can be estimated as shown in Fig.31. For other experiments the conductivity value is used just as a control parameter in the suspension deionization process. In Fig.32 the suspension conductivity versus time is plotted. White squares correspond to the conductivity of a suspension continuously pumped without IEX resins. At t=80 min the IEX-chamber is connected to the circuit. In few minutes the pumped suspension is deionized which is reflected by the fast drop of the conductivity value reaching a minimum and constant value of $\sigma = 55$ nS/cm.

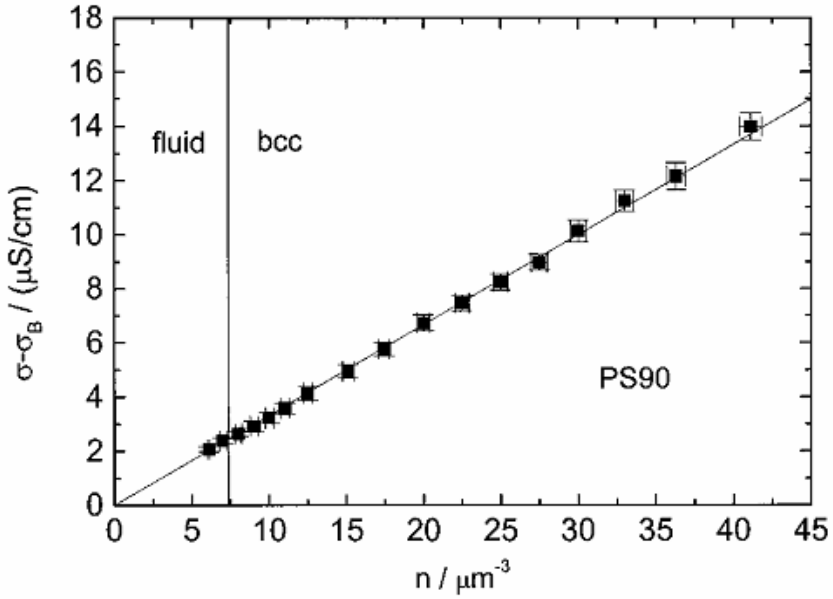

FIG.31: Conductivity measurements of a deionized suspension containing polystyrene particles of 90 nm in diameter as a function of the particle number density n. The solid line is a fit of equation (2) to the data yielding $Z^*_\sigma = 504 \pm 35$. In the plot σ_B includes the value of σ_0. The vertical line indicates the position of the fluid-solid phase boundary [Wet01].

Usually the experiments including the pumping technique, where the interaction between the particles is to be varied, start with suspensions having the highest particle concentration that is going to be tested. Further particle concentrations are obtained by dilution. For that the volume of water to add in the circuit (V_{added}) is calculated a priori in order to obtain the desired particle number density, n_{new}. The proceeding is the next: once the circuit has been made, we first weight it without suspension. After that, we need to know the volume of the tubing system without the IEX-chamber. For that we fill the circuit with water except the IEX-chamber. After that, we obtain the new

measurement of the weight. Finally we fill in completely the circuit with water. This new weight will give us the total mass of water inside the circuit. With these data we know the mass of water in the complete circuit and the mass of water without the IEX-chamber. The latter is useful in case of working with suspensions with added salt. The volume of the circuit can be obtained since we know the water density with precision. After these data have been obtained the circuit is empty of water waiting for complete evaporation. Once the circuit is dry again we can start the experiments adding the same volume of suspension $V_{original}$ that we calculated previously using water. By doing so, we can calculate the volume of water to add, V_{added} to obtain a new particle concentration n_{new} by dilution. Taking into account that during dilution the number of particles N remains constant, we obtain the same relation,

$$n_{new}(V_{original} + V_{added}) = n_{old}V_{original} \tag{5.2}$$

where n_{old} is the particle number density of the suspension after dilution. Once we have diluted the sample, the reading on the conductometer after suspension stabilization can be used to obtain the exact value of n_{new}. A similar process is followed when we want to work with suspensions in no deionized conditions or varying the amount of stray electrolytes in the solvent. In this case we have to use the previously calculated volume of water in the circuit when the IEX-chamber is bypassed, $V'_{original}$. A salt dilution of known concentration c_s has been prepared previously. We usually prepare NaCl or KCl dilutions of concentrations around 1 mM. Once we have decided the amount of salt to dissolve in the suspension, c'_s, we calculate the volume of the original salty solution V_{salt} that we need to add. Again since the amount of salt ions will not vary during the dilution we obtain that,

$$c'_s(V'_{original}+V_{salt}) = c_s V_{original} \tag{5.3}$$

On the other hand we have to take in account the pronounced increasing of CO_2 contamination in the circuit during pumping when we avoid the pass of the suspension through the IEX-chamber as shows the plot in Fig.32. In water, the CO_2 dissociates as, $CO_2 + H_2O \rightarrow HCO_3^- + H^+$. The molar conductivity of both ions is, $\Lambda(H_2CO_3) = 394.15 \cdot 10^{-3} S \cdot 1 \cdot cm^{-1} \cdot mol^{-1}$. The total salt concentration will be then, $c_{s,total} = c_s + c_{H2CO3}$. The underlying salt concentration due to CO_2 saturation, c_{H2CO3} can be obtained from the conductivity lecture and using equation (5.1) to obtain σ_B, yielding

$$c_{H2CO3} = \frac{\sigma_B}{\Lambda(H_2CO_3)} \tag{5.4}$$

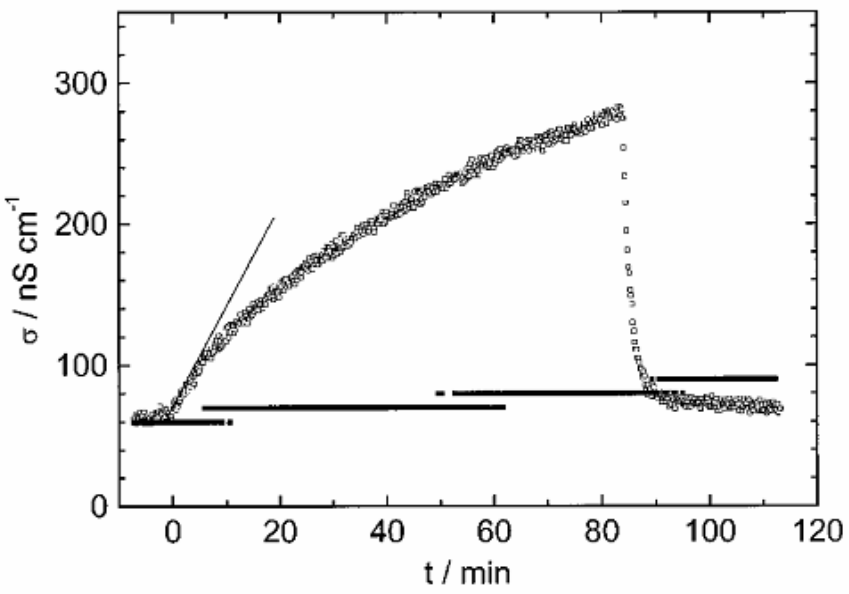

FIG.32: Comparison of two typical conductivity time recordings for pure water in order to demonstrate the deionization efficiency of the pumping setup [Wet01]. The upper curve was taken during continued peristaltic pump and the IEX-chamber bypassed at t = 0 min. The increasing of conductivity is the result of CO_2 leakage. At t = 80 min, the IEX chamber was turned on again implying the progressive drop of the conductivity value close to σ = 55 nS/cm; the value of deionized water. The lower curve was taken under no flow conditions.

5.3 Cells used in the experiments

5.3.1 Wedge-geometry cells

Pieranski and co-workers were the first to use wedge-geometries in confinement of colloidal suspensions [Pie83]. In these cells, the continuous variation of the distance between the cell plates allows the simultaneous observation of the confined suspension for different heights. For very small wedge angles the plate-plate separation changes extremely slowly with distance. Under this condition we can assume that the plates are locally parallel. On the other hand, the plates of the different cells are considered perfectly rigid and smooth in the colloidal scale. Because of that wedge

geometries were the first ones chosen for our experiments. We designed two different wedge cells with different geometries: rectangular and circular. They are described next.

5.3.1.1 Rectangular cells

These cells are made of standard microscopy glass slides (25x75x1 mm). The glass plates were previously cleaned by placing the glass slides in a H_2S0_4 bath for 8h. An alternative method that we used to clean the glass pieces consist in an ultrasonic bath where the glasses were previously placed inside a container with special cleaning soap. The glasses were then rinsed with ultrapure water several times. After that, the glasses were placed in a laminar flow chamber in order to be dried.

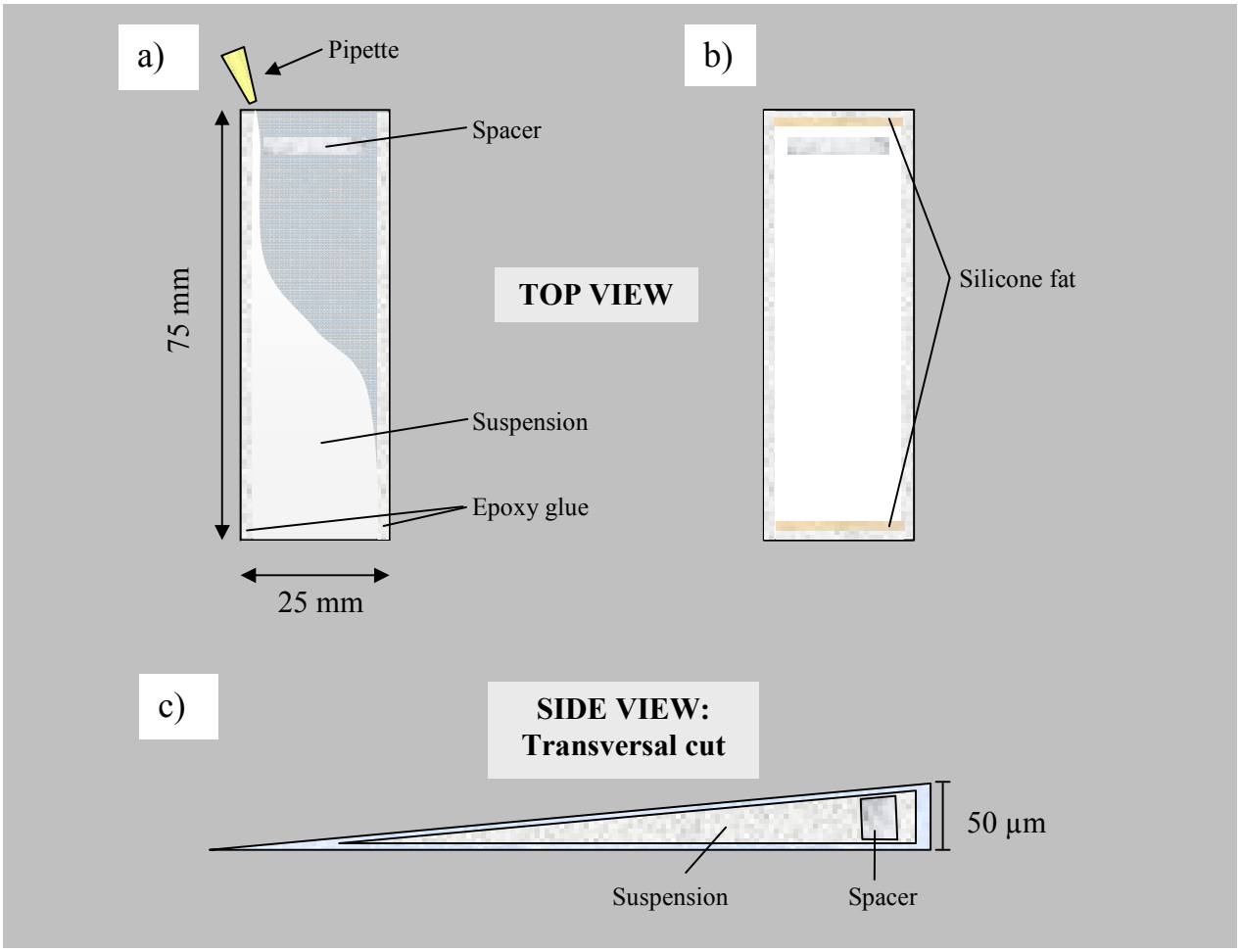

FIG:33. Schematic drawing of a rectangular wedge cell which shows the filling process of the suspension. Top view: a) The glass plates are first glued in the lateral sides. After one day the cell is filled with the suspension

through one of the open sides. b) Once the cell is completely filled, silicon fat is added first on both endings of the cell and after that glue is added to finish the process. Side view: Transversal cut of the cell.

Once the glasses are completely clean and dry, we make the cells by placing together two glass slides. A spacer (polycarbonated foil) of 50 μm thick is placed between them in one extreme as indicates Fig.33. Both glasses are first pressed and then glued with epoxy glue (UHU-Plus Zweikomponenten-klebstoff) in both lateral sides leaving open two regions; one in each extreme of the cell (Fig.33a)). The angles obtained with this procedure are in the order of a few miliradians or even lower. After one day the suspension is introduced in the cell through the hole closer to the spacer being sucked into the cell due to the action of capillary forces. When the cell is completely filled, the holes are first sealed wit silicone base fat (Glisseal HV, Borer, Germany) to avoid the contact between the suspension and the glue (Fig.33b)). Finally, epoxy glue is added closing completely the cell.

The suspension inside the cells can be stable for more than one month at ambient humidity. However water evaporation is unavoidable for long periods of time. To decrease evaporation rate we placed the cells in a constant humidity chamber (~ 80%) being possible now to observe the evolution of the confined suspensions for more than two months. Independently of the evaporation rate (which is very low in both cases) we obtained very satisfactory results if we take into account the low volume inside the cells (less than 0.05 cm^3) and the wide contact surface between the suspension and the glue (just the perimeter of the glass plates). These cells were the first used for the confinement experiments. They were designed at first as preliminary prototypes, but due to the ease in preparing the cells as well the reproducibility of the results, we decided to continue using them along the entire thesis. With these cells, we studied mainly the morphology of the different colloidal crystalline structures found under confinement as well as the structural transition between them. These cells also gave us the first evidences on the trapping particles effect in the narrow part of the cell and were also used to calculate experimental data points for the phase diagram of a crystalline bilayer of charged spheres in confinement [Mes03].

We also designed rectangular cells which incorporate a reserve. As in the former cell these ones were completely made in the laboratory. A picture of one of these cells with the suspension is showed in Fig.34. The reason to build such cells arose in order to work with oil immersion objectives to increase resolution and magnification. In this case we needed al least one of the glass plates of the

cells to have a thickness of 0.17 mm since the oil immersion objectives present very short effective focal lengths and therefore very small working distances. Once we change the thickness of one of the plates, our method to achieve small wedge angles revealed some problems since the thinner plate is now susceptible to be combed. The result was a non-uniform height gradient in the cell being possible to observe more than one contact region between the plates. Four our purposes this was not a big inconvenient since the aim of these experiments was just to characterize some of the crystalline structures found in confinement. However the problem arose due to the fact that an increase of contact points means achieving a smaller volume inside the cell. We have already said, and it is going to be explained in next chapter in detail, that in wedge-geometries the particles do accumulate in the narrow part of the cells. When the concentration of particles in this region exceeds the freezing point, we observe crystals in that region. However with these new cells, due to the low initial volume fractions of the stock suspension and the low volume of the cells it was not possible to obtain extended crystalline domains. In order to solve that problem we decided to introduce a modification in the wedge-cells: The insertion of a small reserve. For that we chose the upper glass plate to be thinner and shorter (23x60x0.17 mm) in order to leave space enough to connect the reserve to the cell-wedge. The reserve consists in four conventional cover microscopy slides (20x20x0.17 mm) fixed either with silicon (Dichtfix Bindulin) or with epoxy glue. The suspension is then introduced into the cell through the reserve and closed. The good results obtained with these cells suggested the possibility to use them also to work in deionised conditions by adding ion exchange resins into the reserve and working in an Argon atmosphere before closing the cells. Since the air is removed by Argon, under these conditions we expected to have lower salt concentrations than in former rectangular cells.

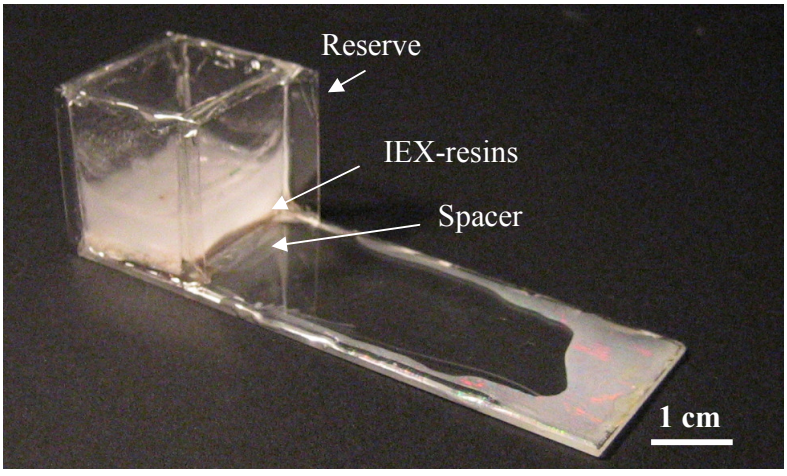

FIG.34: Rectangular cell with reserve. The Bragg reflections indicate the crystalline phase in the narrow part as well as at the lateral sides of the cell. In this case the cell was built to work in quasi-deionized conditions. For that IEX-resins were also added in the reserve.

5.3.2 Spherical-geometry cells

Two different types of spherical-geometry cells were used for the experiments. In both of them the upper plate consists of a spherical cup placed on top of a plane bottom plate. With this geometry the contact point between both cell plates is now in the centre of the plates. Again, this kind of geometry was first used by Pieranski and co-workers [Pier79]. This geometry was very useful to perform complementary measurements to those obtained with the wedge cells since the contact point of both plates is now in the centre of the cell. The bottom plate consists of a circular glass plate placed on a steel support. The upper plate was made of Plexiglas. The dimensions of the cell are shown in Fig.35a). Between both plates a Viton o-ring is added to avoid the contact of the suspension with air. Finally the cell was closed with eight screws. The cell height variation is very soft getting wedge angles in the order of ~ 4 mrad. The angle was calculated from the dimensions of the cell which were known a priori. The curvature of the spherical cup can be approximated by a straight line and then $\alpha \approx tg(\alpha) \approx 0.2/45$). With this cell useful complementary information about the trapping effect of the particles in the narrow part of the cell was obtained. The cell has also two openings in order to connect it to the pumping circuit. Finally, instead of pumping the suspension through the cell, we just introduce the suspension through the holes and after that we close them sealing completely the cell. With this geometry, we continued observing the trapping of particles at the narrow part of the cell. Since now the particles were trapped at the centre of the cell, it was possible to neglect the presence of water leakages in the wedge cells as responsible of the accumulation of particles at small cell separations. In case not, with the spherical geometry the particles should accumulate at the air/water interface due to the action of capillary forces [Den92]. In order to continue focusing our attention in the origin of the trapping effect we needed to use another cell with the same geometry but where both plates are made of the same material since it is well known that the wall surfaces of the cell interact with the different species present in the suspension [Tan98] and different cell material could result in anomalous behaviour of the suspension. To solve that problem we used this time a top plate consisting of a convergent lens of big focal distance (big sphere radius) in a glass flask (Fig.35b)). In

this case the angle of the wedge was much higher than in former cells and the angle was obtained measuring again the cell dimensions ($\alpha \approx 0.2$ rad). Since we are not interested in obtaining wide crystalline regions presenting a unique symmetry this angle does not imply any restriction to our purposes. Once the lens has been introduced in the flask, the suspension is added carefully filling the half of the cell. Finally we sealed the cell adding silicon fat in between both parts of the flask. The results obtained with this cell are shown in next chapter.

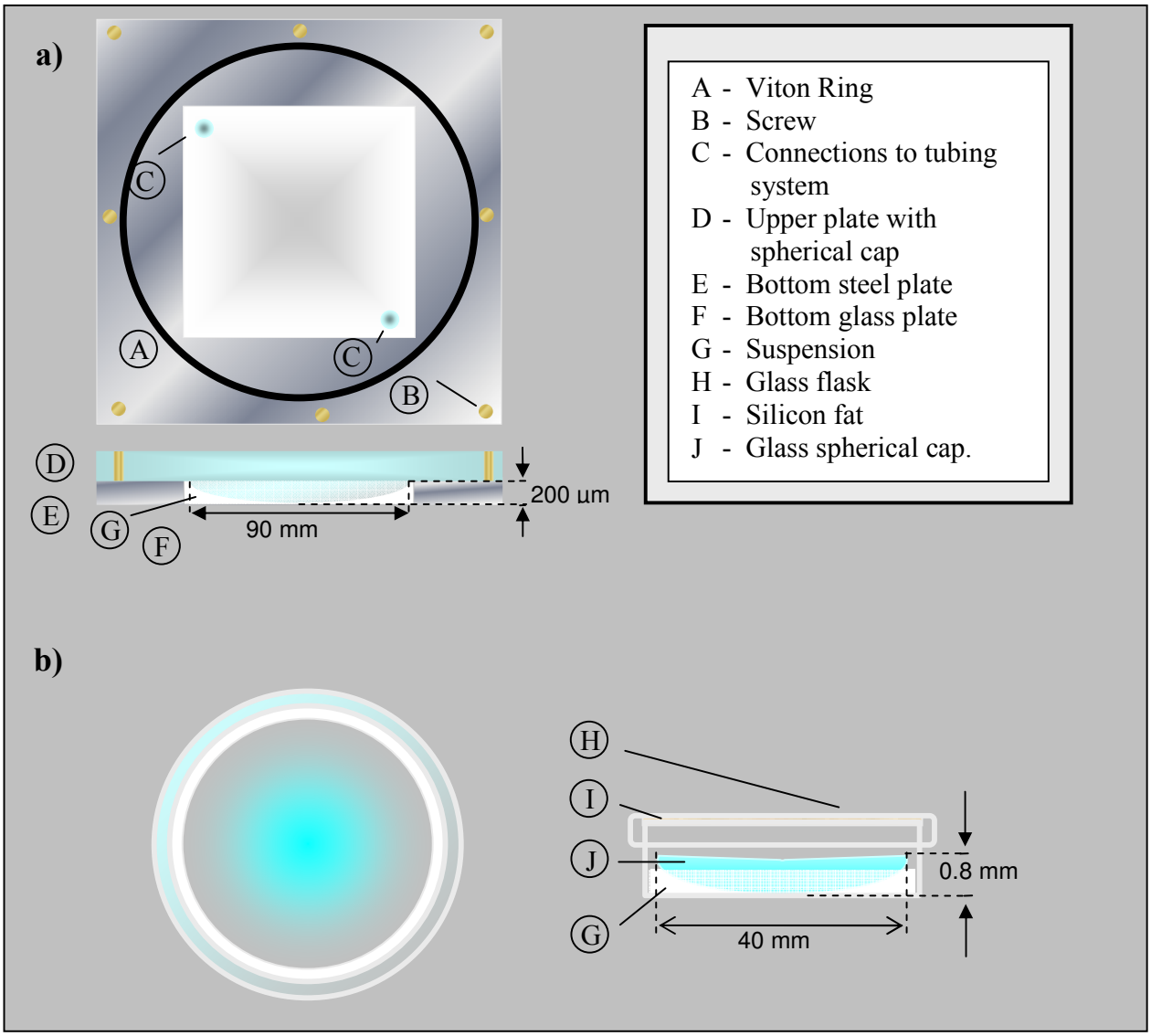

FIG.35: Scheme of the circular cells used in the experiments. In both cases the upper plate consists in a spherical cap. a) Upper plate made of Plexiglas, b) Upper plate made of glass.

5.3.3 Cell with variable height

A cell with adjustable rectangular plates was also designed as a prototype in order to obtain a complete experimental phase diagram of charged colloidal particles in confinement. The interaction between the particles was planned to be varied as usual, by using different particle and salt concentrations. At the same time the cell between the plates should be also varied with high precision. Because of that the cell was designed in order to be connected to a pumping setup. A scheme of the cell is shown in Fig.36. This cell consists of two rectangular glass plates. Each of them is placed in a Plexiglas mount. In between those mounts a Viton o-ring was placed in order to isolate the suspension from outside. Once the cell is closed the two glass plates are separated by a maximum distance of 200 μm. The rectangular upper plate has lower dimensions in order to allow some extra volume around when both plates are separated at very small distances. In this way we obtain a small reservoir around the confinement region. This facilitates the flow of suspension through the cell during pumping. The connections between the cell and the pumping setup are in the bottom Plexiglas mount. To vary the height between the plates, the cell is then screwed in a messing support that presents three holes in the upper part. In these holes, three micrometer screws are added to adjust and control the height of the cell. These micrometric screws has sensitivity of 1 μm and are placed in that way that we can freely tumble the upper plate of the cell being possible to work with both wedge and plane geometries. To avoid leakages the cell was pressed until the o-ring completely sealed the inner volume by means of these micrometric screws. Since our phase diagram will depend also on the confinement height we decided to measure as characteristic parameter the distance between the crystalline layers assuming that the distance between the particles and the plates is the same as between two layers. To measure such distances we added a piezoelectric adapter (P-862 LVPZ Controller, PI) in the objective turret with a sensitivity of 0.1 μm. Such device elevated the objective and hence the microscope table. In order to solve that we substituted the microscope table by an Alumina support with three micrometric screws in order to elevate the cell as well as control that the cell was completely horizontal as shows Fig.37. Once this was done we had to move the condenser turret in order to obtain Köhler illumination with this new configuration.

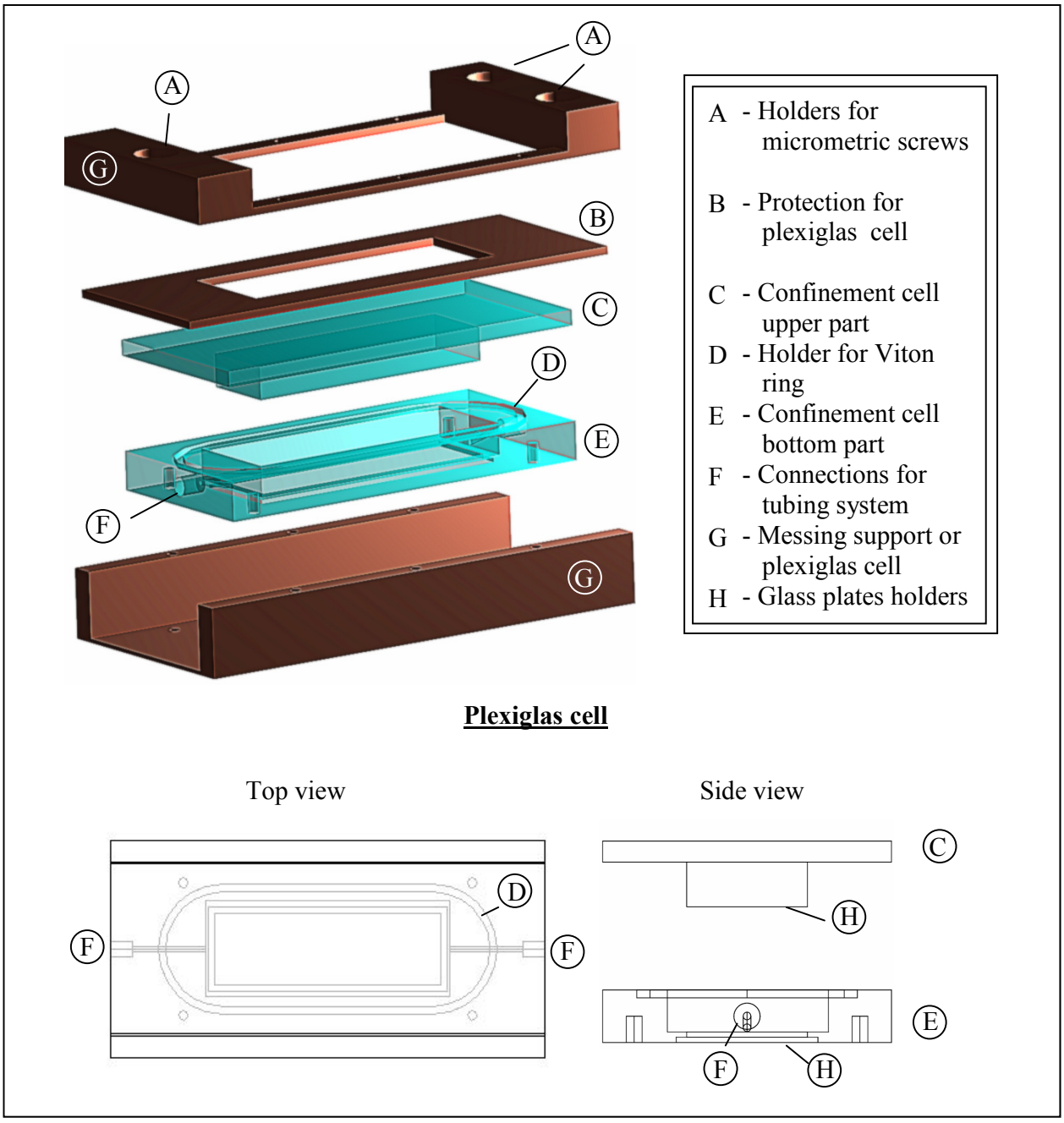

FIG 36: Scheme of the cell with variable height.

In this experiment we found a considerable number of technical and experimental problems. These problems affected seriously the quality of the results. Before the presentation and subsequent discussion of the experimental results which appear in Chapter 7, the objective of this section will be to stress the importance of those problems which appeared during the experiments. Since this cell was just a prototype, some modifications were done in the laboratory to test the response of the system. These modifications included modifying the inner geometry of the cell. Not all the experimental problems have been solved. However we have found possible explanations for them which are presented next. With that we hope that further researchers find here valuable information about some of the experimental problems that can arise when confining colloidal suspensions using a similar setup. We also propose some solutions and additional measuring techniques in order to obtain accurate experimental values in the phase behaviour of confined colloidal particles.

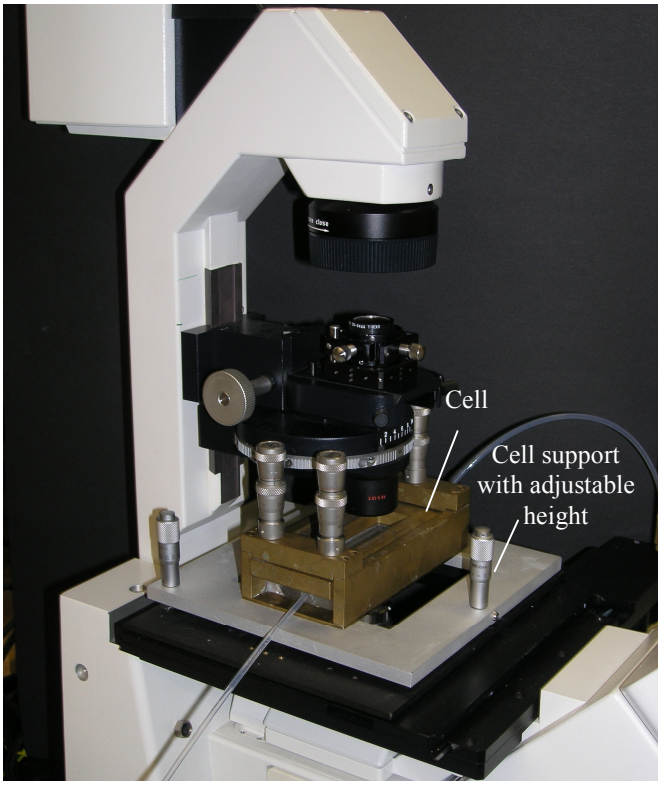

FIG.37: Cell with variable height mounted on the microscope .Between the microscope stage and the cell, an aluminium support was added in order to assure that the cell was perfectly horizontal.

5.3.3.1 Experimental proceeding

For these experiments we started using a stock suspension of polystyrene particles of 1,1 μm in diameter (IDC, Batch No. 2149) with initial volume fraction of 1% ($n_p = 1.4 \pm 0.2\ 10^{16}\ m^{-3}$). The pumping setup consist in the basic elements (conductivity measuring cell, peristaltic pump, IEX-chamber and reservoir) and an optical cell (described in section 2.2) to confine the suspension. The idea of working with big particles arose from the initiative of continuing the measurements of confined systems by means of the optical microscope. However, the use of particles of big size originated instability of the colloidal dispersion after one hour of pumping and big aggregates appeared along the circuit. Because of that we tested colloidal stability during pumping for different polystyrene particle sizes (from 570 nm to 1.2 μm) at volume fractions around 1%. The pumped time around the circuit varied from one to several hours depending on the tested samples. Finally we decided to work with polystyrene particles of 570 nm since we did not observe particle aggregation during the pumping time.

For this new suspension, the initial volume fraction was obtained by weighing measurements. The obtained value was $\Phi = 0.9\%$ ($n_p = 9.5 \pm 0.2\ 10^{16}\ m^{-3}$). At this particle concentration the sample was crystalline in the bulk. After we tested the deionization efficiency of the pumping setup the suspension was introduced. The volume inside the complete circuit was 40 ml. Once the suspension was stabilized and completely deionized we used the reading on the conductometer (σ_c = 0.96 μS/cm) together with the original particle number density to obtain the effective charge, being this: $Z^*_\sigma = 2.2\ 10^5 \pm 3\ 10^4$, a value much higher than expected. The value of the effective charge obtained from extrapolation of the linear regression in the plot of Fig.29 gave us however a value of $Z^*_\sigma = 2236 \pm 70$; two orders of magnitude lower. During this thesis we did not find any experimental work related to the study of the particle size dependence with the effective charge apart from [Wet02]. So, in order to obtain the experimental data to determine the phase behaviour of the suspension we used the value obtained from the conductometer cell. Once the pumping setup was ready and the initial parameters of the suspensions obtained we started the preliminary experiments related with the cell prototype.

- *Cell height calibration*:

In the first test concerning the confinement cell we found several problems. One of them arose from the relative position of both confinement plates. If we take into account that we are interested in confining colloidal suspensions between two parallel plates of big surface and with minimum plate-plate distances of about one micron, we need to have perfectly flat surfaces. Although this was the case of the glasses used in this cell, the insertion of the upper glass plate into the Plexiglas mount introduced slight deviations from its perfect horizontal placement. Due to this it was very difficult to tumble the upper plate not only in order to work with parallel plates, but also to find at least wide regions with a suitable confinement. We tried to solve that by reducing the confinement region. For that we added two thin glass pieces on top of the upper glass plate as shows Fig. 38 fixed with special glass glue (Pattex, Sekundenkleber Glas flüssig).These glass pieces were the typical cover slides for samples used in microscopy of 0.17 mm thickness. During the gluing process, in order to avoid that the glue exceeds the slides surface I did not apply any pressure. Because of that the air between the slides was not completely removed remaining after the glue was dried. They do not affect the experimental results at all and have not to be confused with air bubbles inside the confinement cell once the suspension has been introduced.

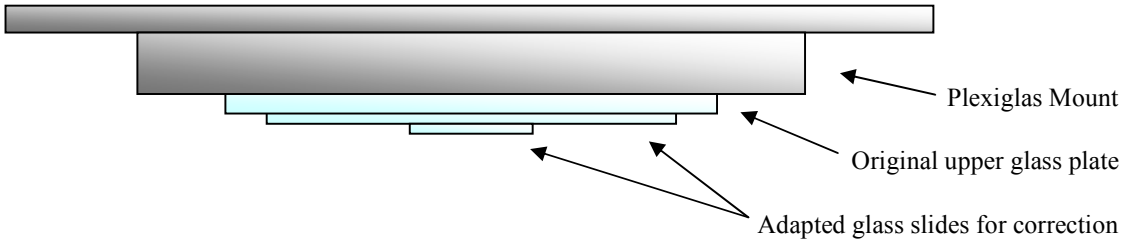

FIG.38: Drawing of the upper plate of the new cell after modification. By adding two new glass slides we reduced the confinement region making easier the adjustment for obtaining parallel plates at small cell heights. Slides air bubbles appeared between the glass slides during the gluing process.

With this new configuration we were able to obtain an extended confinement region on appropriate plate-plate distances for confining the suspension. In order to achieve that upper and bottom plates of the cell were parallel, we calibrated the distance between them by the lecture of the

cell height on the piezoelectric power supply. The main problem was to determine the correct focusing of both, the upper and lower plates of the cell. We solved that by the insertion of small scratches at the four vertex of the confinement region; four on top and four at the bottom at the same x-y position. These scratches were carefully made with a glass cutter pencil. Fig.39 shows the result after height calibration. The cell is seen from top view and the square in the centre is the confinement region. The cell contains the suspension which is in fluid state and it is characterized by its milky appearance. It had been previously introduced in the circuit and pumped in order to deionise the suspension. To pass the suspension through the cell both plates were separated to their maximum plate-plate distance. Due to the new configuration, in the confinement region this maximum height was about 30 μm. After pumping, the cell was carefully pressed until the minimum plate-plate height was achieved. In the centre on the cell we can clearly distinguish the region of maximum confinement. The distance between the plates in the confinement region is around 1μm. Because of that it appears transparent since no particles are allowed to penetrate inside. With this modification we achieved suitable confinement as well as a wide zone where the plates can be considered parallel. However a slight height gradient was still present being the angle between the plates in the order of miliradians.

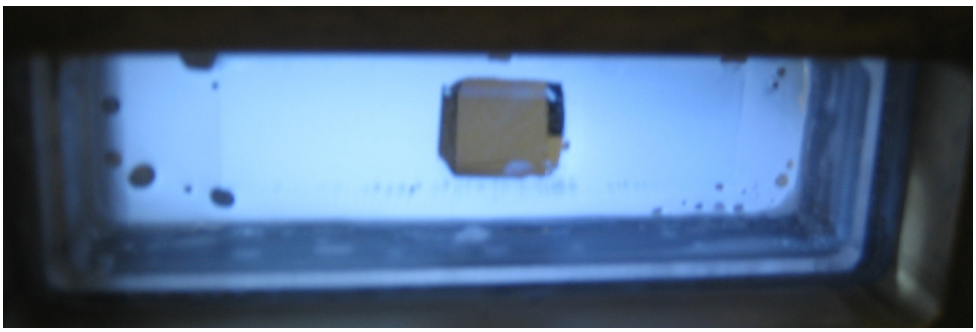

FIG.39: Top view of the cell. The suspension is already inside. A transparent region appears in the centre of the cell. It corresponds to the confinement zone indicating that there is only water and no particles can go inside. This shows the good quality of the confinement even for distances smaller than 1 μm.

In Fig.43 a zoomed image of the confinement region is shown. The bright iridescence under white light illumination indicates that the suspension is crystalline. In this picture is also possible to observe a series of curved stripes which indicates the presence of different crystalline structures. We

worked at wedge cell conditions and the minimum distance between the cell plates is found at the right side of the confinement region being this about 1 μm. With this picture we can clearly observe the gradient in distances also in the top and bottom sides of the confinement region, which indicates slight irregularities of the upper plate position probably originated during the gluing process.

- *Pumping the suspension through the cell:*

Other problem which appeared is related with the flow of the suspension through the cell during pumping. Even at maximum confinement volume, the high pressure reached inside the cell caused flow inhomogeneities. In order to avoid possible problems derived from that, we decided to bypass the optical confinement cell. In that way the suspension was conveniently stabilized through the pumping setup and after it, the bypass valves were opened 30 minutes before stopping the pump. We also decreased the flow speed rate. Even so, the small volume of the cell made also difficult its complete and homogeneous filling of the cell. As a consequence gas bubbles appeared. Most of these bubbles remained at the same position during the experiments as shows the comparison of pictures in Figs.39, 40, and 41 and it was not possible to remove them. Since the measuring time for each data set was around 30 minutes, I consider that possible contamination of the suspension due to the gas bubbles could be neglected.

Due to the new upper cell design, we were able to observe an interesting phenomenon about flowing of colloidal particles in reduced dimensions. We pumped the suspension through the cell choosing a cell thickness in the confinement region of about 5 μm. By observing the confinement region a lighter (more transparent) region appeared which can be observed in Fig.40. This zone was growing in time in the flow direction. This was an indication that during pumping through the cell a big amount of particles "avoided" to flow through the confinement region. This effect is probably consequence of an increase in the collision rate between particles close to the confined zone due to the confluence of the flow stream lines. Once the pump was stopped, the particles were again homogeneously distributed in this confined region.

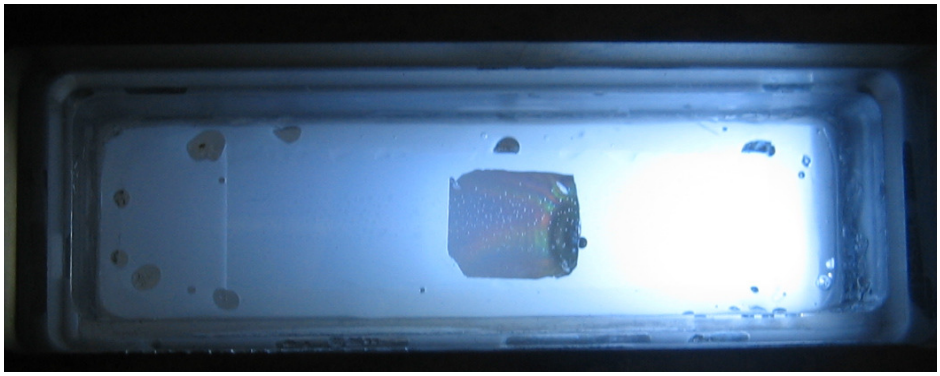

FIG.40: Picture showing a top view of the cell during pumping. In the confinement region we can distinguish a darker region. It is the result of pumping through the cell; during pumping most of the particles flow surrounding the confinement region due to the difference in heights of that region compared with the rest of the cell.

- Pumping a suspension of big particles through the pumping setup:

Once the problems to get confinement and suspension stabilization inside the cell were solved, the cell was now ready to study confinement of colloidal particles. However particles aggregation in the tubing system appeared again after two days of measurements. This was observable due to anomalous variation of the conductivity of the suspension. This time aggregates were not visible flowing through the circuit but rather particles accumulated at the porous tissue of the entrance of the IEX-chamber. In FIG. 43 we show the effect of particle aggregation after five days of pumping the suspension through the circuit. The pump was working about 10 hours per day at intervals of 2 hours maximum. The experiment was repeated in the same experimental conditions but pumping this time at lower speed rate. After two days particle aggregation was observed again at the entrance of the IEX- chamber. In both cases a first set of measurements was already made: in deionised conditions and after CO_2 saturation. At this point it was clear that it was not possible to obtain systematic measurements. Since this pumping setup has widely demonstrated its efficacy in many other investigations it was clear for us that the aggregation problem arose from the suspension itself, probably due to the big size of the particles. We recently found a possible explanation for the particle aggregation when flowing through the circuit.

FIG.41: Top view of the IEX-chamber showing particle aggregation on to of the porous filter. Some particles were removed at the centre to appreciate better the effect.

When using the continuous deionising technique by means of a pumping tubing system, the suspension is exposed to complex flow field including strong extensional components (diverging and converging stream lines). Theoretical studies show that in extensional flow fields, converging stream lines implies an increasing in the contact time between colliding particles. This phenomenon is called flow-induced aggregation [Gre94]. Georgieva, Dijkstra and others recently reported an experimental study about the aggregation process of concentrated polymer dispersions exposed to extensional flow-fields [Geo08]. For that they used a ring-slit device placed at the bottom of a cylindrical reservoir which included a piston which extruded the sample through the slit at different flow rates. Different colloidal suspensions were extruded at different flow rates and slit heights. One interesting result is the strong dependence that they obtained of both, the volumetric flow rate and the slit height in the aggregation probability at the entrance of the ring-slit. The flow rate influence on the colloidal aggregation can be explained in terms of the contact time between colliding particles: as the flow rate increases there is a decreasing in the particles contact time. On the other hand they found that the slit height does not play a relevant role but rather the ratio between the slit gap height and the radius of the cylindrical reservoir influences the particle aggregation at the slit entrance. They also found that for low volume fractions, the particle aggregation probability diminishes. This is because in those cases the mean particle separation is so large that the deformation effect is not sufficient to bring the

particles close enough. In this research work they also make reference to a very interesting publication about the clogging mechanism using microfluidic devices as model porous media with electrosterically stabilized colloidal suspensions with particle diameters on the order of micrometers [Wyss06]. In this work it was observed that the formation of clogs is determined by a critical number of particles that flow through single pores irrespective of both flow rate and particle volume fraction finding that this critical number of particles N* scales with the ratio of the pore W to particle diameter D as $N^* \propto (W/D)^m$ with m = 4 ± 0.1. To interpret that scaling they proposed a model based on irreversible particle sticking events near the pores. In this model they assumed that the flow stream lines must be compressed at the pores (or constrictions). The suspended particles are forced to move relative to the fluid and those particles which have a characteristic distance from the sidewall $\varepsilon << D$ will stick irreversibly to the wall because in this case, the attractive surface forces dominate. On the other hand, since the trajectory of a particle is determined by the balance of the repulsive forces whereas the drag force towards the wall is induced by the fluid, their model shows that the time scale for clogging should depend on the range of the repulsive interactions. Thus, the characteristic length scale of particle capture ε, which is independent of the flow rate, is closely linked to the forces that regulate particle stability. This means that, by increasing the salt concentration, the average clogging time diminish.

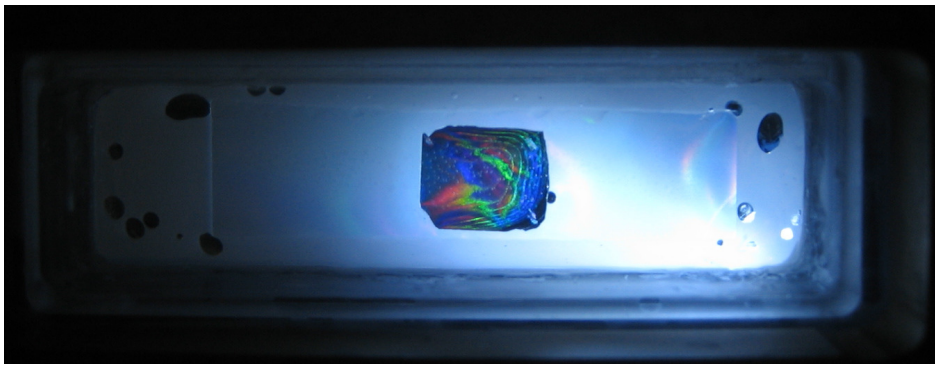

FIG.42: Top view of the cell showing confinement of colloidal crystals. The sample was crystalline also in the bulk as can be appreciated by the light iridescence on the right part of the cell.

I consider that these two works clearly elucidate part of the problems that we found in our experiment. Since filters are porous media, these results could explain the particle aggregation found in the filters of the IEX-chamber. On the other hand from the results obtained by Georgieva et al. it is

possible to conclude that concentrated suspensions will be seriously affected by those parts of the circuit where a drastic reduction of the volume appears. In the circuit this parts are the adapters of the different chambers to the tubing system. The former would explain the observation of particle aggregates flowing in all the circuit when we tested the different suspensions of latex particles with sizes around 1 μm. Moreover, these facts will also explain the behaviour of the particles while flowing through the entrance of the confinement region shown in Fg.40. Despite all the problems, we finally obtained confined crystalline structures as show Fig.42. At this point we decided to continue with the analysis focusing now our efforts in testing the efficiency of measuring technique taking in account that now the initial particle number density will be slightly lower than that in the stock suspension. The new concentration was obtained by the lecture on the conductometer. The measuring technique was the same as in the former section; we recorded the images with a digital-camera and with special image software the unit cell areas of the different crystalline structures were measured. The distance between the crystalline layers was measured by a piezoelectric device adapted between the microscopic objective and the turret. Once the main parameters of the different structures were characterized we compared them with the theoretical results.

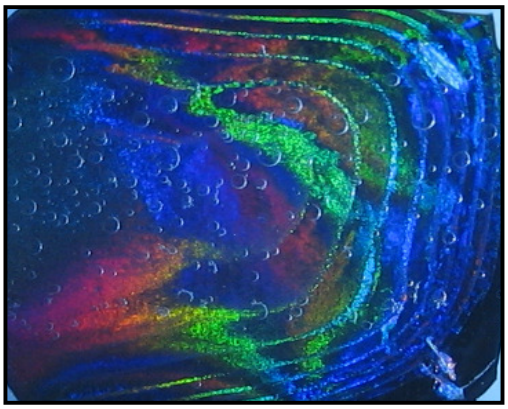

FIG.43: Magnified picture of the confinement region showing the characteristic reflection of crystalline suspensions. In the picture it is possible to appreciate a series of stripes indicating the presence of an alternation of different crystalline structures. The visible air bubbles appearing in the gluing process of two glass slides, i.e., they do not form part of the suspension.

6 Effect of confining charged particles in wedge-like geometries

The idea of using cells with wedge-geometry arose as a suitable way to obtain the first results about the influence of the walls in charged colloidal suspensions. Such geometries can be found in other experimental studies about confinement of colloidal suspensions, for instance, the works of Pieransky [Pie83] and Murray [Mur87]. One of the advantages of the wedge-like cells is that the plate-plate distances increases progressively just by moving out of the cell's cusp. This kind of geometry could give, for instance, a fast qualitative analysis about the critical distance where confinement would affect the physical properties of the colloidal suspension under study. However the confinement of polystyrene particles in wedge-like geometries gave as a result an unexpected effect: after few days we observed a drift of particles to the narrow part of the cell. In this zone, the particles were observed to get trapped, increasing progressively the concentration of particles there and forming a dens fluid layer. For longer times, the accumulation of particles exceeds the freezing density, giving rise to the formation of a crystalline region growing in time to higher plate-plate distances. In order to discern the nature of this migration effect, different experiments have been performed using different wedge geometries, surface charge of the plates, gravity strengths or salt concentrations. The effect was always present except in cases of strong external forces applied over relatively long times.

6.1 General effect

The first cells used in the experiments were wedge cells with rectangular symmetry (see Chapter 5). The suspension consist in polystyrene particles (IDC, Batch No. 2149) of 1.1μm of diameter in water and Φ = 1% with a $c_s = 5 \cdot 10^{-6} M$. They were the first cells which reported evidences of particles trapping at the cell cusp. In Fig.44, a general picture showing this trapping effect is shown. The narrow part of the cell corresponds to the top part of the picture which means that the particles come from the bottom part of the picture accumulating at the interface to contribute to the formation of the crystalline region. In this picture we can distinguish three different zones: a bilayer crystal with compact hexagonal symmetry, a thin fluid intermediate region and a gas-like region with very low density of particles. Also we can observe in the picture that close to the interface, the bilayer presents rhombic symmetry. If we remember the sequence of structures observed in confinement (Chapter3), the rhombic structure precedes the hexagonal bilayer in terms of distance between the plates. However what we are observing here is just the "opposite sequence". Thus the mean interparticle distance is higher close to the interface than far away from it. This behaviour seems to be the result of lateral force acting over the particles pushing them through the cusp cell. Other possibility is that the particles once arrive to that region by diffusion are trapped by the effect of that force. The particles arrived very slowly to the narrow part of the cell. A measurement of the crystal/gas interface position with time gives the crystal growth velocity (Fig.45). For initial volume fractions of 1%, we obtained that v = 11,95 ± 0,40 μm/h. We measured the growing crystal rate at very short lengths. Therefore, due to the small wedge angles we can consider that for such region the plates were locally parallel.

Another important observation is that such trapping effect was not observed for higher heights. This strongly suggests than such effect depends on the distance between the plates. In principle, this unexpected effect could be due to several causes: salt gradients, gravity strength effects, surface charge of the cell plates or, the most obvious and simple possibility: additional convection originated by evaporation effects. The latter case would be due to the constant presence of microscopic leaks in the narrow part of the cells. In order to discern the nature of this phenomenon, a series of different experiments were planned in order to obtain systematic qualitative as well as quantitative results. Thus, each experiment presented in this chapter was thought to give an answer about the influence of a particular field or gradient above mentioned. These experiments are presented next. At the end of the chapter complementary theoretical work will be presented. The

former was developed by Löwen et al. and has to be considered as a first step in the understanding of the particles behaviour inside wedge cells, giving an explanation about the origin of such lateral force.

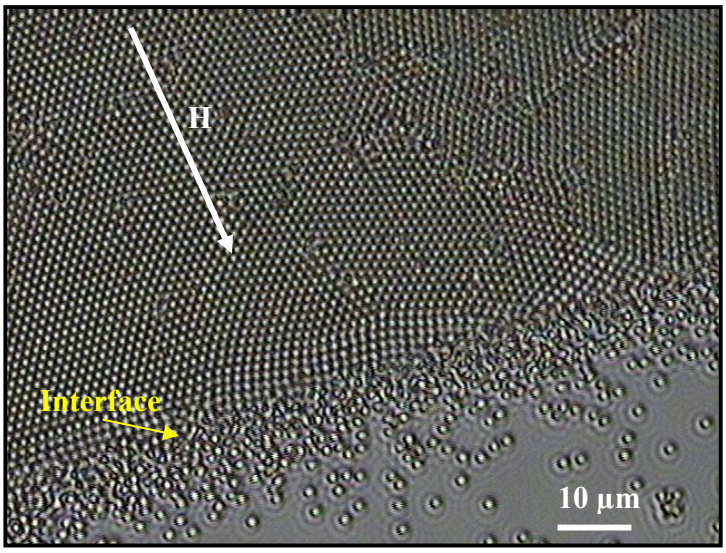

FIG.44: Crystal growing due to the accumulation of particles in the narrow part of the cell. Three different regions can be distinguished: A crystalline bilayer region with hexagonal or rhombic symmetry (the latter close to the interface), a high density fluid region and very low density region.

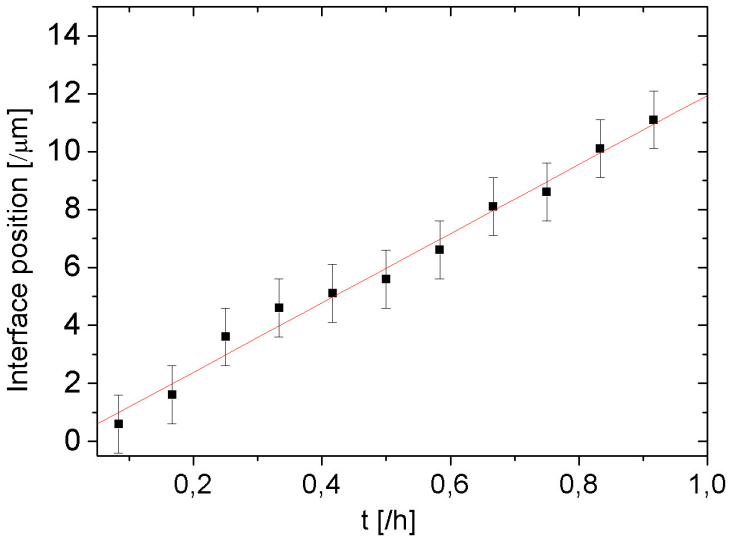

FIG. 45: Plot showing the crystal growth rate by measuring the crystal/gas interface the temporal evolution of the interface close to the wedge cusp formed by migration effects. For such distances the cell can be considered as locally parallel.

6.2 Testing evaporation currents

One possible reason for the formation of a crystalline region in the cell cusp would be the presence of some leaks in the narrow part of the rectangular wedge cells. This will originate the formation of a growing crystal following the same physical principles explained above. From studies on particle assembly processes driven by solvent flows, it is known that colloidal particles partially immersed in a liquid film interact due to capillary forces. These forces are strong enough to cause particle aggregation and 2D ordering [Den92]. There, capillary interactions are entirely governed by the surface forces which are responsible for the disjoining pressure and the three phase contact angle [Kra94]. The deformation of the liquid meniscus around the particles present in the air-liquid interface gives rise to interparticle attraction. Moreover, water evaporation will increase the local capillary pressure, sucking the liquid and causing the formation of a partially ordered array of particles. At the same time, convective currents originated by water evaporation from the menisci will transport particles towards the ordered region increasing progressively the crystalline domain. The quality of the colloidal crystals will depend on the water evaporation rate, the meniscus shape, the particle surface wetting and the solvent composition. In order to rule out lateral capillary forces as a responsible of the migration effect the experiments were repeated using other spherical geometry cells. In Fig.46 we can see observe a sequence of images of the wedge-cell with circular geometry where both plates are made of glass (to distinguish it from the other spherical cell we will call it cell A). The pictures were taken immediately after the cell was closed, after one day and after two days (a), b) and c) respectively).

At the beginning, homogeneous distribution of particles in the cell was observed. The existence of a diffuse zone of enhanced transmission in the centre of the cell reveals the uniform cell variation of the upper glass plate of the confinement cell. In contrast, after one day an inner transparent region appears delimited by sharper borders indicating a centrosymmetric zone depleted of particles as confirmed observations at these regions made with the microscope. In Fig.46 we can see the particles density d) close to the centre of the cell, e) at the intermediate depleted region and f) with lower magnification, showing the abrupt density change at the end of the depleted region. In the three former pictures the increment in height goes from left to right. After two days we could distinguish a crystalline region in the narrow part of the cell (small white ring in Fig.46 c)).

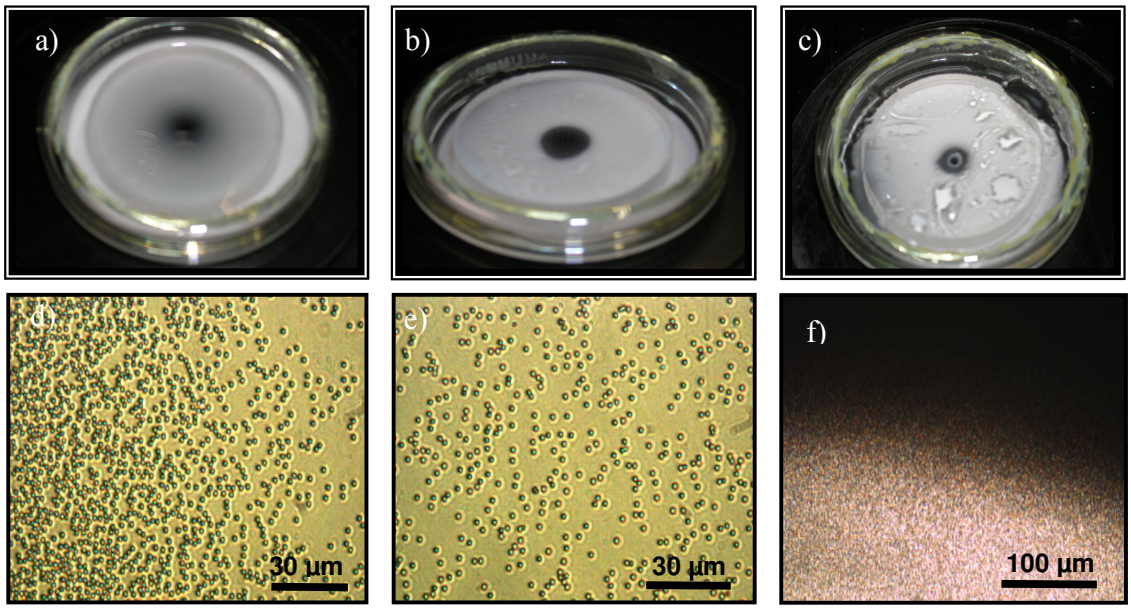

FIG.46: a) to c) Three different images of circular cell A, at different times. a) Just after filling the cell. The suspension is uniformly distributed and the transparent diffuse zone in the centre indicates the curvature of the upper glass plate. b) The cell after one day. A well defined zone depleted of particles appears in the centre. c) After two days, a concentric ring in the narrow part of the cell has been formed. The suspension in this region was found in crystalline phase. d) and e) high magnification pictures showing the accumulation of particles in the narrow part of the cell and the region depleted of particles respectively. f) Low magnification picture showing the sharp border between the depletion zone and the rest of the suspension in the wider region of the cell. In the wider region the concentration of particles is too high to allow light transmission through the microscope.

We did the same experiment with the cell whose spherical cap was made of Plexiglas (cell B) in order to measure the position of the beginning of the monolayer with respect to the centre of the cell. The cell was filled following the same proceeding as before; once the cell was closed we introduced the suspension through one of the holes of the cell. After that, we sealed the cell and started to measure. Different pictures of the crystal growth process at different times are shown in Fig.47a). By measuring the position of the beginning of the crystalline region we obtained a very interesting result which is show in Fig.47b). After filling the cells the particles were able to arrive to positions from the centre of the cell that we considered the zero position. But during 8 h the particles moved outwards from the centre. After this time, the particles moved again towards the centre until they reached a fixed position starting the crystal to growth at t ~ 30 h.

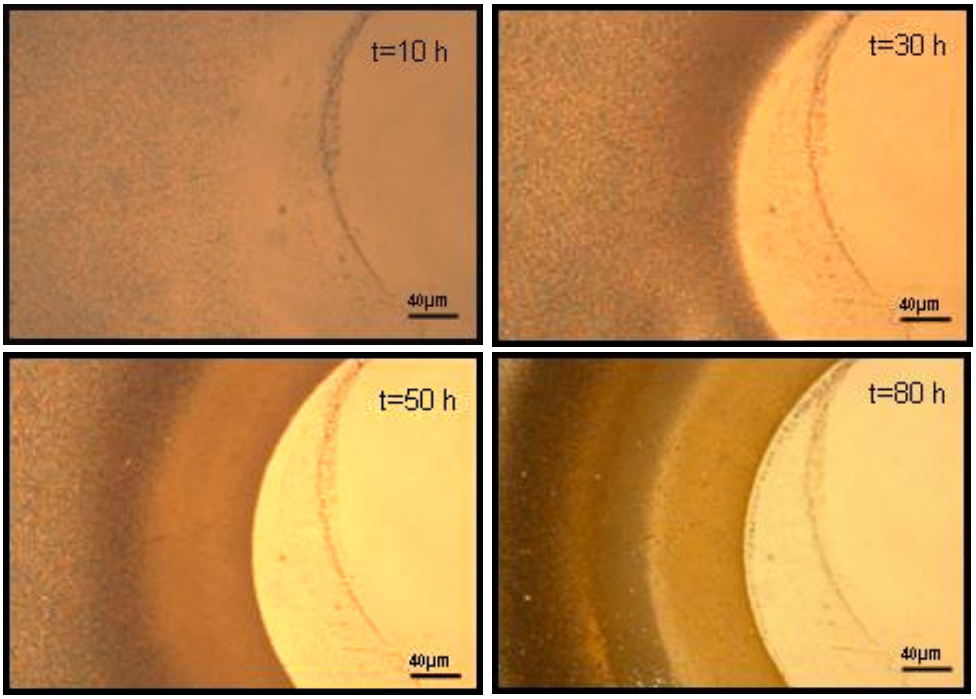

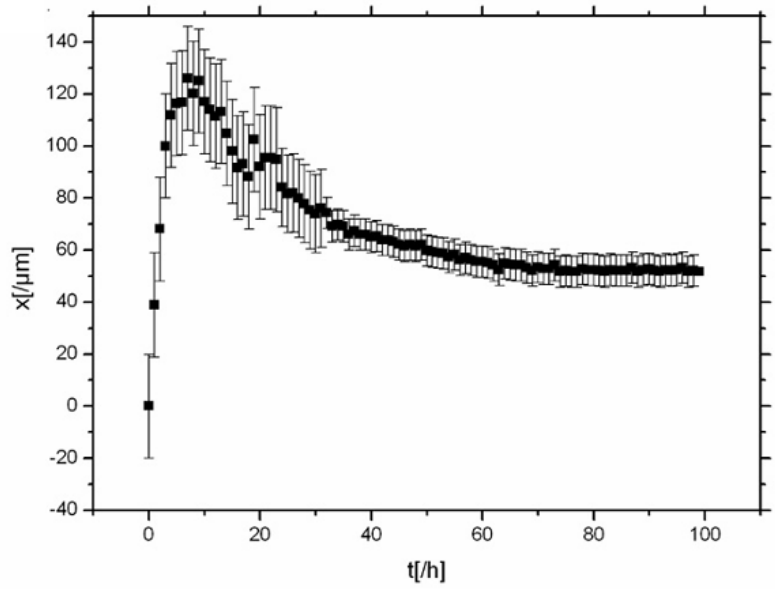

FIG.47: High magnification pictures showing the migration effects in a wedge cell with circular geometry. a) Homogeneous suspension close to the narrow part of the cell. b) After 30 h a denser region close to the narrow part of the cell is observed. c) When the freezing concentration is achieved the particles form a crystalline monolayer. d) For longer times a series of concentric rings are observed. Each colour indicated a particular ordering and/or number of layers.

From that time on, particles do clearly accumulate in the narrow part of the cell forming a dense region. For longer times we can distinguish almost perfect concentric rings of different colours. Each ring corresponds to a specific crystalline structure in accordance with the known sequence. In Fig.48 we can see a macroscopic picture of the same cell with suspension inside and Bragg reflections showing the existence of a crystalline region in the centre of the cell. However that picture corresponds to other experiment where just a big drop of suspension was placed on the bottom plate closing then the cell. This simple test gave us first evidence that the particles go to the centre of the cell independently of possible evaporation effects. That picture was taken after a week of adding of suspension inside the cell. In the picture it is possible to distinguish a white outer ring at the air fluid interface. This ring formation has also been observed in the drying drops processes of colloidal suspensions in contact with air [Dee97]. Since the air present in the cell is at ambient humidity, the evaporation of water in the cell originates convective particle flows towards the interface being a fraction of the particles accumulated there due to the action of lateral capillary forces as it was explained at the beginning of the section. Despite the existence of these evaporation currents the particles continued accumulating in the narrow part of the cell. This was a clear indication that some kind of attraction acts over the particles at small plate-plate distances.

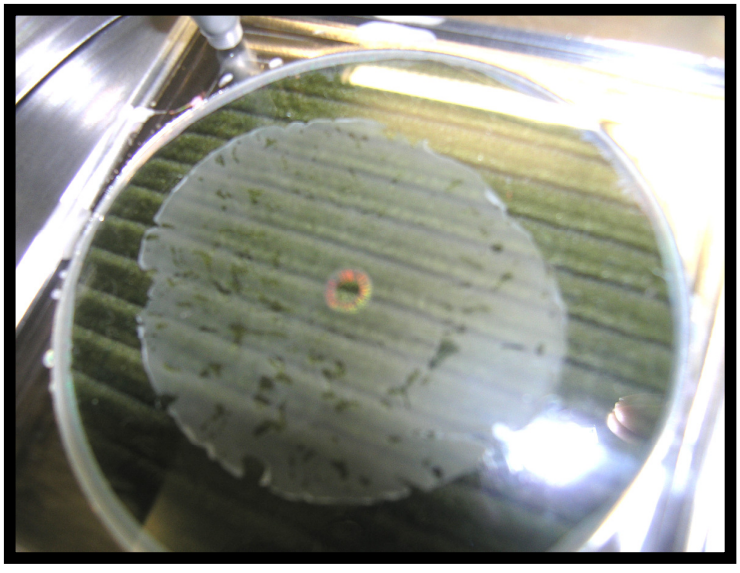

FIG.48: The result of adding a drop of suspension in circular cell B. The picture was taken after a week. Bragg reflections reveal a crystalline region in the centre of the cell.

There is a significant difference between the results obtained between both cells, A and B. In cell B no depletion region was observed in any case (not having only a drop, nor with the cell completely filled). Studies about drying drops of colloidal suspensions made by Okubo [Oku07] reported the existence of a zone depleted of particles. In this work, the coupled action of sedimentation and evaporation currents would be the reason of these particular patterns of dried suspensions. In our case the depletion region seems to have the same origin. Besides that, the high curvature of the spherical cap in cell A resulting in higher cell volume, allows the existence of more pronounced gravity effects inside the confinement region, another experiment was of crucial importance to corroborate the implication of both processes in the formation of this inner region depleted of particles. In this new experiment cell B had been slightly tilted from its horizontal position. The results are shown in Fig.49. 36 hours after filling the cell, an asymmetric lighter zone can be observed with a regular concentric crystalline ring in the narrow part of the cell (Fig.49b)). As a consequence of this asymmetry, later on, particle accumulation in the centre is also asymmetric (Figs.49 c) and d)). This fact will reveal the existence of flow currents. Despite the former the crystalline region is circularly symmetric which reflects the non dependence of this region with the local convection currents depending only on the height between the plates. This result suggested us to plan a new set of experiments testing the possible influence of the gravity strength as we are going to explain next.

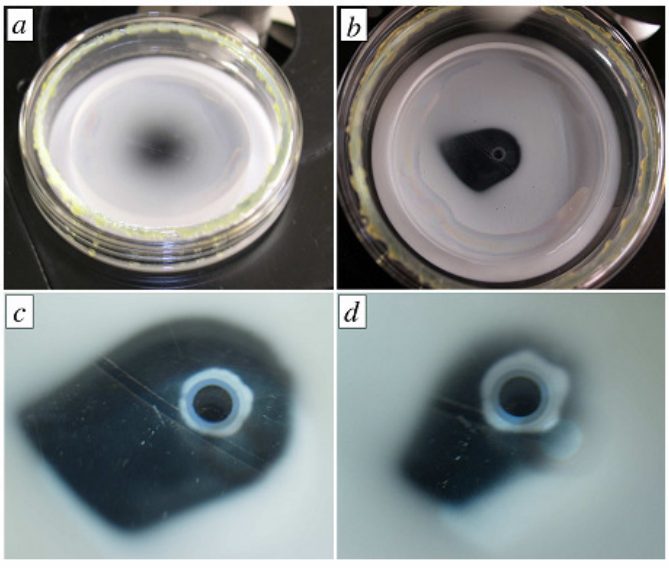

FIG.49: Sequence of images taken for circular cell A which has been slightly tilted. a) Cell just after the suspension has been filled. b) After 36 h the accumulation zone can be distinguished in the centre of the cell. Also an asymmetric convection zone has evolved. c) and d) Close up of the ring after 36h and 48 h respectively.

6.3 Testing the gravity strength

Gravity alone can not be the responsible of the drift of particles to the narrow part of the wedge cells. However it is not possible to exclude it a priori as a possible factor influencing the particles accumulation effect. To test the possible influence of gravity in migration effects, different experiments have been performed. A first set of simple experiments consist in tilting the cells at different angles following the evolution of the system over several days. The other set of experiments consist in density matching the solvent diminishing in that way the gravity strength acting over the particles. Interesting results were obtained just by tilting the cells. We performed the experiments with rectangular wedge cells as well as the spherical cells.

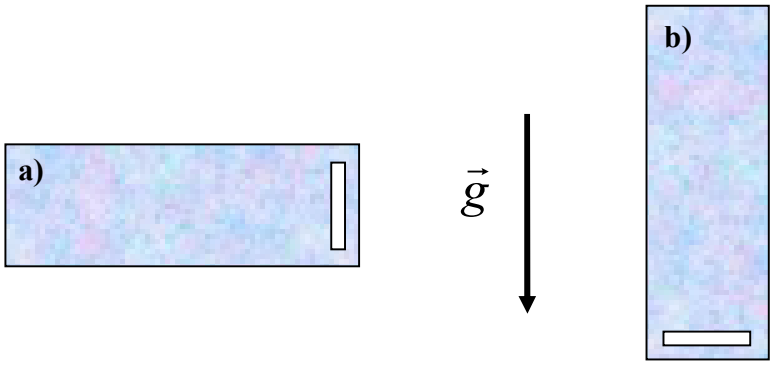

FIG. 50: Position of the rectangular wedge cells with respect to gravity in order to test its possible influence in the accumulation effect of particles in the narrow part of the cell.

Two different tilt experiments were done for the rectangular cells. One consists in turning the cell from its usual horizontal placement by an angle of 90° as shows Fig.50a). After one day there was direct evidence of particles sedimenting to the bottom side of the cell. Close to the narrow part of the cell, the sedimentation is slower than for higher plate-plate distances possibly due to the coupled action of the accumulation particles effect and hydrodynamic forces slowing down the sedimentation rate at this region. After one week practically all particles have sedimented. The other tilt experiment with rectangular wedge cells consist in placing the cells vertically in such a way that gravity points now toward the spacer (Fig.50b)). After two weeks, direct inspection with the eye indicated that all particles had been sedimented. However observations made with the microscope revealed that there were still freely moving particles along the cell being the concentration of

particles higher in the narrow part of the cell than in the middle. This fact evidences a strong trapping effect in the narrow part of the cell. However under these conditions the particle density was too low to form an ordered phase.

Continuing with the tilt experiments we changed now the geometry using spherical wedge cell B. A drop of suspension was placed in the middle of the bottom plate. The cell was then sealed and turned over in such way that the spherical cap was the bottom plate. After one day a concentric crystalline ring had started to form in the narrow part of the cell. Additionally the same experiment was repeated but now slightly tilting the cell an angle ~ 10° as shown Fig.51. The accumulation effect is also present but now the crystalline ring is asymmetric being the lateral extension of the ring larger at the upper side. This shows that gravity induced additional large scale flow of suspension leading to additional accumulation which is absent at the low side.

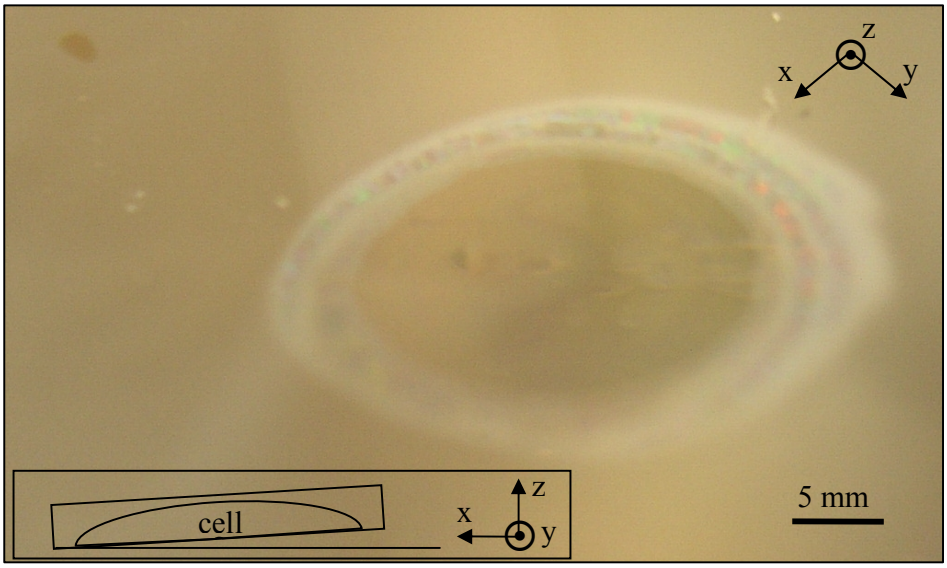

FIG.51: Detail of the crystalline region around the centre of the circular cell B. The cell had been tilted. The coupled action of trapping effect and sedimentation results in an increasing in the length of the ring in the higher in the higher part of the cell.

The last experiments concerning the influence of gravity strength were done comparing the effects of using water as a solvent or using a mixture 1:1 of water and deuterated water. For these experiments we used the spherical cell A. The volume fraction was 1% in both suspensions. Again, the accumulation effect was present in both cases, but remarkable differences were found. The

position of the accumulation region/fluid interface was measured as shows the plot in Fig.52. The evolution of the interface is in both cases practically identical indicating that density matching the solvent does not affect the migration effect. However the interaction forces between the particles in the accumulation zone seems to be different. In the density matched suspension no crystals but high density fluid phase was found, while in the aqueous sample a crystalline region was observed as usual in the narrow part of the cell. It is not clear, whether this observation is due only to the absence of gravity, or whether in addition, slight differences in the dielectric constant of the different solvents influence the charge state of both suspensions differently. In the graph it is possible to distinguish a plateau-like region which is simply a consequence of the wedge geometry of the cell; as the distance between the plates increases, a higher number of particles are needed to fill the volume to increase the length of the high dense region and consequently shifting in the interface position. The accumulating region grows slightly faster in the case of having only water as a solvent.

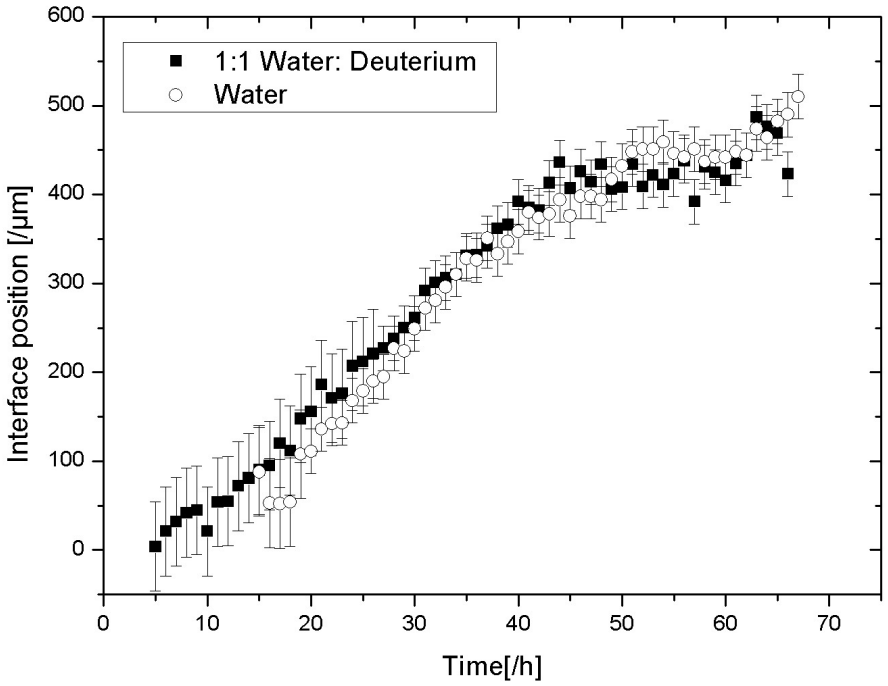

FIG.52: Evolution of the interfaces position with time for particles in water and for particles in a mixture 1:1 Water, deuterated water.

6.4 Testing the influence of the charge at the cell plates

The different cells used in the experiments were made of different materials (glass, plexiglass and even quartz plates were used). Each material has a specific surface charge developed by the walls in contact with water. However it seems that slight differences in surface charge do not affect the trapping of particles in the cusp cell. In order to check the influence of higher surface charges in the plates, a new experiment was performed. This time an external DC-voltage was applied to the cells. Rectangular glass plates sputtered with gold were used. The rectangular cells were prepared as usual being the conducting parts of the plates in the inner part of the cell. In the external narrow part of the cell a conducting silver varnish was added in order to fix the cable connecting the cell to the circuit. In that way the plates are equally charged. Once the suspension is inside, and the cell is completely closed, different voltages and polarities were applied to the plates.

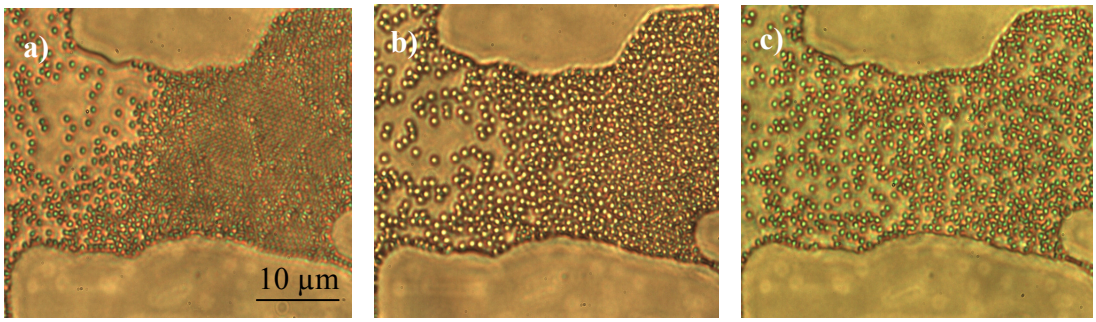

FIG.53: High magnification pictures showing the influence of negative highly charged (V = -30V) at different times. a) Before the current was applied. b) After one day the crystal has melted. At this moment the current was stopped. c) Six hour after the current was stopped we can still see particles moving out the wedge cusp.

The external fields were applied in all cases after observation of a crystalline region in the narrow part of the cell. For negative voltages the sample reaction depended on the length of the crystal (in the increasing plate-plate distance direction) as well as the duration of the voltage application. For voltages higher than -10V applied when only mono- and bilayer crystals are formed, the crystals melt via an increase of the lattice constant. For longer times the particles move backwards the wedge as shown Fig.53. For longer assembly times and again for voltages higher than -10V the behaviour depended on the region in the crystal. Close to the interface the crystal reacted as in the former case. However going deeper in to the wedge it was possible to observe the crystal moving outward as a whole. In some cases, a switch of structure was observed possibly due to an

adjustment of the crystal with the increased height. But in other cases, apparently under the same initial conditions as before, it was also observed that when the crystals reached certain position in the outgoing movement from the wedge, they beaked up into crystalline chunks. For positive charged plates, we applied first low voltages from 1.2V up to 10 V observing an inversely proportional relation between the applied voltage and the growth of the crystals as shows Fig.54. For higher voltages the crystal structures collapsed to form dense amorphous lumps being the samples unstable in practically all the cases. For longer times, the particles were found strongly attached onto the glass plates. The results obtained with these experiments have to be considered as a first approach to the study of confined suspensions between charged plates. It seems that independently of the polarity of the plates a threshold voltage has to be applied to observe a reaction of the suspension. These results can not be conclusive since more measurements for specific voltage ranges and longer time scales should be performed. However the influence of electrostatic forces in the trapping effect has been demonstrated.

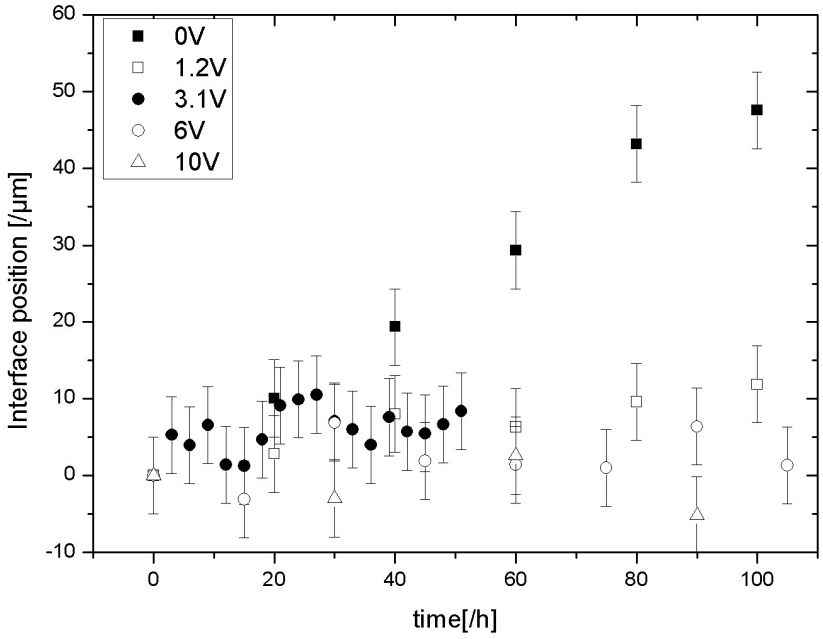

FIG.54: Fluid crystal Interface position for different positive voltages applied to the cell plates. The interface position values correspond to $x=x'-x_0$, being x_0 the initial distance between the cell cusp and the interface when the voltage was applied. We assumed local parallel plates since the crystal presented square symmetry along the entire measurement time. Thus the volume is constant for that region. Once the voltage is applied, the crystal grows more slowly.

6.5 Testing the influence of salt gradients

The presence of a leak in the cell will not only induce migration of particles to the air water interface due to capillary forces and solvent flow due to evaporation currents. but also the CO_2 present in the air reacts with the aqueous solvent to form H^+ and HCO_3^-. The equilibrium pH of deionised water in contact with air will be then on the order of 5.5. This means that both ionic species are in a concentration of $5 \cdot 10^{-6}$ M. A cell with a leak or in contact with air (as in the case of the circular cells reported in this chapter) implies the formation of salt gradients inside the suspension because the cations are highly mobile whereas the anions are slower. Thus a negatively charged colloidal particle (macroion) will tend to move up to higher cation (counterions) concentrations due to a combination of interdiffusion and electrophoretic motion due to the local electric fields generated by the salt gradient; an effect known as diffusiophoresis [Dhu74].

During cell construction, a leak in the rectangular cells can be found in any side of the cell. Assuming the possibility of a homogeneous distribution of microscopic leaks in those cells, the CO_2 may enter at all sides but, due to the geometry of the cell, the gradients will be larger in the narrow part of the cell, where the solvent volume is smaller. By contrast in the circular cells, the CO_2 can only enter by the wide side of the cell. In that case, for short times, the salt gradients will be higher in this region and the particles should tend to it. To test the influence of salt gradients we introduced a deionised suspension in spherical cell B placed in an Argon atmosphere to avoid initial contact with the air. After the cell was closed it was placed in an air environment. Since it is not possible to avoid the presence of air for longer times with such cells we assume the presence of salt gradients in the wider part of the cell. As in former experiments it was observed that the particles moved towards the narrow part of the cell. Thus, we conclude that the migration of particles to the narrow part of the cell is not inducedby the salt gradients.

The last set of measurements, intended to check the influence of salt in the migration effect, consist in using suspensions with different salt concentrations. An increase in the salt concentration implies a higher screening of the repulsive Coulomb interaction between particles. We used three different concentrations: $c_{s1} = 5 \cdot 10^{-6}$M (CO_2^- saturated), $c_{s2} = 1.5 \cdot 10^{-5}$M and $c_{s3} = 8.5 \cdot 10^{-5}$M. As a result, the accumulation effect was less pronounced in those samples with higher salt concentrations. But in all cases this effect prevailed. At the same time, it was interesting to observe in situ how the

different phases in the accumulation region where the salt concentration varied, being crystalline at low salt concentrations and fluid in the samples with higher salt concentration. For samples with moderate electrolytes concentration the accumulation region was also crystalline but with higher amount of punctual defects and dislocations. Thus, the trapping effect seems to be influenced moderately by the presence of stray ions which suggest the possible influence of electrostatic forces.

6.6 Discusion

The confinement of charged colloidal suspensions between slightly charged plates in wedge geometry cells induces a trapping effect of particles at the narrow part of the cell. The particles do accumulate in this region forming a dense layer. The accumulation of particles in that zone is independent of gravity as well as evaporation currents. Different wedge geometries, tilting angles and salt concentrations reveal a strong trapping since the effect is always present. The experiments performed with salt concentrations and the application of different surface charges to the cell plated suggests that the forces responsible of particle accumulation could have an electrostatic origin. Recently, theoretical studies as well as computer simulations proposed by Löwen et al. shows qualitative and semi-quantitative agreement with our results [Lö08]. They considered a macroion inside a perfect linear wedge formed by two semi-infinite plates carrying a constant surface charge density. The calculation of the effective potential acting on the macroion as a function of the distance to the wedge cusp was calculated using linear screening theory. The results predict a local attractive trapping force which draws particles into the wedge Fig.55. The range of this attraction is of the order of the Debye screening length. For higher distances between the particle and the wedge cusp the interaction force diverges logarithmically being this repulsive. This is quantitatively confirmed by computer simulations of the so called primitive model. Thus the effect would be fully consistent with like charge repulsion [Neu99], [Sad00] in opposition to an actual controversial discussion about like-charge attraction in confined geometries [Baum06]. The work done by Löwen et al. is based on single particles, avoiding many body-effects in the calculation. This makes difficult a direct comparison of the experimental and theoretical results. However the theory explains three important facts observed in the experiments:

- In those experiments with inverted cells where gravity tends to push out of the wedge the colloidal particles (Section 6.3), the presence of particles in the narrow part of the cell in concentrations higher than in the middle of the cell will be due to an attractive trapping force as predicted by theory. This is the most direct comparison between theory and experiments since in that case the experiments work in the low density regime

- Linear screening theory explains the existence of a depleted region between the dense inner region and the outer region concentration (Section 6.2). This depleted zone should coincide with the region around the potential barrier.

- Since theory predicts a direct dependence of the range and strength of the attraction with the Debye screening length, linear screening theory would explain why the accumulation effects are less pronounced when increasing salt concentration.

It would be interesting to continue these studies by designing new experiments with highly diluted suspensions using optical tweezers to measure lateral forces on particles close to the narrow part of the cell. Also theory and simulations including many-body effects would help to fully contrast the actual experimental results with theory.

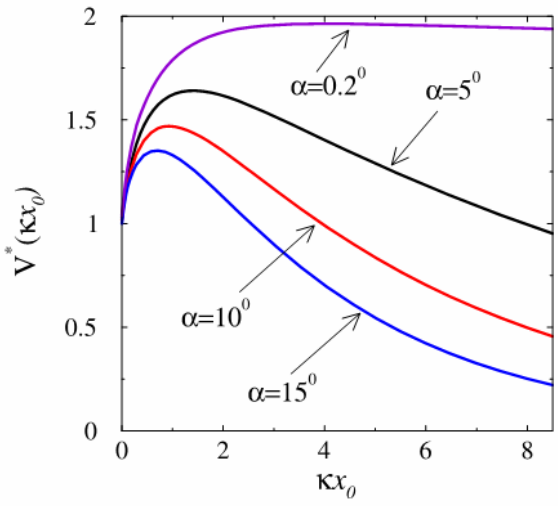

FIG. 57: Reduced effective potential $V^*(\kappa x_0)$ obtained by Löwen et al. acting on a single macroion at a distance x_0 from the wedge cusp. $V^*(\kappa x_0)$ is plotted versus reduced distance κx0 for three different opening angles α = 0, 2°, 5°, 10°, 15° [Lö08]. As smaller the angle is, higher is the traping effect.

Finally, it is important to remark here that migration effect was not mentioned by other authors working with colloidal suspensions in confinement under similar conditions. A research work has been done where DNA chains were confined in a wedge cell showing migration of the macromolecules to the wedge cusp [Kri07]. The migration effects can be however dominated by other mechanism there. Also some analogies can be found for Lennard-Jones liquids confined in wedge shaped pores [Ca04]. There, molecular computer simulations show that small deviations from a perfectly parallel geometry can induce nonuniform pressure and density variations along the wedge. The interplay between the pore geometry and thermodynamic conditions can induce a phase transition at specific regions. In particular, for thermodynamic states close to the triple point.

7 Experimental phase diagrams

A deeper understanding about the behaviour of charged particles in confinement requires the search for the complete phase diagram. For such systems the phase behaviour is completely described by the particle number density, the salt concentration and the distance between the cell plates. The theoretical phase diagram of a bilayer system of particles interacting via Yukawa potential presented by Messina and Löwen [Mes03] motivated us to obtain experimentally the same parameters as appear in it in order to compare both results. The first experimental results about the phase diagram were performed at the beginning of this thesis coming from the early wedge-cell experiments [Fon05]. However, the trapping effect observed in this kind of geometries as well as some experimental inconveniences like the determination of some of the characteristic interaction parameters once the suspension was confined, suggest us to design other kind of confinement cell in order to modify the initial parameters needed to complete the experimental phase diagram. And so then, in the new cell the initial particle and salt densities are controlled by a pumping setup whereas the cell height is controlled by three micrometer screws. The cell and the experimental setup have been already presented in Chapter 5.

Although this new experimental setup allowed us to control the initial parameters solving some of the former problems, new difficulties arose as it was already explained in that chapter. Even so, with this new prototype cell we were able to confine the colloidal suspensions as well as measuring the distance between the crystalline layers as well as the volume fraction of the system in

confinement in bight field microscopy. In this chapter we will first present the results from the rectangular wedge cells. These experimental data is compared with the theoretical phase diagram obtained by Messina. Next the results obtained with the cell with parallel plates and adjustable height will be presented. The chapter will finish proposing some suggestions for future work and outlook.

7.1 Comparison between the theoretical and experimental phase behaviour in closed wedge cells.

In last section of Chapter 3 the complete phase diagram for a crystalline bilayer of Yukawa particles was presented. In it, different crystalline structures appeared as stable for different screening lengths, particle densities and distance between the layers. Our aim here is to compare the experimental $1\triangle \rightarrow 2\triangle$ transition in the wedge cells with the former theoretical predictions. To do so we needed to obtain experimentally the same parameters that appeared in the phase diagram, that is, the relative screening strength, $\lambda = \kappa D$ and the reduced layer density $\eta = \rho D^2/2$ being κ the inverse screening length, D, the distance between the layers and ρ the total area density.

The suspension used in these experiments consists of polystyrene spheres (IDC, Batch No. 2149) of 1.1 μm in diameter in water. The suspension was initially prepared in contact with ion exchange resins at particle density of $n \approx 20\ \mu m^{-3}$. The effective charge of these particles, $Z^*_\sigma = (6860 \pm 150)$ was extrapolated from the linear regression obtained from conductivity measurements [Wet02]. The stock suspension was left in contact with air obtaining saturation with air-borne carbonate. According to the literature [Mil95] the salt concentration in carbonate saturation conditions is $c_s = (6 \pm 1)\ \mu M$ at room temperature $T = (295 \pm 2)$. To obtain the relative screening strength and the reduced layer density I measured the area density from the pictures obtained with the microscope in real space. For example, for the buckling phase $\mathscr{B}$, $n = 2/(a \cdot b \cdot H)$ where a and b are the side lengths of the rectangular unit cell used in the bilayer plasma notation [Mes03], [Gol96] and H the distance between the plates. From that value the area density was obtained simply as $\rho = n_p \cdot H$. The distance between the layers D was measured also with the microscope in real space by placing a piezoelectric adapter between the microscope turret and the objective. Applying different voltages to the piezoelectric we focussed the objective at different focal planes which allowed us to

obtain a precision of 0.1 μm in the focussing. From this value we give estimation about the distance between the plates H since we could not measure this distance directly. For the counterions concentration we assumed a Debye-Hückel inverse screening length used in early work [Wet02]. In these experiments, the major contribution to the screening of the electrostatic repulsion stems from the particle counter-ions and we neglected here the charge surface density contribution of the plates. This fact results in a slight underestimation of κ. Different particle concentrations were prepared to test the confinement effects being all of them originally in fluid phase. However, due to the trapping effect observed in the wedge cells, we always obtained the same final crystalline sequence being the crystal growth rate the only difference between the different cells. As a direct consequence of the former the layer area density for a given crystalline phase was found to be always practically the same. Because of that the experimental values presented here come from a unique cell. The results are shown the plot of Fig.56. The data are presented with different colours indicating different crystalline phases and phase transitions. These symbols do correspond to the crystalline phases as follows: △ to the hexagonal phase, ○ to the buckling phase, □ to the square phase and ◇ to the rhombic phase A (I, II, III IVa and V in the plasma notation; see plot description in Chapter 3). The experimental uncertainly in the area density ρ and the distance between the layers D are the responsible of the big error bar in both, η and λ. Despite this fact we can see that the experimental data are in good agreement with the theoretical predictions for the locations of the different crystalline phases. On the other hand, from the experimental observations, in the original comparison which appear in [Fon05] the rhombic phase B was left because at that time such phase had not been yet observed. Later, we were able to observe it measuring the state variables. Its location in the phase diagram has been now added (◇ in cyan or IVb).

Although the experimental results, which are considered preliminary, reveal good agreement respect to the location of the different crystalline phases, several important facts detailed next made us to consider the necessity of some improvement in the experimental setup in order to obtain not only more accurate measurements but also a more rigorous control of the initial parameters. The study of the different crystalline structures with the microscope revealed that the mean interparticle distance is just a few hundred nanometres larger than the particle diameter. This can be observed in any of the pictures presented along this thesis, especially in next chapters. This indicates that the system can be considered as a quasi hard-sphere system and not a highly repulsive particle system. However in the plot, the hard sphere limit does correspond to $\lambda \to \infty$ and we can clearly see that our

results do correspond to a highly repulsive system. The immediate conclusion is that the inverse screening length considered at the beginning of the experiment has a different value in the final state. Nowadays the reason for this drastic change seems to be solved, being the geometry of the cell and the surface charge density the main responsible on the increasing on the screening of the particles in the narrow part of the cell. The same reasons seem to underlie in the fact that with these rectangular wedge cells and for low and moderate salt concentrations the final state in the narrow part of the cell is always the same. Thus, after these results, the next step was to design the new confinement cell presented previously.

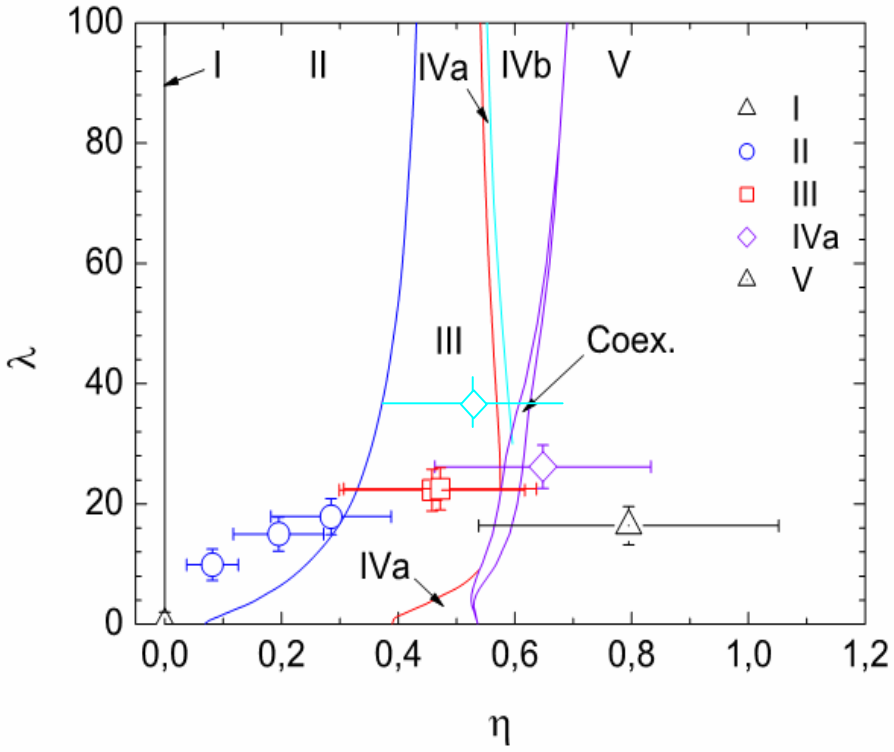

FIG. 56: Comparison between experimental data and theoretical [Fon05] predictions for a bilayer of charged spheres in confinement .Despite the big uncertainty in reduced layer density, η the data points are in agreement with theory respect to the phase behaviour. However the relative screening strength, λ of our systems is much lower that the observations with the microscope reveals. The symbols indicate the next crystalline phases △ to the hexagonal phase, ○ to the buckling phase, □ to the square phase and ◇ to the rhombic phase A (in violet) and B (in cyan) For details see text.

7.2 Results obtained with the cell with parallel plates.

With a pumping setup we can monitor and control the main parameters that determine the phase behaviour of the charged particles in confinement. We used a suspension of latex particles of 570 nm in diameter. By means of the conductometer and knowing previously the effective charge Z_σ^* the different bulk particle and salt concentration can be precisely determined. The preliminary measurement of Z_σ^* is explained in Section 5.3.3.1. In this section all the problems derivated from using big particles are also explained. After stabilization and by means of the optical microscope we measured the particle number density of the system in confinement for different cell heights H. The measuring technique was the same as in the former section; we recorded the images with a digital-camera and with special image software the unit cell area of the different crystalline structure were measured. The distance between the crystalline layers was measured by a piezoelectric device adapted between the microscope objective and the turret.

Sample A		Sample B	
Deionized conditions	CO2 Saturation	Deionized conditions	CO2 Saturation
$\sigma = 0.96$ μS/cm	$\sigma = 1.54$ μS/cm	$\sigma = 1.05$ μS/cm	$\sigma = 1.53$ μS/cm
$n = 6.48 \cdot 10^{16}$ 1/m^3	$n = 6.48 \cdot 10^{16}$ 1/m^3	$n = 7.12 \cdot 10^{16}$ 1/m^3	$n = 7.12 \cdot 10^{16}$ 1/m^3
$c_s = 2 \cdot 10^{-7}$ M	$c_s = 5 \cdot 10^{-6}$ M	$c_s = 2 \cdot 10^{-7}$ M	$c_s = 5 \cdot 10^{-6}$ M

Table 1: Initial parameters of the two samples of polystyrene particles of 570 nm in water used in the experiments.

The results presented here correspond to two set of measurements with very similar initial parameters. Each set is subdivided at the same time in other two sets: the suspension at deionised conditions and the suspension with a salt concentration corresponding to CO_2 saturation. The measurements were made only for the structures appearing in the bilayer. In Table 1 the main initial parameters of the different samples are present. It is important to say that we assumed than in CO_2 saturation conditions the particle number density was the same as in deionized conditions. Coming back to the problems derived of working with big particles in the tubing system, we have to remember that the the IEX-chamber caused particle aggregation. However during the measuring time

in salty conditions that chamber was bypassed. Since during this time we did not appreciate aggregation in any other part of the circuit just by eye or inside the confinement cell with the microscope we can conclude that the particle concentration should be the same as before.

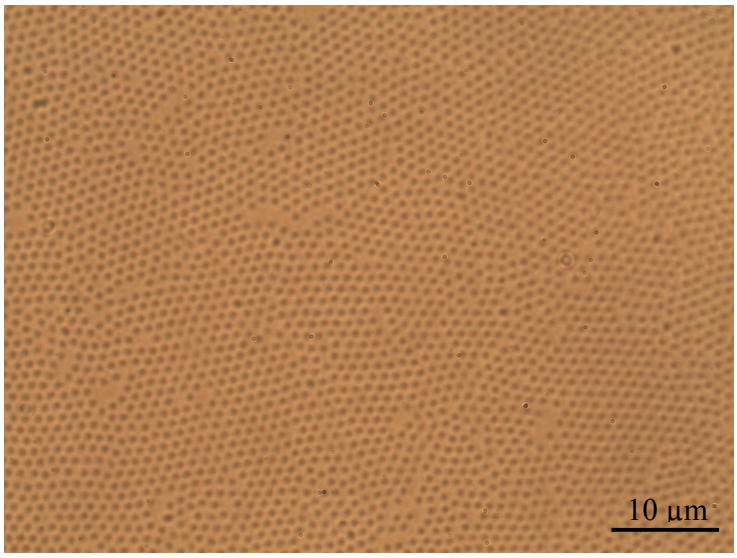

FIG.57: Monolayer formation of polystyrene particles of 570 nm in diameter in a confining cell with parallel plates and variable height.

The resolution of the different images is 1027 x 768 which means than 1 pixel is equivalent to 0.05 µm, the error that we estimated in the different measurements of the distances between the particles. The surface area was calculated from the measurements of the length parameters of the different unit cells. The main error source comes from the measurements of the distance between the plates. Unlike in close wedge cells the fluctuation of the particles in this experiment was much more pronounced in z direction. The reason is that the mean interparticle distance was around twice the particle diameter whereas in the close cells this value it was just a little bit higher than the particle diameter. Although the height was measured carefully for each structure, this technique is not appropriate for determining the relative position of the layers. The typical values for the measured distances between the layers varied from 0.4 to 2 µm. We estimated an error of 0.3 µm; approximately the radius of the particles. These measurements introduce the main uncertainty in the reduced layer density. On the contrary it seems that does not affect to the relative screening strength which presents very low values independently of measured D. This time we included the surface charge contribution of the glass plates in order to calculate the complete electrolyte concentration.

Since we did no determine the exact value, we recurred to literature [Beh01] choosing an intermediate value $\rho_{plates} = 6 \cdot 10^{14} e\ m^{-2}$. The final expression for the screening parameter is then:

$$\kappa = \sqrt{\frac{e^2}{\varepsilon\varepsilon_0 k_B T}\left(2 \cdot 1000 \cdot N_A c_s + 2 \cdot \rho_{plates} / (e \cdot H) + Z * n'_p\right)} \qquad (7.1)$$

Comparing the former with equation (2.2), apart of the charge density of the plates we have to take in account the particle number density n'_p measured in confinement where H is the distance between the plates. We tested than in this experiment any of the values given in the former reference will not influence the final value of κ. We found that the inverse screening length have the same values for the two deionised samples. The same happened in the case of CO_2 saturation. These values were $\kappa_{deionized\ susp} = (1.45 \pm 0.04) \cdot 10^6 m^{-1}$ and $\kappa_{CO2} = (7.27 \pm 0.04) \cdot 10^6 m^{-1}$. This clearly indicates that the electrolytes concentration dominates in the interaction between the particles for small variations of the n_p. The results obtained are shown in Fig.58. Undoubtedly, they give no valid information about the behaviour of charged colloidal particles in confinement. However they account for the main experimental source of errors.

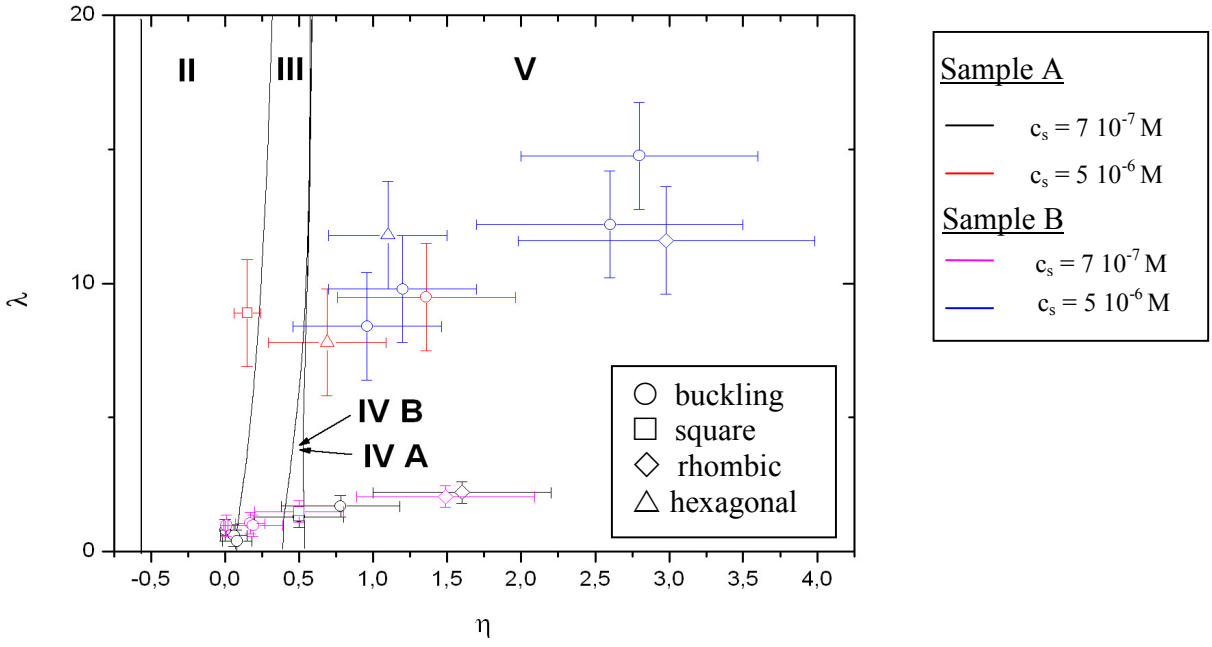

FIG.58: Experimental results obtained with the new setup and theoretical predictions. Due to all the problems in derived from the measurement technique it is not possible to compare both results.

7.3 Comparison and discussion of the experimental phase diagrams

The obtained data allows considering several important points. It is clearly seen, that the data present a better agreement in the reduced layer density for closed cells than in the cell of variable height. As it has been already explained, this is due to the higher interparticle distance obtained with the cell of parallel plates which originates from strong particle fluctuations in z direction which makes the accurate determination of the distance between the layers difficult. It is also important to remark than these fluctuations were much less pronounced in the x-y plane. We think that this difference comes mainly from the influence of the slightly charged plates. Other result that we consider very important to discuss here refers to the low values in the relative screening strength obtained in both, open and closed cells. By taking a look to the different picture presented in the former section, and in general along the entire thesis, it is clear than the system can be not considered highly repulsive. However the experimental data indicates just the contrary in both cases. We checked that small variations of the distances between the layers do not change significantly the value of λ, thus the experimental screening parameter seems to be much lower than expected. In this case, variations in the particle density presented here would not affect the κ value. On the other hand the value of the effective charge is around two orders of magnitude higher than expected. Since we expect that the real value be lower, the amount $Z_{\sigma}^{*} n_p$ appearing in (7.1) should be neglected under these experimental conditions, being the salt concentration the main parameter governing the particle interaction in confinement, at least for the interaction ranges that we tested. Since the salt concentration takes into account all the ionic species present in the solution, other possible contributions apart of those already considered would increase the inverse screening value. In this case the experimental λ values here obtained would be more realistic. Nevertheless, according to the results and considering that the interaction parameters calculated for the bulk are correct, it seems that a considerable increase of the electrolytes concentration occurs in confinement. Next we propose some possibilities to study these differences observed in bulk suspensions and confined suspensions simultaneously.

Considering the results of the former experiments, it is clear that the experimental techniques have still to be improved. In closed cells with wedge geometry the trapping effect due to electrostatic forces is present. Although this effect is of relevant importance in the confinement of colloidal suspensions and has to be necessarily taken into account, we need a constant distance between the

plates to evaluate its influence along bigger regions. On the other hand, building perfectly parallel closed cells whose cell distances vary from say 0.1 μm to 20 μm, in order to continue working with particles between 500-1000 nm, is an unnecessary as well as expensive effort. Above all, if we take in account the unavoidable particle aggregation of those particles in the tubing system. All these unfavourable events suggest a different approach to study confinement.

One possibility is just to find an alternative method to deionise and stabilize the colloidal suspensions as well as to control the initial parameters. With that it would be still possible to use big particles in order to analyse their behaviour with the optical microscope. Nevertheless it has already shown that the method used here to measure the distance between the layers introduces a huge uncertainty in the measurements. Other possibility would be to use smaller particles. We consider that this is the best solution since this change offers the possibility of improving the efficiency in the measurement technique. Besides the possibility to continue using the pumping setup whose efficiency has been probed in numerous research works, we can use light scattering techniques to estimate the state variables which describe the phase behaviour of the confined suspensions being possible to obtain the particle number density in the bulk as well as in confinement with high accuracy. It will be also possible to measure the distance between layers and the number of layers. In this sense we hope that the diffraction patterns of each crystalline structure presented in this thesis help further researches to analyze the experimental data. Finally, in order to obtain good experimental results it is equally important to design a cell where both plates are perfectly flat in order to reach the condition of having parallel plates. At the same time the cell has to be able to work also for distances between the plates lower than the diameter of the particles to be sure that we can have monolayer.

8 Structural sequence of colloidal crystals in confinement

In chapter 6 I have described the crystal growth process for charged colloidal spheres confined in a wedge cell. The present chapter deals with the description of the different structures found in those experiments. In the narrow part of the cell, once the colloidal crystal has been formed, the mean interparticle distance is very close to the particle diameter. Because of that, for that region we assume hard sphere behaviour in the high pressure limit. Under this situation, the colloidal structures found in confinement are mainly characterized by the cell height. Due to the small angles achieved in our wedge cells, the height variation is very smooth and the crystalline sequence is more abundant in crystalline phases that in former works. Our experiments reveal that almost all these new structures are the result of a continuous structural transformation mechanism between the hexagonal (nΔ) and the square (n□) phases. For specific cell heights, superstructures have been also observed. They appear in small isolated domains and do not form part of the structural transformation mechanism. These particles arrangements were never observed before and they have no atomic counter part. All the crystalline structures have been identified using high resolution optical microscopy, Fourier microscopy and Scanning Electron Microscopy. Complementing the structures characterization I also propose packing models based on geometric arguments to explain the transition between structures. From them, a relation between the dependence of the volume fraction with the cell height is obtained. These models are in good agreement with the experimental results.

The chapter starts with a general description of the complete sequence together with a schematic explanation of the structural transformation mechanism. After that, the different crystalline structures and the corresponding models explaining the structural transformations are reported. The chapter finishes with the proposed theoretical phase diagram of a hard sphere system in the high pressure limit where the results from all the proposed models are shown.

8.1 Introduction: The structural sequence

The crystalline structures reported here correspond to that region of the phase diagram where $\lambda \rightarrow \infty$, that is, where the colloidal system shows a very week repulsive interaction between spheres. In this chapter, to describe the formation of the different structures and the structural changes appearing when the distance between the cell plates varies, I will consider that we have a system of nearly hard spherical particles subject to an external force in a given direction. In our case this force is applied towards the cell cusp and the particles move slowly in that direction until they arrive to equilibrium position forming ordered structures. In this sense the crystal growth mechanism observed in the wedge cells is analogous to the experiments reported by Neser et al. where fluid evaporation induced lateral forces compressing the particles to form a dense colloidal solid [Nes97]. At the same time, both physical systems can be considered analogous to a sedimentation process where particles, heavier than the fluid, move towards the bottom of a container due to the gravitational effect. On the other hand, in this thesis the wedge geometries were proposed to be used sealing the cells completely or allowing evaporation as in former literature. In our case the idea was to compare the crystalline sequence before and after water evaporation. As a result we observed that most of the crystalline structures remained unaltered after the action of capillary forces during the drying process. However other structures slightly changed their final configuration.

The main advantage of working with wedge geometries is that the whole sequence of structures can be observed simultaneously. From previous works found in literature we know that the first sequence reported by Pieranski et al. consist in an alternation of well defined and separated crystalline phases with square and hexagonal symmetry [Pie83]. Later, in similar experiments reported by Neser et al. new crystalline phases appeared forming part of the original sequence [Nes97]. For one and two layers these new structures appeared as a consequence of a smooth and

continuous transformation between the square and the hexagonal phases. For higher number of layers also a new crystalline phase was found. This new phase also appeared to mediate in the structural transformation process but, from the experimental observations the exact transformation mechanism was unclear. In our experiments the sequence is still richer in structures than in former cases for more than two layers. As it is going to be shown, these structures appeared also forming part of a smooth and structural transition between structures. For systems considered as nearly hard spheres, since the angles of the wedge cells reported by Pieranski, Neser and ourselves were around 10^{-2} rad, 10^{-4} rad and 10^{-4} rad respectively (corresponding particle diameters 1μm, 0.84μm and 1.2 μm) it seems quite obvious that the richness of structures will depend on the wedge angle. Since hexagonal and square structures were the first ones reported we consider them as the basic crystalline structures in the sequence whereas all the new structures appeared after decreasing the wedge angle are going to be called intermediate.

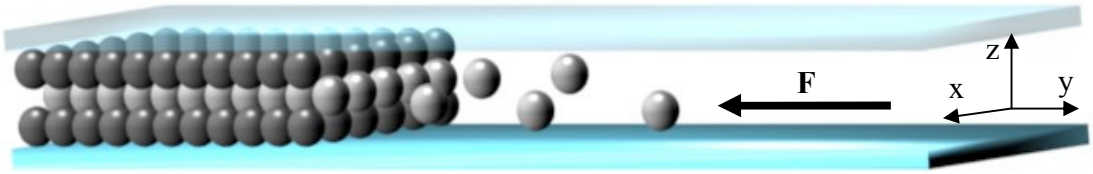

FIG. 59: Scheme of the wedge cell showing the crystal growth process. For the purposes of this chapter it is enough to consider that the particles arrive from the wider part of the cell (right part of the drawing) to the cusp due to the action of a lateral force. The particles are compressed forming colloidal structures whose symmetry depends on the distance between the cell plates.

Continuing with the model proposed by Pansu et al., the stability analysis for the some of the crystalline phases as well as the structural transitions found in this thesis will be analyzed assuming a system of hard spheres in the high pressure limit. This means that only geometric considerations are going to be contemplated and the stable structures have the maximum volume fraction at any distance between the plates. With that, we will obtain a bidimensional phase diagram for all the structures where, in terms of volume fraction and cell height, the problem of the most efficient filling of the available space will be analyzed. This physical system must not to be confused with the process where a crystal suffers a structural deformation upon compression; here what we have is a smooth transformation along the cell due to an increasing of the cell height, i.e., the particles arriving

to the fluid/solid interface will contribute to the crystal formation adopting the most stable configuration for each plate-plate separation. In Fig.59 the growing process of the crystal is schematized showing the solid-fluid interface. At the left part a three-layer FCC crystal is filling completely the cell volume and the (010) planes are oriented perpendicular to the cell cusp. At this particular cell height the particles arriving to the interface will find well defined local equilibrium positions. However, as the height of the cell increases, the free space in z direction modifies the former equilibrium distribution and the particles arriving to the interface will fluctuate around local stability regions. In both cases, the progressive increment of particles arriving at the interface forces the system to adopt the final configuration. As it is going to be shown, for some confinement volumes, more than one stable structure can appear.

A complete overview of the general sequence of crystalline structures can be observed in Fig.60. The picture shows a longitudinal view of the rectangular wedge cell giving us an idea about how the sequence looks like. We can distinguish the existence of different structures just by the observation of the different coloured regions. For the smallest cell thickness we always observe a region with low particle density being the system in the fluid phase. There are two reasons to think that this phase does not belong to the structural sequence as an underneath phase to the monolayer. First, from the experimental results we observe that the density of the fluid phase is frequently much lower than it would correspond for a pre-freezing fluid phase as shows Fig.61. In second place, it has been already shown that for short cell heights the particles behave as nearly hard spheres subject to a strong pressure. As a result, a system originally in fluid phase forms in equilibrium a dense colloidal solid. Because of the former, it has no sense to observe a fluid phase preceding the crystalline sequence. Probably it is a consequence of the polydispersity of the sample (~ 5 %): Since the diffusivity of the particles is inversely proportional to their diameter, the smaller particles will arrive faster to the narrow part of the cell [Hun86]. At the same time, due to their smaller diameter, they will be able to reach positions closer to the cell cusp. The concentration of the smaller particles in this region is not enough to form a crystal and because of that we observe a fluid phase.

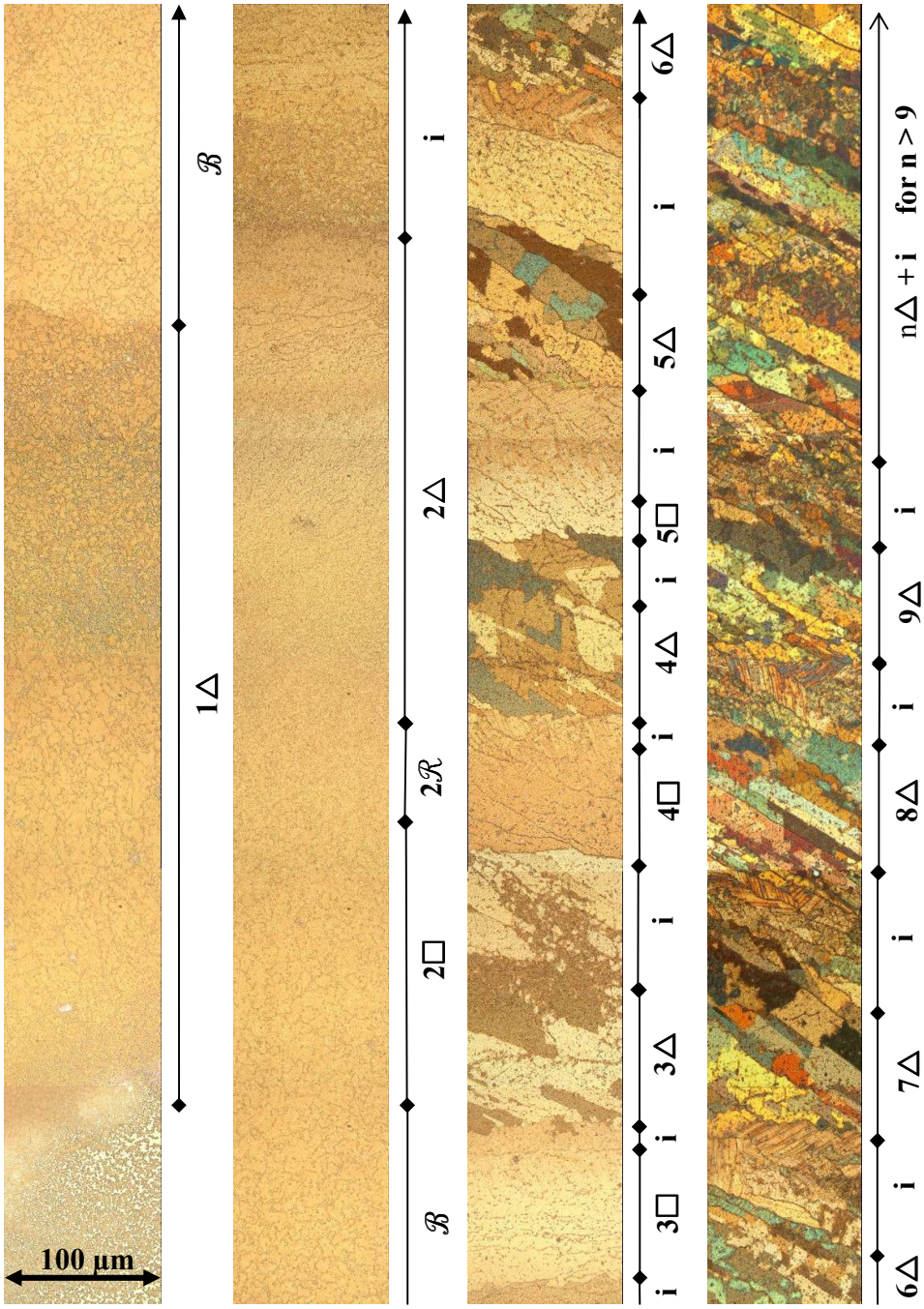

FIG. 60: Structural sequence of charged colloidal spheres confined in wedge-like geometries up to more than 10 layers. The height of the cell progressively increases from bottom to top and from left to right. The different structures are denoted by: △, hexagonal; □*, square;* ℬ*, buckling;* ℛ *rhombic; i, other intermediate structures. The numbers indicate the number of layers of the different crystalline structures. The pictures for this structural sequence were taken by the student Thomas Shots.*

Continuing with the general view of the sequence in Fig.60, we see that the monolayer and the bilayer (1△→$\mathcal{B}$→2□→$\mathcal{R}$→2△) present very similar colours. This is due to the small phase differences in the light waves passing through these extremely thin crystals. From three to five layers we can observe an alternation of regions with only one light colour and regions with several colours at the same cell height. The centre of the light zones does correspond to the square structure, n□. The beginning of the regions with more than one colour will correspond to the hexagonal structure n△, where each colour indicates a different stacking sequence. Between the square and the hexagonal structures we find intermediate structures, i. Some of them have been already observed and some of them have been reported for the first time. For more than four layers the squared structure comes in competition with other intermediate structures. From six layers on the square structure appears rarely. The experimental sequence it transforms then in n△ → intermediate phases → (n+1)△. As the distance between the cell plates increases, the length of the crystalline domains decreases being the n△ phases progressively closer. In our experiments, from nine layers on, the confinement effects practically disappear and the crystalline sequence consist in different stackings of hexagonal phases and continuous increasing of the number of layers. On the other hand, detailed analysis of the structures in the sequence has been only done until seven layers.

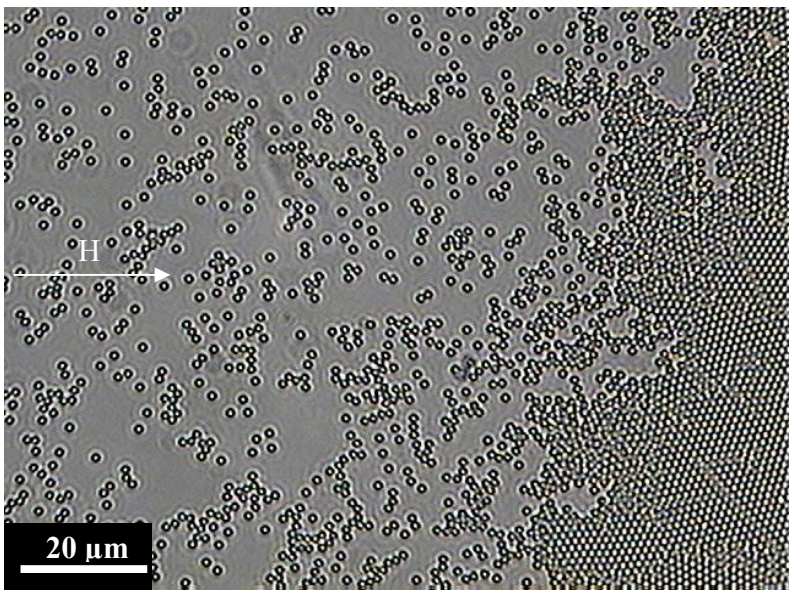

FIG. 61: Particle distribution at the beginning of the crystalline sequence. The cusp of the wedge cell is in the left part of the picture. The existence of a fluid phase in that region is probably due to the polydispersity of the sample (~ 5 %). The smaller particles would arrive faster to the cusp being also able to penetrate to the narrower region of the cell. The right part of the picture shows the beginning of the monolayer 1△.

From two layers, as the number of layers increases, more possibilities of packing are possible. As a result we found coexistence of structures. The identification of the different arrangements revealed that each intermediate structure belonged to a specific part of the structural sequence. This had been already observed for one and two layers finding that the buckling phase is characteristic of the 1△→2□ transition or the rhombic phase which mediates in the 2□→2△transition. Because of that in this chapter the intermediate structures are going to be presented grouped in those who belong to the n△→(n+1)□ transition and those who belong to the n□→n△ transition.

8.2 The n△ → (n+1) □ transition

This structural transition is mainly characterized by the pass from n to (n+1) layers in the crystal. The number of different structures that appear in this transition depends on the number of layers. As it has been described in Chapter 3, the 1△ → 2□ transition is mediated entirely by the buckling phase. However as the number of layers increases more than one stable phase can appear. Some of these new phases are observed at any n△ → (n+1) □ transition; others appear only for a specific number of layers in the sequence. A general view of the transition is shown in Fig. 62. This picture shows the central region of a transition going from three to four layers. The plate-plate cell distance increases from left to right as the direction of the white arrows indicate. The beginning of the transition starts with the hexagonal phase. Since in this phase, different stacking sequences are possible, we found that the structural transformation will depend on the original stacking sequence. The identified structures derived from the hexagonal phase are two: the n-hcp⊥ structure (hexagonal close packed structure with the close packed planes oriented perpendicular to the cell plates) and the n-$\mathcal{P}_{\triangle}$ structure which consist in a regular distribution of triangular prism blocks with hexagonal symmetry in the planes parallel to the cell plates. It is possible to find as many different n-$\mathcal{P}_{\triangle}$ structures as different hexagonal stackings appear in the previous n△ phase. Both phases are found in coexistence, that is, both are equally probable to mediate in the structural changes which take place at beginning of the transition.

Continuing with the sequence, as the height of the cell increases, other structure is found. It was already observed by Neser [Neser97] and the particles are arranged forming prisms with square symmetry in the basis placed parallel to the cell plates. I will rename it as n-$\mathcal{P}_{\square}$-A structure. This particle arrangement has only observed for n = 2 and n = 3. Its stability region in the transition is very short appearing after it the (n+1) □ phase. In Fig.62 another kind of structures are left. They appear at the beginning of the n△ → (n+1) □ transition forming isolated crystalline domains. In them, the colloidal particles are arranged forming superstructures of exotic symmetry. They do not form part of the transition mechanism between the structures and because of that I do not consider them as intermediate structures. These exotic structures will be described in next chapter.

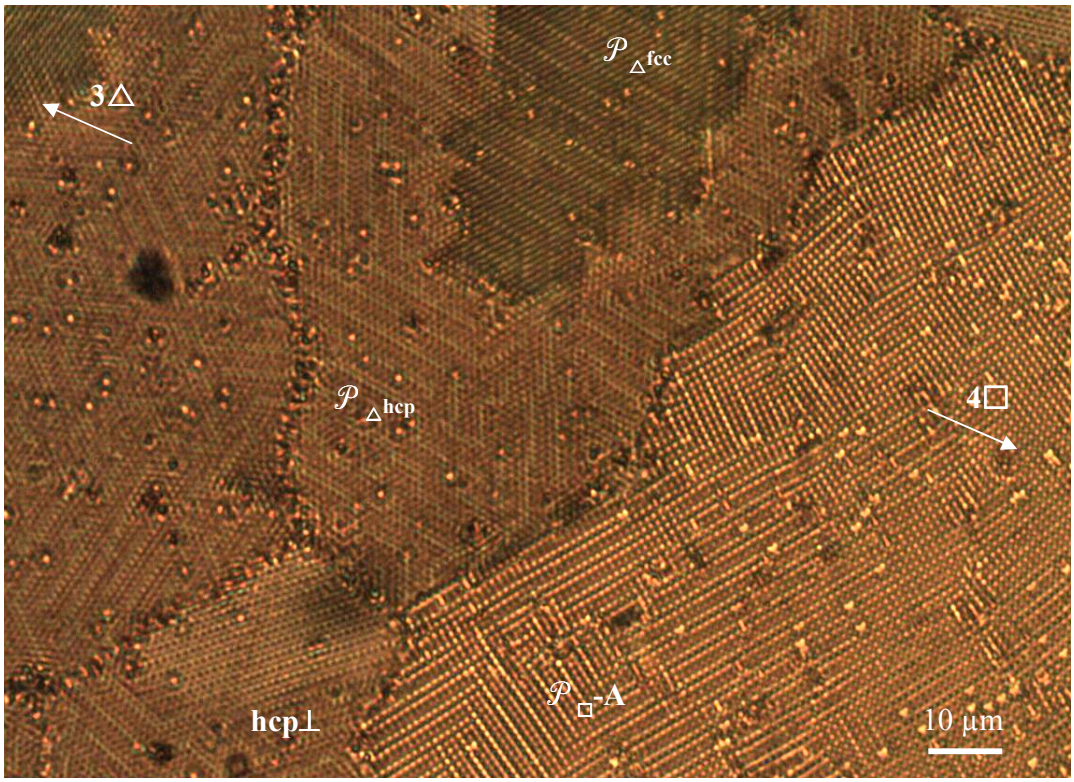

FIG. 62: The 3△ → 4□ transition showing the main intermediate structures presented there. The grain boundary which define the limits for the n-hcp⊥ or n-$\mathcal{P}_{\triangle}$ structures to the n-$\mathcal{P}_{\square}$-A or n□ structures is present in every experimental sequence found in this thesis and captured the inexistence of a continuous structural transition between them.

The n△ → (n+1) □ transition has been observed in our experiments up to seven layers. A very important feature of this structural transition is the abrupt change between the n-hcp⊥ , n-$\mathcal{P}_{\triangle}$ structures and the n-$\mathcal{P}_{\square}$-A structure. In none of the studied sequences have we observed a continuous transformation between these structures. On the contrary, they are always separated by a grain boundary as can be clearly observed in Fig.62. We will come back over this structural discontinuity later. In the next sections these intermediate phases are going to be described. First, the buckling phase is briefly mentioned to compare former theoretical predictions with our experimental results. For higher number of layers the intermediate structures will be described finishing each section with the corresponding transformation model of hard spheres in the high pressure limit. Once the three phases have been described, the discussion about the stability of the different phases as well as the comparison with the predictions of the proposed models will be discussed together.

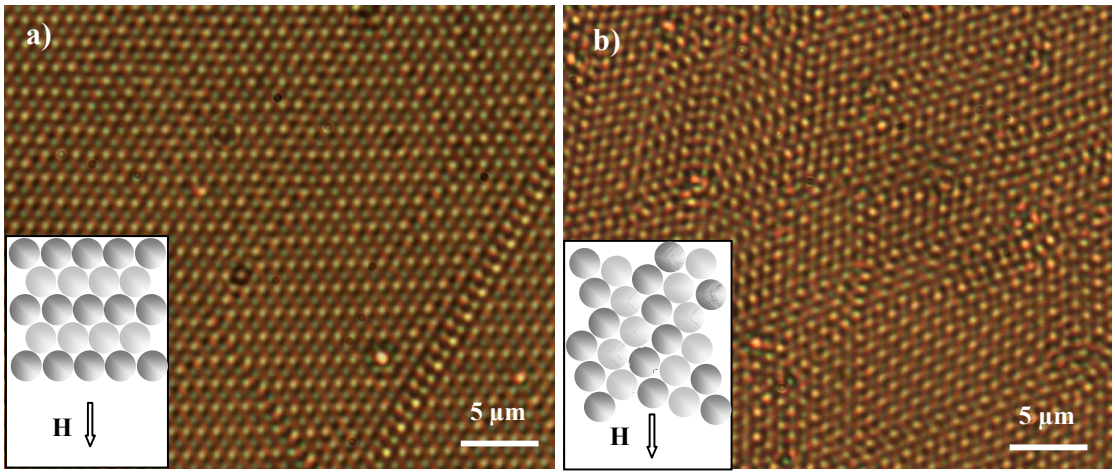

FIG.63: Two equivalent configurations for the buckling phase. a) Linear buckling. b) Zigzag buckling. In the wedge cell experiments both orderings will depend on the relative orientation of the previous hexagonal domains during the crystal growth. The different colours in the insets indicate different heights.

8.2.1 The buckling structure

This intermediate structure takes place between the monolayer and the bilayer and has been already described in Chapter 3. Schmidt and Löwen proposed three equivalent configurations for the buckling phase [Sch97]. In our experiments we observed two of them: the linear periodic buckling (Fig.63a)) and the zigzag buckling (Fig.63b)). However we did not observe the random buckling

phase which consists in the random alternation of the two former orderings. Probably, the reason underlying the absence of this phase is related to the specific characteristics of the wedge cell experiments: The orientation of the preceding hexagonal phase respect to the cell cusp, influences the resulting configuration. A row of particles oriented parallel to the cusp will favour the formation of long domains with linear buckling whereas for any other orientations of the rows, the variation of the cell height will condition their growth along a given direction. Both possibilities are schematized in the insets of pictures a) and b) in Fig.63. Under this circumstance, the crystal will be buckled changing successively the direction of the rows.

8.2.2 The hcp⊥ structure

For more than two layers the *n-hcp vertical* or n-hcp⊥ structure is one of the possible particle arrangements that we can find in the n△ → (n+1)□ transition. In Fig.64 a) and b) a top views of this structure (after drying and with solvent respectively) are shown. This structure remains unaltered upon drying. Furthermore both high resolution Optical Microscope and Scanning Electron Microscope observations reveal that this structure forms high quality crystalline domains being possible to observe extended regions up to 1000 x 200 μm^2 for the complete n△→ n-hcp⊥ transition (Fig.65 a) and b)). The structure is characterized by an alternation of stacking rows of elevated particles separated by low-lying rows as in the buckling phase. During the experiments we realized that each of these rows belongs to one of the hexagonal close packed planes of a HCP crystal, being those planes oriented perpendicular to the confining walls. Thus with the microscope we are observing its characteristic stacking sequence of hexagonal planes. In crystallographic terms, this means that the HPC crystal is oriented with the (100) planes parallels to the cell plates. Therefore, together with the n△ and the n□ phases we have found another close-packed structure. The vertically oriented hexagonal layers facilitate the observation of twin structures with three possible orientations (Fig.65c)).

The inset in Fig. 64a) shows a transversal cut of the 3- hcp⊥ structure. In the top as well as in the side views the [001] direction is indicated by a white arrow in order to help in the identification of the close packed planes in both crystal projections. In this picture also the lattice vectors $\mathbf{a}_2$ $(\hat{y})$ and $\mathbf{a}_3$ $(\hat{z})$ corresponding to the conventional HCP unit cell have been also drawn in order to show

the reciprocal vectors in the corresponding diffraction patterns of the n-hcp⊥ structure (Fig.64 d)). The diffraction pattern of Fig.64c) was obtained illuminating the sample with white light whereas in Fig. 67 d) the sample was illuminated with monochromatic light (λ = 488.7 nm). Comparing these two pictures we can see the wavelength dependence with the intensity maxima distribution: blue light shows (2,0) and $(\bar{2},0)$ reflections. On the contrary, yellow and red light results in very weak reflections not visible in the picture. The stop diaphragm in the rear focal plane of the objective has been marked in white for clarity. Something similar happens with the (1,0) and $(\bar{1},0)$ reflections where the maxima for blue light are very weak compared with the maxima given by red light.

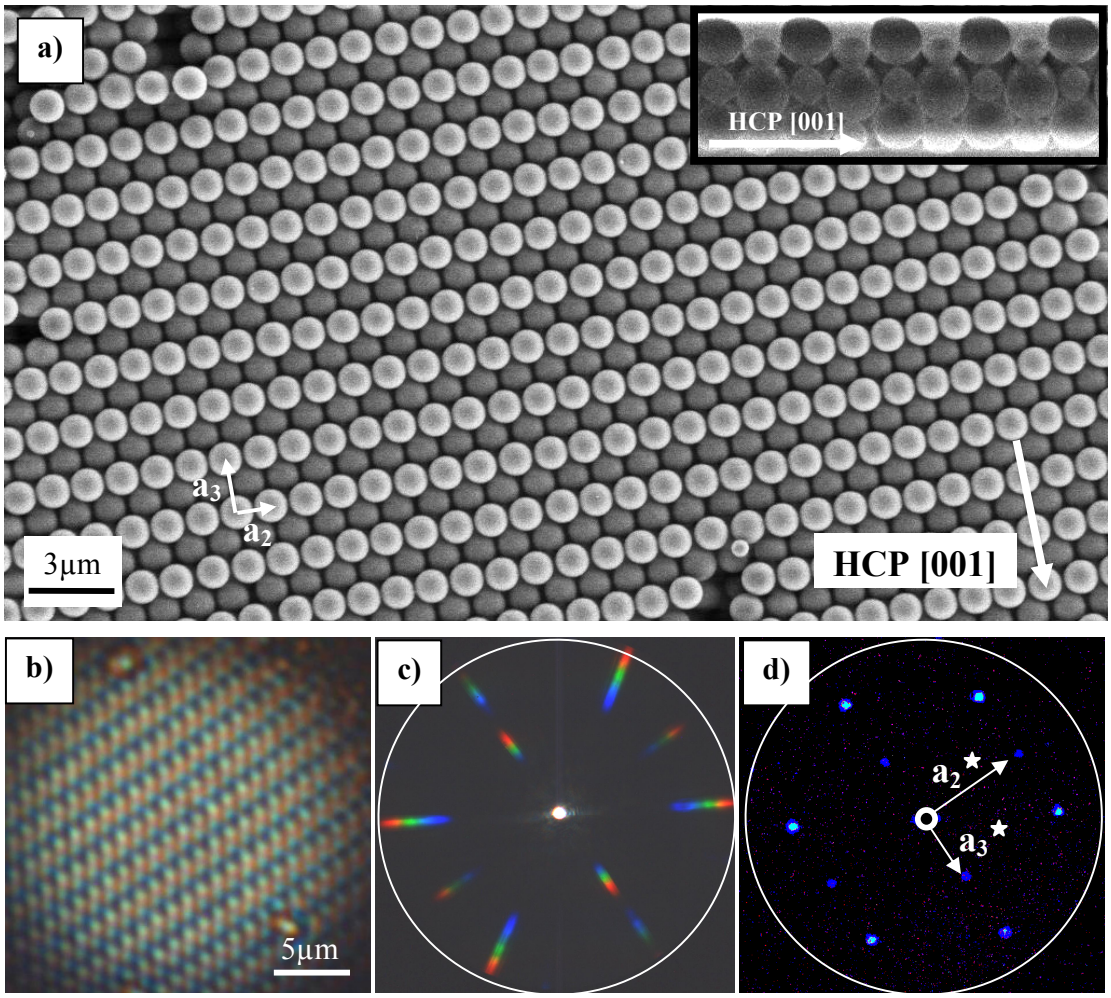

. FIG. 64: hcp⊥ structure. a) SEM picture showing the top view of the structure once dryed. Zhe inset shows a transversal slice for three layers. b) Optical microscopic picture for the 2-hcp⊥ structure in real space. c) Diffraction pattern of the 2-hcp⊥ structure shown in b). In his case the sample was illuminated with white light. d) The same patern as in c) but with blue illumination. We can observe here the similarities between the diffraction patterns of the buckling and the n-hcp⊥ structure.

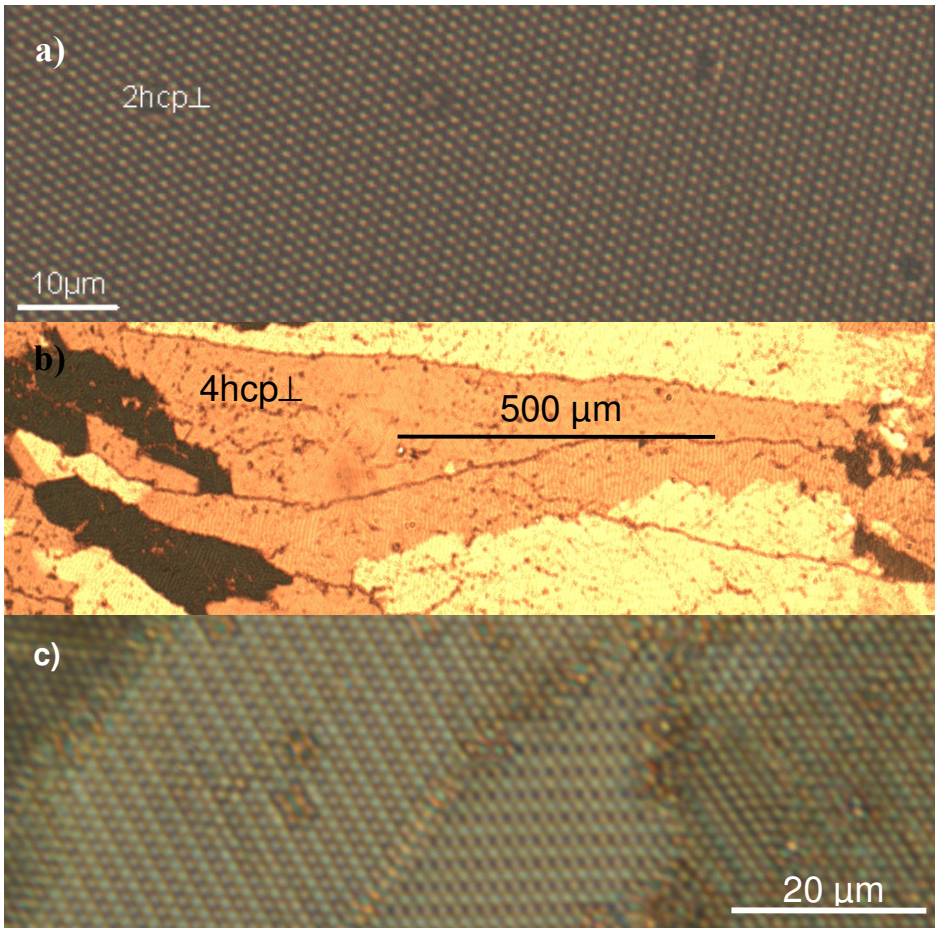

FIG. 65: a) and b) The n-hcp⊥ structure form extended and good quality crystalline domains. c) The hexagonal symmetry of the structure allows the formation of twinned hcp⊥ structures[Fon07].

Since the n△→ n-hcp⊥ transition takes place as a continuous structural transformation we propose here a mechanism to explain the process assuming maximum packing efficiency at any height for hard spheres of diameter σ. For this transition, in the same way that for the buckling phase, the hexagonal planes get smoothly distorted giving rise to an alternation of rows *going up* and *going down* where the distance between the in-plane rows decreases as the height of the cell, H increases. However since now there are more layers involved, the transformation mechanism is a little bit more complex. The starting point is to define a two-dimensional unit cell for the planes parallel to the confining walls. For practical purposes we are going to choose an orthogonal reference system as indicates the drawings in Fig.66. In this way, a rectangular unit cell of sides a x b will be defined by the two lattice vectors $\mathbf{a'}_1 = a\,\hat{\mathrm{x}}$, $\mathbf{a'}_2 = b\,\hat{\mathrm{y}}$ being the colloidal particles at the lattice points. With this election it is clear that in this case, $a = \sigma$. At the beginning of the transformation, still in

the hexagonal phase, $b/a = \sqrt{3} \approx 1.732$. At the end of the transformation, the ratio of lengths for the n-hcp⊥ structure is $\sqrt{8/3} \approx 1.633$. Therefore, during the n△ → n-hcp⊥ transition b varies as, $1.732a \le b \le 1.633a$.

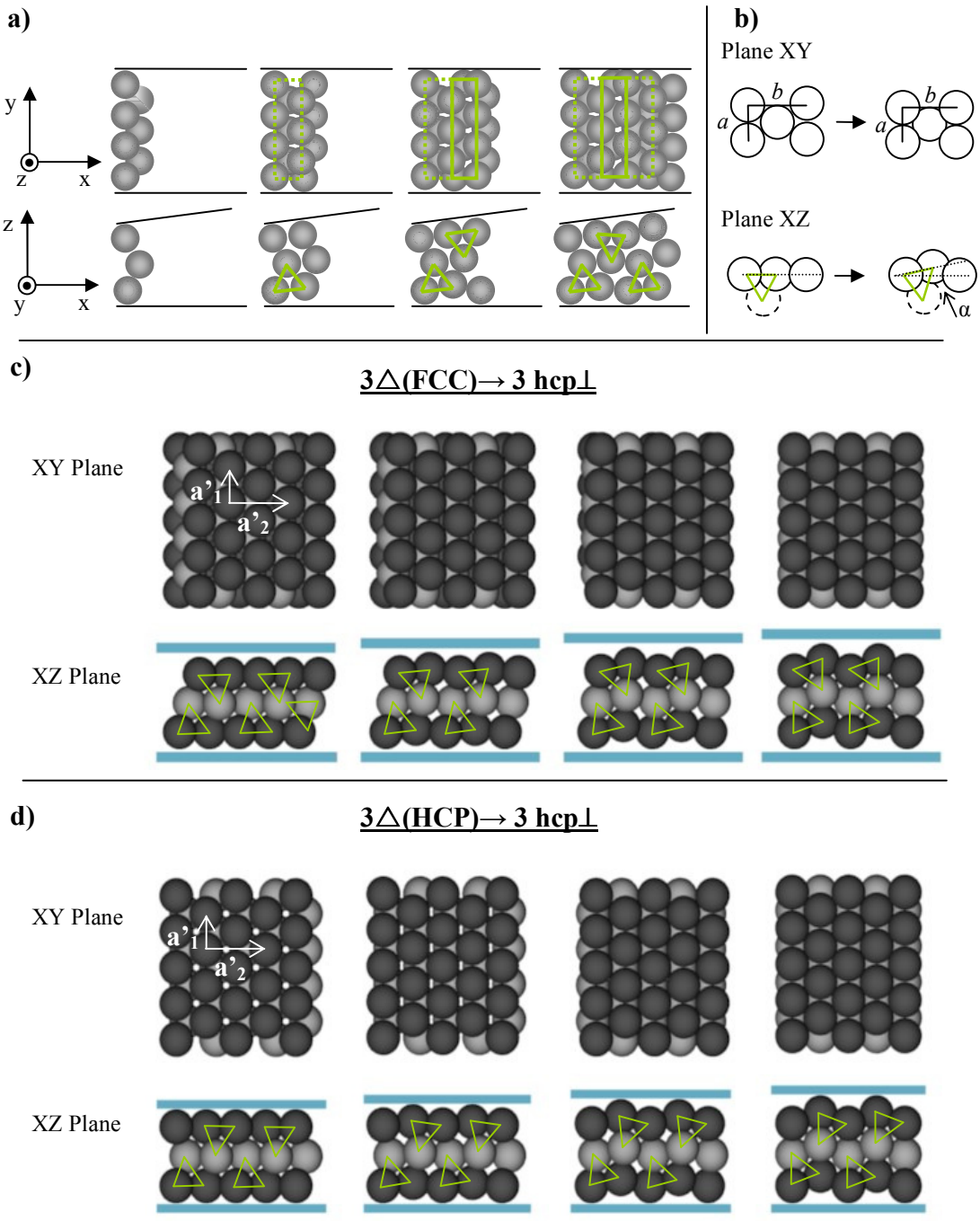

FIG. 66: Different schematic representation for the proposed model for the n△→ n-hcp⊥ transition. As example I chose the case n = 3. For details see text.

Now we have to establish the relation between the length of longer side of the rectangular unit cell and the distance between the confining walls. For that, we have to take into account that in principle all the possible stackings for the n△ structure could give rise to the n-hcp⊥ structure. This assumption comes from the experimental results where there are no evidences of any preferred stacking sequence in the n△ phase in the transformation to the n-hcp⊥ structure. Because of that I have developed two different structural models for the two different stacking sequences in the 3△ phase ($3\triangle_{fcc}$ and $3\triangle_{hcp}$ structures). Both transformations are schematized in Fig.66 where the initial, final and two intermediate steps have been drawn. To visualize how the transformation takes place it is convenient to remember the crystal growth process. This is schematized in Fig.66a). At the beginning of the transformation, still in the 3△ phase, the boundary of the crystal at the solid/fluid interface is made of only some particles. Next particles contributing to the crystal growth will be placed following the assumption of maximum packing efficiency but taking into account that now the particles will find a little bit more space in z direction. I modelled this situation with free software for 3D animation (Blender). Starting from the interface I placed next row of particles a little bit higher with the constriction of maximum contact surface for any packing of the spheres. As a result I obtained a structural transition consisting in a distribution of triangular prisms. In Fig.66, the projection in both, the xy as well as xz planes have been marked in green for clarity. Each of these prisms is in contact with its neighbours and show different orientations respect to the cell plates depending on H and on the original stacking sequence.

The former construction helps in finding a way to obtain a mathematical expression for both, the volume fraction and cell height variation for the complete structural transformation at any n. For that, the crystal growth process in the wedge cell for this transition has been considered analogue to the process where, as H increases, the prisms conforming the 3△ phase rotate along a given direction. In Figs.66 c) and d) I have represented four steps of the two possible 3△→ 3-hcp⊥ transitions. First, the triangular prisms in the 3△ phase are identified (in green). Depending on the stacking sequence (and also on the number of layers) these prisms will rotate clockwise or anti-clockwise along the axis defined by one of the rows of the prism. In particular, for the $3\triangle_{FCC}$ structure the prisms will rotate anticlockwise around the crystallographic direction $[1\bar{1}0]$ whereas in the $3\triangle_{HCP}$ structure the prisms will rotate alternated, clockwise or anticlockwise, around the same crystallographic plane [210]. When the 3-hcp⊥ structure is formed, the prisms are perfectly packed

between them again. Similar prism identification and transformations can be obtained for higher number of layers.

Once we have modelled the structural transformation it is possible to establish a relation between the height of the cell and the rotation angle of the prisms, α. For that we can build a pyramid similar as in the case of the buckling phase (Chapter 2). This time the height of one of its sides it corresponds to the width of one of the sides of the triangular prisms. Using the limiting values of b/a for the 2D-unit cell, the limiting rotation angles for the prisms are obtained. These angles are 0 rad for the n△ phase and arctg$\left(\sqrt{2}/4\right)$ rad for the n-hcp⊥ structure. From that geometrical construction we can also obtain the final expression for H which depends on the number of layers as well as the rotation angle α as shows equation 8.1. From that, by choosing a convenient section of the crystal the volume fraction variation is deduced. Therefore the volume fraction is also function of α and n as can be seen in Equation 8.2.

$$H(\alpha,n)=\sigma\cdot\left((n-1)\cdot\left(\frac{\sqrt{3}}{6}sin\alpha+\sqrt{\frac{2}{3}}cos\alpha\right)+\frac{\sqrt{3}}{2}sin\alpha+1\right) \tag{8.1}$$

$$\Phi(\alpha,n)=\frac{\pi}{3}\frac{n}{\sqrt{3}cos\alpha\left((n-1)\left(\frac{\sqrt{3}}{6}sin\alpha+\sqrt{\frac{2}{3}}cos\alpha\right)+\frac{\sqrt{3}}{2}sin\alpha+1\right)} \tag{8.2}$$

For $0\le\alpha\le\text{arctg}\left(\frac{\sqrt{2}}{4}\right)\approx 0.34$

where σ is the particle diameter. The resulting curves are shown in red in Fig.67. In this parametric plot the phase behaviour of the crystal corresponds to the particular case of hard spheres subject to a high pressure. With this new result we are contributing to the original phase diagram calculated under the same physical conditions by Pansu et al. [Pan84]. Because of that I have maintained their calculations for the close packed structures n△ or n□ as H varies (dotted lines). Also the curves calculated by Neser for the square prism phase are shown (dashed line) as well as the points for the final square prism structure (white circles). The curves corresponding to the n△→ n-hcp⊥ transition are plotted in red whereas the values for the n-hcp⊥ structure are indicated by red squares.

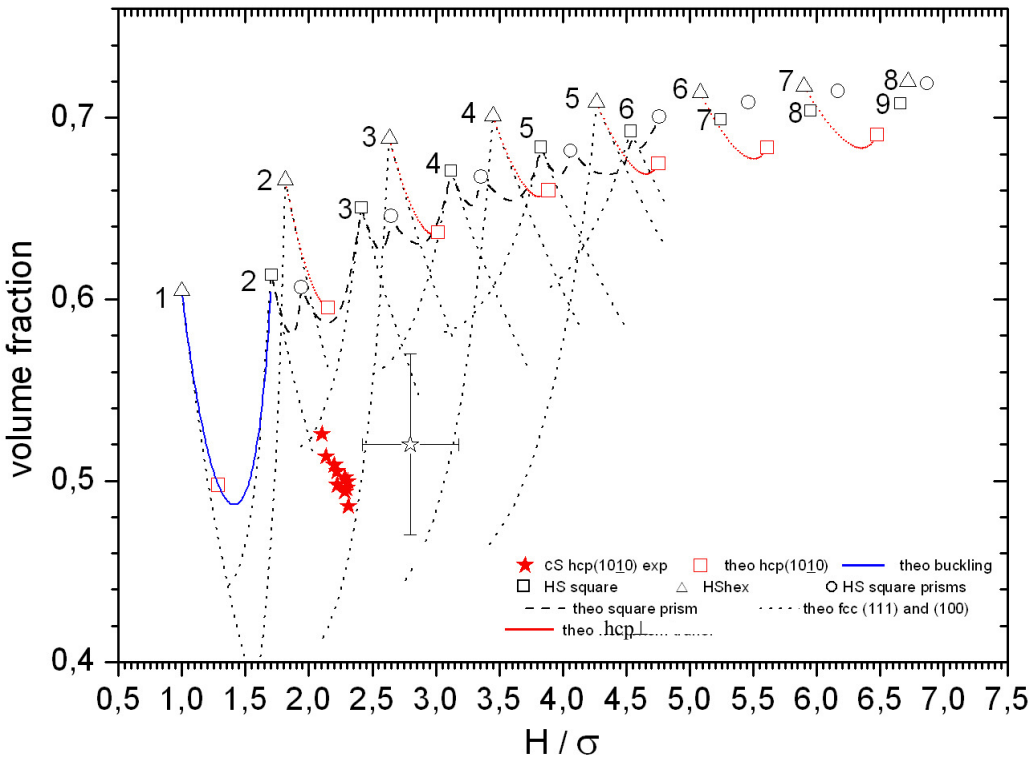

FIG.67: Volume fraction versus normalized cell thickness showing the hcp⊥ curves (in red) of the transformation together with former results. The red squares show the position in the phase diagram for the hcp⊥ structure. The former are the limiting values for such structure. For higher values of H new structures appears without any continuity relation with the hcp⊥ [Fon07].

In order to compare these curves with the experimental results some experimental data points (Φ, H) have been obtained for the 2△→ 2-hcp⊥ transition in the wet and the dry state. The error bars represent the data dispersion. In the experiments we obtained limiting ratios of b/a = 1.70 ± 0.01 close to the 2△ phase and b/a = 1.62 ± 0.01 for the 2-hcp⊥ structure. Accordingly, the volume fraction varied from Φ(2△) ≈ 0.53 to Φ(2-hcp⊥) ≈ 0.49. The height of the cell was obtained assuming that in the wet state the particles have a diameter a little bit higher than the real one. This extra volume was estimated from the experimental values of b/a. These experimental results differ from the model of hard spheres where, for the 2-hcp⊥ structure Φ ≈ 0.595 (b/a ≈ 1.633). In the dry state b/a(hcp⊥) = 1.65 ± 0.01 is close to the ideal value. For all suspended structures it was found that $\Phi < \Phi_{HS}$. The differences in the suspended and the dry states are due to the surface charge of the particles but the repulsive interaction is so weak that the crystal is mechanically stable under

evaporation. These experimental data are going to be used as a reference for the comparison between the density of the crystals coming from the experiments and from the models. That is, we will assume that the volume fraction difference in both cases is around 15% for all the structures.

In this plot also the curve for the buckling phase calculated by Pansu et al. [Pan84] is shown (continuous blue line). As a simple test, equations (8.1) and (8.2) where also used for the case n =1. The resulting curve exactly matches the volume fraction variation given by Pansu. This means that the proposed transition mechanism deals with the buckling phase as a particular case for the n△→n-hcp⊥ transition where there are not triangular prisms but planes of two rows rotating around an axis passing along one of them. Since the buckling phase mediates in the complete 1△ → 2□ transition, the maximum rotation angle is different. For this transition, $0 \leq \alpha \leq \arccos(1/\sqrt{3}) \approx 0.95$ rad. Because of that, I also plotted the data corresponding to a hypothetic 1-hcp⊥ structure. Considering these results, the buckling phase is clearly related to the n△→ n-hcp⊥ transition. Also from the diffraction patterns we can clearly see the similarities between both transitions at the same ratio of lengths for the units cells *b/a*. In Fig.68 three different Fourier micrographs of the 2△→ 2-hcp⊥ transition are shown. Picture 1 corresponds just to the beginning of the transition where secondary maxima are not visible yet. Picture 2 shows an intermediate step in the transition and finally picture 3 shows the diffraction pattern corresponding to the 2-hcp⊥ structure.

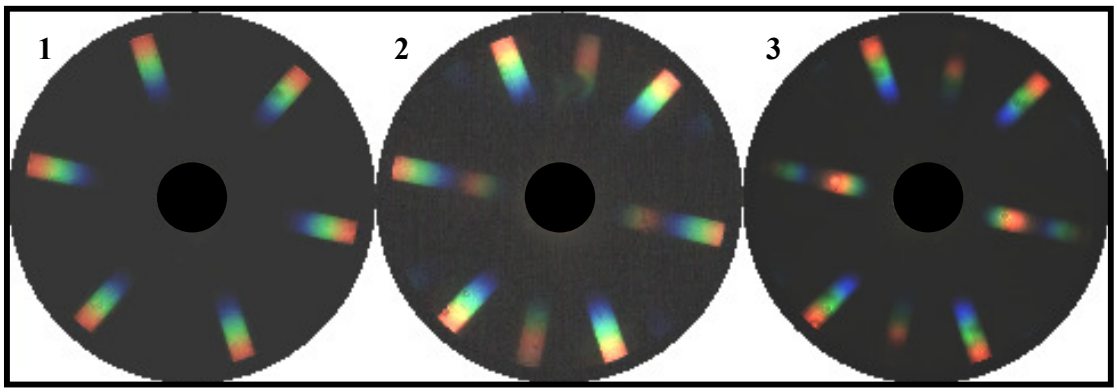

Fig.68: Fourier micrographs showing three different steps in the 2△→ 2-hcp⊥ transition. 1. Just after the 2△ phase. 2. An intermediate phase. 3. 2-hcp⊥ .In this sequence the intensity distribution variations is similar to that observed at the beginning of the buckling transition.

Despite the similarities found between both transitions, it is also important to remark the differences between them. For instance, the bucked phase completely mediates between the hexagonal and square structures whereas the n△ → (n+1)□ transition for n > 2 is not continuous and there more than one structure mediates in the transition. In particular, in this thesis no evidences have been found about any intermediate rectangular structure which mediates in the n-hcp⊥→ (n+1) □ transition (n > 2). On the contrary, an abrupt transition between the former structures has been always observed. This is just shown in the general view of the transition of Fig. 64. as well as in the SEM picture of Fig.69 which shows the transition for n = 2. In this picture we can see that the length of the longer side of the 2D- rectangular unit cell varies very fast with H whereas for H smaller this variation is really slow. It is interesting to observe there that despite the fact that the structures are separated by a grain boundary a possible retention of orientation is maintained in the transition to the (n+1) □ structure.

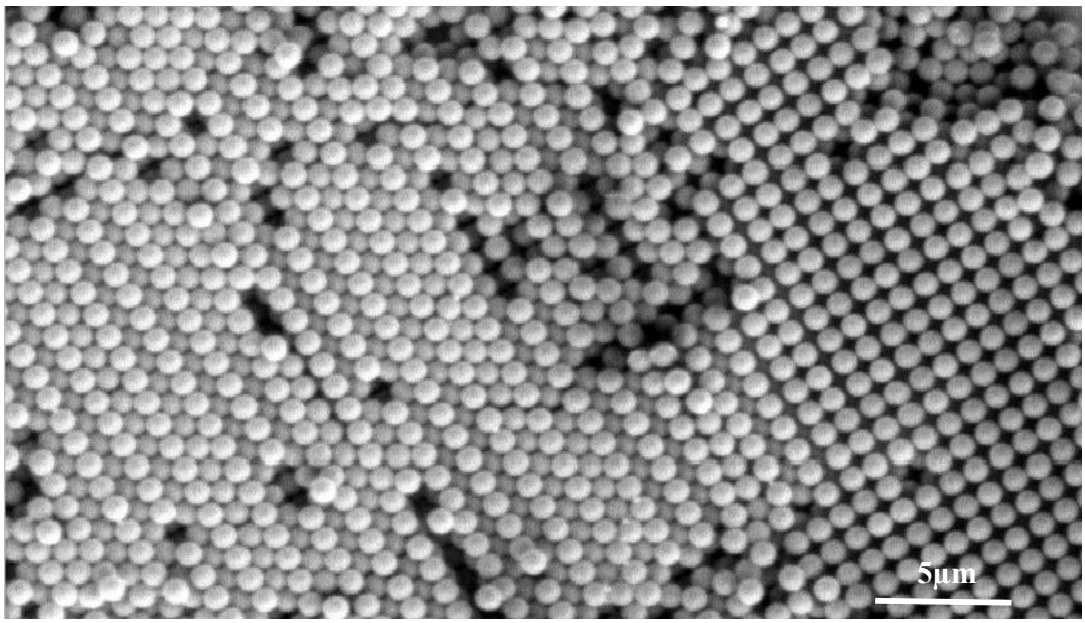

FIG.69: SEM picture showing the abrupt transition between the n-hcp⊥ and (n+1)□ structures. Both structures are separated by a grain boundary as can be observed clearly in Fig. 64.

The hcp⊥ has been studied simultaneously by Ramiro-Manzano et. al [Ram07] showing an alternative transition mechanism for the n△ → (n+1)□ transition via what they call the hcp⊥-like mechanism. This mechanism is very similar to that proposed here for the n△→ n hcp⊥ transition

and is based in rotation of particle rows. However they found a continuous transformation mechanism for the n-hcp⊥ → (n+1)□ transition. They argue that, for H increasing, after the hcp⊥ structure has been formed, the particle rows will continue following the same mechanism until the (n+1)□ is formed. As we already said we never observed such transition but an abrupt change where the structures are clearly separated by a grain boundary. Due to the fact that in [Ram07] does not appear any picture showing the intermediate structure n-hcp⊥-like before the formation of the new (n+1)□ structure, we think that the sequence observed by them should be the same as that observed in our experiments. Moreover in between the n-hcp⊥ and the n□ structures we have observed other intermediate structure which will be described in section 8.2.4.

8.2.3 The hexagonal prism structure

The first references about the hexagonal prism structure, n-$\mathcal{P}_{\triangle}$ are found in the PhD of S. Neser [Nes98]. He observed those particles arrangements and also proposed a model for a hypothetical n△ → (n+1)△ transition where the transformation would took place via these intermediate n-$\mathcal{P}_{\triangle}$ structures. In 2006, Fortini et al. reported a phase diagram of hard spheres in confinement coming from theory and simulations where this structure appears as one of the stable phases [For06]. Also in experiments where a confined suspension of PMMA spheres is subject to large oscillatory shear, hexagonal prism structures have been observed [Coh04]. In our case, the hexagonal prism phase appears together with the n-hcp⊥ structure as another possible structural transformation in equilibrium from the preceding n△ phase when the distance between the confining walls increases. This structure also remains practically unalterated upon drying. This fact permits the observation of the hexagonal prism structure with the SEM as shows the pictures in Fig.70. The n-$\mathcal{P}_{\triangle}$ phase can be visualized splitting up the hexagonal structure in triangular prisms and shifting them along z direction. The side of the prisms which are oriented parallel to the cell plates present hexagonal symmetry and their width depends on the number of layers n; the higher the number of layers is, the wider the prism sides are. For instance, as shows the pictures a) and b) for three layers the width of the prism will have three rows of particles. Each of the prisms is close packed and

maintains the same height as the preceding hexagonal structure. However the structure is not close-packed as can be seen in the same picture.

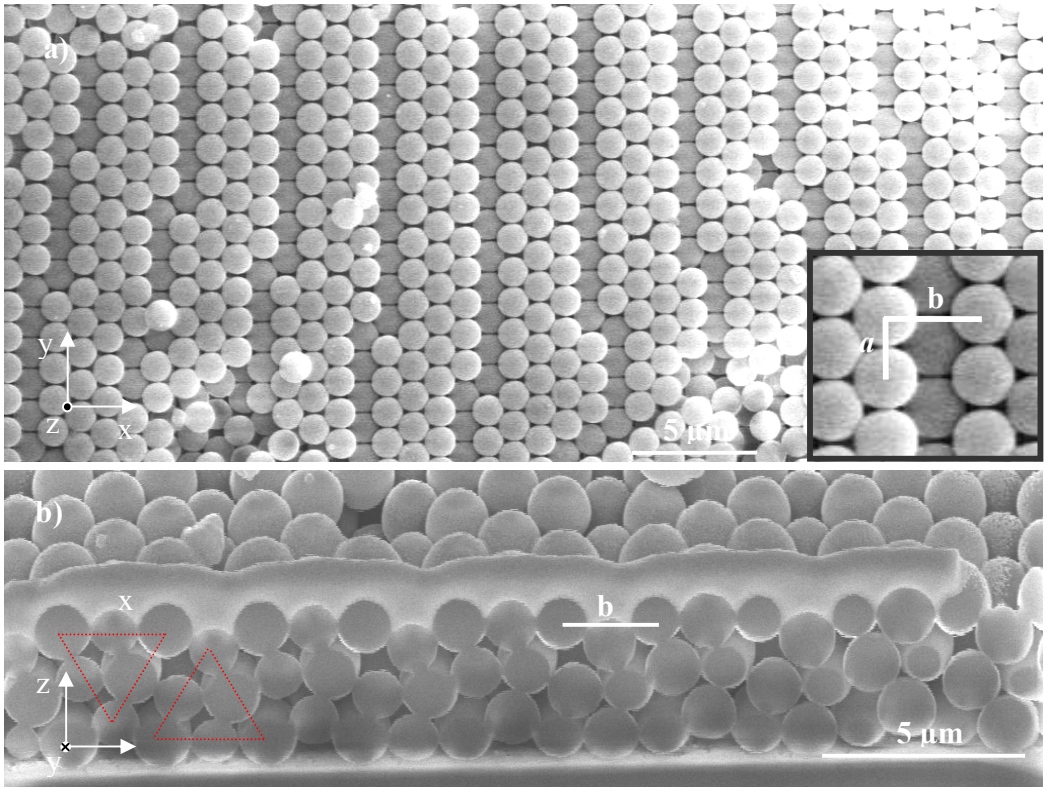

Figure 70: SEM pictures showing the dry 3-$\mathcal{P}_{\triangle}$ (ABA) structure for three layers. a) Top view of the structure. The inset shows the lengths of the rectangular 2D-cell which defines the prism separation. The length b decreases as H increases whereas a remains constant during the structural transformation. b) Lateral cut showing the ABA stacking of the particles which conforms the prism.

Unlike the n-hcp⊥ transition, the n-$\mathcal{P}_{\triangle}$ phase can present as many configurations as initial stacking possibilities have the preceding n△ phase, i.e., during the transition, the prisms will maintain the initial stacking sequence. The diversity of n-$\mathcal{P}_{\triangle}$ structures in the transition will also depend on the number of layers. In Fig.70b) the transversal cut along the xz plane shows the ABA stacking sequence of a 3-$\mathcal{P}_{\triangle}$ structure. On the other hand, the lateral sides of the prisms coming from different n-$\mathcal{P}_{\triangle}$ structures will present a particular symmetry. Consequently it is not possible to generalize about the packing between the prisms.

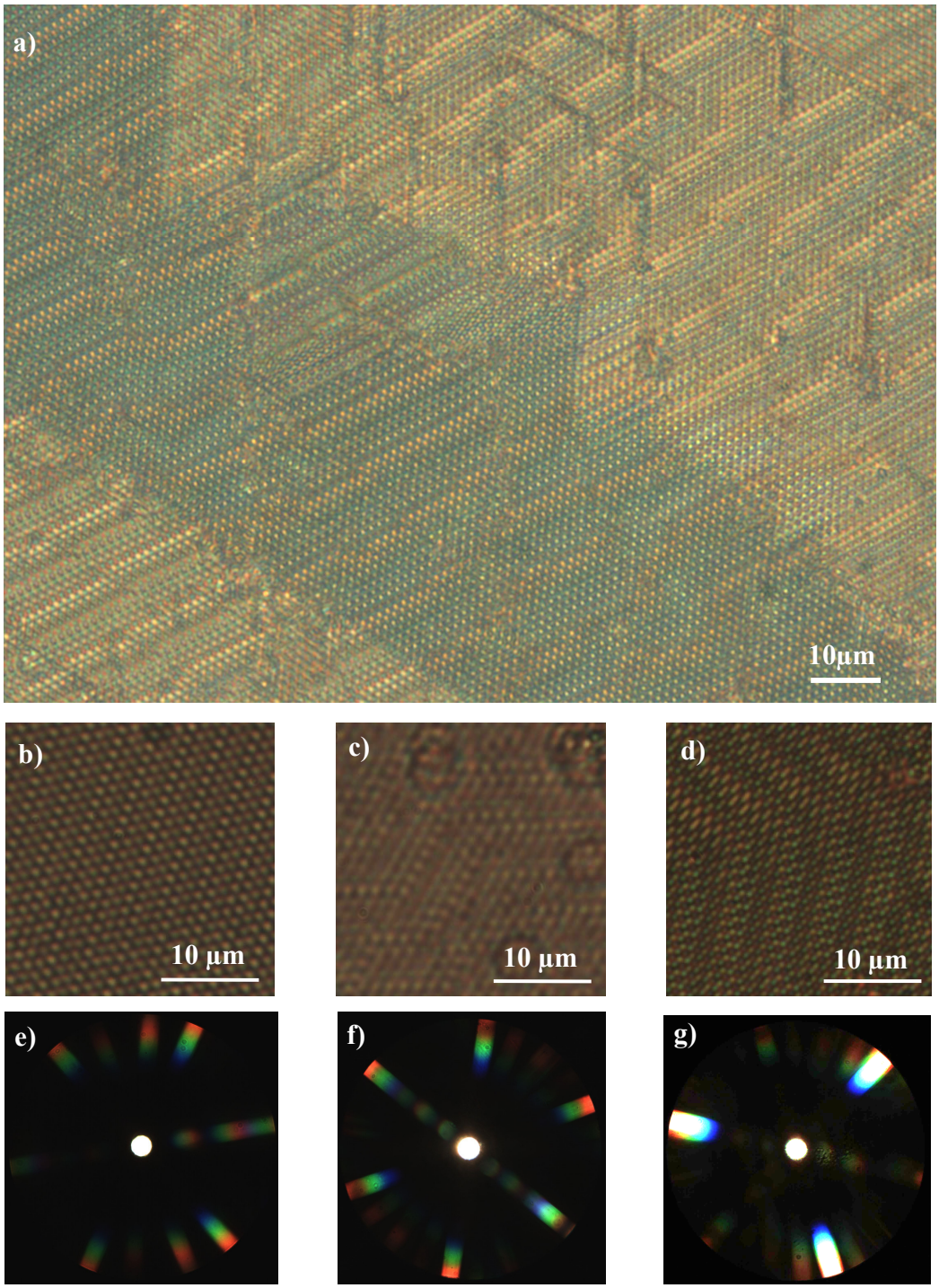

FIG 71: The hexagonal prism phase for different number of layers. a) 4-$\mathscr{P}_{\triangle}$. The three different regions corresponding to three different hexagonal stacking sequences from the original 4△ phase. b) 2-$\mathscr{P}_{\triangle}$ structure. c) 3$\mathscr{P}_{\triangle^{ABA}}$ structure. d) 3-$\mathscr{P}_{\triangle^{ABC}}$ structure. e) - g) Corresponding diffraction patterns for the structures appearing in pictures b), c) and d) respectively.

In Fig.71 different hexagonal prism structures in suspension and three representative diffraction patterns are shown. Fig.71a) shows a general view of the 4-$\mathcal{P}_{\triangle}$ transition. Since there are three different possible packing sequences in the 4$\triangle$ phase it is possible to observe three different prism structures. Fig.71b) shows the only possibility for the 2-$\mathcal{P}_{\triangle}$ structures. Figs.71 c) and d) are the two 3-$\mathcal{P}_{\triangle}$ possible configurations corresponding to the hexagonal ABA and ABC stackings respectively. In these pictures it is possible to see how the width of the prism increases with the number of layers. In Figs. 71 e) – g) the corresponding diffraction patterns of Figs. 71 b) - d) are shown. In Fig. 71 g) we had to oversaturate the picture in order to appreciate the secondary maxima which are too weak. The hexagonal stacking of the prisms is recognisable in these diffraction patterns, being possible to distinguish the characteristic six-fld symmetry of the ABA stacking (Fig. 71 f)) or the three-fold symmetry corresponding to the ABC stacking (Fig.71 g)). In general these diffraction patterns have *fan* appearance being more intense the maxima corresponding to the hexagonal symmetry of the prisms.

From these experimental observations we can also explain the n$\triangle\rightarrow$ n-$\mathcal{P}_{\triangle}$ transition using a model of hard spheres in the high pressure limit. This transition presents two fundamental differences with respect to the n$\triangle\rightarrow$ n-hcp$\perp$ transition. The first one is that the n-$\mathcal{P}_{\triangle}$ phase is present from the beginning of the transformation, i.e., the prisms can be observed from the beginning of the transformation. Only the relative position between the prisms is different. The second difference it was already mentioned: the n-$\mathcal{P}_{\triangle}$ is not a close packed structure but rather as close packed building blocks. In terms of modelling the structural transition this means that the final structure can be only determined from experimental observations.

Modelling all the possible n$\triangle\rightarrow$ n-$\mathcal{P}_{\triangle}$ transition is easy. In Fig.72b) the basic scheme is shown for two layers. Once the triangular prisms have been identified we define a line (dotted white lines) going from each of the external spheres of the prisms, to the closest external sphere belonging to the next prism. For the model I considered that as H increases some prisms remain at the same position and the others will move up in z direction with the constrainz of maximum packing efficiency. This is analogous to consider that the imaginary lines joining the prisms act like hinges where the rotation takes place around an axe parallel to the y-axe (in the drawing) which passes through the centre of each of the external spheres of the fixed prisms. By doing this, we can define a

rotation angle, β. This rotation angle is directly related with the separation between the prisms, *b* as well as with H. Thus by knowing the limiting values of that angle, it is possible to obtain an expression for the continuous height variation as well as volume fraction variation as a function of the rotation angle. This model is valid for any stacking sequence. This means that the resulting curves Φ-H does not depend on the symmetry of the prisms. This result coming from the model is supported by the experiments, where as shown in Figs. 64 and 71 different hexagonal prism structures with the same number of layers coexist at the same range of heights. In the wedge experiments this means that for particles having the same interaction energy, the particle number density at constant height of the different structures has to be the same or very similar.

In order to visualize the transformation model, in Fig.72c) four steps of the 3△→ 3-$\mathcal{P}_{\triangle}$ transition have been drawn taking into account both possible stacking sequences. Due to the hexagonal symmetry of the n△ phase the rotation axes can be parallel to any of the lattice vectors defined in Fig.72a). Because of that we observe in the resulting crystals this zig-zag patterns which can be seen in the pictures of Fig.71. The election of the crystalline system to prefer one or other direction for the transformation is probably due to the relative orientation of the crystal with respect to the direction of the height increment as in the case of the buckling phase. However, as we will see later in the proposed model, independently of the different possible packings and stacking sequences the volume fraction variation during the transition is the same for all the possible n-$\mathcal{P}_{\triangle}$ structures.

Once the transition model has been deduced, the expressions H(n,β) and Φ(n,β) can be obtained being these,

$$H(\beta,n)=\sigma\cdot\left((n-1)\sqrt{\frac{2}{3}}+\frac{\sqrt{3}}{2}sin\beta+1\right) \tag{8.3}$$

$$\Phi(\beta,n)=\frac{\pi}{6}\frac{n(n+1)}{\left((n-1)\frac{\sqrt{3}}{2}sin\beta+\sqrt{3}cos\beta\right)\left((n-1)\sqrt{\frac{2}{3}}+\frac{\sqrt{3}}{2}sin\beta+1\right)} \tag{8.4}$$

where σ is the particle diameter.

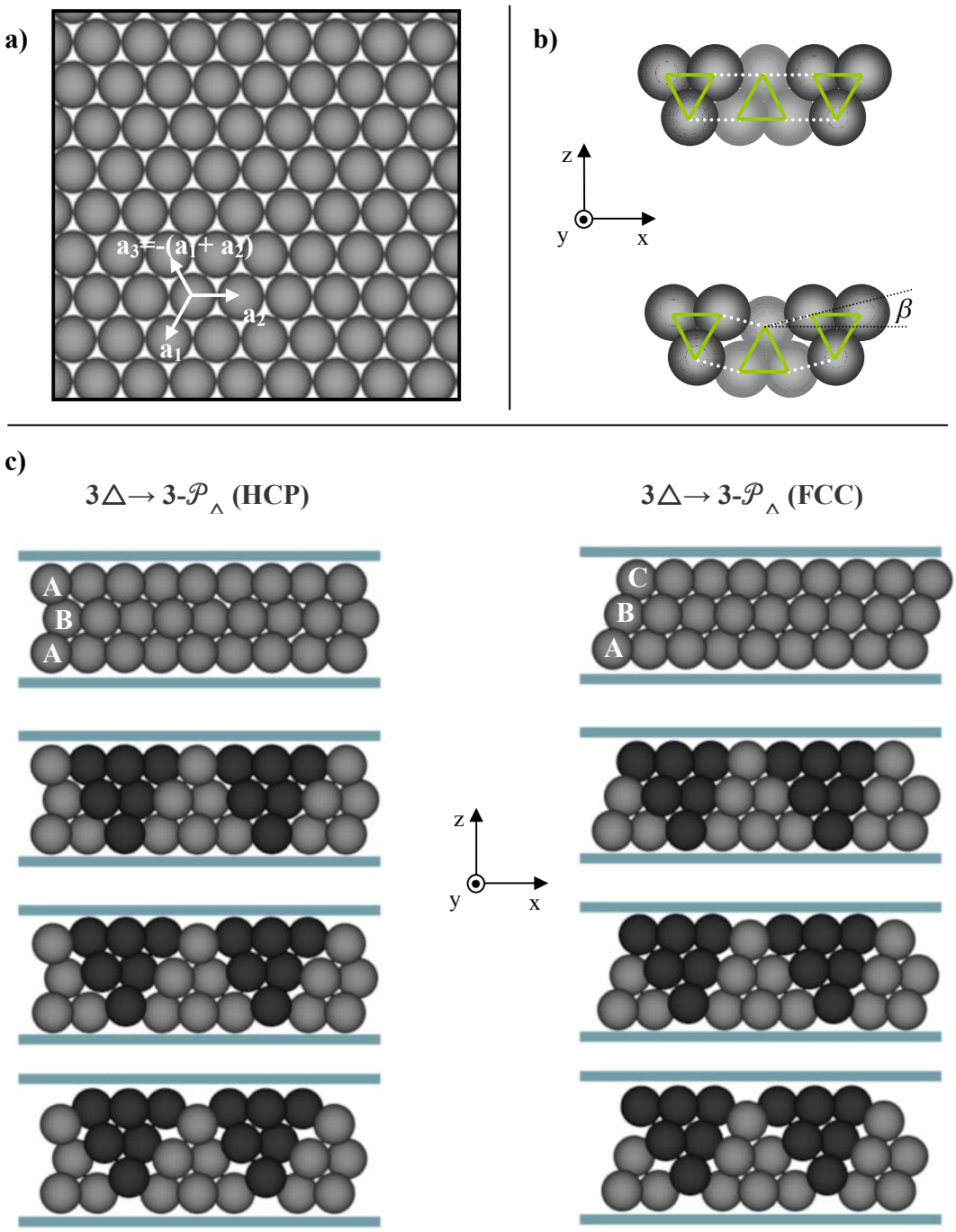

Figure 72: Scheme showing the transformation model for the n-$\mathcal{P}_{\triangle}$ phase in the case of three layers and therefore showing the two possible transformations coming from the two possible preceding 3△ structures.

Since the final configuration for such transformation is not a close packed structure, we have to establish an upper limit for the rotation angle. This maximum angle is obtained from the experimental observations. As in the hcp⊥ case, there is not a continuous transition n△ → (n+1)□ via the n-$\mathcal{P}_{\triangle}$ phase finding only a smooth transformation between the n △ and n $\mathcal{P}_{\triangle}$ structures. Furthermore, the n-$\mathcal{P}_{\triangle}$ and n-hcp⊥ structures coexist along all the transition and until the next structure in the sequence is observed. As it was already mentioned, n-hcp⊥ and n-$\mathcal{P}_{\triangle}$ structures are separated from the new structure by a grain boundary. Because of that I have established that the maximum height allowed for the n-hcp⊥ structure should be the same as for the n-$\mathcal{P}_{\triangle}$ structure. So, from H_{max}(n-hcp⊥) = H_{max}(n-$\mathcal{P}_{\triangle}$) we can obtain the maximum rotation angle β that we have defined to characterize the slicing between prisms. From that relation using eq. (8.1) and (8.3) we obtain that.

$$\beta_{max}(n) = \arcsin\left[\frac{2\sqrt{3}}{3}\left[(n-1)\left(\frac{\sqrt{3}}{6}\sin(\alpha_{max}) + \sqrt{\frac{2}{3}}(\cos(\alpha_{max}) - 1\right) + \frac{\sqrt{3}}{2}\sin(\alpha_{max})\right]\right] \qquad (8.5)$$

being α_{max}=arctg$\left(\sqrt{2}/4\right)$ the maximum rotation angle obtained for the hcp⊥ structure. The minimum value for the angle is zero. As we see, β_{max} will depend on the number of layers. It is easy to check in the structural building model that the distance between the prisms *b*, will diminish as n increases. This is also observed in the experiments. In Fig.73 two different prism structures, 3-$\mathcal{P}_{\triangle}$ and 4-$\mathcal{P}_{\triangle}$ are shown. In them the distance *b* is clearly smaller for 4 layers.

The curves coming from the data points (Φ,H) are plotted in the previous phase diagram (in green)in order to compare with the curves obtained for the n-hcp⊥ transition as is shown in Fig.74. We can see that for crystals with a low number of layers both the n-$\mathcal{P}_{\triangle}$ and n-hcp⊥ curves vary in a very similar way. Only for more than four layers we can appreciate significant differences between both curves. At the beginning of these intermediate phases both curves are identical. However at the end of the transition the volume fraction of the structures varies significantly. This means that at these heights, the n-$\mathcal{P}_{\triangle}$ phase will be more stable than the n-hcp⊥ phase. Nevertheless this is not what can be observed in the experiments where both structures are present for the same range of

distances independently of the number of layers. A possible explanation is found in the sequential nature of the crystal growth which takes place in these wedge cells. The structures are formed as the crystal is progressively growing from the cusp. For degenerate crystalline phases where more than one structure is stable, once one of the structures appears, the crystal will continue grow with this symmetry despite other structure are more energetically favourable. Since both intermediate phases are equally probable at the beginning of the transition and due to the growth process we will observe coexistence of both structures even for those cell heights where some are more favourable than others. In this sense the less stable structures could be considered metastable. On the contrary, for other cell geometries where the crystal formation process is different (with parallel plates for instance), probably only the most stable structures will appear.

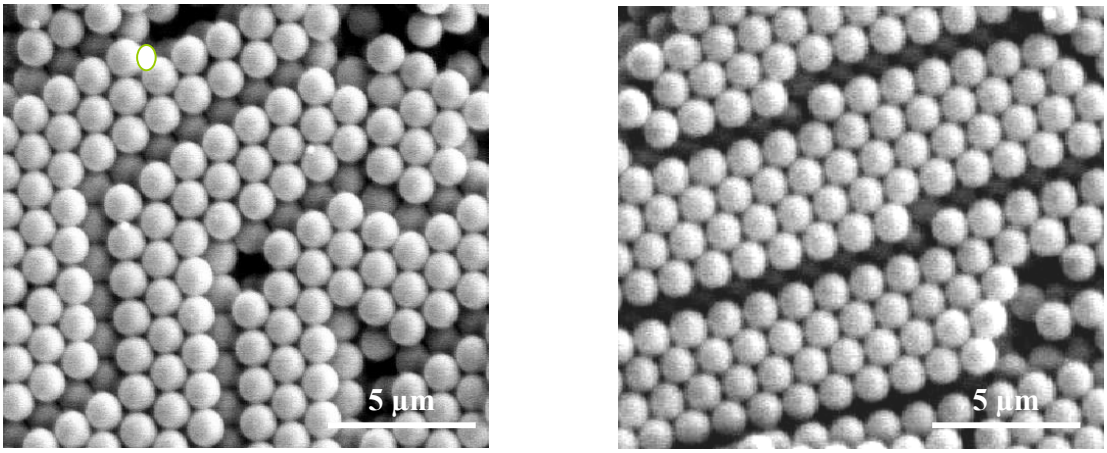

FIG.73: The minimum distance between equally oriented neighbour prisms reached decreases as the number of layers increases as can be seen in the comparison of the a) 3-$\mathcal{P}_{\triangle}$ and b)4-$\mathcal{P}_{\triangle}$.

Attending to the dependence of the width of the prism with the number of layers a prism structure in this transition would manifest just the width corresponding to n = 1. This does correspond just to the buckling structure. Because of that we could consider the beginning of the buckling as the 1-$\mathcal{P}_{\triangle}$ structure as it was already considered for the 1-hcp⊥ structured. I proceeded as in the former case and plotted the data coming for (8.3) and (8.4) with a different rotation angle in such a way that the transition finishes in H(2□). Again, the resulting curve perfectly fits the buckling transition curve calculated by Pansu.

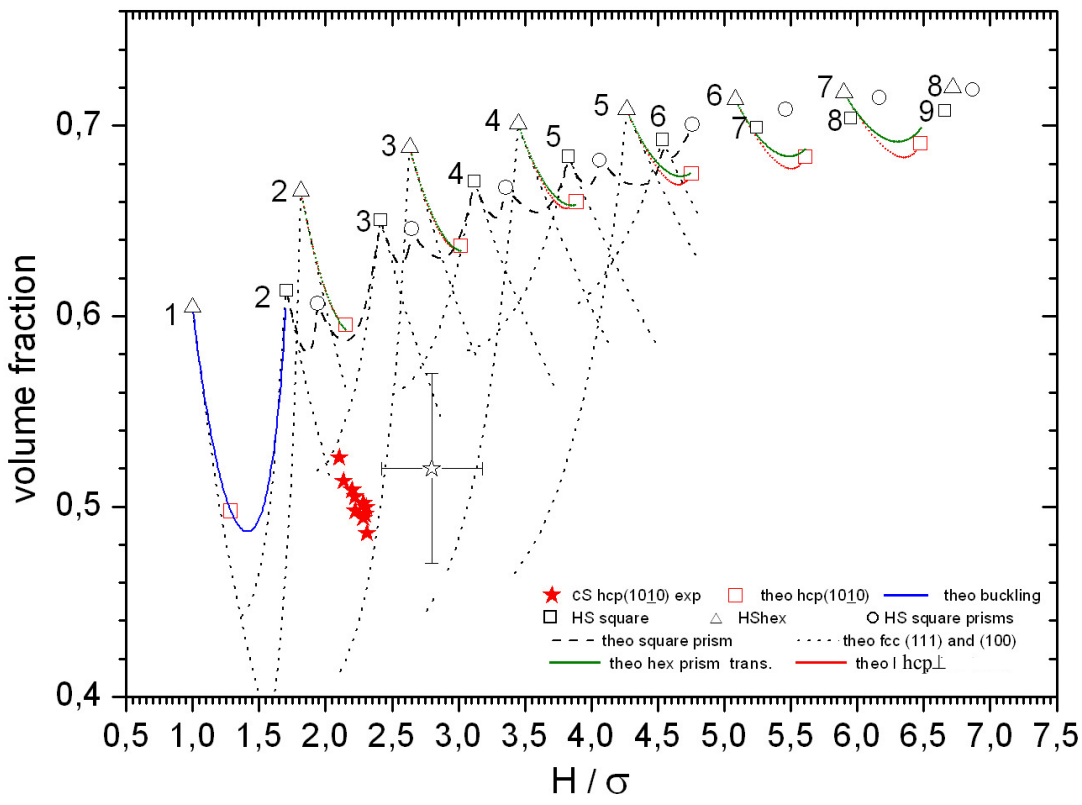

FIG.74: *Volume fraction versus normalized cell thickness showing the hcp⊥ curves (in red) and 3-$\mathcal{P}_{\triangle}$ (in green) of the transformation together with former results.*

With the models here proposed it is easy to see that there is direct connection between the buckling phase and the n△ →n-hcp⊥ /n-$\mathcal{P}_{\triangle}$, as one could expect intuitively. For n =1 the transition is quite simple since the number of layers goes from one to two. However, once the number of layers increases the resulting structures are more complex as well as the structural transition. In a way analogous to that for the 1-hcp⊥ transformation, this will be only valid until the volume fraction of the buckling phase is the same that would correspond to the 1-$\mathcal{P}_{\triangle}$ structure. In conclusion, the 1-$\mathcal{P}_{\triangle}$ and the 1-hcp⊥ transitions are also included in the buckling transition up to H ≈ 1.29 σ .

8.2.4 Square prism structure, $\mathcal{P}_{\square}$-A

This structure have been observed in the n△ → (n+1)□ transition only for n = 2 and n = 3. It is found after the n-hcp⊥ and the n-$\mathcal{P}_{\triangle}$ phases. The square prism phase, n-$\mathcal{P}_{\square}$-A consists of triangular prism structures with one of their sides having square symmetry. We use the letter A to distinguish it from the other square prism phase (n-$\mathcal{P}_{\square}$-B) which was already introduced in Chapter 3 and appears in the n□ → n△ transition. The n-$\mathcal{P}_{\square}$-A structure is formed by prismatic building blocks of constant size independently of the transition (n = 2 or n = 3) and it is not a close packed structure. The structure can be distinguished in Fig. 64 after the grain boundary. Also different pictures are shown in Fig.75. Picture a) does correspond to the beginning of the 2-$\mathcal{P}_{\square}$-A structure, where we see again that there is no continuous structural transformation between the n-hcp⊥ or the n-$\mathcal{P}_{\triangle}$ structures and the n-$\mathcal{P}_{\square}$-A structure, being these separated by a grain boundary. In picture b) also for n = 2 the suspended structure is shown. Here, polystyrene particles of 2.5 µm in diameter where used. Finally, picture c) shows the 2-$\mathcal{P}_{\square}$-A structure after evaporation. From the former image we can consider that this structure also remain practically unaltered after drying.

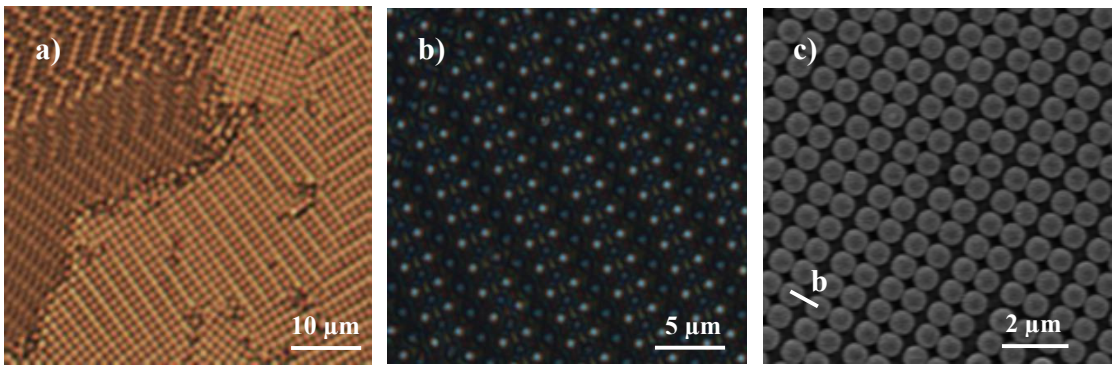

FIG. 75: The prism structure 2-$\mathcal{P}_{\square}$-A. a) Beginning of the transition after the 2-hcp⊥ structures. The crystalline phases are separated by a grain boundary. b) Wet state for polystyrene particles of 2.5 µm in diameter. b) Dry state for polystyrene particles of 1.1 µm in diameter.

The distance between equally oriented prisms, defined by the length *b* (indicated in Fig.75c)), is maximum at the beginning of the transition. At the same time, the ratio between the prism separation *b* and the minimum particle length *a* inside the prism, is very small and in the crystalline suspension ($b/a \approx 1.2 \pm 0.2$). In fact, in most of the samples it is difficult to recognise the structure in the dry sate using the Scanning Electron Microscope. However with the optical microscope the diffraction effects coming from the particles indicate that we have something different than the square structure.

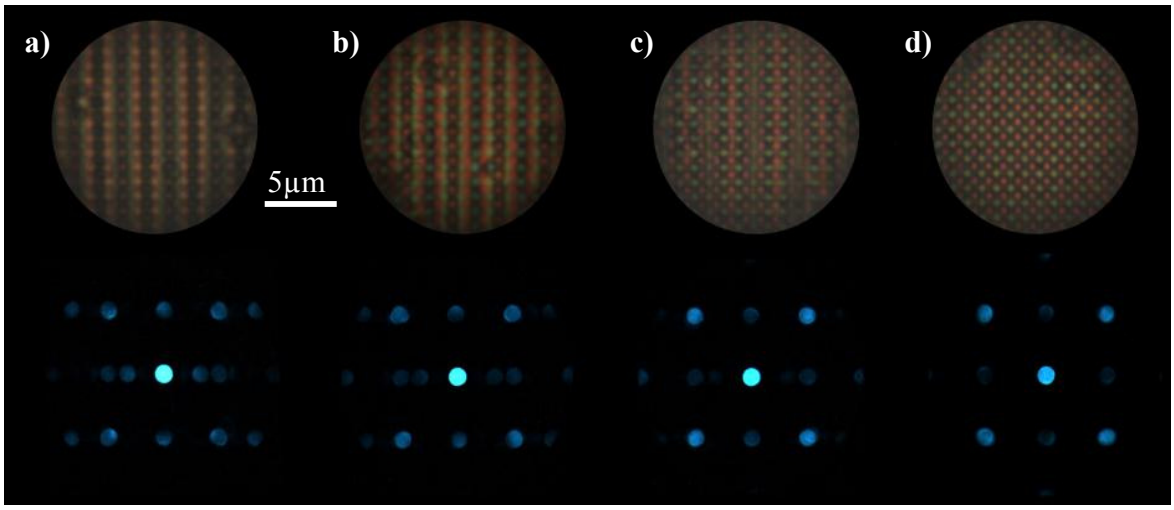

FIG. 76: Real and reciprocal space images of the 2$\mathcal{P}_{\square}$-A transition. a) The structure just after the grain boundary. b) and c) Intermediate steps in the structural transformation. d) 3□ structure.

In the experiments it was observed that, as the cell thickness increases the prisms are progressively closer until the (n+1)□ structure is formed. This transition is shown in Fig.76 for the 2-$\mathcal{P}_{\square}$-A→3□ transition in real as well as reciprocal space. We ca clearly see that as the prisms come closer the intensity maxima distribution looses the information corresponding to the prismatic symmetry giving rise to the well known square reciprocal lattice. The region where this phase appears is very narrow (100 μm at mos) especially if we compare it with the extension of the n-hcp⊥ and the n-$\mathcal{P}_{\triangle}$ phases (about 1mm as maximum observed).

The building model for these structures starts with a bottom layer where the rows of particles are placed alternatively at distances *a* and *b* as shows Fig.77a). The next layer of particles is placed

in such a way that the contact surface between the spheres is maximum. The third and four sublayers are formed following the same criteria. For n = 3 the result is a set of triangular prisms shows Fig.77 c). From that structure, by adding now a fourth layer with the particles sitting in the most stable positions, we find the structure as shown in Fig.77d). The side view indicates that now also rhombohedric prisms have been formed. On the other hand, the top view of this structure (xy – plane) is characterized by equally spaced rows. This kind of arrangement has been however, observed for n = 3 too as can be seen for instance in Fig 64. This suggests the possibility of building the 3-$\mathcal{P}_{\square}$-A structure model from layers 2, 3, 4 (Fig.77d)) instead of using layers 1, 2, 3. In both cases the volume fraction is the same.

We propose here a model for the n-$\mathcal{P}_{\square}$-A→(n+1)□ transition which is illustrated also in Fig.77. The model is based in the experimental observations following, as always, the maximum packing criteria. Independently of the final structure or the number of layers the equations for the volume fraction variation and hence the height of the cell variation are calculated in the same way being possible to obtain a generalized equations. In Fig.77b) the side view of two prisms has been drawn. Between them a row of particles A is placed on top. The separation *b* between the prisms can be associated with the rotation of row A around an axis passing along row B. This rotation is characterized by an angle γ. Once the structural transformation model has been parameterized we obtain that,

$$H(\gamma, n) = \sigma \cdot \left((n-3)\frac{\sqrt{2}}{2} + \frac{\sqrt{3}}{2}\sin\gamma + 1 \right) \tag{8.5}$$

$$\Phi(\gamma, n) = \frac{\pi}{3} \frac{(n-1)}{2\left((\sqrt{3}\cos\gamma + 1\right)\left((n-3)\frac{\sqrt{2}}{2} + \frac{\sqrt{3}}{2}\sin\gamma + 1 \right)} \tag{8.6}$$

where σ is the diameter of the spheres.

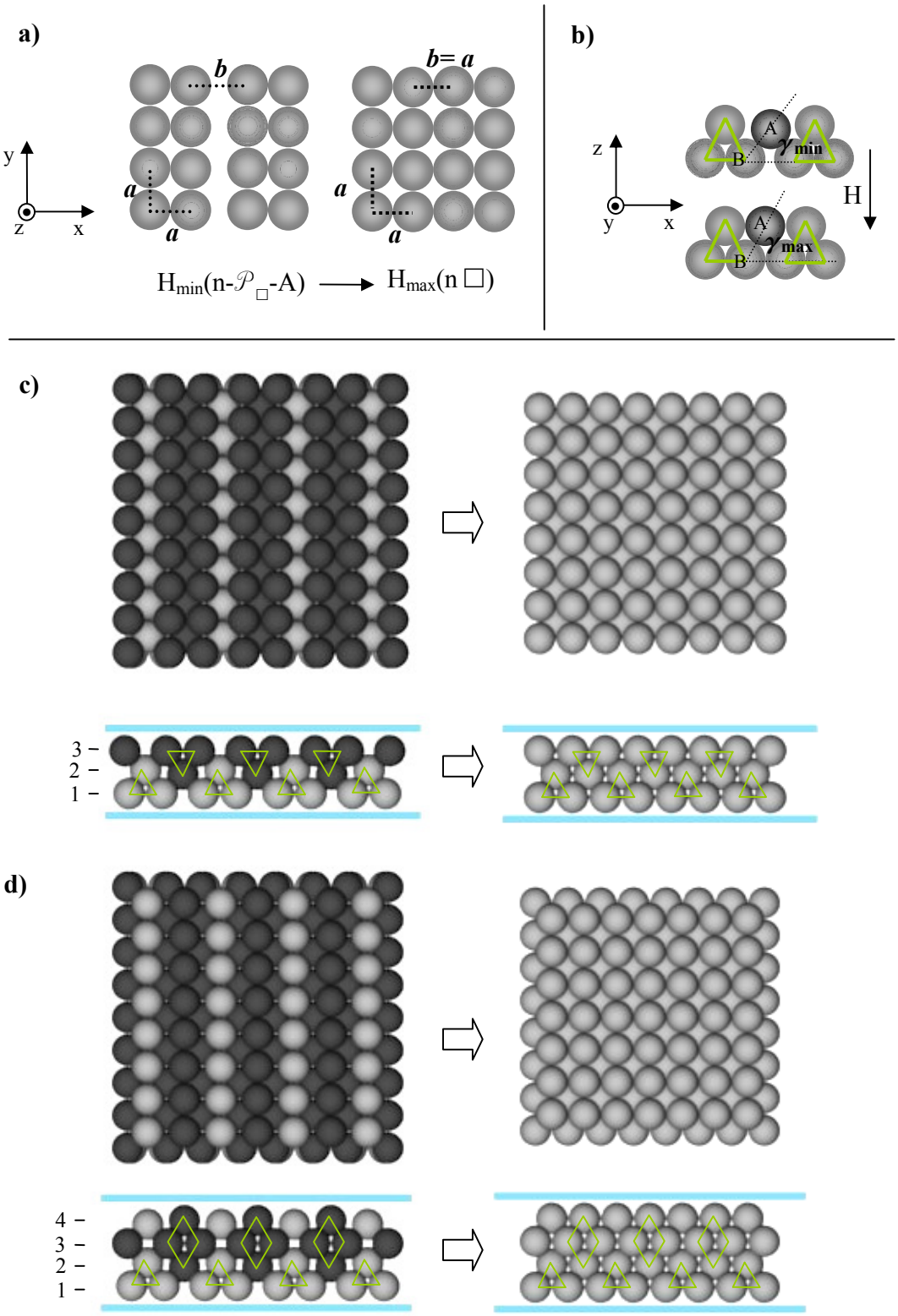

FIG.77: Transformation model proposed for the $3\mathcal{P}_{\square}$-A → 4□ transition. Only taking sublayers 1, 2 and 3 we can see also how the transformation $2\mathcal{P}_{\square}$-A → 3□ should be. For details see text.

As in former cases we have to establish the limiting values for this angle. The maximum value is easy to obtain by knowing the angle defined by the spheres in the n□ structure. This value is: $\gamma_{max} = \arcsin\left(\sqrt{2/3}\right)$. On the contrary, γ_{min} will depend on the number of layers. These values have been obtained from the experimental observation as well as former conditions imposed in the former models. In this case the minimum value for the angle comes from the condition: H_{max} (n-hcp⊥/n-$\mathcal{P}_{\triangle}$) = H_{min}(n-$\mathcal{P}_{\square}$-A). The resulting curves are shown in the plot of Fig.78 for n = 2 and n = 3. These two curves fit almost completely the Pansu et al. predictions for the square structure formation [Pan84] and for n =2 the curve perfectly fits in the 2□ → 3□ transition of the model proposed by Neser. It is a striking fact that, for the same heights, the volume fraction of the n-hcp⊥ and n-$\mathcal{P}_{\triangle}$structures is significantly higher than the corresponding in the n-$\mathcal{P}_{\square}$-A structure. But on the other hand, the slope of the n-$\mathcal{P}_{\square}$-A curves is very pronounced. In this case it is possible to argue from the model that these small height intervals in the phase diagram where Φ(n-$\mathcal{P}_{\square}$-A) < Φ(n-hcp⊥/n-$\mathcal{P}_{\triangle}$) will correspond to the grain boundary region.

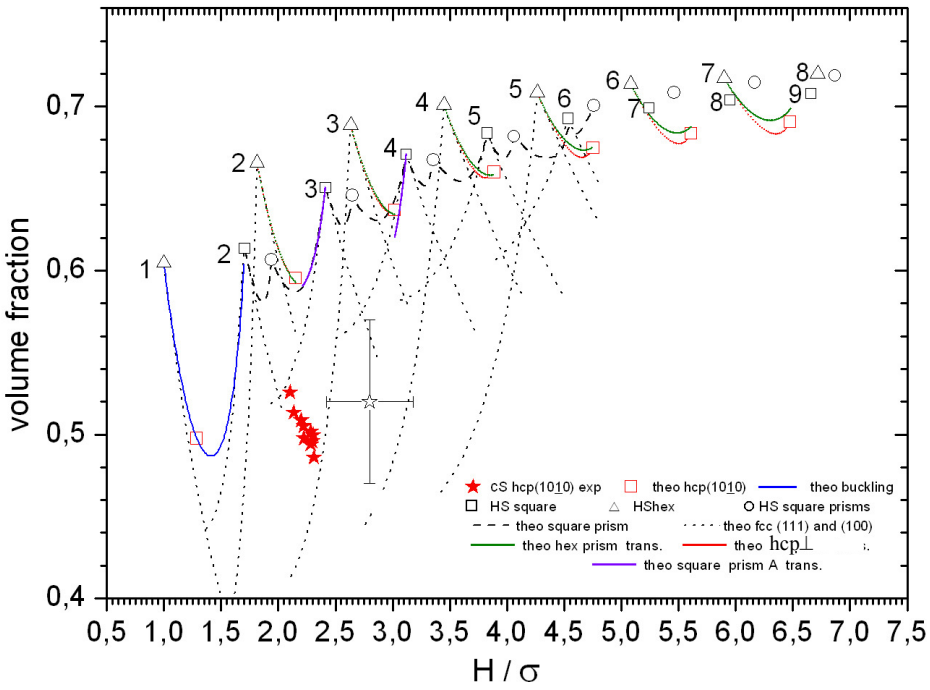

FIG.78: Phase diagram in the hard sphere limit showing all the structural transition models for the crystalline phases involved in the n△→ (n+1)□ transition.

8.3 The n□ → n△ transition

The n□ → n△ transition can be defined as the transition inside the structural sequence where the colloidal crystal does transform maintaining constant the number of layers. For two layers the transition has been already studied experimentally as well as theoretically as it was shown in Chapter 3. In this case the transition is completely mediated by the rhombic phase. As it is going to be shown, for higher number of layers the transformation mechanism is similar. A representative images of the n□ → n△ transition when n > 2 can be observed in Fig.79. In particular the transition does correspond to 4 layers and the increasing of the confining walls goes in diagonal from left to right as the white arrow indicates. In general at low magnifications this transition seems to be characterized by a series of nearly parallel stripes without any significant difference between them. At the same time, it is also possible to observe that the stripes can appear along different directions. At higher magnifications however the transition shows very interesting particle arrangements. As it is going to be shown along this section the n□ → n△ transition is highly degenerated being possible to observe different periodic structures at constant H and even aperiodic arrangements as shows the inset in Fig.79 where only at the top left corner a periodic structure is observed. The existence of aperiodic structures mediating in the structural transition is maybe one of the most important differences respect to the former structural transition[8]. At the beginning of the n△ → (n+1)□ transition we found two different phases in coexistence. After them for higher distances between the cell plates another phase can be observed which is precursor of the square structure. Each of these intermediate phases follows a different structural transformation mechanism. On the contrary, in the n□→n△ transition, the solid-solid transition follows a unique transformation mechanism which can give rise to many different structural configurations.

This section starts first with the description of the structural changes which take place in the n□→n△ transition. In that way, the basis underlying the transformation process and the factors which influence the formation of the different particle arrangements will help to understand some of the most representative intermediate structures found in the experiments. After that, once the

[8] Next chapter deals with exotic crystalline domains found at the beginning of the n△→ (n+1)□ transition. In these domains also aperiodic structures have been observed. However these structures are not considered as intermediates in the transition mechanism but rather isolated domains which appear at specific cell heights. Because of that the exotic structures are not included in the discussion about the different transitions mechanism found in the structural sequence.

different structures have been described, the section will be concluded presenting a model of hard spheres in the high-pressure limit to describe the complete n□→n△ transition.

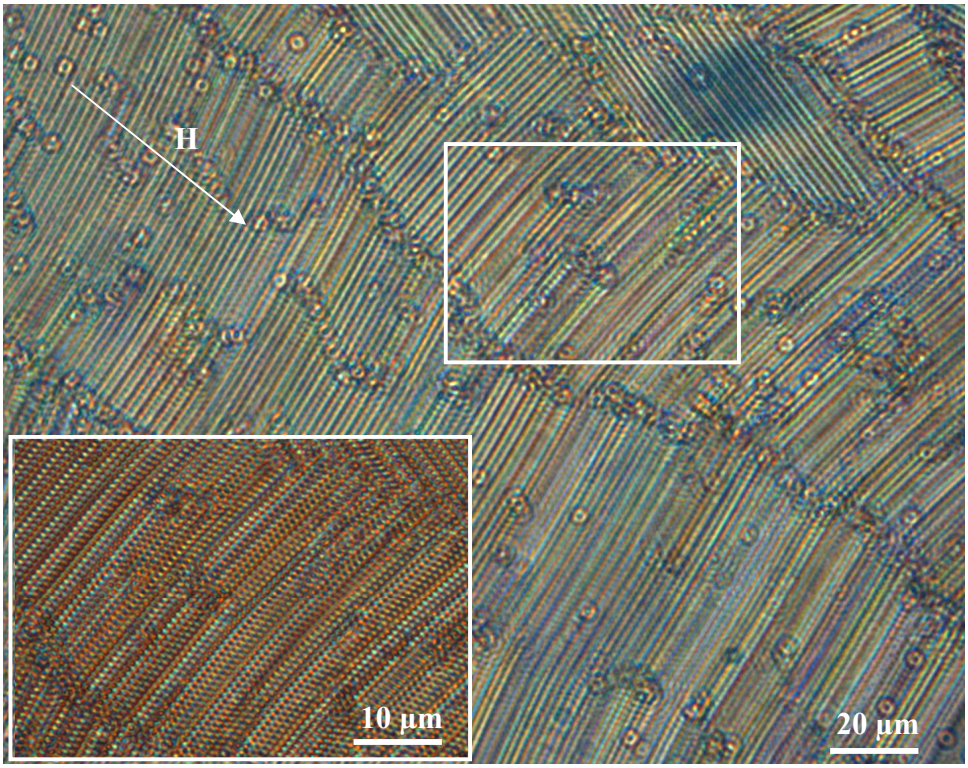

FIG.79: General view of the n□ → n△ transitions. In this case the picture does correspond to a four layers system. The inset shows a magnified picture of the region selected by a white square. At first glance we can say that the transition is characterized by a series of nearly parallel stripes.

The experimental observations show that when the distance between the plates of the cell increases the square structure slowly distorts. Due to the symmetry of the original crystalline phase, this deformation can take place along two different crystallographic directions. As we already said, the n□ structure can be considered as a *slice* of a FCC crystal with its (100) planes oriented parallel to the substrate. For each of those planes, the morphological changes can be characterized in a first outline by shifts between neighbouring rows along the [11] or [$1\,\bar{1}$] direction. These shifts give the transformation rhombohedric symmetry. The initial orientation of the n□ square domains respect to the direction of the height increment in the wedge cell, will determine the specific particle arrangements of the intermediate structures. That is, the rhombohedric transformation takes place along a specific direction. At the same time this direction will be also predetermined by the

preceding crystalline domains in the transition. This fact will condition the morphology of the intermediate structures that will appear during the structural transition. In Fig.80 two different regions of the 4□→4△ transition are shown. The pictures do correspond just to the beginning of the transition being still possible to observe the 4□ structure. If we take a look to the orientation of the square structure (inside the dotted rectangles) is easy to see that it distorts along the two crystallographic directions previously mentioned (white dotted lines). At the same time it is possible to observe different crystalline domains separated by grain boundaries. The orientations of the stripes belonging to different domains are different and not perpendicular between them (as indicate the black dotted lines). They are an indication of the previous orientations of the 4□ structure which was also forming different domains. The different orientations can give rise to different intermediated structures (but not necessarily). For instance, we see in Fig. 80a) that the left crystalline domain present a different stripe distribution than in the central crystalline domain (black arrows) whereas in Fig. 80b) independently of the orientation of the stripes the particle arrangement is the same.

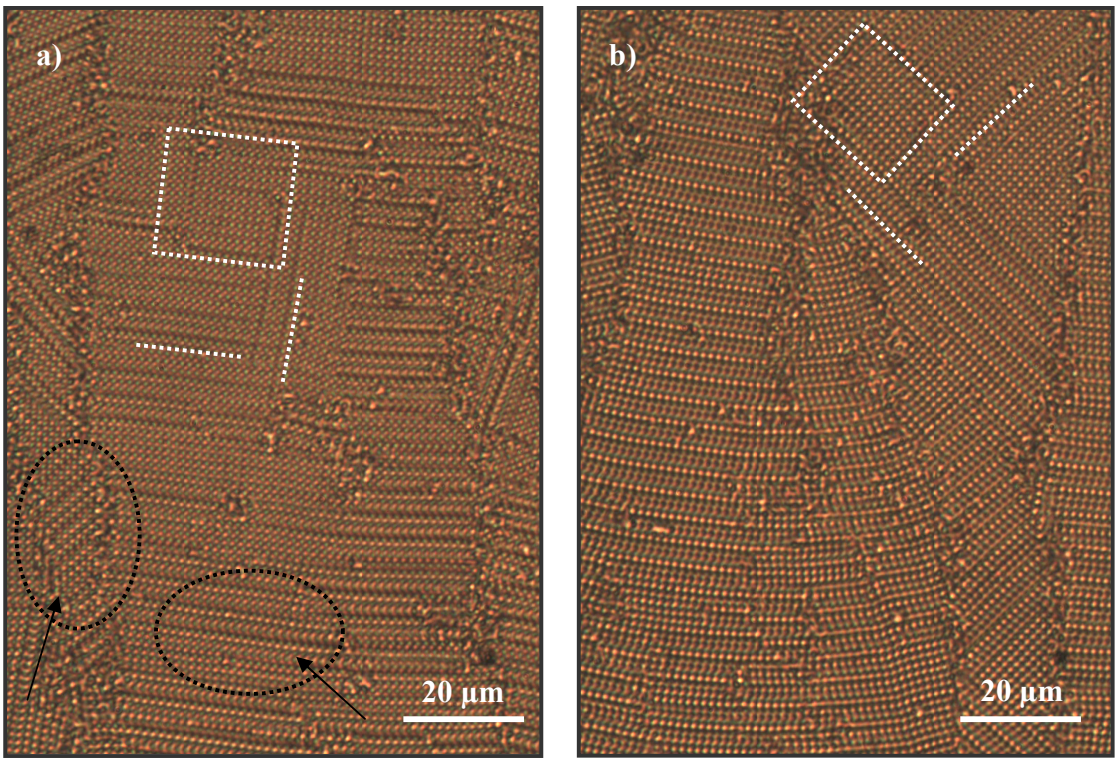

Fig. 80: Two different pictures showing the beginning of the 4□→4△ transition. The orientation of the 4□ structure respect to the crystal growth direction is one of the possible factors which will determine the particle arrangement of the intermediate structures.

Once that the description about the transformation mechanism has been outlined, the next step is to describe this structural process taking into account not only one layer of particles but the complete structure. For two layers, the rhombohedric transformation has been already explained for the rhombic phase [Pan84]. For higher number of layers the underlying transformation process is the same. Taking into account the growth crystal process in the wedge cell, let's consider a crystal block with the n□ symmetry with the (100) planes oriented perpendicular to the crystal growth direction as shows Fig.81a) The coordinate axes have been drawn according to the crystallographic axes of an FCC crystal. Fig.81b) schematizes the complete n□→n△ transformation showing just a section of the crystal. In the equilibrium, a particle close to the solid/fluid interface at H(n□) will be packed at stable positions (marked with white dots) in order to minimizes the free energy of the system. At the end of the transition, for H(n△) the particles find a new stable position (marked with green dots). At intermediate cell heights, the particles will not find a well defined equilibrium position but a metastable region due to the symmetry of the square phase. Because of that, the final position of each particle will depend on all the other particles around which are contributing to the crystal formation at the same time. As a result we are going to find a rich variety of possible configurations at the same height, all of them characterized by shifts between particle rows or even (as we are going to see) complete crystallographic planes. It is also important to notice that these shifts row-to-row take place parallel to the ground but out of plane due to the increment of space in x direction. This height increment is also indicated in Fig. 81b).

In Fig.81c) a SEM picture shows the beginning of the n□→n△ transition. This is a very representative image of the different packing possibilities. In it we can see a structure characterized by an aperiodic lattice being possible to distinguish square, rhombic and even hexagonal lattice cells at the same cell height. Therefore it is easy to imagine all the possible intermediate structures that these arrangements originate. In this picture it is also possible to see two important features of this phase. One is that for some configurations the structure does not remain stable upon drying (red arrow). The other is the presence of hexagonal lattice cells. This is due to the relative position of rows forming pairs (black arrow). In principle this should be just the limiting case during the transition for the position of two rows as we have already explained. However, for more than two layers this configuration is possible. The only limitation is that the structure does not exceed the allowed height.

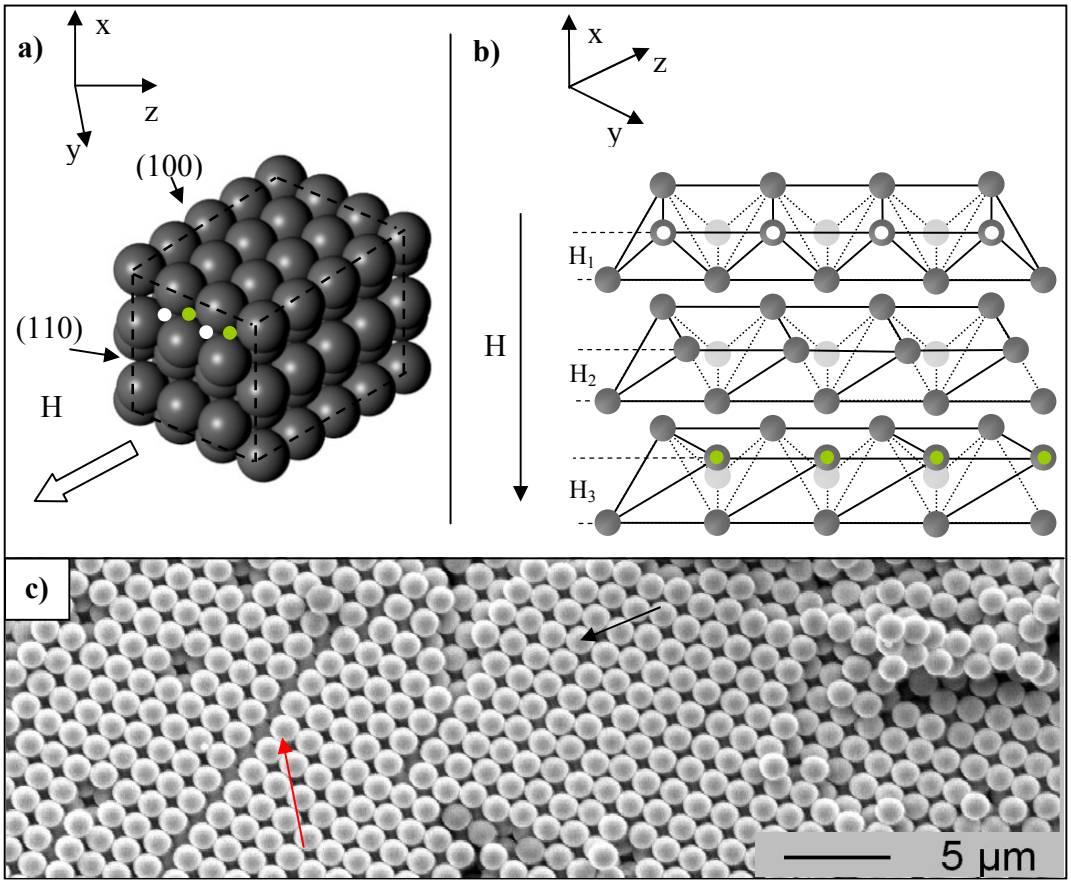

FIG.81: a) Schematic drawing of a crystalline FCC structure showing the position of the particles at the beginning of the transformation, still in the n□ structure (white dots) and after the complete transition when the n△ phase has been formed(green dots). b) Schematic representation of three steps in the transition. c) SEM picture showing the arrangement of particles at one intermediate region of the n□→n△ transition.

Despite the enormous amount of possible configurations we have distinguished up to four different intermediate particle arrangements which appear often in the transition: structures with rhombic symmetry n-$\mathcal{R}$, prisms with square symmetry in their sides parallel to the cell plates n-$\mathcal{P}_{\square}$-B, and hexagonal close packed structures with their (101) planes oriented parallel to the cell plates, n-hcp$\angle$. These three groups of structures have been observed in both wet and dry states. However, some times slight differences have been observed between them. In general terms we could say that the rhombohedric lattices have been observed much more frequently in the wet state whereas alternation of square and hexagonal local orderings appeared more frequently in the dry state. This is

probably due to difference of degrees of freedom of the particles in one and the other state: In suspensions the particles fluctuate around a stability region whereas during evaporation the effect of the capillary forces tends to reduce the free energy of the system resulting in the formation of more compact structures. Because of that square and hexagonal symmetries will replace to big extent the former dominance of the rhombic symmetry. This fact does not mean that the rhombic symmetry completely disappears in the dry state but simply that this particle ordering appears less frequently if we compared it with the wet state.

Next we are going to show these intermediated structures. Although the stability region for each structure is not well defined being not possible to found a sequential order for the different structures, it is possible to differenciate those belonging to the beginning of the transition and those belonging to the end of the transition. In the first group the most representative orderings do correspond to the n-$\mathcal{R}$ and the n-$\mathcal{P}_{\square}$-B structures whereas close to the n, the n-hcp$\angle$ structure can be considered as the most representative. After these structures have been described we will show some experimental observations which support the structural transition process previously mentioned. Also mechanisms based in a model of hard spheres following the maximum packing criteria will be presented. In this case the model describes the complete n□→n△ transition.

8.3.1 The rhombic phase, n-$\mathcal{R}$.

This phase has been already explained for the bilayer. It completely mediates in the transition from the square to the hexagonal structure. This structural transformation is continuous and smooth. Compared to other intermediate phases, the phase is stable for a very short range of plate-plate distances (this is illustrated in Fig. 14 in Chapter 3). It was experimentally observed by Neser [Nes98] but previously it had been predicted in the model of hard spheres in the high pressure limit proposed by Pansu and the Pieranski Brothers [Pan84]. In the phase diagram Φ-H the rhombic phase appears at distances between the confining walls ranging from H(2□) ≈ 1.71σ and H(2△) ≈ 1.82σ which is a very small height variation. Also in our experiments the stability region for this phase was significantly smaller when compared to other intermediate phases. Despite that, the low angle wedge-cells obtained for these experiments, allowed the study the rhombic phase 2-$\mathcal{R}$ in detail. Since

the transformation mechanism was already explained, in this section we just show experimental evidences which confirm some theoretical predictions and simulations coming from literature.

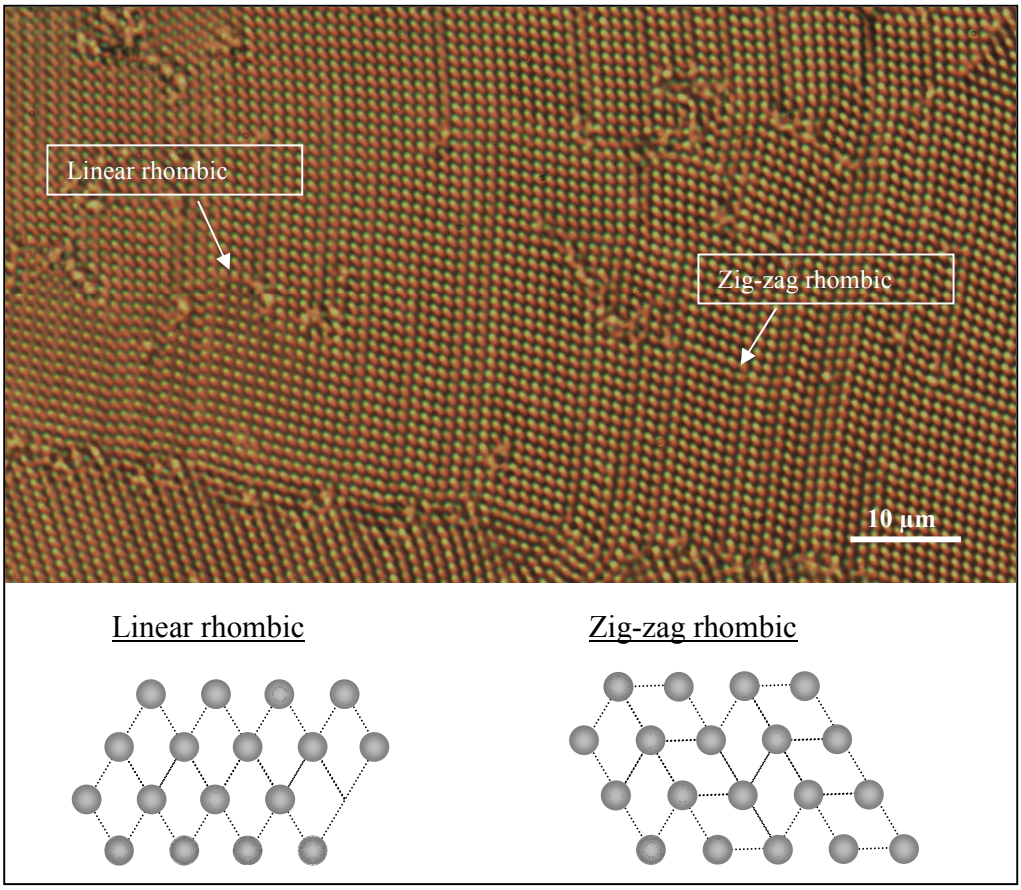

FIG. 82: Optical Microscope picture showing the rhombic phase n-$\mathcal{R}$ for n = 2 indicating the two degenerate stables phases: linear rhombic and zig-zag rhombic.

In the n□→n△ transition two degenerate stable phases are possible. One is the linear rhombic phase and the other is the zig-zag rhombic phase [Sch97]. They are schematized in Fig.82. Both phases coexist giving to the transition a wavy aspect as can be appreciated in the picture. In these experiments it was possible to observe the rhombic phases predicted by Messina and Löwen [Mes03]. They found two different phases 2-$\mathcal{R}$-A and 2-$\mathcal{R}$-B (IV-A and IV-B in their notation) as possible stable phases in a bilayer system of charged spheres under geometrical confinement. In this case the crystalline phase is characterized by two rhombic lattice layers. In the rhombic phase 2-$\mathcal{R}$-

A, each particle of one of the layers lays in the geometric centre of the rhombic unit cell of the other layer. On the contrary, in the rhombic phase $\mathcal{R}$-B the particle of one of the layers does not lie in the centre of the rhombic unit cell of the other layer but is shifted along the major diagonal. In FIG. 83 both $\mathcal{R}$-A and $\mathcal{R}$-B phases coming from our experiments are shown. In particular the system is formed by of polystyrene particles of 2.5 μm of diameter in water. In this picture we can clearly see the continuous transformation between both phases. This experimental observation together with the model proposed by Pansu et al. [Pan83] suggested us that not all the minor angles of the rhombic unit cell ($60° \leq \delta \leq 90°$) are allowed for any of the rhombic phases but rather the $\mathcal{R}$-A structure would be characterized by angles between 90° and ~ 80° and the $\mathcal{R}$-B phase by angles between ~ 80° and 60°. The 2□→ 2△ transition is then a continuous structural transformation mediated by two rhombic phases. In the sequence, the rhombic phase $\mathcal{R}$-A appears after the 2□ structure and as the cell thickness increases, it smoothly transforms into the rhombic phase $\mathcal{R}$-B before the 2△ structure appears.

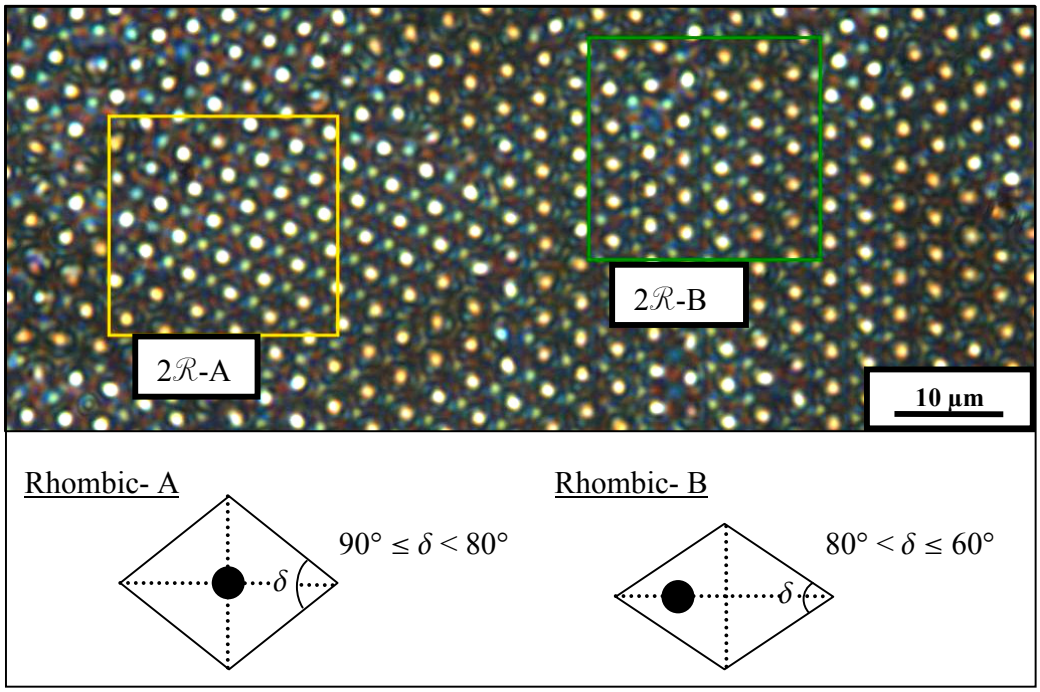

FIG. 83: Experimental evidence of the two different rhombic phases predicted by Messina and Löwen [Mes03]. For details see text.

For higher number of layers the rhombic phase has been also observed in the same transition. In Fig.84 a SEM picture corroborate its stability also after drying. However, from high resolution pictures obtained with the optical microscope, we can not conclude that the n-$\mathcal{R}$ structure completely mediates in the n□→ n△ transition for n > 2 but rather it appears as one of the possible intermediate phases in competition with other arrangements like for instance the n-$\mathcal{P}_{\square}$-B structure at the beginning of the transition. As we can see in Fig.84, the unit cells for the n-$\mathcal{R}$-A and n-$\mathcal{R}$-B phases appear randomly distributed and consequently for higher number of layers there is no indication about any sequential order of these structures. In this case, the rhombic phase can be simply considered as a distortion of the rhombohedric nature of the square lattice.

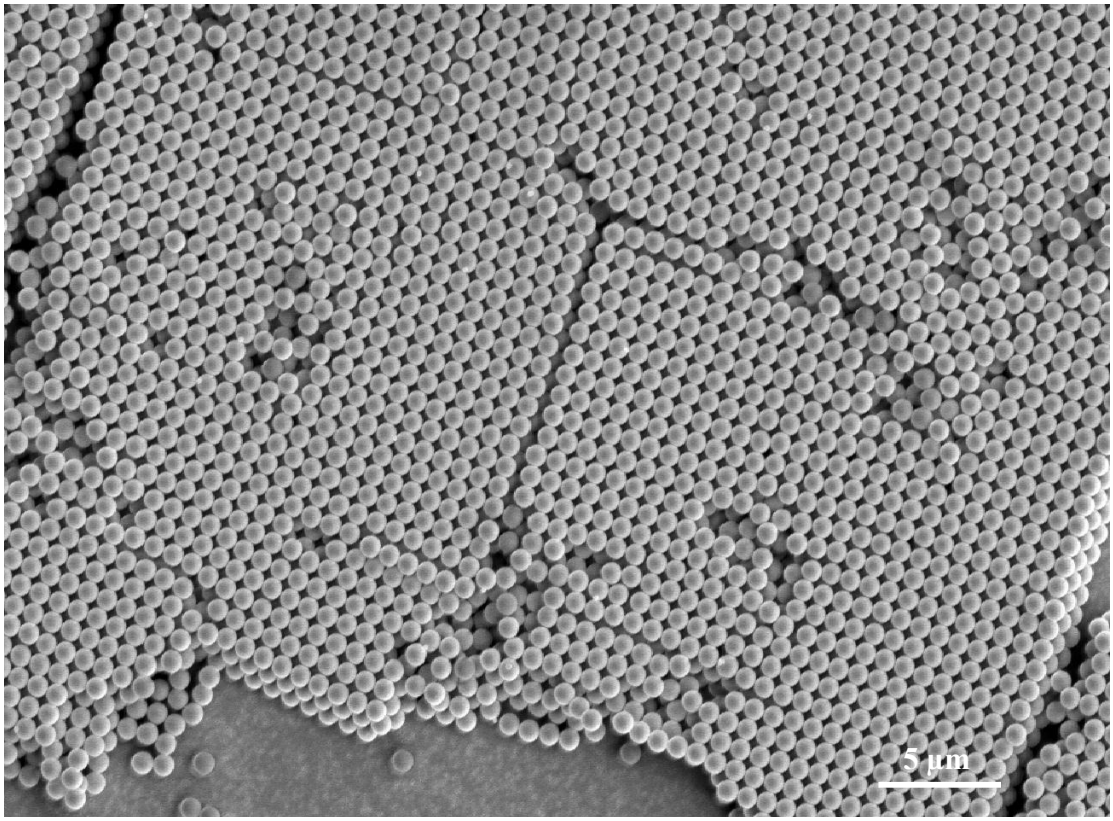

FIG.84: SEM picture showing the 3-$\mathcal{R}$ structure in the dry state. In general we can interpreted this crystalline phase simply as the slightly distortion of the n□ phase due to an increasing of the confinement volume.

8.3.2 The square prism phase, n-$\mathcal{P}_{\square}$-B

This structure is characterized by triangular prisms where its sides which are parallel to the cell plates present square symmetry. The morphology of this structure was already studied by Neser in detail (See Chapter 3). As we will see, this structure gives us one of the clues to explain the transition mechanism. As in the n-$\mathcal{P}_{\triangle}$ structure, the width of the square prisms depends on the number of layers. A top view image of the 3-$\mathcal{P}_{\square}$-B structure is shown in Fig.85 for the wet state. The inset to show the 2D diffraction pattern when the sample is illuminated with white light. The intensity distribution is fan-like as in the case of the n-$\mathcal{P}_{\triangle}$ structure. This time it is possible to recognise four brighter spots which indicate the presence of the square symmetry in the crystal. This structure remains unaltered after drying as shows Fig.86. In picture a) a SEM picture of the 5-$\mathcal{P}_{\square}$-*B* structure after lateral cutting shows the particles arrangement. In the inset, the top view of the structure is shown. The distance between equally oriented prisms is denoted by the length *b*.

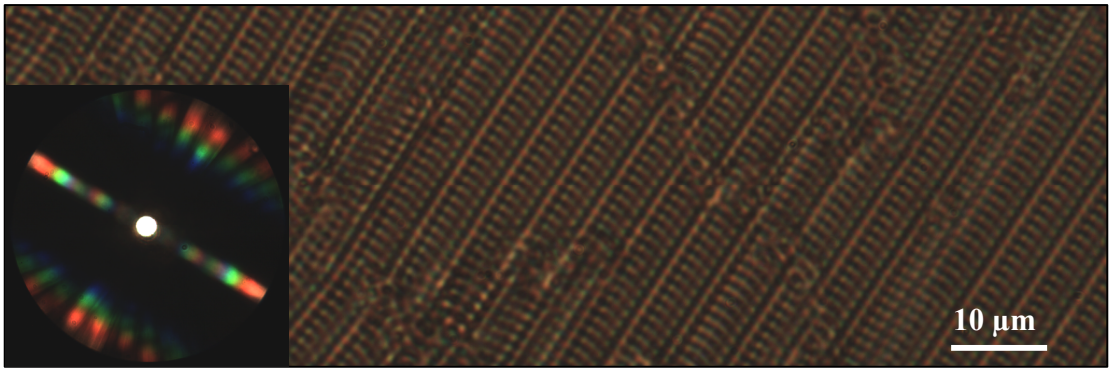

FIG.85: High resolution optical microscope picture of the 3- $\mathcal{P}_{\square}$-B structure. The inset shows the intensity distribution in the Fourier space.

The transversal cut allows the identification of the prisms. From the picture we can deduce that, the formation of the n-$\mathcal{P}_{\square}$-*B* structure starts with the smooth shift of (111) and $(1\,\bar{1}\,1)$ planes in the FCC structure (n□). These shifts define a local rhombohedric transformation which will be of fundamental interest to understand the complete n□→ n△ transition as well as the formation process of its derivated structures as H increases. These shifts between the former crystallographic

planes results in the smooth formation of stacking faults in the FCC structure. Therefore the n-$\mathscr{P}_{\square}$-*B* structure can be defined as a FCC structure with periodic stacking faults. This means that it is a close-packed structure.

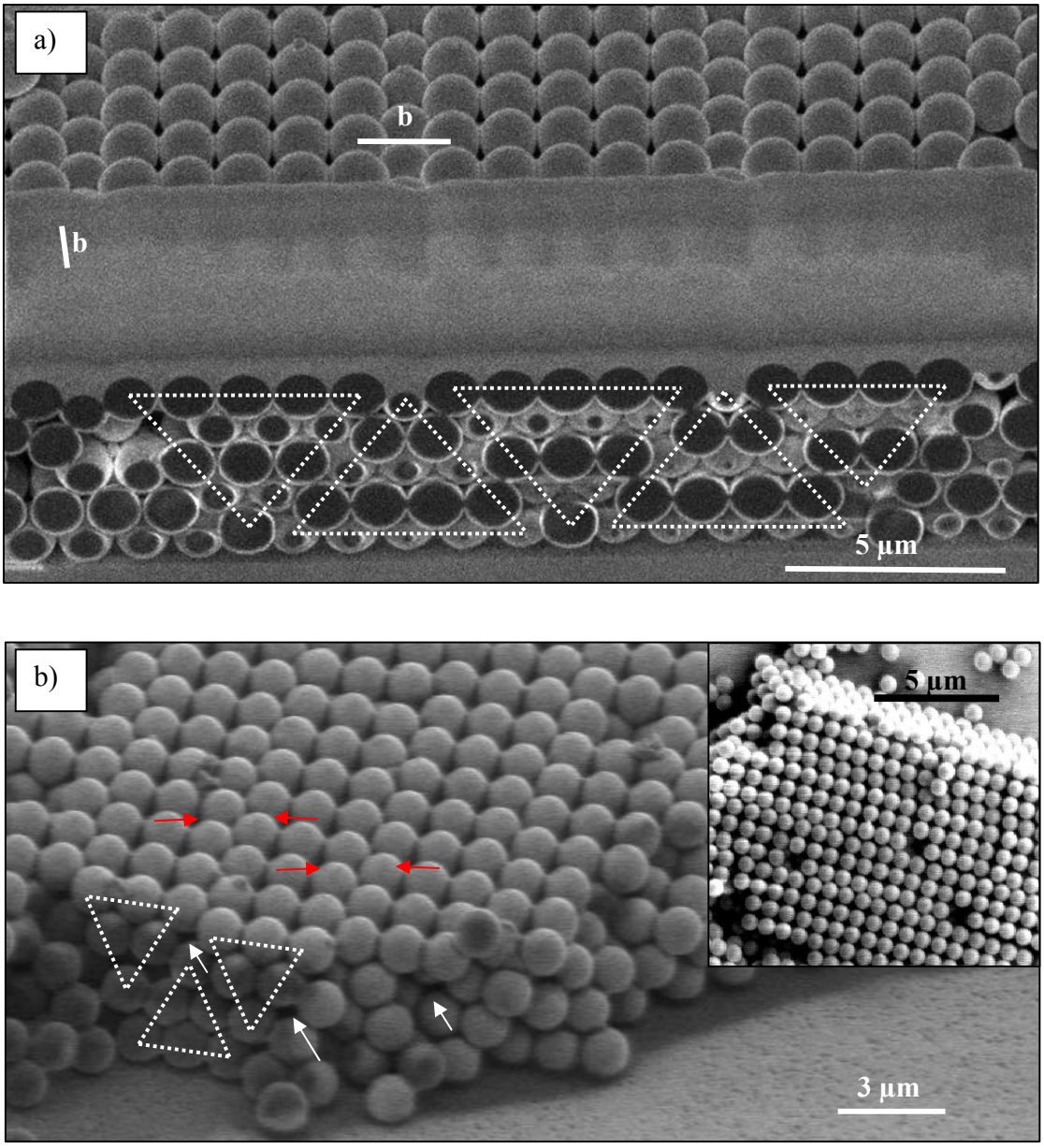

FIG. 86: SEM pictures showing: a) Transversal cut of the 5-$\mathscr{P}_{\square}$-B phase after drying. b) Final structure of the 3$\mathscr{P}_{\square}$-B phase. The insets show the top view of the structures.

In Fig. 86a) a significant feature also appears: at the right part of the picture it is possible to identify a square prism with only four layers. In principle this can be understood as a structural defect. However if we take a look at Fig.86b) another non-expected arrangement appears. The picture does correspond to the 4-$\mathcal{P}_{\square}$-*B* structure but the prisms only have three layers of particles. These two experimental observations invalidate the application of the model proposed by Neser in our experiments. This model was explained in Chapter 3 and predicts a continuous n□→ (n+1) □ transition. However, prisms with less number of layers than the corresponding phase have been found here as the result of the structural transformation. Picture b) is showing us another possibility of packing from prism structures with square symmetry on top. In this case the structure is not close-packed as the presence of voids indicates (white arrows). It is probably the same that appears at the left part of picture a) which would be just the next step in the transformation (one of the possible from several possible arrangements). If this structure was the final stable position in the transformation of the n-$\mathcal{P}_{\square}$-*B* phase (that is, exists a continuous transformation between close packed, n-$\mathcal{P}_{\square}$-*B* and non close-packed, n-$\mathcal{P}_{\square}$-*B* structures) then we have found how the complete n□→ n-$\mathcal{P}_{\square}$-*B* transition takes place. The final structure is not a periodically stacked FCC structure but the shift between close-packed planes continues until the top rows of the prism are close-packed as can be seen in the picture.

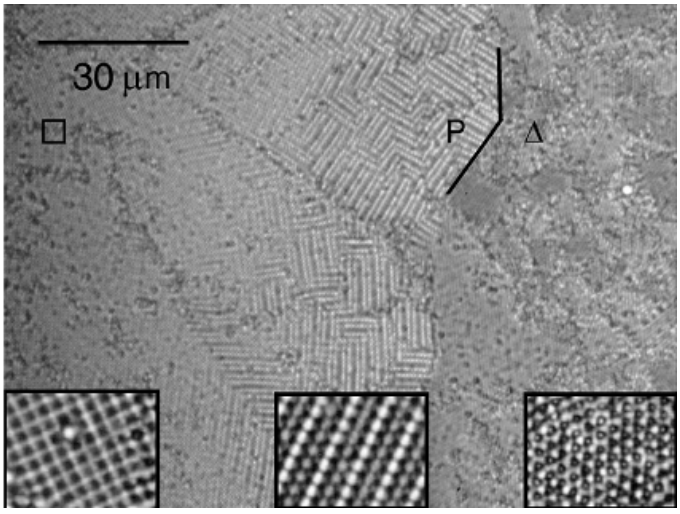

FIG. 87: Low magnification picture of the 2△→ 3 □ transition observed by Neser where it is possible to observe the 2-$\mathcal{P}_{\square}$-A phase. [Nes97].

I think that the model proposed by Neser arose as a logic interpretation from his experimental results since he also observed the square prism phase n-$\mathcal{P}_{\square}$-A which takes place just before the square structure in the n△→ (n+1) ☐ transition as shown in Fig.87. However, in this thesis we observed a completely different transformation mechanism for both prismatic structures. Moreover, in the n-$\mathcal{P}_{\square}$-A phase for any of the lattice parameters a close packed structure is formed. Because of this we consider it important to distinguish between both square prismatic phases.

8.3.3 The (101) hcp phase, n-hcp∠

This is another of the possible arrangements that we can find in the n☐→ n△ transition. Its stability region is closer to the hexagonal phase than to the square phase. In Fig.88 a high resolution picture shows the bottom part of this structure for six layers. It is characterized by alternated pairs of rows shifted upwards and downwards being possible to define a rhombohedric unit cell for each layer as is indicated in the inset. The diffraction pattern is similar to those of the other structures present in this transition. Now, in the fan-like intensity distribution, it is possible to recognize four brighter intensity maxima (white arrows) which indicate that the transition is close to the n△ phase.

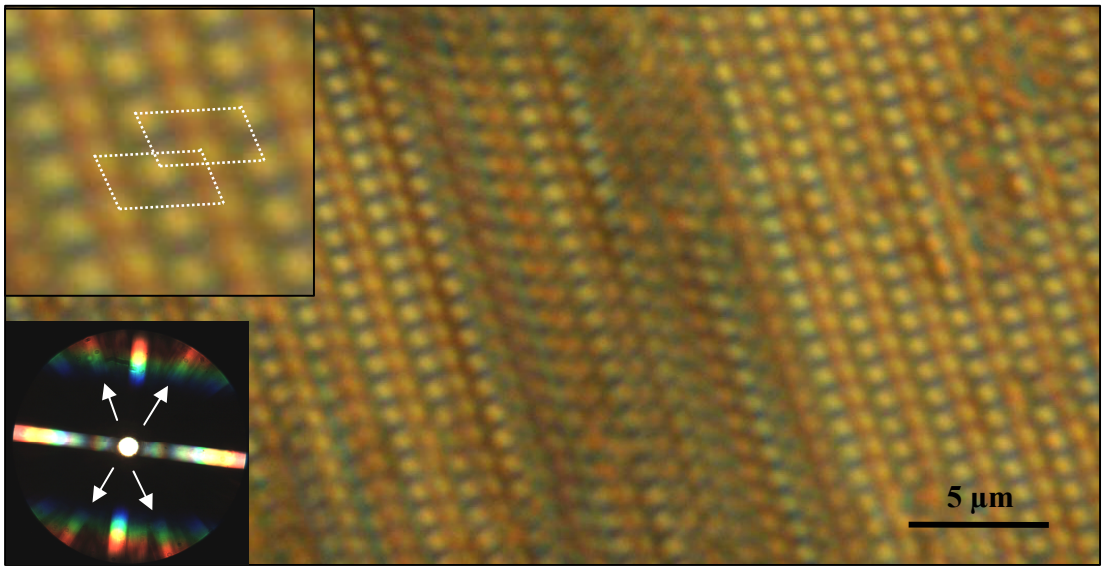

FIG.88: Bottom view of the 6-hcp∠ structure. The insets show a magnified image to indicate the unit cells of the bottom layers as well as the diffraction pattern of the structure.

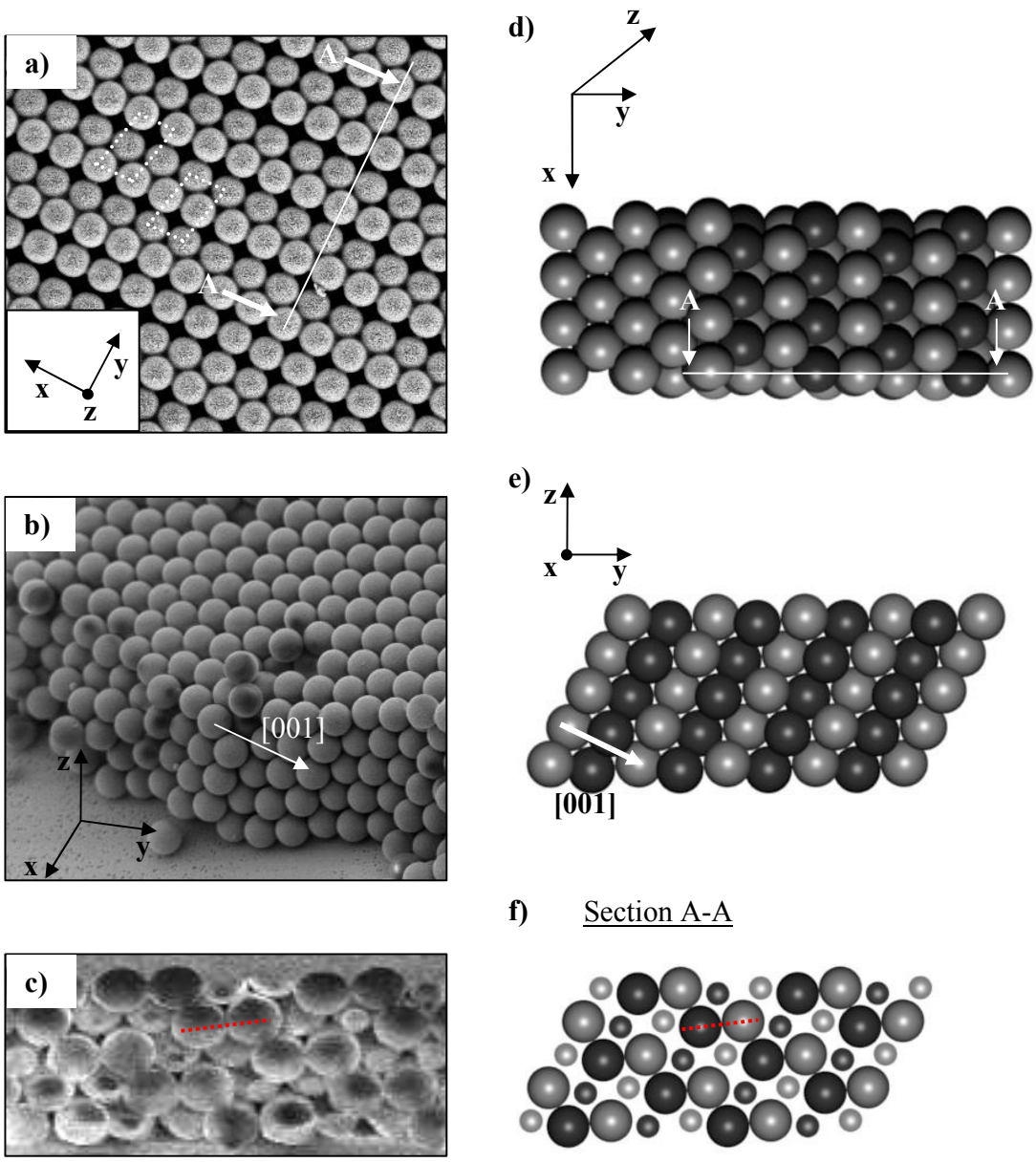

FIG 89: SEM pictures showing a) General top view of the n-hcp∠ structure. b) Perspective showing the disposition of the close-packed planes for the 5-hcp∠ structure. c) Transversal cut. d)-f) Different views of the modelled structure. The size of the particles is 1µm.

This structure is stable upon drying. In Fig. 89a) a SEM picture shows the top view of the n-hcp∠ structure. In terms of rows positions in the layers it is possible to see the periodic alternation of rows forming local square as well as hexagonal symmetries. The general view of the 5-hcp∠ structure shown in Fig.89b) as well as the transversal cut of the structure shown in Fig.89c) helped me to

model such structure. As a result I obtained a hexagonal packed structure where the (101) were oriented parallel to the substrate. This is shown in Fig.89d) to f). The hexagonal planes appear forming an angle of 58.5° respect to the substrate. In Figs. 89b) and f) the crystallographic direction of those planes is indicated. In Fig.89f) the section A-A of drawing d) has been drawn in order to compare with the SEM picture in c). As we see the particles disposition is the same. I also drew a dotted red line joining two particles to facilitate the comparison between the dry structure and the packing model.

8.3.4 Other arrangements in the n□→ n△ transition

This section is mainly focused in the description of several arrangements which helped in the modelling of the transition. As it was explained at the beginning of the chapter the transition consists of the relative shifts between particle rows giving rise to a transformation of rhombohedric nature. Now that some relevant structures belonging to this transition have been shown, it is easier to show other intermediate arrangements that made me arrive to that conclusion. In particular some arrangements which appear after the n-$\mathscr{P}_{\square}$-*B* structure in the sequence have been very helpful. For instance, frequently a structure consisting in the alternation of square and hexagonal regions has been observed. In Fig.90 a representative image taken with the microscope for a four layer system is shown. As an inset, the corresponding 2D-diffraction pattern has been included.

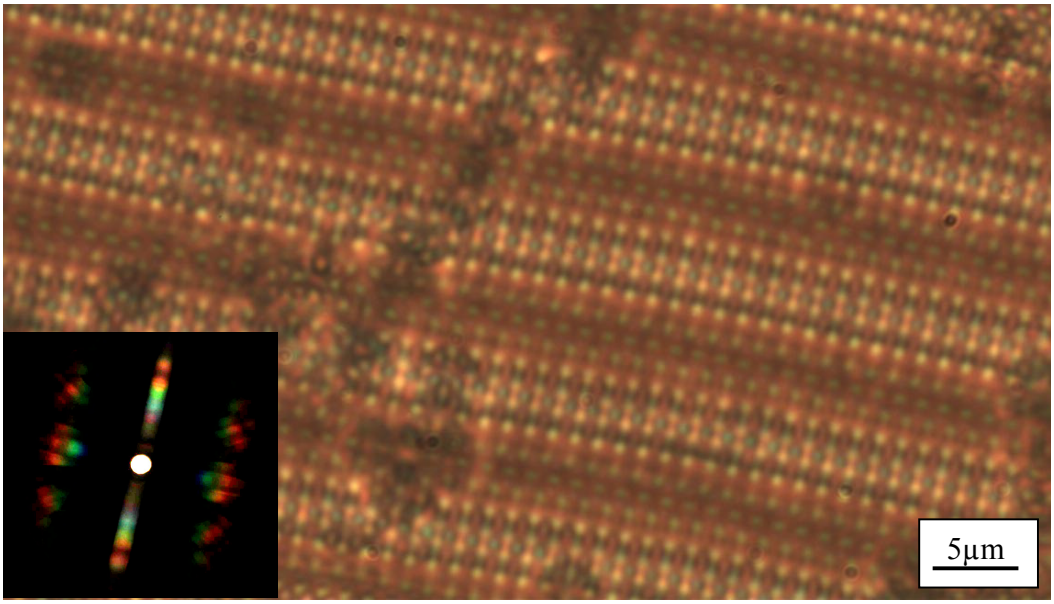

FIG. 90: Another possible arrangement found in the 4□→ 4△ transition. The structure is characterized by the periodic alternation of regions with square and hexagonal symmetry.

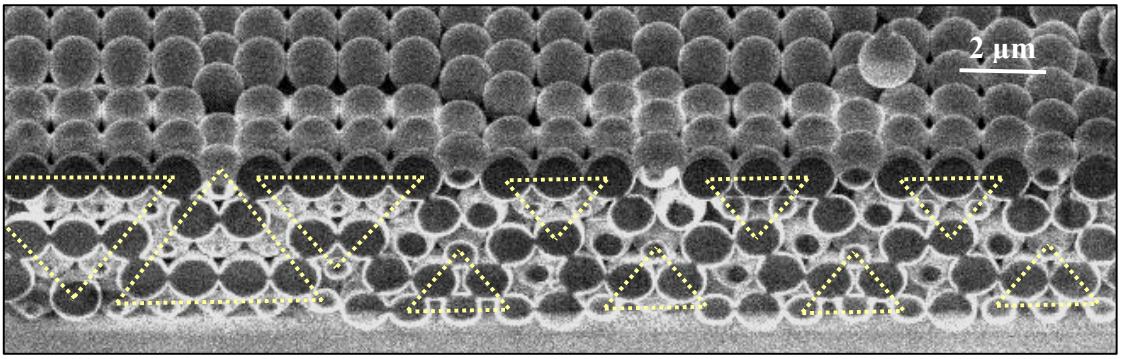

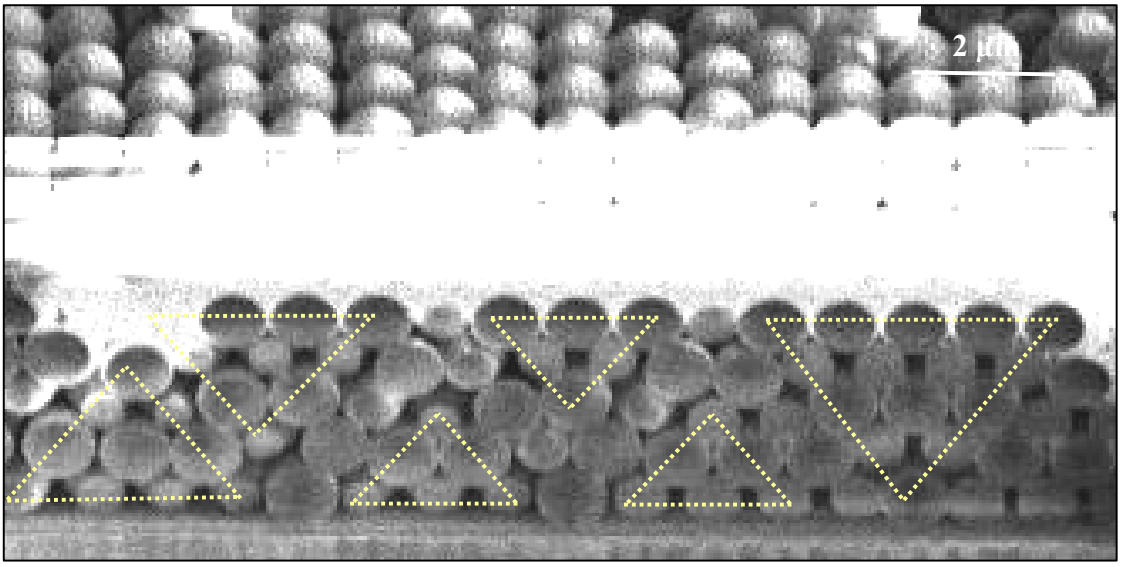

FIG. 91: Transversal cuts of intermediate structures in the 5□→ 5△ transition. *The dotted yellow triangles indicate square prisms structures.*

Once the samples are dried these structures remain stable. Fig.91 shows two SEM pictures showing how these intermediate structure looks like when looking at the transversal cuts. The square prisms are denoted by yellow dotted triangles. Both structures have been found for a five layer system. In both pictures it is possible to distinguish a prism belonging to the 5-$\mathcal{P}_{\square}$-*B* structure. However, smaller prisms consisting of three or four layers are also present. It is possible to interpret these arrangements as the evolution of structural transition from the 5-$\mathcal{P}_{\square}$-*B* structure once the distance between the plates increases. The transformation starts with particles arriving to the solid-fluid interface taking up positions which result in the slow shift of the external planes of the prism. Next particles contributing to the crystal growth will form again square prisms structures but of

smaller volume. These structures are non close-packed as can be observed in the pictures. As we see, the resulting structures are a combination of regions with square and hexagonal symmetries. At the same time, for the distribution of the square prisms in the pictures, the rows which participate in the transformation do not obey any sequential transformation. Because of that it is possible to observe square prisms of different sizes without any sequential order.

Finally I will conclude this section showing how the transition looks like before the hexagonal phase appears in the sequence. In Fig.92 a SEM picture shows how the phase looks like. In the wet state this region will correspond to the inset of Fig.79. As we see in that region there is a coexistence of multiple degenerate intermediate phases being possible to appreciate the presence of the hexagonal phase. Even the square structure is present but I consider that the n□ phase appears due to some anomaly in the cell plates.

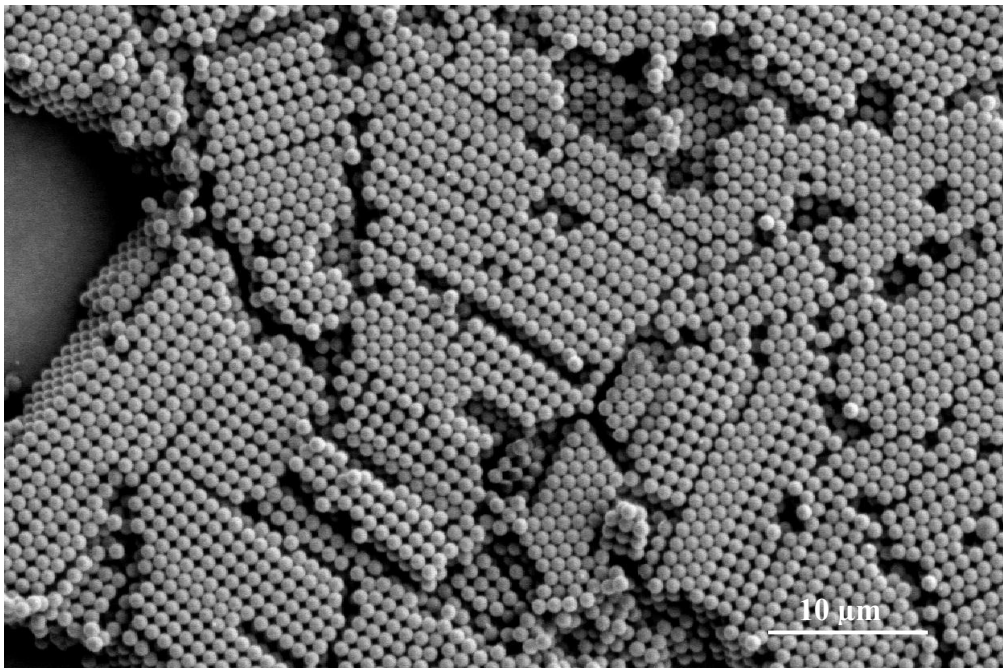

FIG. 92: End of the 5□→ 5△ *transition where is possible to observe the beginning of the 5*△ phase.

8.3.5 Transition model for hard-sphere system in the high pressure limit

In this thesis no information about the final step in the structural transition has been found. That is, we do not have any experimental result about how the particle rows finally transform giving rise to the n△ phase. This information would have been very useful in studying how the structures

transform in different stacking sequences of hexagonal close-packed planes. In Fig. 93 the 3□ → 3△ transition is shown for a wedge cell where the angle between the plates was around 10^{-3} rad (one order of magnitude higher that usual). Because of that the stability region for this phase is only about 50 μm. The interest of this picture lies in two important observations. On one hand, we can clearly see how the rhombohedric transformation smoothly transforms to both stacking sequences in the 3△ phase. Notice that the structural changes retain the orientation during the transformation. On the other hand in this picture it is also possible to see the smooth and continuous transition between the square and the hexagonal phases.

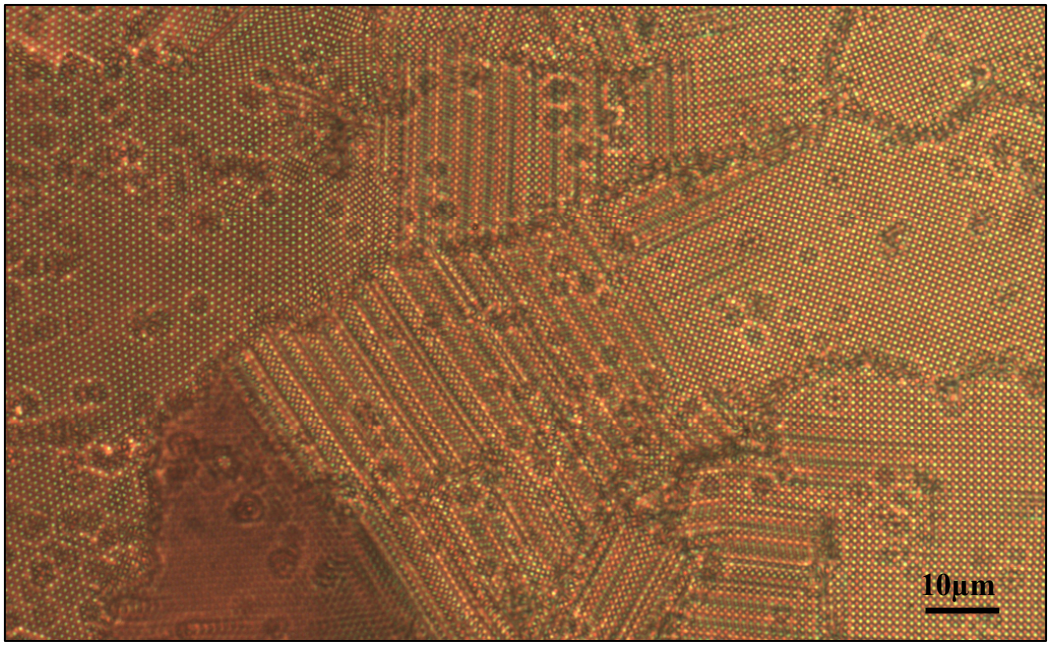

FIG.93: 3□ → 3△ transition showing the retention of orientation as well as the smooth and continuous symmetry changes between the square and the hexagonal phases.

From all the information about the particles arrangements in the transition, as well as the information about how the structural changes which take place as the distance between the confining walls increases, I have modelled the transformation for a system of hard-spheres in the high pressure limit. The transformation, independently of the number of layers has been assumed to follow a continuous rhombohedric transformation as in the case of the 2-$\mathcal{R}$ structure. In principle one can refuse this transformation since we have seen that for more than two layers this phase is highly degenerated giving rise to multiple particle arrangements for the same cell height. However I am

going to assume that the volume fraction of the structures is the same at a given H independently of the particle arrangement that we found. Following this hypothesis, the transformation was modelled obtaining the relation between the height of the cell and the angle δ defined between two of the sides of the unit cell as it was shown in Fig.94. Thus this angle will vary for any of the phase transitions from 90° to 60°. From that the relation of the volume fraction variation with the angle is also obtained.

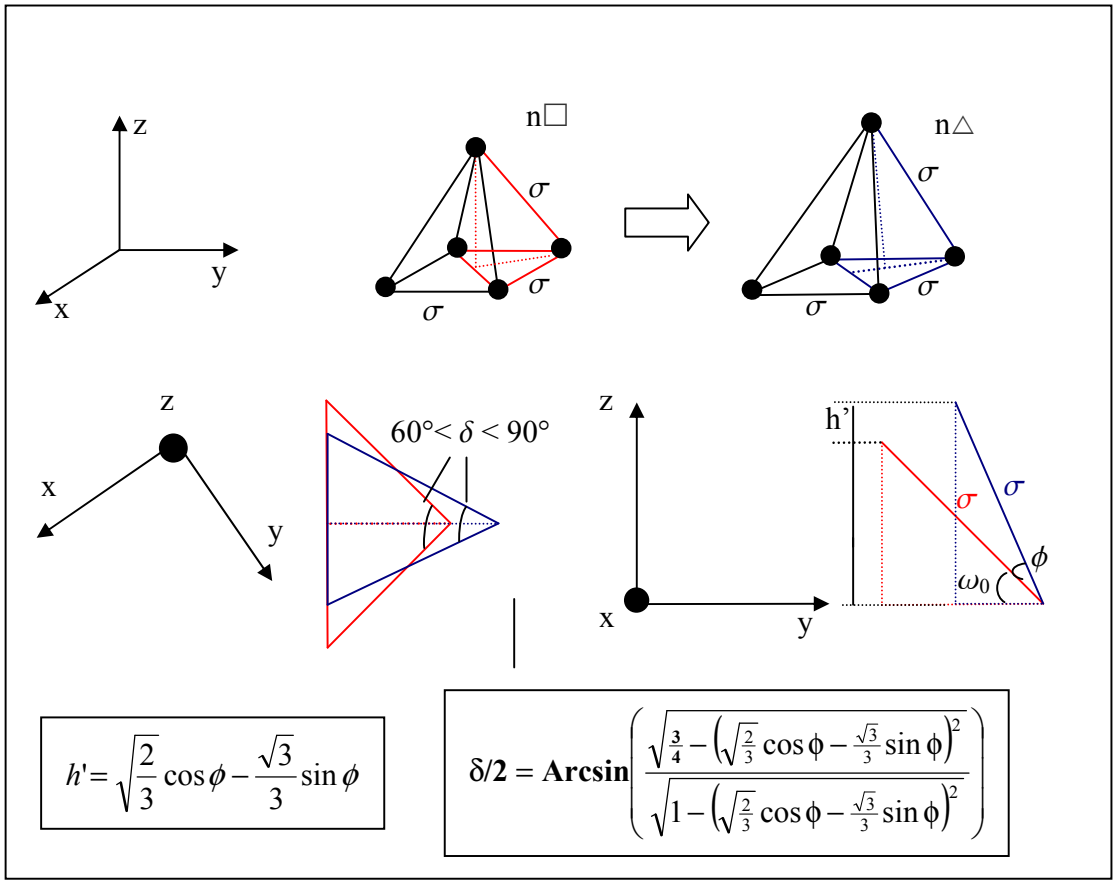

FIG. 94: Basic parameters in the modelling of the n□ → n△ transition.

In Fig. 94 two pyramids corresponding to the n□ and the n△ have been drawn in order to define the relevant parameter involved in the transition model. Starting with the square symmetry as H increases the height of the pyramids h', as well as the angles which define the basis of the pyramid, will change. Both obtained expressions depend on the variation of the angle ϕ.As a result we obtain that,

$$H(n,\phi)=\left((n-1)\left(\sqrt{\frac{2}{3}}\cos\phi-\frac{\sqrt{3}}{3}\sin\phi\right)+1\right)\sigma \tag{8.7}$$

$$\Phi(n,\phi)=\frac{\pi}{6}\frac{n}{2\left((n-1)\left(\left(\sqrt{\frac{2}{3}}\cos\phi-\frac{\sqrt{3}}{3}\sin\phi\right)+1\right)\right)\cos\phi\sin\phi} \tag{8.8}$$

where n is the number of layers and σ the diameter of the spheres. The curves are plotted in the graph of Fig. 95. This transformation model was originally proposed by Pansu et al. for two and three layers [Pan84]. My model was based in their assumptions but was obtained following my own calculations. Since we arrived to different expressions, I just compared both series of curves obtaining a perfect fit between them.

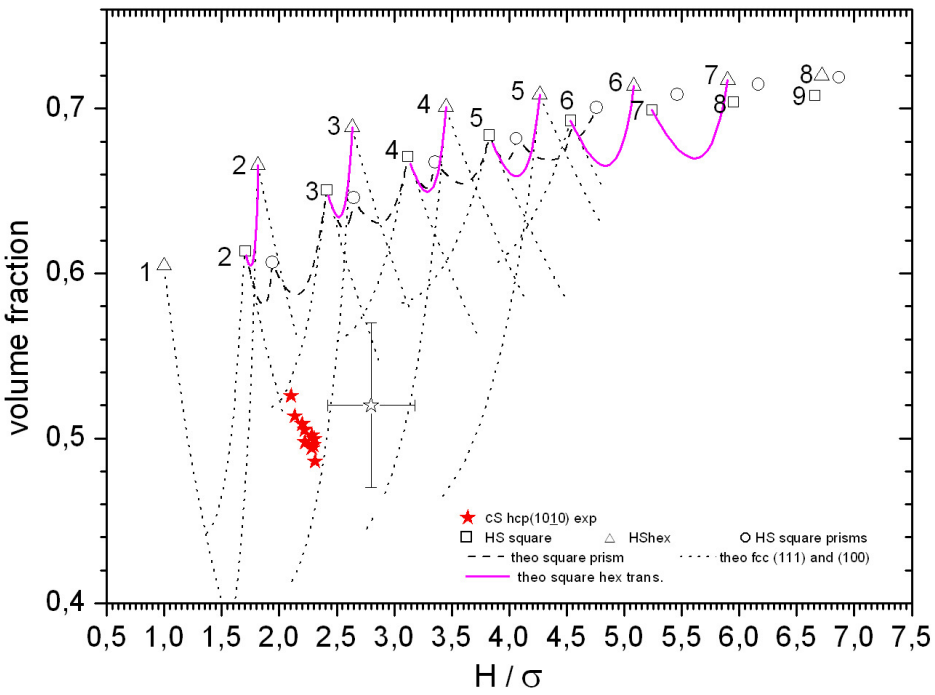

FIG. 95: Plot showing the volume fraction versus cell height for the n□ → n△ transition. The curves have been obtained from a transition model of hard-spheres in the high pressure limit.

Although we have a perfect agreement in the phase behaviour it is important to remember that this is just a model which could be valid for a very particular case in the complete phase diagram. Furthermore it has been also assumed that all this highly degenerated phase can be considered as a continuous rhombohedric passage. Actually the presence of multiple configurations means a notable increment in the isotropy of the system. This is directly related with an increase in the entropy of the system. Therefore, we probably have to consider for this phase entropic effects in its formation and neither the proposed model nor the resulting curves would have validity. However as we are going to see in the next section these curves confirm some of the experimental results here obtained. Because of that, they can be simply considered as a first approximation in the analysis of the phase behaviour of the system leading for further research a deeper understanding in the nature of this phase and the possible contribution of the entropy in the final phase configuration.

8.4 Discusion

In this chapter, the results when confining a colloidal suspension in wedge-like geometries have been shown. The original suspension was in the fluid phase. At the equilibrium the cell shows an extended crystalline region in the narrow part of the cell. When looking at this region with the microscope a rich variety of structures has been found. They appear forming part of a crystalline sequence. Some of the structures had been already observed and studied but the low wedge angles reached during the cell construction in this thesis allowed to find out new structures as well as smooth structural changes between them in the sequence. The investigation of the dried samples with the SEM, with and without the implemented Ga^+ ion beam, was essential to determine the morphology of the new structures as well as the proposed transition models assuming a hard sphere system in the high pressure limit. If we neglect forces of entropic origin, then the minimum free energy of the crystal will correspond to that configuration which minimizes its volume (maximizes its volume fraction). We have observed that each of the intermediate phases is characteristic of one of the two possible transitions: the n△→ (n+1)□ transition or the n□→ n△ transition. In the former transition, up to three different crystalline phases are implied in the structural transition have been found whereas the latter transition is characterized by a highly degenerate phase.

Different crystalline structures which have identical packing volumes might have different thermodynamic properties and stabilities. However here I have only consideried a hard sphere system subject to a strong lateral force. By doing so, the stability of the structures will only depend on their packing fraction. That is, I am taking into account only geometric considerations. However, the real system studied in this thesis consists in the geometrical confinement of a suspension of charged colloidal spheres between slightly charged plates. In the equilibrium the crystalline phase reveals that the repulsive interaction between the particles is very low being possible to consider them as a nearly hard spheres but any quantitative measurement has been made to extract determinant conclusions. The stability analysis presented here corresponds to a particular region of the complete phase diagram at T=0 and therefore the comparison with the experimental results that I am going to do now is just qualitative.

In the phase diagram of Fig.96 I have plotted all the curves from the proposed transition models calculated in this thesis as well as former calculations from literature. The experimental data obtained for the 2- hcp⊥ transition has also been plotted in order to remember the differences in the volume fraction (and hence the stability region) between the models and the experiments. The first interesting result in this phase diagram arises just calculating the volume fraction and corresponding height for the close packed phases, n□ and n△. If we follow the position of the different n□ structures as H increases with respect to the n△ structure, we see that for n = 8 the square structure appears at the same height as the 7△ phase. Consequently from this number of layers the n□ structure will not be observed. For lower number of layers, concretely from five to seven layers, the n□ structure is in competition with the intermediate structures. In principle the volume fraction values indicate that the square structure is more stable. However in the experiments we have observed more frequently the presence of the n-$\mathcal{P}_{\triangle}$ and the hcp⊥ phases whereas for five layers the square structure has been observed only occasionally. For six layers on we do not have experimental evidences about the stability of the square structure and probably it completely disappears. On the other hand we can see in the plot that from n = 7 on the volume fraction of the 7□ and the intermediate phases is practically the same. In the experiments, the typical structural transition for more than four layers is shown in Fig.97. In particular this picture corresponds to n = 5. In the pictures we see that the transition passes directly from 5-hcp⊥ to the rhombohedric phase also with five layers.

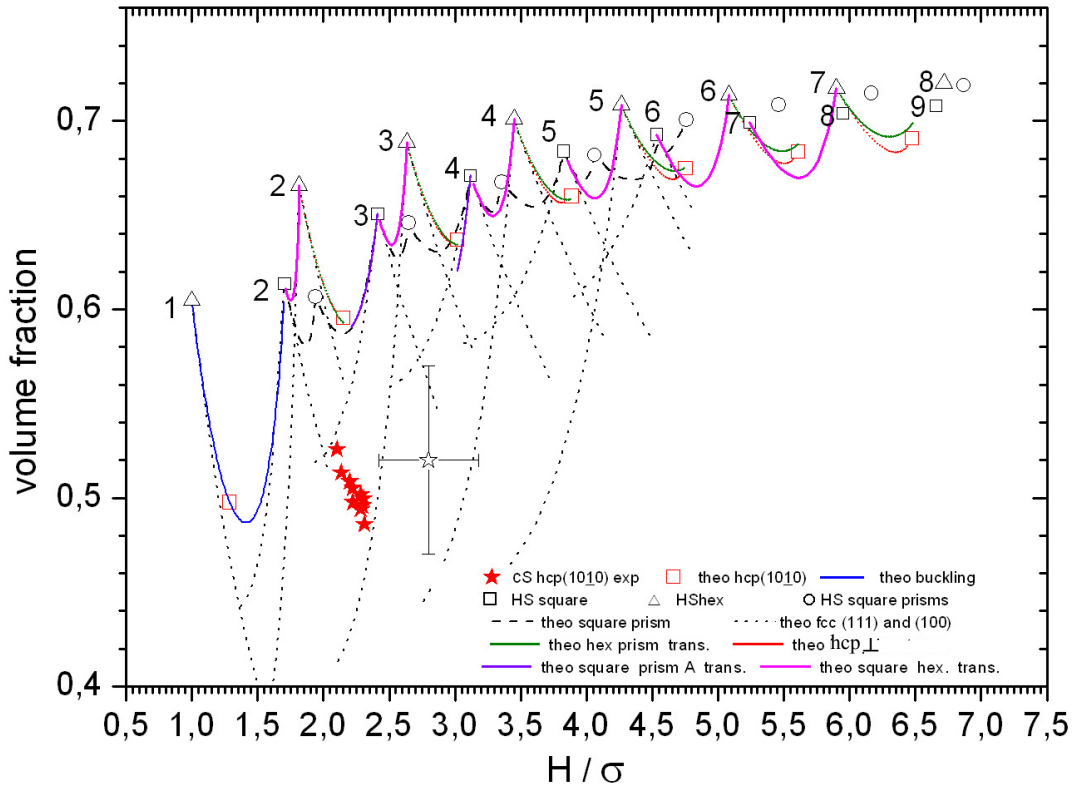

FIG.96: Phase diagram Φ-H for a hard sphere system in the high pressure limit showing the curves from all the proposed models.

I think that the underlying reason stems from the crystal growing mechanism; Once one of the crystalline phases have been formed it costs more energy to form a more stable phase than continuing with the initial crystalline order which is taking part of the phase transition. The same arguments can be applied in the case of the competition between the n-hcp⊥ and the n-$\mathcal{P}_{\triangle}$ phases. The curves in the phase diagram indicate that the volume fraction variation as H increases is identical for both phases at the beginning of the transition. For higher heights the prism phases are more stable than the n- hcp⊥ phases. However in the experiments both phases appear with the same frequency even at the end of the transition.

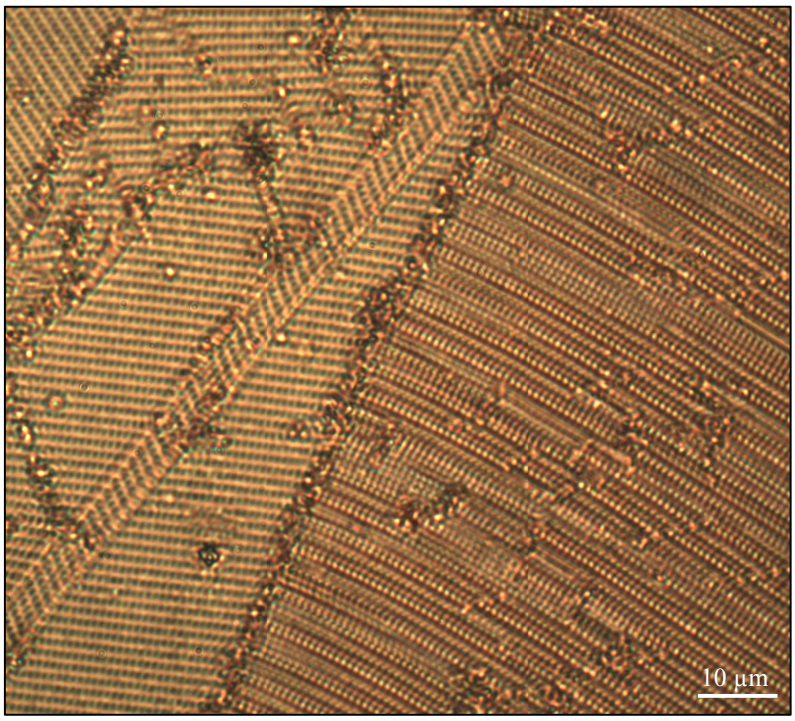

Fig. 97: For five layers the n□ phase appears rarely and for more layers there are no experimental evidences in this thesis about its existence. Here the transition pases from hcp vertical to the rhombohedric transformation. Both phases are separated by a grain boundary.

The competition between structures also could explain the absence of the n-$\mathcal{P}_{\square}$-A structure for n > 4. If we look at the 5□ position in the graph it is easy to realize that, unlike for lower number of layers, a hypothetical 5-$\mathcal{P}_{\square}$-A will be competing with both the 5-hcp⊥ and the 5-$\mathcal{P}_{\triangle}$ phases. From H ≈ 3.5 σ, only the 5$\mathcal{P}_{\square}$-A phase should exist since it is more stable. Again I think that if we do not observe this phase behaviour is just because of the particular crystal growth mechanism that we find in these experimental cells.

For all this cases where there is a competition between structures we can consider that all the observed phases which are less stable than others, and even so are observed in the experimental crystalline sequence, are metastables phases. This suggests that these phases at these height intervals maybe will not appear if the experimental conditions of the system changes. For instance, if other confinement geometry is chosen (parallel plates) and/or the particles have a stronger repulsive interaction.

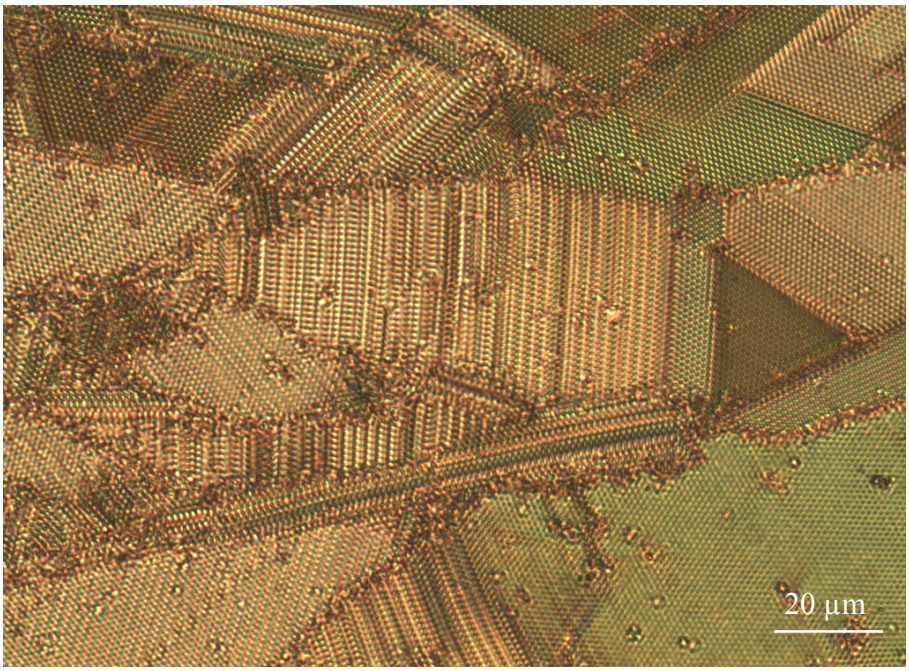

FIG 98: Picture showing coexistence of different intermediate structures at the beginning of the 6△ phase.

We have also experimental observations which are not explained in the theoretical phase diagram of Fig. 96. For instance in Fig.98 a region of the structural sequence for five to six layers. In this case the angle of the wedge cell was higher than usual and because of this we see a very small region where the rhombohedric phase appears. The striking fact here is that the 5-hcp⊥ phase appears stable practically up to the beginning of the 6△ phase. However this phase behaviour is not predicted by the theoretical phase diagram. Maybe this non-expected coexistence of structures is due to the higher angle of the cell which would imply a faster variation of the cell height.

Having seen all these results I consider that the structural sequence of colloidal crystals under confinement consist mainly in the succession of n△ phases. At smooth and continuous cell height variations, other intermediate crystalline arrangements would mediate in the formation of a new layer of hexagonal packed structures. In this sense I consider the square structure as other intermediate crystal ordering in the transition since for higher number of layers it is not stable anymore. The sequence then can be written as:

$$S(H) = n\triangle \rightarrow \text{intermediate phases} \rightarrow (n+1)\triangle$$

It is important to remember at this point that the crystalline sequence here studied corresponds to a specific region in the complete phase diagram. Because of that it is necessary to completely determine the phase behaviour of charged colloidal spheres under geometrical confinement to work with parallel-plates geometries where lateral forces are not expected and at the same time to vary the strength of the interaction between particles.

9 Crystalline Superstructures

9.1 Introduction

Together with the n-hcp⊥ and n-$\mathcal{P}_{\triangle}$ structures, isolated crystalline domains with complex symmetry have been observed at the beginning of the n△ → (n+1)□ transitions. These exotic structures were found in practically all our experimental wedge cells and can be observed from two to six layers (they have been never observed in the 1△ → 2□ transition). Unlike all the other intermediate structures present in the sequence, they do not form part of the continuous structural changes in the crystalline sequence being these structures separated from the rest by grain boundaries. Many different exotic particle arrangements have been observed forming crystalline domains of small surface area (40-300 μm^2). In Fig.99 the general aspect of these structures is shown. As in the picture, it is often possible to observe two or more of these exotic structures coexisting in the same domain. In that case, a smooth transition between the structures is appreciable. These structures follow the same process of formation as all the other structures. This is shown in FIG. 100. This means that these structures are not the result of particle rearrangements after the application of any external stress.

The identification and characterization of these structures was complicated for several reasons. On the one hand, the particular particle arrangements in these domains generate interference

effects which complicate the identification of the different crystalline layers with the optical microscope. On the other hand, we have found that not all the particles which in principle will belong to the same layer are at the same height. Because of that we have tried to classify these exotic structures assuming that each layer is divided in two sublayers. However, since these structures appear at the beginning of the transition, the relative distance between the different sublayers is very small being these not distinguishable in a typical SEM picture. Fig.101a) shows a SEM picture of one of these regions. Fig.101b) shows the same image after picture enhancement with Image Pro 6. As we see, even after the application of different digital filters and contrast enhancement it is difficult to identify the structure. Because of that, for dry samples we used other imaging techniques like the Atomic Force Microscope. Although the symmetry and periodicity of these structures were slightly modified upon drying, the AFM pictures clearly revealed the existence of height differences between the particles being it possible to verify the presence of new structures as clearly shows Fig.102.

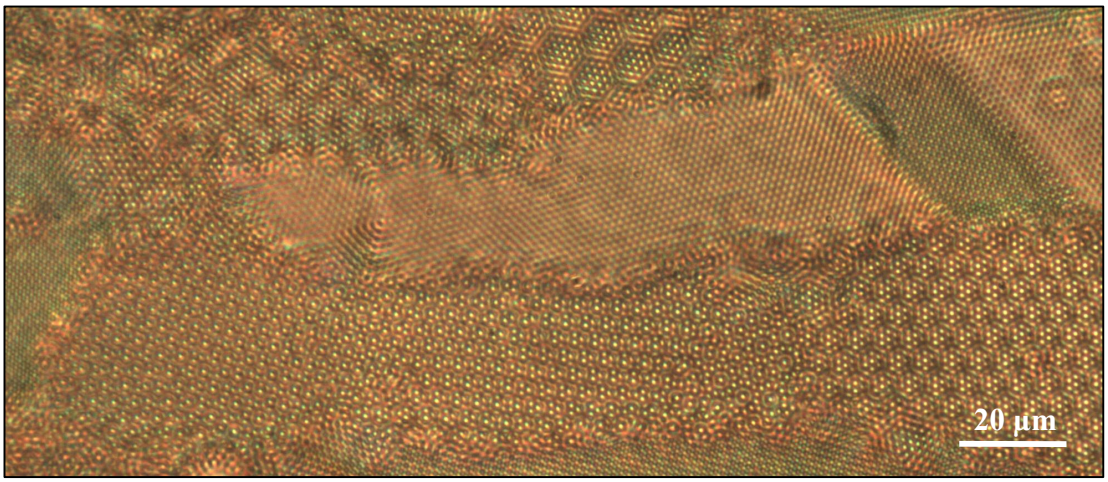

FIG. 99: General view of the superstructures found al the beginning of the 3△ → 4□ transition, In this picture they appear together in the same crystalline domain but also these domains can be characterized by only one particle arrangement.

Although the origin of these structures is still unclear, from the experimental results we can see these structures as stacked hexagonal layers subject to periodic or aperiodic lattice dislocations. With this simple definition we can just describe these structures as a hexagonal lattice with a basis composed by different groups of particles which form different motifs. Structural models are going to be proposed for the simplest cases where the structures are assumed to be periodic. Since in these

structures only the first layer was clearly distinguishable, the models were built starting with the particle coordinates of these layers obtained from the real space pictures. Next pairs of layers were assumed to be identical as the first pair being stacked at specific positions. Once the modelling was done, the corresponding diffraction pattern was calculated and compared with the intensity distribution observed in the experiments. To calculate the diffraction patterns we used special software for crystallography (CaRIne). The similarities found between the experimental diffraction pattern and the one derived from the modelling of the structures reinforces the proposed models. We will also show other exotic arrangements where no model is proposed for them. Although in principle these structures have no atomic counter part in the discussion we will compare with other physical systems where similar structures where observed.

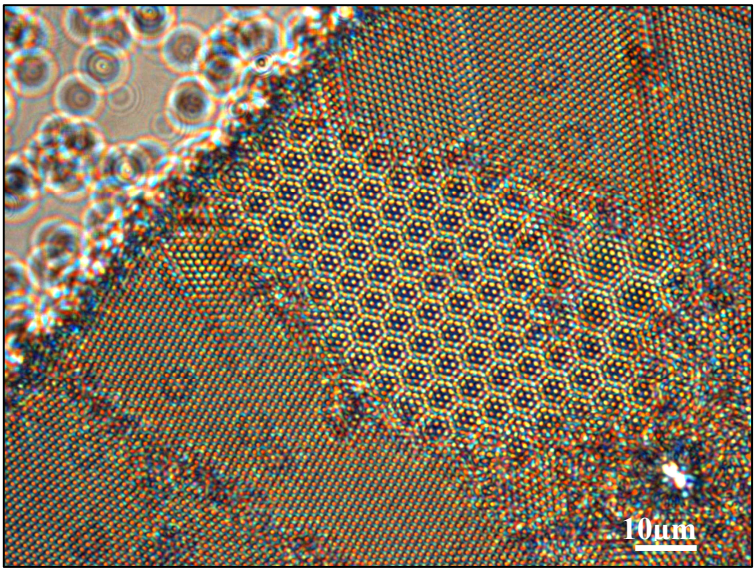

FIG. 100: The formation of these structures does not arise as a consequence of any additional mechanism. As we can se in the picture the crystal formation follows the same growing process as in the other structures..

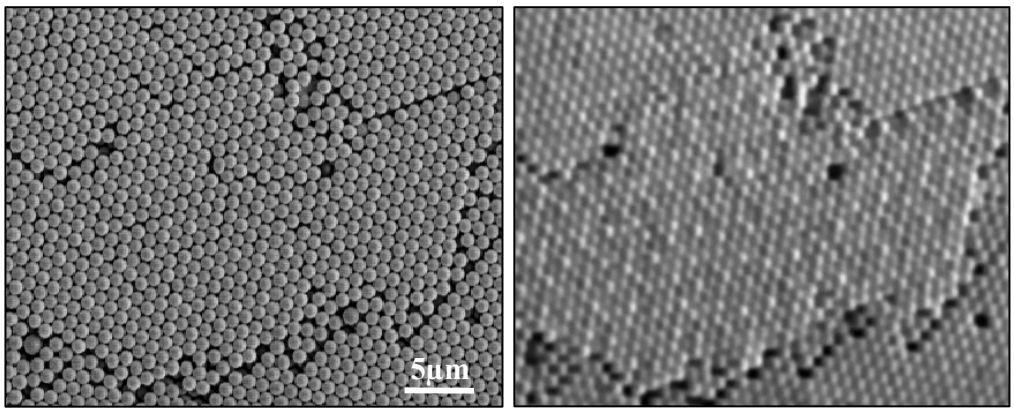

FIG.101 Scanning Electron Microscope picture a) before and b) after digital enhancement.

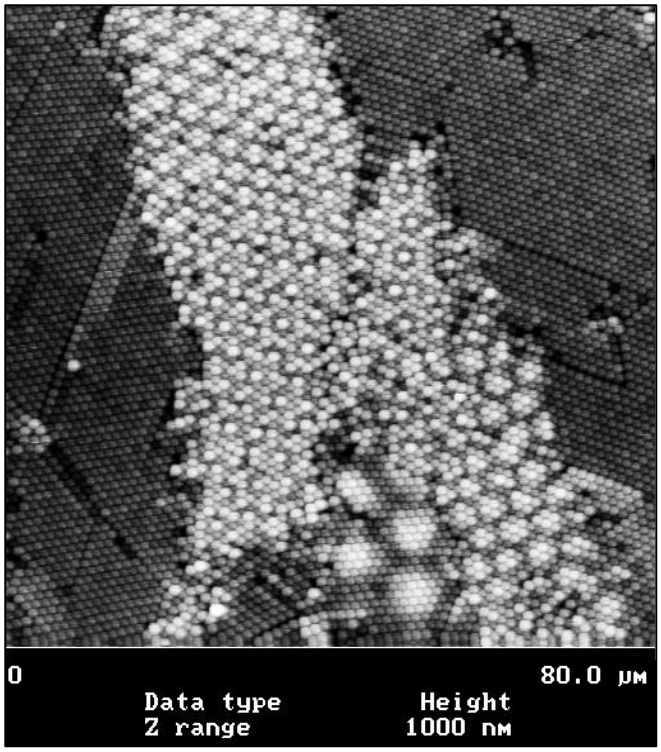

FIG.102: AFM picture showing different exotic arrangements.

9.2 The n-S1 Structures

In general this structure is characterized by hexagonal lattice planes where the basis consists of particles grouped forming hexagons. These hexagons are equally oriented and they are shifted respect to the perfect hexagonal packing by $\sigma/2$. Inside the n-S1 structures we find many different kinds of possible configurations. The different size of the basis leads to hexagons formed by seven (n-S1-A) and nineteen (n-S1-B) particles. At the same time not all the particles in the basis are at the same height and it seems that there is not a preferential arrangement. This is shown in Fig.103. Three basis of the structure have been highlighted to easily identify the hexagons. The increment of height allows different possibilities for the arrangement of particles in the basis. As a result it is possible to observe different ordered structures and also this kind of irregular arrangement.

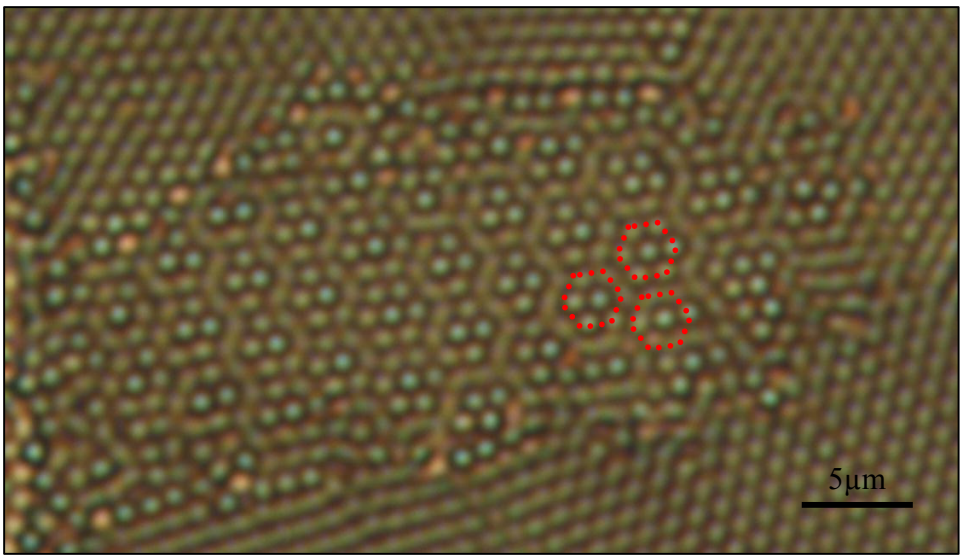

FIG.103: The 2-S1-A structure showing aperiodic arrangement. Three hexagonal basis have been highlighted for clarity. The lattice is periodic but particles in the basis are irregularly distributed.

In all cases the aspect of the structures observed with the microscope reminds of a wavy surface. In other words, the particles seem to build a bucked-like macrostructure where the particles are just placed to result in a continuous curvature. The continued bended effect is more pronounced as more particles form the basis. This buckling-like geometry is not necessarily symmetric being possible to observe tumbled-like hexagons oriented in different directions. For the n-S1-A structures where the basis posses the minimum size these particle arrangements result in the observation of different periodic motives where one, two or more particles are grouped at height different from the rest. However all of them are characterized by a similar intensity distribution in their corresponding diffraction patterns. This is the main reason to group these structures under the n-S1 definition. Fig.104b) as well as Fig.104c) show the complex diffraction patterns for the n-S1-A and n-S1-B structures respectively. Six weak intensity spots at low scattering angles indicate the hexagonal symmetry of the lattice. For higher angles we observe two patterns of six bright spots rotated respect to each other by an angle which varies from 10° to 15°.

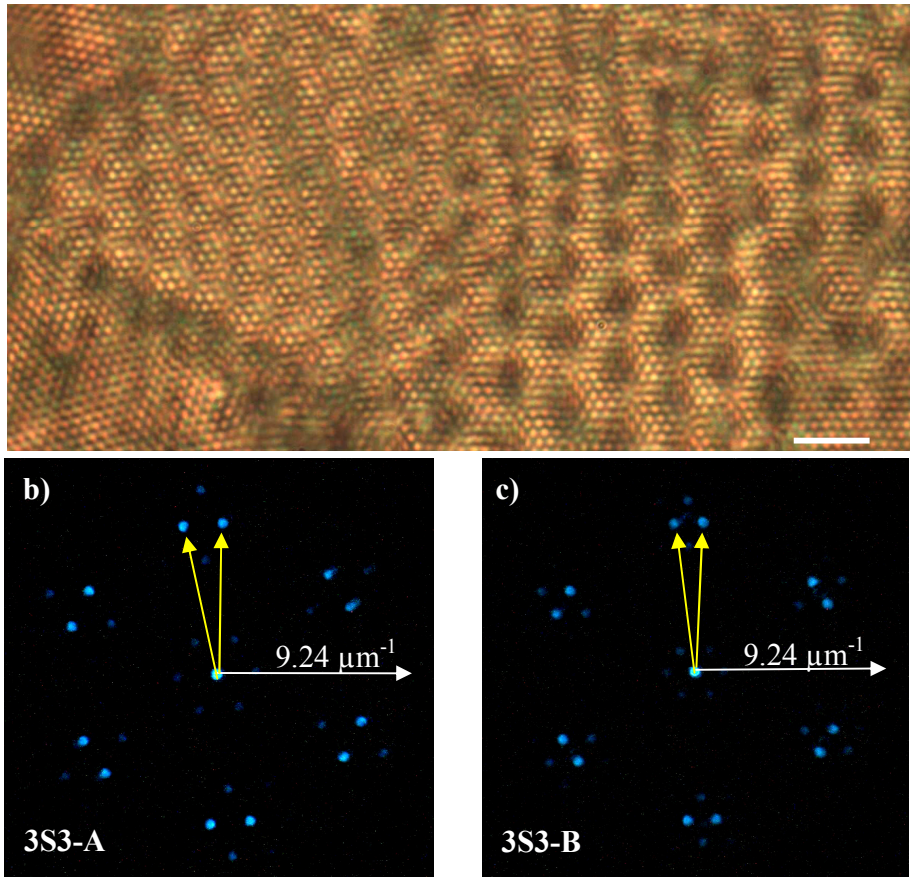

FIG. 104: a) Two different 3-S1 superstructures characterized by a hexagonal lattice. The basis of the 3S1-A crystalline structure has seven particles whereas the basis of the 3S1-B has nineteen particles. Pictures b) and c) show the correspondent experimental scattering patterns of both structures.

The irregular distribution of the particles in the basis makes it difficult to model such structures. The reason is that in the real crystal there is more than one way in which the buckled hexagons appear. Consequently, this will also strongly influence the particle positions of next layers which still complicate more the modelling. In Fig.105 we can see high resolution pictures of three different particle arrangements that can be considered as representatives of the n-S1-A structure. Below the pictures their corresponding layer model is also shown highlighting the hexagons of the basis in red just for clarity. They were modelled following the experimental observations. The different colours indicate the different sublayers. In the simplest case (Fig.105 a) and d)) the central particle of the basis appears at different height from the rest. It is also frequent to observe groups of three particles forming trimers. In that case they generate a pattern as observed in Fig.105 b) and e).

It also is possible to observe groups of four particles forming rhombus where the two central particles are a little bit higher than the other two (Fig.105 c) and f)).

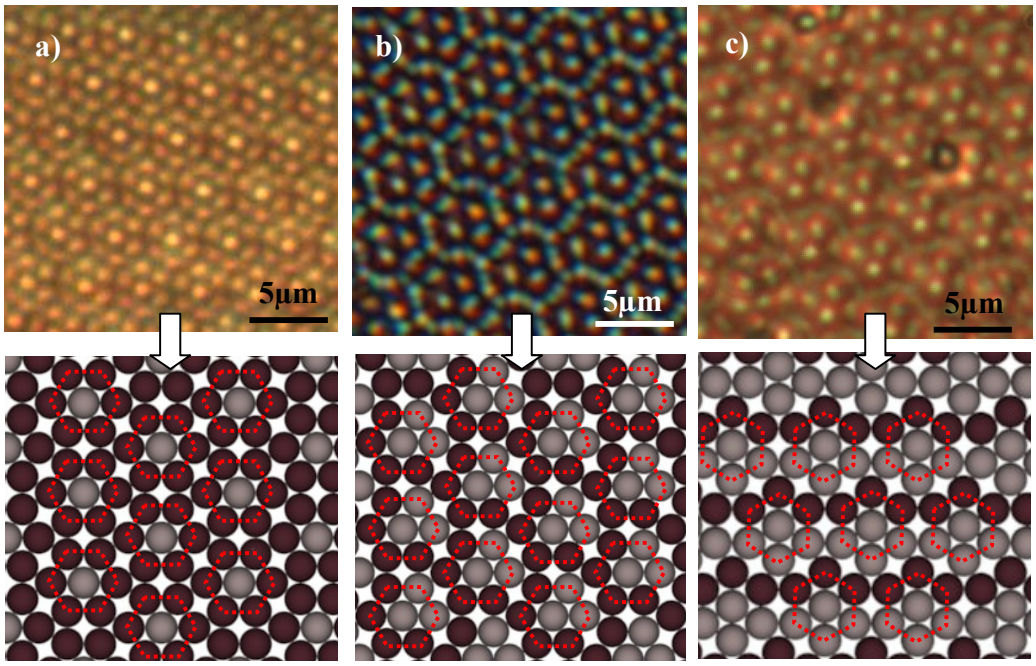

Fig 105: Different sublayer orderings for the n-S1-A structure with the corresponding layer modelling. The different colours indicate different particle heights which range from 0.1 µm to 0.3 µm. In all cases we can define a hexagonal lattice. The different models arise from varying the motifs of the basis. For details see text.

We modelled the S1-A structure for the simplest case, that is, we propose a two layer system where for each layer the central particles in the hexagons are at different height from the surrounding particles. In the modelling of the S1-A structure each layer is a hexagonal lattice described by a lattice unit cell of lattice constants a, b and c. At the same time, each layer is formed by two sublayers. The first sublayer consists of a particles placed at the lattice points (blue particles in Fig.106 c)). The second sublayer is characterized by six particles arranged around the particle in the first sublayer (Fig.106 c) in red). The vertical shift between the sublayers varies with the cell height up to $\Delta z \approx 1/3\ \sigma$ where σ is the diameter of the particle. In our model each subsequent layer is shifted laterally by a = 2/3 and b = 1/3 (Fig.106c) particles in light blue and pink). The scattering pattern calculated from that model (FIG. 106 d)) matches the experimental one (FIG. 106b)) except for some small deviations around a scattering vector $q \approx 9\mu m^{-1}$. These differences could arise from a different disposition of successive layers in the real structure.

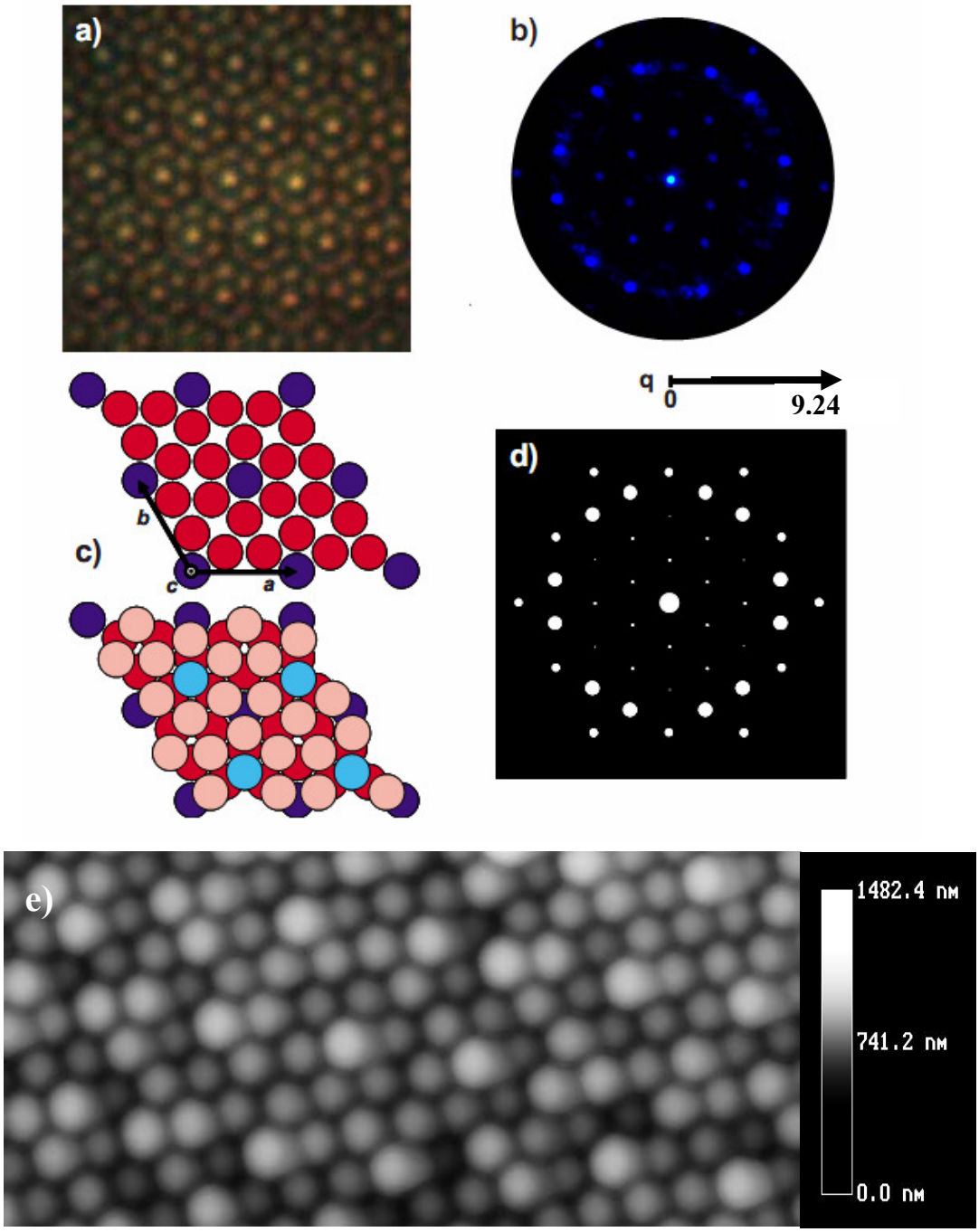

FIG.106: Real model proposed for the 2-S1-A structure in the simplest case; the central particle of the hexagon which forms the basis is a different height than the other six particles. a) and b) experimental observations in real and reciprocal space. c) Proposed structure model. d) Calculated diffraction pattern with CaRIne. e) AFM picture of the same structure after drying where it is possible to observe the changes in symmetry and the loss of periodicity of such structure [Fon08].

In Fig.106e) it is possible to observe the changes in symmetry of this structure after drying. The image was obtained from scanning with an AFM in non contact mode over the surface of a 2S1 structure. The picture shows how the first sublayer remains unaltered whereas in the second sublayer the twins have disappeared. Now the structure just reminds of a hexagonal layer where a periodic distribution of particles with hexagonal symmetry is slightly shifted in the vertical direction. In this picture it is also possible to observe the loss of periodicity in layer one. The measured height differences between the sublayers in the dry state vary between 0.1 and 0.3 µm.

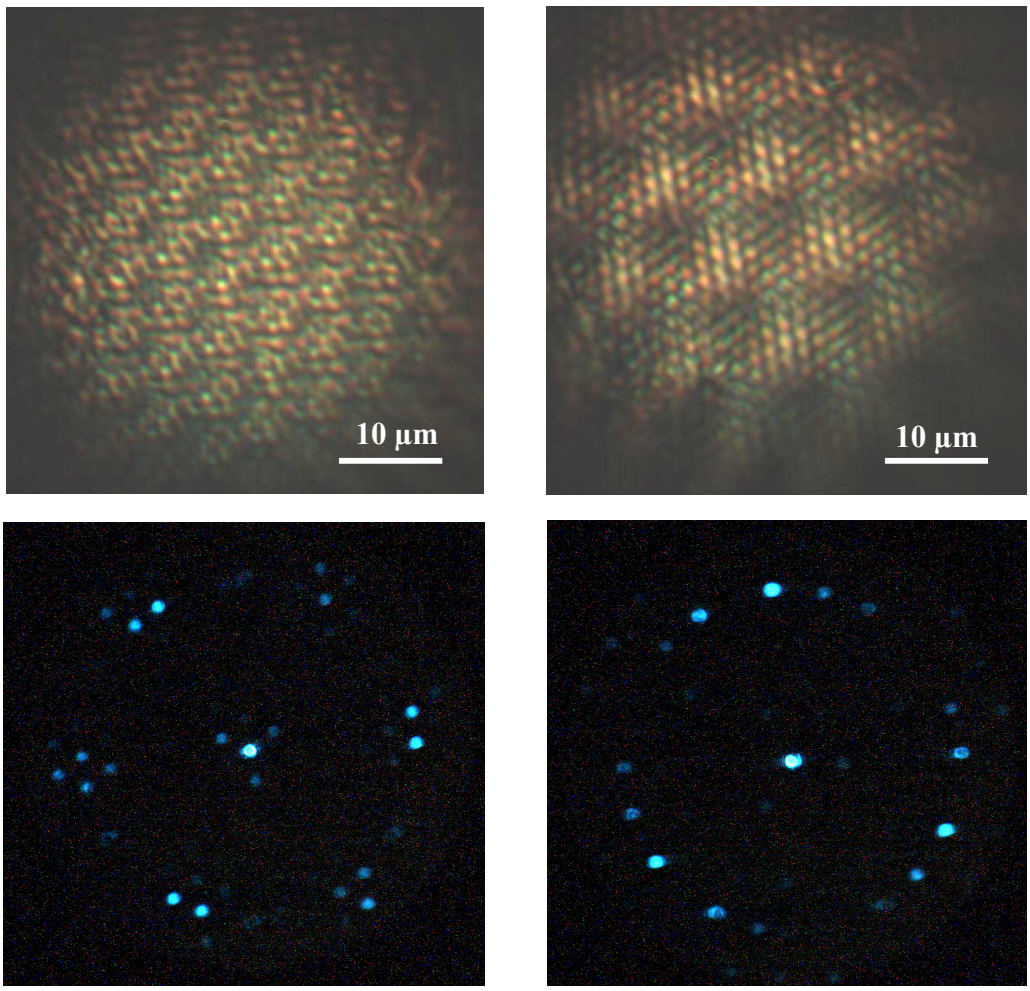

FIG. 107: 3S structures A and B respectively with hexagonal ABC stacking. The intense spots are indications of the original three-fold symmetry as in the case of non-twinned fcc crystals.

The modelling for the rest of structures belonging to the n-S1 group was more complicated being possible to obtain acceptable results only for the modelling of the first layer assuming that in there all the particles were at the same height. However we did not obtain successful results for our models since with only one layer with all the particles placed at z = 0, no information is obtained about the lattice symmetry. For more than three layers it is difficult to obtain information about the layer arrangements. However the diffraction patterns give a hint about the stackings sequence. In particular for some structures we can recognize the three fold symmetry of the fcc structure whereas in others the hexagonal symmetry remains. This is an indication that we have underlying hexagonal structures with ABA are the corresponding to Fig.104 whereas examples of those with ABC stacking are shown in Fig.107.

9.3 The n-S2 Structure

Other arrangement present in these domains is the corresponding to the superstructures n-S2. The structure shown in FIG. 105a) is characterized by a dodecagonal motif which remembers the $(Ta,V)_{151}Te_{74}$ clusters found in atomic systems after crystallization [Kru00]. The first layer corresponding to the modelling (Fig.108c) dark green and dark blue particles) is again an hexagonal lattice with a basis with lattice constants a, b and c composed by twelve particles forming a dodecagon and a particle in the center. The central particle coincides with the points of the hexagonal lattice. The second layer (Fig.108c)) in red) consists of hexagons formed by six particles around the central particle of the first layer. The relative distance between layers will depend on the cell thickness being $\Delta z \approx 2/3\ \sigma$ the maximum vertical shift. Next layers will appear pairwise laterally shifted respect to the first one by a = 1/3 (Fig.108c) bottom). The scattering pattern calculated with CaRine from the model reflects the experimental one quite well. Once the sample is dry the structure slightly looses its symmetry and periodicity as shown in Fig.108e). The measured height differences between the sublayers in the dry state vary between 0.1 and 0.3 μm. This structure gives rise very often to the appearance of quasicystalline order of twelve-fold symmetry as shown in Fig.109.

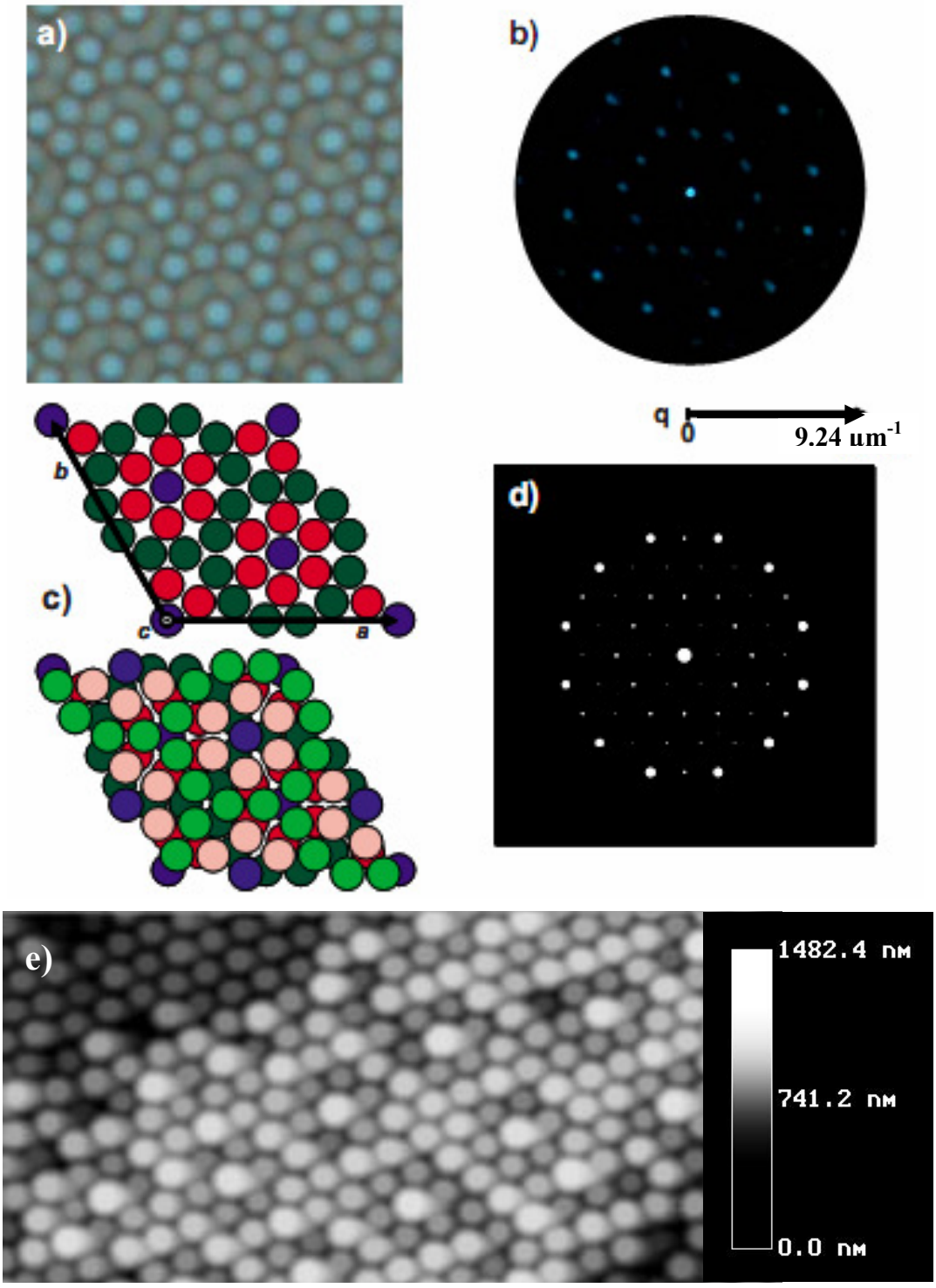

FIG. 108: a) Light microscopy picture of the 2S2 structure. b) Scattering pattern. c) Proposed model for two a pair of layers. d) Calculated scattering pattern obtained with CaRIne. e) AFM picture showing the loss of symmetry and periodicity of such structures after drying [Fon08].

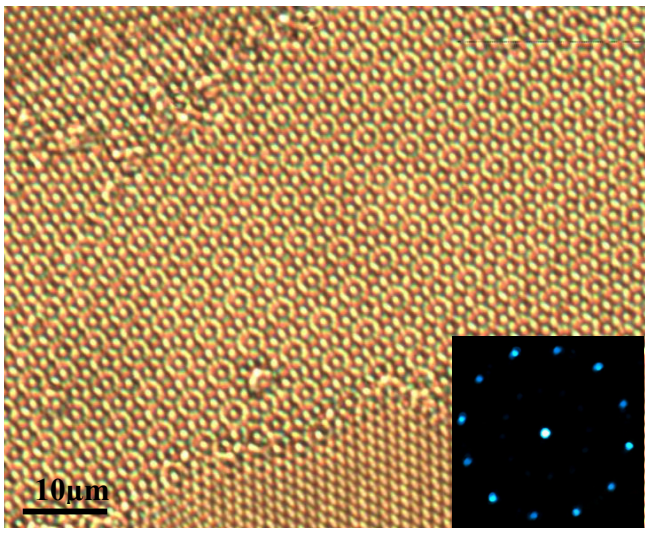

FIG.109: The n-S2 structure in its aperiodic arrangement has the aspect of quasycristalline order twelve-ford symmetry as is confirmed by its diffraction pattern.

9.4 Other arrangements

We also found other arrangements which appear only occasionally in the wedge cells. For instance in Fig.110 we show a structure which similar to the n-S1 structures. However in this case the dislocations seem to occur only in the vertical direction. As a result we observe a honeycomb motif which conserves the particles alignment of the original hexagonal layers.

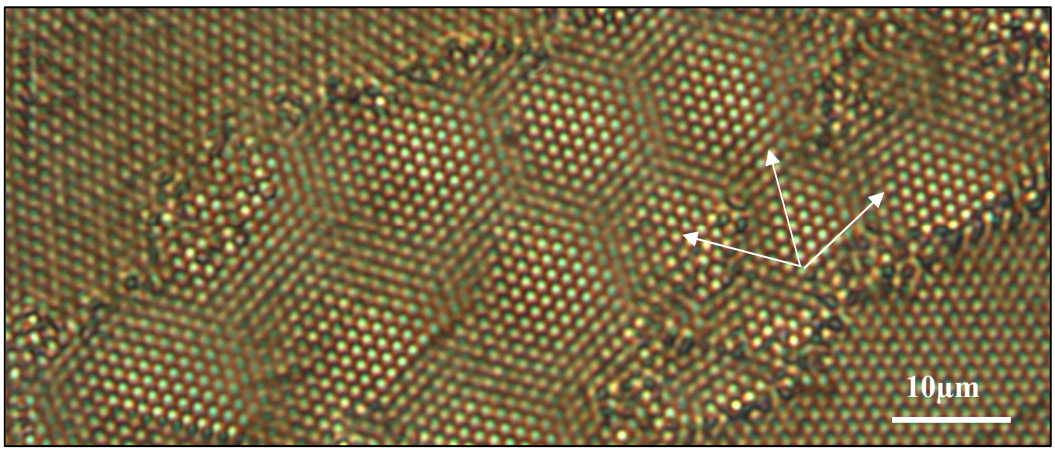

FIG.110: Other possible arrangement found at the beginning of the n△ → (n+1)□ transition. Although this kind of ordering is similar to the n-S1 structures, in this case the hexagonal motifs maintain the original particle alignment of the hexagonal planes as indicated the white lines.

We have also observed regions where the dislocations result in the observation of a rhombohedric motif as shown in Fig.111. These domains have been observed only once in one of our wedge cells. This arrangement seems simpler that former cases and unlike the former structures, it is not separated from the rest by grain boundaries. This suggest the possibility that the origin of this crystalline structure is based in the intergrowth of two initial $n\mathcal{P}_{\triangle}$ phases with different orientation.

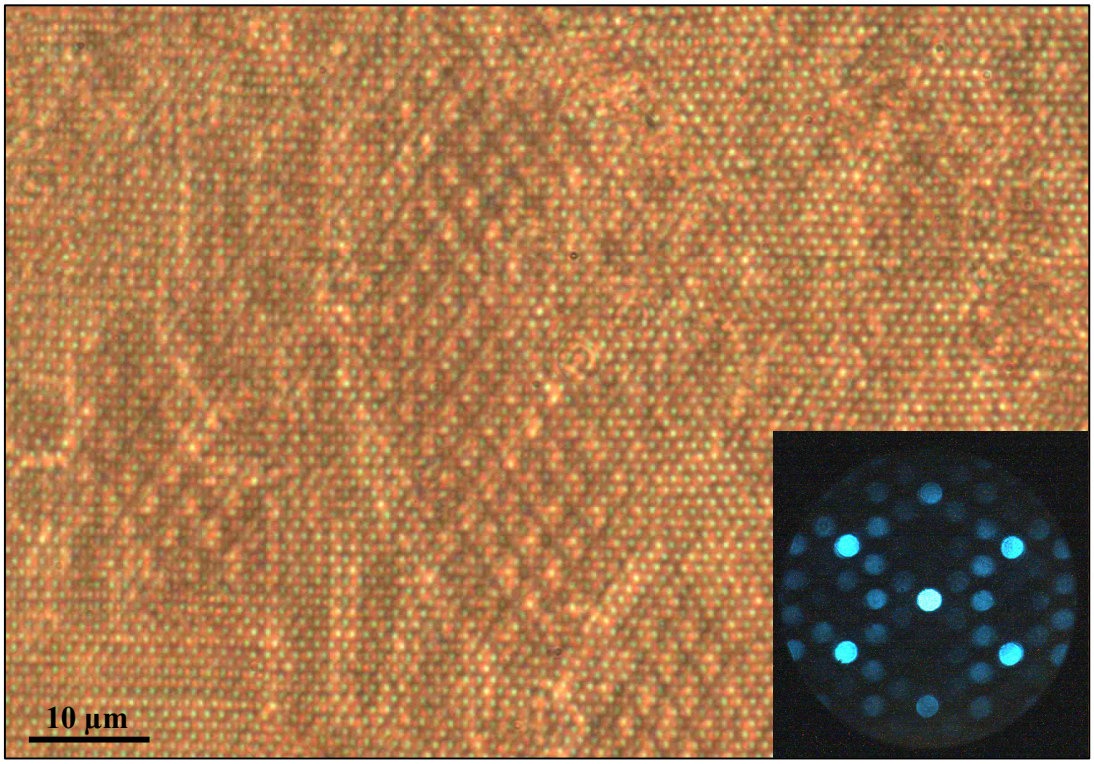

FIG.111: Other possible arrangement for the particles at the beginning of the n△ → (n+1)□ transition. In particular the picture corresponds to n = 2.

9.5 General discussion

New particle arrangements of charged colloidal particles in confinement have been presented. The description of the former structures was made assuming long orientational and translational order for simplicity. In this sense they can be described as a complex structures or superstructures characterized by a hexagonal lattice and a complex basis or cluster. However the structures coexist and smoothly transforms from one particular arrangement to the other as shown in Figs. 99 and 102. We also observed aperiodic arrangement of the structures has been observed in Figs.103 and 109.

For the n-S1 structures the aperiodic arrangement is given in terms of changes in the size of the basis – and consequently in the size of the lattice vectors-. This can be clearly seen in the 2-S1-B structure appearing in Fig.100. Other possibilities of aperiodic order for such structures are given for the n-S1-A structures where an asymmetry in the structural motifs of the sublayers is present in the domains, that is, we observe random distribution of the basis elements which characterize a sublayer. In reference to that, it is important to remark here that in the former case no qualitative differences in the diffraction spots have been observed when compared with periodic orderings.

The aperiodicity shown by these structures is even more interesting in the case of the n-S2 structures. In this case the diffraction pattern shows twelve-fold symmetry. Nowadays it is well known that this symmetry is an indication of quasicrystalline order. But, do we really have a crystalline structure or, as in the former cases, is it just the result of two superimposed diffraction patterns rotated 30° (or 90°) one respect to the other? We do not know the answer since no atomic counterpart has been found. However, we have found in the literature some resemblances with complex atomic systems that I pass to describe next.

On one hand we can interpret these structures just as distortion modulated structures. For instance, we find that transition metals dicalchogenides such TaS_2 often yield electron diffraction patterns with spots which do not coincide with superlattice positions [Will74]. The extra spots are interpreted as resulting from periodic lattice distortions. The latter receive the name of structure modulation. In this case the complex structures are considered to be due to rearrangement of atomic vacancies in response to the occurrence of charge-density waves. Similar interpretation about quasicrystalline complex alloys like $Ta_{62}Te_{38}$ has been given from analysis of high-resolution transmission electron microscopy images [Uchi98]. They propose an explanation for the twelve-fold symmetry based again in crystals subject to structure modulation. Their careful analysis of the diffraction patterns hints at interpreting the resulting intensity spots as superposition of two sets of patterns. The sharp and intense diffraction spots originate from an atomic arrangement with long-range translational order, and the weak ones (with smaller q vectors) will be due to structure modulation. Using the same arguments we can give a possible explanation for the symmetry of these complex structures found when confining polystyrene particles. In the real space we observe different hexagonal structures periodically distorted. At the same time, the corresponding diffraction patterns consisting of the superposition of two hexagonal lattices plus satellite spots would reinforce that assumption. Furthermore, the arguments given in reference [Uchi98] easily explain the twelve-fold symmetry characteristic of the aperiodic ordering of the n-S2 structures.

On the other hand, the physical reasons which can explain the origin of these structures are still unclear. In principle the only superimposed restriction in the crystal formation in these experiments lies in the distance between the cell plates. At the same time, unlike all the other structures found in confinement, they are mechanically metastable (attending to their structural changes upon drying). This means that the free energy of these structures is higher than those correspond to the other structures which coexist for similar plate-plate distances. Under identical physical conditions, coexisting crystalline structures must have very small differences in their free energies. As we have explained in Chapter 2 this is just the case of the coexistence of FCC and HCP structures in the n$\triangle$ phase. However this is not what we are observing now. Is it possible therefore that the existence of these structures is due to an increase of the entropy of the system. It is well known that the ordered states of a system have minimum entropy. However the crystallization process implies an increase of the entropy since once the elements of the system are ordered the accessible volume of such system increases. An increase in the volume of the cell implies an increase in the number of possible configurations inside this accessible volume, and hence and increase in the entropy. It is then possible than the existence of these structures has an entropic contribution. Under this situation one can even expect not only aperiodic arrangement but even amorphous structures. Anyway, the question about the small domains and, overall, the specific location of such domains is still open. A possibility is that the existence of these structures arises as the result of intergrowing domains with n-hcp$\perp$ and/or n$\mathcal{P}_{\triangle}$ ordering. Therefore the different arrangements would be due to different crystalline orientation of such structures when forming the intergrowth domains. We have found an interesting work in the literature dealing with the study of twinning and intergrowth domains of boride carbide phases of rare earth metals which would support this hypothesis [Oeck02]. On the other hand we have found a very interesting work related with interference patterns obtained in the surface of a fluid via parametric forces with two commensurate frequencies [Ar02]. They also calculate interference patterns for some of the structures which are shown in Fig.112. I consider these results important since they reinforce the idea of thinking of these new structures just as the resulting arrangement from the intergrowth of other crystalline domains.

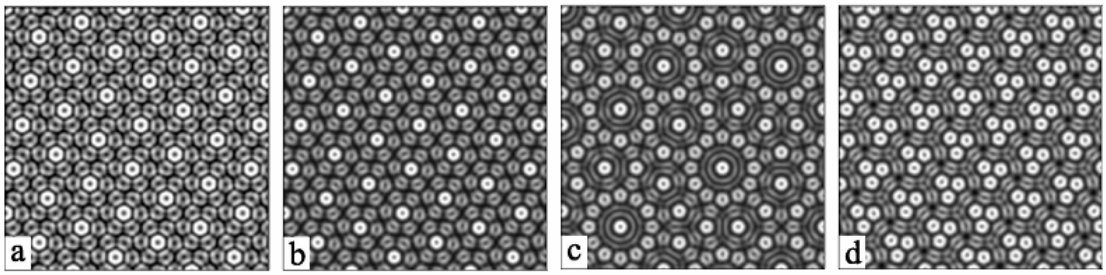

FIG.112: Superlattice patterns calculated for two hexagonal set of wave vectors with harmonic temporal response and rotated by an angle of 22°. The different images correspond to different spatial phase differences except between figures a) and b) where the difference is the time.[Ar02]

Summarizing: new particle arrangements have been observed in the confinement of charged colloidal spheres. They have appeared in practically all the cells under study and for different number of layers. These structures have no atomic counterpart and their physical origin is still unclear. These are complex structures whose particle arrangements give rise to different orderings being possible to even observe twelve-fold quasicrystalline order in some cases. We give here different interpretations for the structure classification as well as their possible physical origin in the sequence. We propose also some structure models to elucidate the particular ordering of the structures. The study presented here is mainly qualitative and further experimental analysis has to be done in order to analyze the origin and stability of these exotic phases.

10 Conclusions and Outlook

The properties of colloidal suspensions are strongly influenced by the presence of solid boundaries. When confining a colloidal fluid of charged particles between two charged plates with wedge geometry, the particles accumulate in the narrow part of the cell forming ordered structures. The experiments showed that this effect is independent of gravity or evaporation currents. Different wedge geometries, tilting angles and salt concentrations revealed a strong trapping effect since the effect is always present. Recent theoretical predictions confirmed by simulations show qualitative and semi-quantitative agreement with our results. Although their work is based on single particles, avoiding many body-effects in the calculation, their results predict a local attractive trapping force of electrostatic origin which draws particles into the wedge. The range of this attraction is of the order of the Debye screening length. For higher distances between the particle and the wedge cusp the interaction force diverges logarithmically being this repulsive. However further theoretical analysis is needed to completely determine the phase behaviour of charged particles confined in wedge-geometries.

The low angles achieved for the wedge cell allowed the observation not only of a rich variety of new structures but also the structural transition which takes place between them. The different particle arrangements follow a well defined structural sequence which depends on the distance between the confining walls. This sequence is of the form, n$\triangle$ $\rightarrow$ intermediate phases $\rightarrow$ (n+1)$\triangle$, where $\triangle$ indicates FCC, HCP or RCP structures where the close packed planes are oriented parallel to the cell plates. Our structural analysis revealed that most of the intermediate arrangements are also

close packed structures with different crystallographic planes parallel to the cell plates or with periodic stacking faults which give rise to the formation of prismatic structures. We have also contributed to the phase diagram Φ-H of hard spheres in the high pressure limit by modelling the solid-solid phase transitions between most of the structures found in the wedge cells. These calculations explain some of the experimental observations found in the wedge. We have also observed exotic structures in small isolated domains which do not form part of the transition mechanism between structures. They have been found forming periodic, aperiodic and even quasi-crystalline structures. We have proposed some simple models in order to elucidate some of these structures. The corresponding diffraction patterns show qualitative agreement with the experimental diffraction patterns. Although the origin of these particular arrangements is unclear, we have found similar diffraction patterns in complex alloys or transition metals compounds subject to structure modulation. Also some resemblances have been found with the superlattice patterns generated on the surface of a fluid via parametric forcing with two commensurate frequencies. These interference patterns hint at interpreting the exotic structures found in confinement as the resulting structures coming from the intergrowth of different neighbour domains with hexagonal prism or vertical HCP symmetries. Other experimental techniques are needed to continue studying these exotic arrangements. One possibility is to use confocal microscopy techniques in order to completely reconstruct all the possible orderings and the differences found as the number of layer increases. Confocal microscopy will be also a useful technique to study the limits of confinement, that is, to study the structural sequence for more than seven layers. At the same time the optical properties of all these new structures are still left. I consider that this kind of study is essential from the point of view of possible applications to novel technologies.

We also have designed a cell with variable height in order to study the phase behaviour of charged spheres confined between parallel plates at different particle densities and salt concentrations. Unfortunately we have found many technical problems and the obtained results can only be considered as preliminary. However I hope that the detailed description of all the problems as well as their interpretation included in this thesis shall be useful for further research. Probably better results as well as more accurate measurements will be obtained using highly charged spheres of smaller size. This implies the use of light scattering techniques or more sophisticated microscopy techniques in order to study the phase behaviour as well as the degenerency of the different phases in detail. In that sense I hope that the qualitative description of the diffraction pattern presented in this thesis as well as the theoretical summary included (with all the corresponding literature) can be

helpful on that purpose. It would be also very interesting to use different confinement geometries in order to obtain quantitative measurements of their influence in the phase behaviour.

I would not like to finish without mentioning the implications of this work from a conceptual point of view concerning the idea of scientific research. At the beginning of this thesis, the field of structural phase transitions of charged spheres at confining geometries subject to a lateral pressure was considered to be well understood. Usually, scientific advances are considered to go a step further in investigations supported by accepted previous results. However most of the relevant results presented here were found at the very beginning of this thesis when trying to reproduce former experiments. First we found unexpected particles behaviour in the wedge cells. But also crystallization of the system in the narrow part of the cell resulted in the observation of many more structures than previously reported. Most part of the time invested in this thesis consists in the study of these new findings and thanks to that, many interesting questions are now open. Further work has to be done not only in the study of the phase behaviour of these systems but also in the optical properties of the confined crystalline structures, the crystal growth mechanism and even about the stability of charged colloidal suspensions of big particles. I strongly hope that the results presented in thesis can suggest many new fruitful ideas.

Appendix: Drawings

1- Spherical open cell

Top plate
Material: Plexiglass

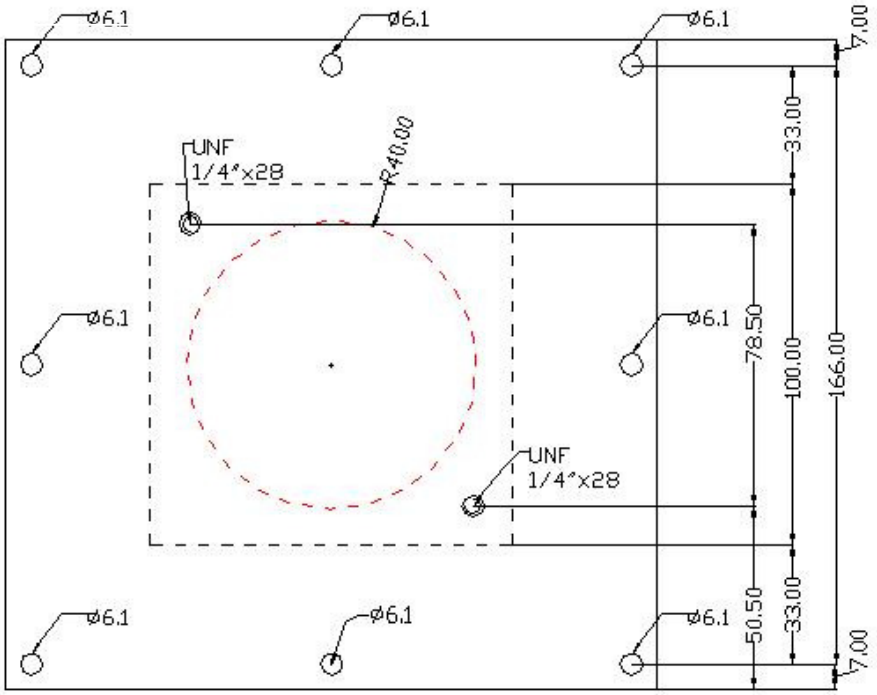

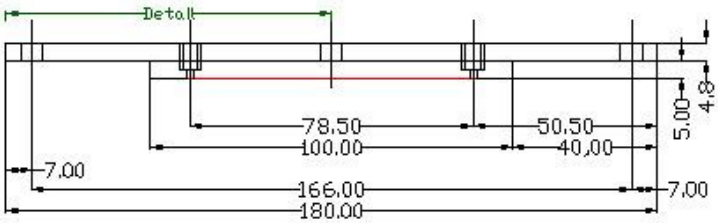

Detail:

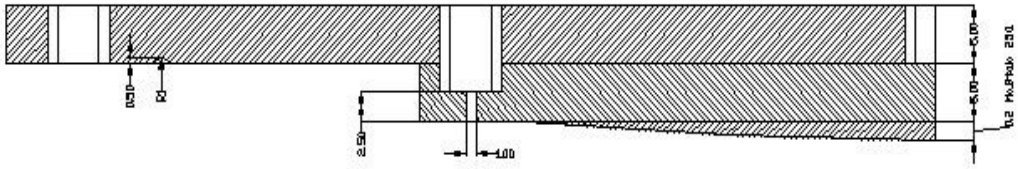

Bottom plate
Material: VA-Steel

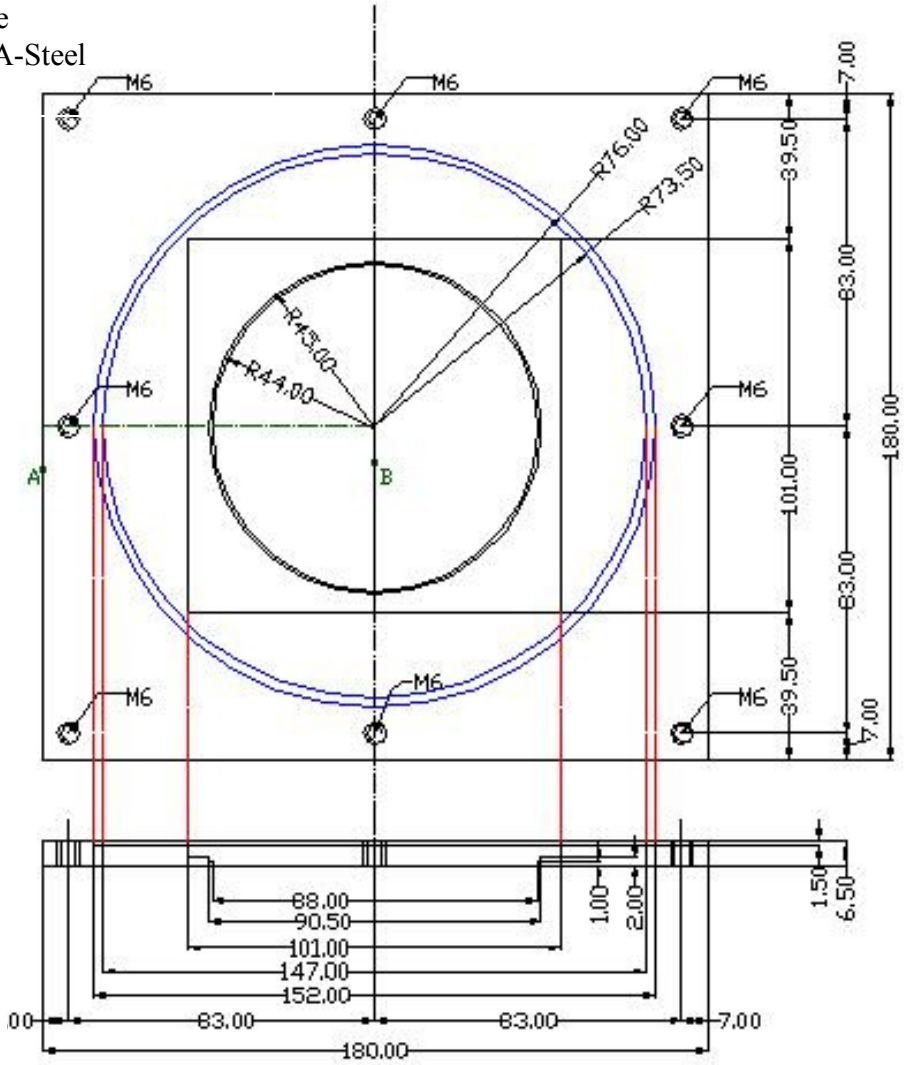

Detail:

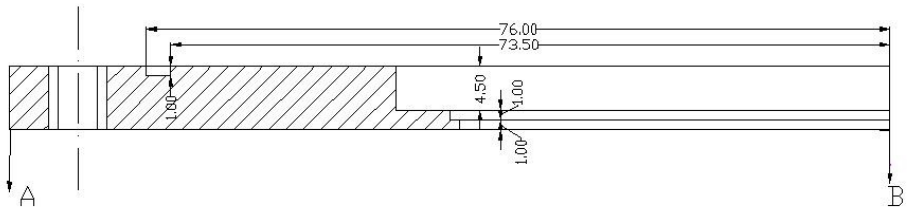

2- Cell with variable height

Top piece for adapting micrometer screws
Material: Messing

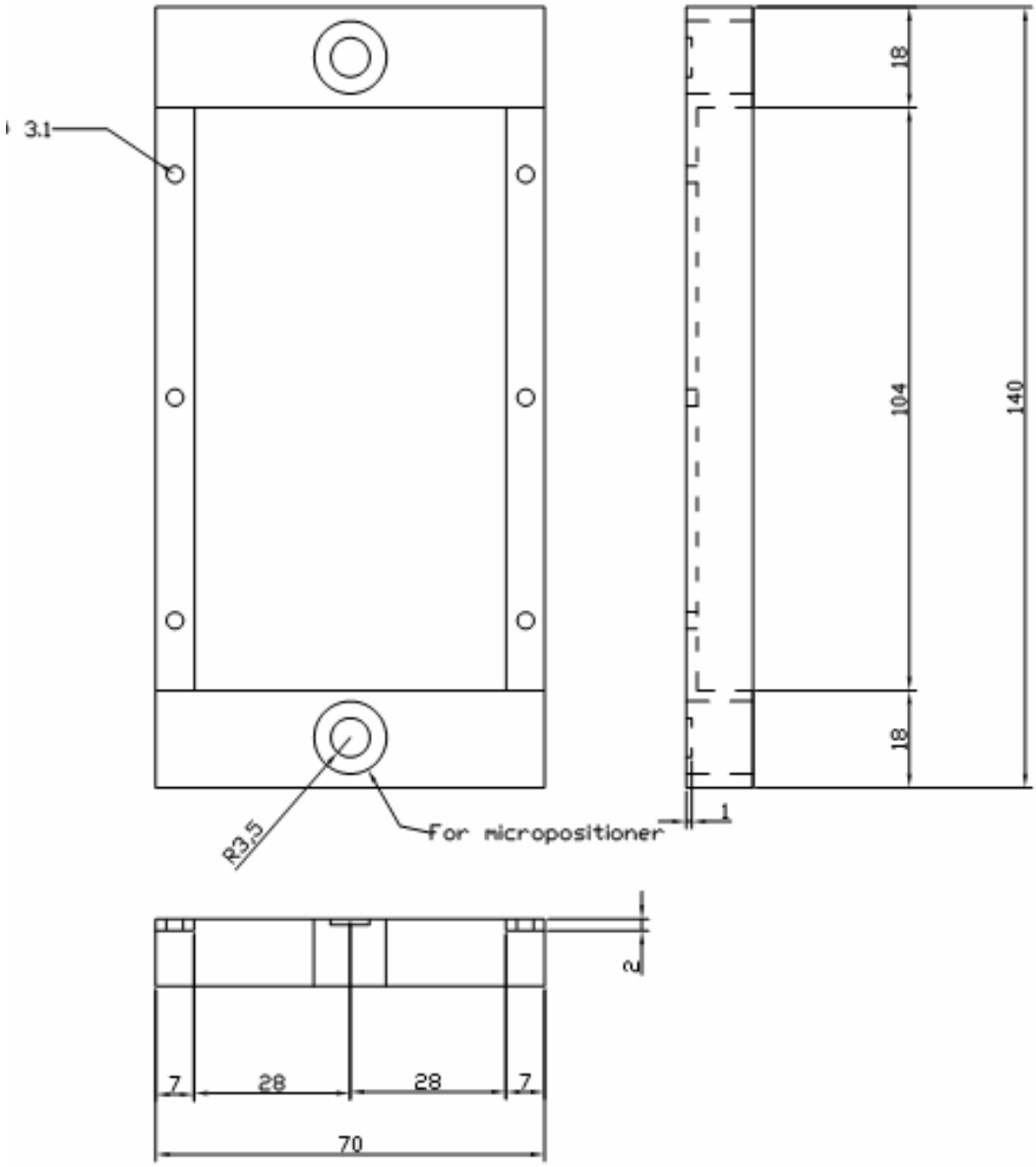

Bottom piece for adapting micrometer screws
Material: Messing

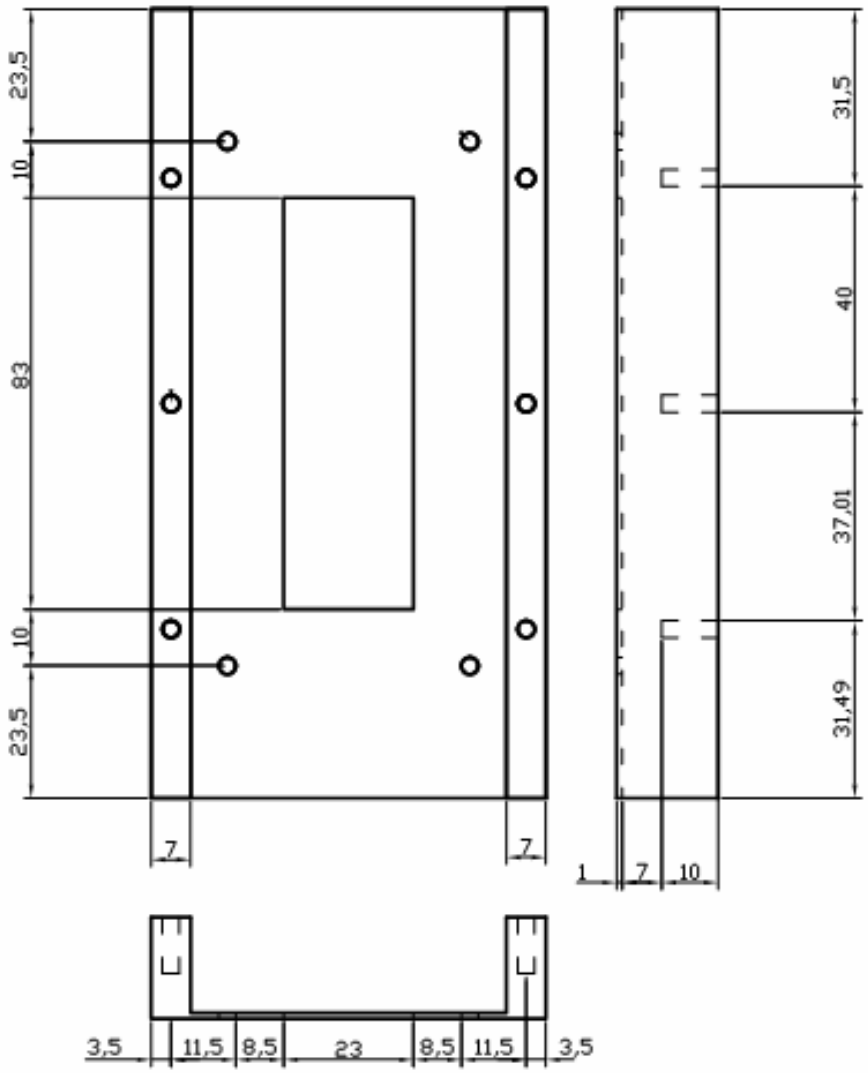

Component between the top messing piece and the upper Plexiglass part

Material: Messing

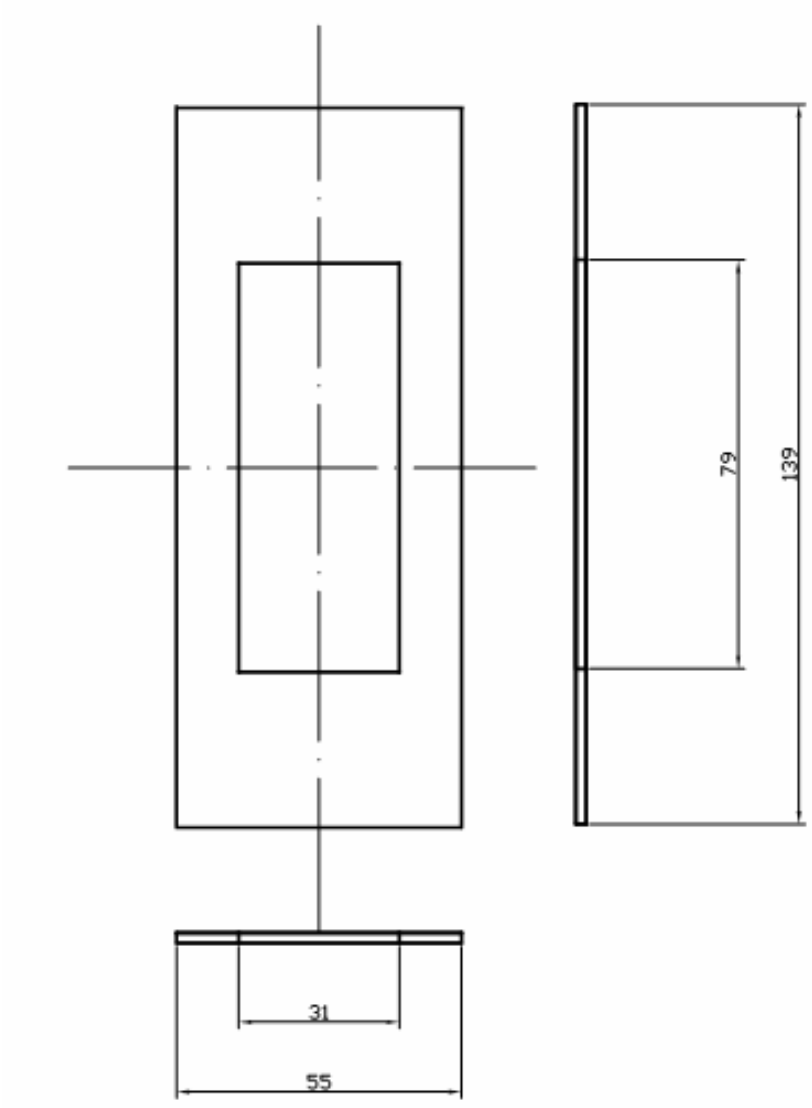

Top confinent cell piece
Material: Plexiglass

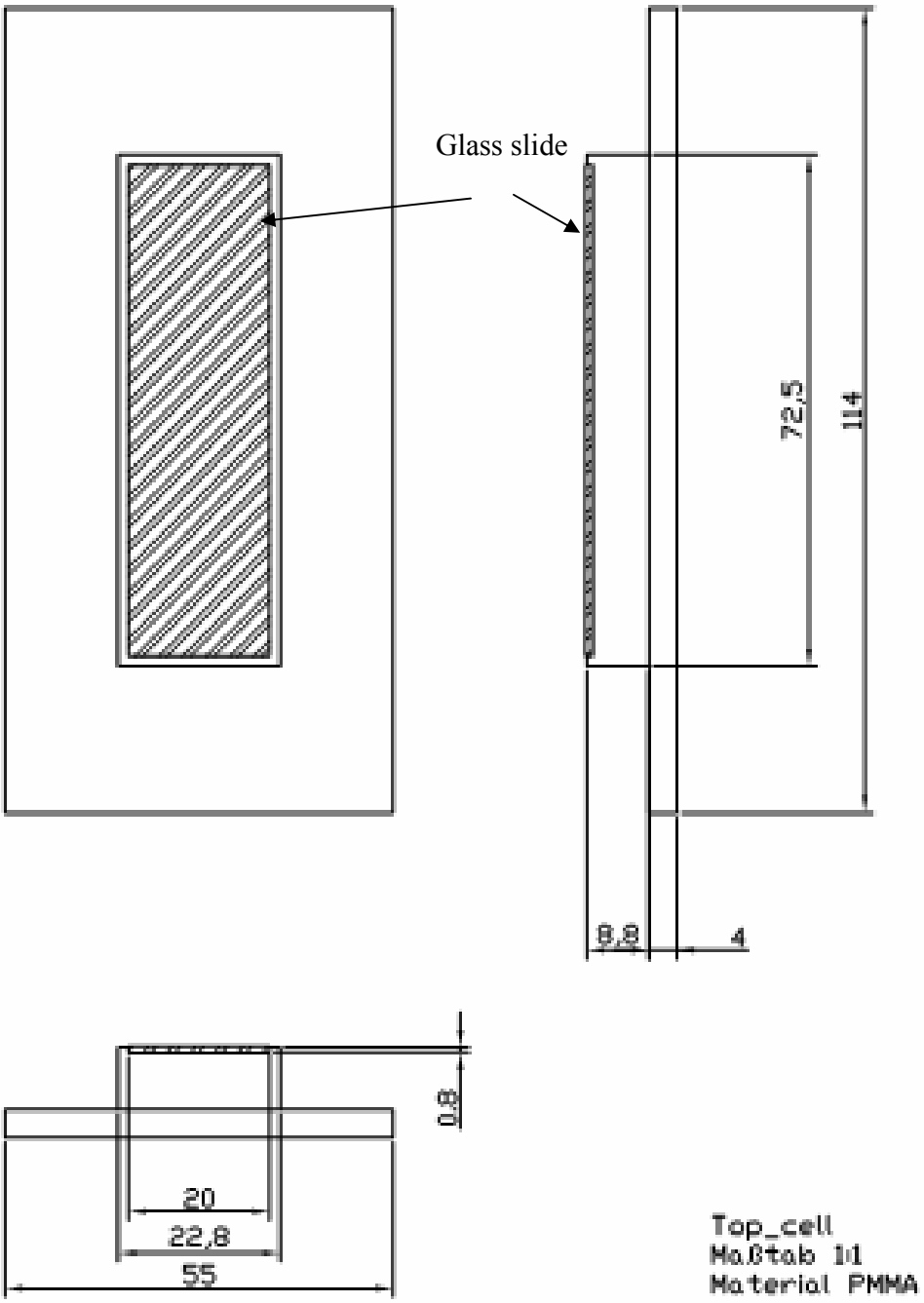

Bottom confinent cell piece
Material: Plexiglass

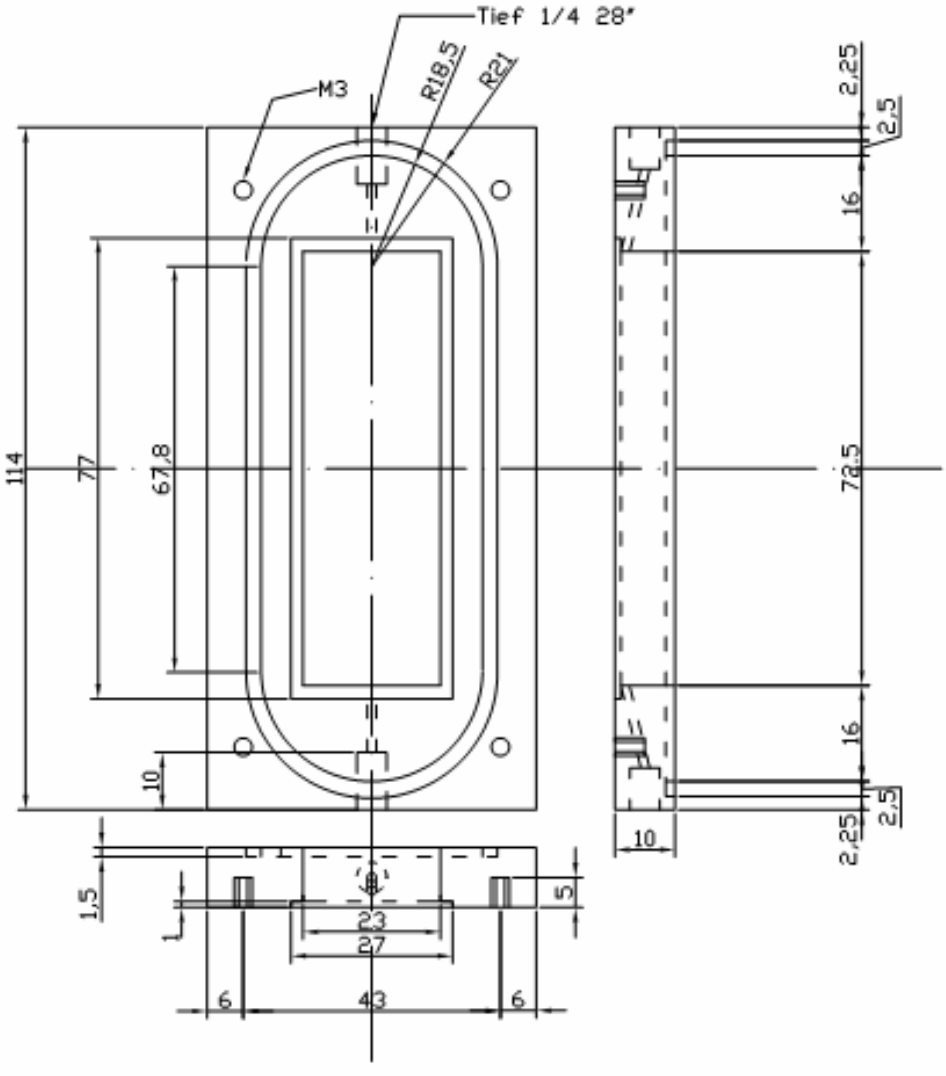

Bibliography

[Ab73] Abbe, E. (1873). *Archiv. Mieroscop. Anat*. **9**, 413.

[Al84] S. Alexander et al, *J. Chem. Phys.* **80**, 5776 (1984)

[Al88] J.V. Alsten, S. Granick, *Phys. Rev. Lett.* **61**, 2570 (1998)

[Ar02] H. Arbel, *Phys. Rev. E* **65**, 036224 (2002)

[Ash76] N. W. Ashcroft and N. D. Mermin, "*Solid State Physics"*. W. B. Saunders Company (1976).

[Baum06] J. Baumgartl, J.L. Arauz-Lara, C. Bechinger, *Soft Matter* **8**, 361 (2006)

[Beh01] S. H. Behrens, D. H. Grier, *J. Chem. Phys.* **115**, 6716 (2001)

[Bell00] L. Belloni, *J.Phys.: Condens. Matter* **12**, R549 (2000)

[Bu99] R. Bubeck, *Phys. Rev. Lett.* **82**, 3364 (1999)

[Bol97] P. G. Bolhuis, D. Frenkel, S.-C. Mau, D. A. Huse *Nature* **338**, 235 (1997)

[Ca04] L. G. Cámara and F. Bresme, *J. Chem. Phys.* **120**, 11355 (2004)

[Cam92] C. Cametti, F.D. Luca, A. D'Illario, G. Briganti, M. A. Macri in "*The Structure and Conformation of Amphiphilic Membranes"*, edited by R. Lipowsky, D. Richter and K. Kremer, Springer *Proceedings in Physics* Vol. **66** (Springer-Verlag, Berlin 1992)

[Chai82] P. M. Chaikin et al, *J. Colloid Interface Sci.* **89**, 555 (1982)

[Cho93] T. Chou, D. R. Nelson, *Phys. Rev. E* **48**, 4611 (1993)

[Cho05] Y.-S. Cho et al. *J. Am Chem. soc.* **127**, 15968 (2005)

[Coh04] I. Cohen, T. G. Mason and D. A. Weitz, *Phys.Rev. Lett*. **93**, 0460011 (2004)

[Cow80] R. A. Cowley, *Adv. Phys*. **29**, 1-110 (1980)

[Cui01] S.T. Cui, P.T. Cummings, H.D. Cochran, *J. Chem. Phys.* **114**, 7189 (2001)

[Dee97] R. D. Deegan, O. Bakajin, T. D. Dupont, G. Huber, S. R. Nagel, T. A. Witten, *Nature*, **389**, 827 (1997)

[Den92] N.D.Denkow et al. *Langmuir* **8**, 3183 (1992)

[Dhont83] J. K. G. Dhont, *Physica A* **120**, 238 (1983)

[Dhu74] S. S. Dhuking, B. V. Derjaguin, Surface and Coll. Sci. vol 7 ed Matijevic E (New York: Wiley)

[Dins99] A. D. Dinsmore, *Langmuir* **15**, 314 (1999)

[Ev98] M. Evers et al. *Phys. Rev. E* **57**, 6774 (1998)

[Fon05] A. B. Fontecha, et al., *J. Phys: Condens. Matter* **17**, 2779 (2005)

[Fon07] A. B. Fontecha, H. J. Schöpe, T. Palberg, *Phys. Rev. E* **76**, 050402 (2007)

[Fon08] A. B. Fontecha, H. J. Schöpe, *Phys. Rev. E* **77**, 061401 (2008)

[For06] A. Fortini, M. Dijkstra, *J. Phys: Cond. Matter* **18**, L371 (2006)

[Gall67] J. G. Gall, *J. Cell. Sci.* **2**, 163 (1997).

[Gas78] J. D. Gaskill. "*Linear Systems, Fourier Transforms and Optics"*, John Wiley & Sons (1978)

[Gat99] B. Gates, Y. Yin, Y.N. Xia, *Chem Matt.* **11**, 2827 (1999)

[Geo08] K. Georgieva, A.Jurjiu, N. Willenbacher, D. Dijkstra, to be published. e-address: http://digbib.ubka.uni-karlsruhe.de/volltexte/1000008614 (2008)

[Gol96] G. Goldoni, F. M. Peeters, *Phys. Rev. B* **53**, 4591 (1996)

[Gre94] M. Greene, D. Hammer, W. Olbricht, *J. Coll. Int. Sci.* **167**, 232 (1994)

[Gui63] A. Guinier. "*X-Ray diffraction*", W. H. Freeman and Company, (1963)

[Hach74] S. Hachisu, Y. Kobayashi, *J. Colloid Interface Sci.*, **46**, 470 (1974)

[Hach90] S. Hachisu, *Phase Trans.* **21**, 243 (1990)

[He86] E. Hecht, A. Zajac. "*Optics"*, Addison-Wesley Publishing Company (1987)

[Hess00] D. Hessinger, M. Evers, and T. Palberg, *Phys. Rev. E* **61**, 5493 (2000).

[Hulst81] H. C. van de Hulst, "*Light Scattering by Small Particles*", New York, Dover (1981)

[Hun86] Foundations on Colloidal Science (Volume I), R. J. Hunter. Oxford University Press Inc., New York (1994)

[Ib02] H. Ibach, *"Solid-State Physics: An introduction to Theory and experiment."* Springer-Verlag Berlin (2002).

[Kamp05] U. Kamp, *Adv. Mater*. **17**, 438 (2005)

[Kit76] C. Kittel, "Introduction to Solid State Physics" 5th Edn, Ch1. Wiley, New York, (1976)

[Kle95] J. Klein, E. Kumacheva, *Science* **269**, 816 (1995)

[Koch05] H. Koch, C. Radin, L. Sadun, *Phys. Rev. E* **72** 016708 (2005)

[Kra94] *Capillary Forces between Colloidal Particles*, P.A. Kralchevsky and K. Nagayama, Langmuir 10, 23 (1994).

[Kri07] M. Krishnan, I Mönch and P. Schwille, *Nano Letters* **7**, 1270 (2007)

[Kru00] F. Krumeich et al. Matherials Sci. & Eng. **294-296**, 152 (2000)

[Lan95] H. Lange, *Part. Part. Syst. Charact*. **12**, 148 (1995)

[Lau97] N. Lauinger, M. Pinnow, E. Görnitz, *J. Biol. Phys.* **23**, 73 (1997)

[Lid90] David R. Lide, *CRC Handbook of Chemistry and Physics*, 71 ed. Boca Raton, Ann Arbor, Boston: CRC Press, 1990-1991.

[Liu00] J. Liu, H. J. Schöpe, T. Palberg, *Part. Part. Syst. Charact.* **17**, 206 (2000)

[Loo94] W. Loose, B. J. Ackerson, *J. Chem. Phys.* **101**, 7211 (1994)

[Lö01] H. Löwen, *J. Phys.:Condens. Matter* **13**, R415 (2001)

[Lö08] H. Löwen et al., *J. Phys: Condens. Matter* **20**, 404221 (2008)

[Luck63] W. Luck, M. Klier, H. wesslau, Ber. Bunseges, *Phys. Chem.* **67**, 75 (1963)

[Ma03] V.N. Manoharan et al., *Science* **301**, 483 (2003)

[Mau99] S.-C. Mau, D. A. Huse, *Phys. Rev. E* **59**, 4396 (1999)

[Mes03] R. Messina, H. Löwen, *Phys. Rev. Lett.* **91**, 248301 (2003).

[Mil95] F. J. Millero, *Geochim. Cosmochim. Acta* **59**, 661 (1995)

[Mo89] Y. Monovoukas, A.P. Gast, J. Colloid Interface Sci. **128**, 533 (1989)

[Mur87] C. A. Murray and D.H. van Winkle, *Phys. Rev. Lett.* **58** 1200 (1987)

[Mur01] D. B. Murphy, "Fundamentals of Light Microscopy and Electronic Imaging", John Wiley & Sons, INC (2001)

[Nes97] S. Neser, T. Palberg, C. Bechinguer, P. Leiderer, *Progr. Colloid Polym. Sci.* **104**, 194 (1997)

[Nes98] S. Neser, PhD Thesis (1998)

[Neser97] S. Neser, C. Bechinguer, P. Leiderer, T. Palberg, *Phys. Rev. Lett.* **79** 2348 (1997)

[Net92] R. R. Netz, in "*The Structure and Conformation of Amphiphilic Membranes"*, edited by R. Lipowsky, D. Richter and K. Kremer, Springer *Proceedings in Physics* Vol. **66** (Springer-Verlag, Berlin 1992)

[Net06] A. van der Net et al. *Soft Matter* **2**, 129 (2006)

[Neu 99] J. C. Neu. Phys. *Rev. Lett*. **82**, 1072 (1999)

[Oka00] T. Okamoto, I. Yamaguchi, *Opt. Letters* **25**, 372 (2000)

[Oku07] T. Okubo, N. Nakagawa, A. Tsuchida, *Coll. Pol. Sci.* **285**, 11 (2007)

[OSh08] P. O'Shea, M Somekh, W. Barnes, "Shedding Light on Life", www.pysicsworld.com (2008)

[Pal92] T. Palberg et al. *J. Phys. Chem.* **96**, 8180 (1992)

[Pal99] T. Palberg, *J. Phys.: Condens. Matter* **11**, R323 (1999)

[Pan84] B. Pansu, Pi. Pieranski, Pa. Pieranski, *J. Physics (Paris)*, **45** 331 (1984)

[Pie79] P. Pieranski, J. Finney, *Acta Cryst.* **35**, 194 (1979)

[Pier79] P. Pieranski, L. Strzelecki, and J. Friedel, *J. Phys. (Paris)* **40**, 853 (1979).

[Pie80] P. Pieranski, *Phys. Rev. Lett.* **45**, 569 (1980)

[Pie83] P. Pieranski, L. Strzlecki and B. Pansu, *Phys. Rev. Lett.* **50**, 900 (1983)

[Pier83] P. Pieranski, *Contemp. Phys* **24**, 25 (1983)

[Pre07] B. G. Prevo, E. W. Hon, O. D. Velev, *J. Mater. Chem.*, **17**, 791 (2007)

[Ram07] F. Ramiro-Manzano, E. Bonet, I. Rodríguez, F. Meseguer , *Phys. Rev. E* **76**, 050401 (2007)

[Ray96] Lord Rayleigh. *"On the theory of Optical Images with reference to the Microscope"*. *Phil. Mag*., **42**, 167 (1896)

[Rob88] M.O. Robbins, K. Kremer, G.S. Grest, *J. Chem. Phys.* **88**, 3286 (1988)

[Sad00] J.E. Sader, D. Y. C. Chan, *Langmuir* **16**, 324 (2000)

[Sai94] A. Saint-James, F. Graner, F. Gallet, *Europhysics Lett.* **28**, 565 (1994)

[Sch97] M. Schmidt, H. Löwen, *Phys. Rev. E* **55**, 7228 (1997)

[Schä07] W. Schärtl. "*Light Scattering from Polymer Solutions and Nanoparticle Dispersions*". Springer Laboratory (2007)

[Schö00] H.J. Schöpe PhD thesis (2000)

[Schö01] H.J. Schöpe, T. Palberg, *J. Coll. Int. Sci.* **234**, 149 (2001)

[Schö06] Schöpe et al. *Langmuir* **22**, 1828 (2006)

[Sir89] E.B. Sirota et. al, *Phys. Rev. Lett.* **62**, 1524 (1989)

[Soo91] A. K. Sood, "*Structural ordering in colloidal suspensions"*, *Solid State Physics* vol. **45** Academic Press, Inc. (1991)

[Stra41] A. Stratton, *"Electromagnetic Theory"*, New York: Mc Graw-Hill (1941)

[Uchi98] M. Uchida, S. Horiuchi, *J. Appl. Cryst* **31**, 634 (1998)

[vBlaa04] A. van Blaaderen, *MRS Bulletin* **29**, 85 (2004)

[Vel00] O. D. Velev, A. M. Lenhoff, *Curr. Opin. in Colloid Interface Sci.* **5**, 56 (2000)

[Ver48] E.J.W. Verwvey, J.Th..G. Overbeek, *"Theory of the stability of Lyophobic Colloids"*, Elsevier, Amsterdam (1948)

[Wet01] P. Wette, H.J. Schöpe, R. Biehl, T. Palberg, *J. Chem. Phys.* **114**, 7556 (2001)

[Wet02] P. Wette, H.J. Schöpe, T. Palberg, *J. Chem. Phys.* **116**, 10981 (2002)

[Wet06] P. Wette PhD thesis (2006)

[Win86] D. H. Van Winkle, C. A. Murray, *Phys. Rev. A* **34**, 562 (1986)

[Wood97] L. V. Woodcoock, *Nature* **385**, 141 (1997)

[Wyss06] H. M. Wyss, et al. *Phys. Rev. E* **74**, 0614021 (2006)

[Xia00] Y. Xia et al., *Adv. Mater.* **12**, 693 (2000)

[Zan00] R. Zangi, S. Rize, *Phys. Rev*.E **61**, 671 (2000)

[Zol05] C.I. Zodelsi, A. Inhof, *Adv. Mater.* **17**, 924 (2005)